Numerical study of helical vortices and their instabilities

Savas Can Selçuk

To cite this version:

Savas Can Selçuk. Numerical study of helical vortices and their instabilities. Fluid mechanics [physics.class-ph]. Université Pierre et Marie Curie - Paris VI, 2016. English. NNT : 2016PA066138 . tel-01397575

HAL Id: tel-01397575

https://theses.hal.science/tel-01397575

Submitted on 16 Nov 2016

THÈSE DE DOCTORAT
DE L'UNIVERSITÉ PIERRE ET MARIE CURIE

Spécialité : Mécanique

« Ecole doctorale Sciences Mécaniques, Acoustique, Electronique & Robotique »

réalisée au

Laboratoire d'Informatique pour la Mécanique et les Sciences de l'Ingénieur (LIMSI)

présentée par

Savaş Can Selçuk

pour obtenir le grade de :

DOCTEUR DE L'UNIVERSITÉ PIERRE ET MARIE CURIE

Sujet de la thèse :

Numerical study of helical vortices and their instabilities

soutenue le 9 mai 2016

devant le jury composé de :

M. Thomas Leweke	Directeur de Recherche au CNRS, IRPHE, Marseille	Rapporteur
M. Jens Sørensen	Professeur de la Danmarks Tekniske Universitet, Lyngby, Danemark	Rapporteur
M. Pierre Brancher	Professeur de l'Université Paul Sabatier, IMFT, Toulouse	Examinateur
M. Vincent Brion	Ingénieur de Recherche à l'ONERA–DAFE, Meudon	Examinateur
M. Stéphane Popinet	Directeur de Recherche au CNRS, d'Alembert, Paris	Examinateur
M. Ivan Delbende	Maître de Conférence de l'Université Pierre et Marie Curie, Paris, LIMSI–CNRS, Orsay	Directeur de thèse
M. Maurice Rossi	Directeur de Recherche au CNRS, d'Alembert, Paris	Directeur de thèse

Remerciements

J'aimerais profiter de cet espace pour remercier toutes les personnes qui, de près ou de loin, m'ont soutenu durant ces trois années de thèse. Merci tout d'abord à mes deux encadrants, au duo de choc : Maurice Rossi et Ivan Delbende. Merci à vous deux pour m'avoir fait confiance et partagé avec moi vos idées, votre expérience et surtout votre enthousiasme à toute épreuve. Merci également pour m'avoir poussé à présenter mes travaux à de nombreuses occasions en France et à l'étranger. Plus individuellement, merci Ivan pour ta gentillesse, ta pédagogie et cette patience infinie dont tu es capable de faire preuve. Merci Maurice pour cette rigueur scientifique, cette capacité d'analyse et pour avoir toujours eu en stock la blague et/ou la vanne pour redonner le sourire et remotiver les troupes.

Tous mes remerciements aux rapporteurs Thomas Leweke et Jens Sørensen pour leurs examens minutieux de ce travail. Merci aux membres du jury, Vincent Brion et Stéphane Popinet, ainsi qu'à Pierre Brancher qui m'a fait l'honneur de le présider.

Cette thèse aurait été beaucoup plus triste si je n'avais pas aussi partagé beaucoup d'excellents moments avec les autres personnes du laboratoire. Merci Wietze pour ta constante bonne humeur, ta passion de la recherche, des steaks de deux kilos et des soirées bien arrosées. Merci également à Jalel sans qui les clusters du labo auraient déjà implosé. Aucun calcul n'aurait pu voir le jour sans tes délicates interventions sur ces machines diaboliques.

Je pense également à tous les doctorants et doctorantes qui ont marqué de leurs empreintes leurs passages au LIMSI. Merci Ludomir, pour ton aide toujours précieuse et efficace sur Matlab. Loïc, Charles, Christelle, Ma, Zhenlan, Lionel , merci à tous pour les moments sympa qu'on a passés autour d'un verre et d'un repas. Merci Florian (aka the Hipster) pour les soirées feutrées et pour la "touch" Germano-Argentine que tu as apportée durant ton séjour.

J'ai également une pensée pour Eli, Marko et Shrayes qui m'ont toujours affectueusement soutenus. Merci également aux nouveaux et particulièrement à Julien pour avoir égayé le bureau durant ma dernière année.

Je remercie aussi les stagiaires passés au labo, notamment Antoine (aka Macgyver) pour son humour toujours tranchant. Merci aussi à la nouvelle équipe méca fort sympathique : William pour les explications (très) détaillées, Chloé pour l'accent toulousain ensoleillé, Aurore pour les tourbillons éclatés, Moubarak et Fadila pour leurs avis éclairés, Valentin pour son sex-appeal infini et Robin parce qu'il encaisse (presque) bien les pintes.

J'aimerais aussi saluer mes frères d'armes de la fac, ceux avec qui j'ai bataillé de longues heures dans les bibliothèques de Jussieu pour décrocher la licence et le master : Guillaume Le Clerc pour son humour unique et décalé (et les pâtes/steak-hachées entre deux cours), Ronan Serre pour sa bienveillance et sa vision poétique des choses et le duo Jo-Sung Lee/Jeremy Oignet pour avoir toujours assuré le quota de blagues pourries (mais toujours drôles j'avoue).

Enfin, mes remerciements les plus vifs vont à ma famille : à ma mère qui a énormément sacrifié pour nous et à mon frère Mete qui a toujours été solide dans les moments les plus rudes de notre histoire. Merci Mete d'avoir été un pilier sur lequel j'ai pu m'appuyer. Merci Intissar pour avoir été à mes cotés durant toutes ces années et d'avoir toujours cru en moi. Merci également pour les encouragements constants et sans faille malgré mes humeurs changeantes et capricieuses ...

... à tous et à toutes, un grand merci.

Contents

Chapter 1

Introduction

Contents

In this chapter, we briefly introduce the general context of the study and focus on the helical rotor flows.

1.1 Context

The present Ph.D. thesis deals with a fundamental topic in fluid mechanics: the structure, dynamics and instabilities of concentrated vortices having a helical geometry. Despite being of fundamental nature, numerous real life applications exist: indeed, any rotating blade in a fluid (air or liquid) sheds vortices in its wake, their structure having a helical geometry.

1.1.1 Renewable energy: wind turbines

Among all possible applications, one directly concerns the current economical and political context of the renewable energies. With our fossil-fuel supplies running lower every day and the CO_2 concentration in the atmosphere increasing, governments and companies are heavily investing in the development of alternate technologies to exploit the power of clean and renewable energy sources. Thanks to its potential to produce large quantities of energy without generating greenhouse gases, the extraction of wind energy with wind turbines is currently one of the most advanced technology. In history, apart from the sailing ship, windmills (the ancestor of the wind turbines) are the oldest devices to utilize the wind energy. The first documented use of wind energy on land dates 200 years B.C. (Ivanell et al., 2007). According to the American Wind Energy Foundation, « In China, water was pumped with simple windmills while the first vertical-axis windmills with woven reed sails were grinding grain in Persia and the Middle East. » While mostly used for food production for more than one thousand years, the discovery and development of the electric

Figure 1.1 – Wake of wind turbines revealed by fog (Hasager et al., 2013) on the offshore wind farm, Horns Rev 1 in the North sea. Turbines within the array can be seen to be operating in the wake of upstream turbines. (80 wind turbines, 160 MW of production capacity.)

power during the late 19th century led to a new purpose for wind power: provide electricity to houses located too far away from the central power plants. This was the motivation source for the pioneering work of the Danish inventor Poul La Cour who was among the first to generate electricity from wind power. Since the 20th century, the interest in wind energy varied according to the oil prices. During the 1973 crisis, the high oil prices had a decisive impact on the interest for wind power and on the research on wind turbines. Today, the continuous evolution of the technologies and techniques has led wind turbines to become the biggest rotating devices on earth. The research in the field has focussed on the rotor efficiency to convert energy. In order to further improve the production capacity of wind farms as well as the quality of predictions, fundamental studies on the wake are found necessary. In particular, the study of instabilities in such helical vortex systems is a first step towards the prediction of the complex wake dynamics.

1.1.2 Helicopter wakes and VRS

In stationary flight conditions, helicopter wakes are constituted of helical vortices shed below the rotor towards the helicopter fuselage. A phenomenon, which is well-known to helicopter manufacturers and pilots, but still poorly understood and even less controlled, is the transition of this wake to a so-called Vortex Ring State (VRS). It occurs when the vertical descent speed of the helicopter exceeds a certain limit: the blade tip vortices accumulate in the rotor plane, leading to a lift crisis and highly unsteady flow, which can cause a loss of control and a helicopter crash. This phenomenon, which has caused a number of fatal accidents, sets a forbidden range of descent speeds. Current helicopter flight rules include a considerable margin, due to a lack of physical understanding of this transition but helicopter manufacturers and operators wish to reduce this margin. The goal is to reduce the descent time and the associated acoustic nuisances. Fundamental mechanisms responsible of the transition thus need to be better understood in order to elaborate control strategies. A link with rotor wake instabilities has been established by Bolnot (2012) using a vortex ring analogy. Instabilities in helical vortex systems are thus pertinent in this context.

1.1.3 The ANR project: HELIX

This thesis is part of a project entitled HELIX under the leadership of Thomas Leweke and funded by the French National Agency for Research (ANR). This project covers the years 2013 – 2016 and involves several laboratories and partners:

- IRPHE, Aix-Marseille Université: Thomas Leweke, Stéphane Le Dizès, Malek Abid, Mohamed Ali, Umberto Quaranta and Francisco J. Blanco-Rodriguez.
- LIMSI-CNRS: Ivan Delbende
- ∂'Alembert-Université Pierre et Marie Curie: Maurice Rossi.

The aim of the project is to improve our current understanding on the dynamics and instabilities of helical vortex systems, with relevance to applications involving flows around rotors. The project is mainly divided into four distinct but complementary tasks:

1. finding numerical (quasi)-steady solutions involving one or several helical vortices with a central hub vortex. It is performed by the LIMSI and IRPHE teams with two different approaches: the first computes the idealised configuration of an infinite and spatially periodic helical flow while the second uses a semi-infinite approach with the actuator line technique.
2. studying the instability modes of these solutions.
3. running experiments on one- or two-bladed rotor wakes in a water channel and triggering instabilities by modulating the rotation speed
4. use the above findings to model the dynamics of helical flows encountered in applications such as helicopter and wind turbines or more generally for flows around rotors.

The present thesis contributes mainly to the first and second tasks of this project.

1.2 Flows behind rotors

Rotor systems are commonly used in a broad range of applications where a transfer of energy between a mechanical device and the surrounding flow is needed. Here, the rotor refers to a set of blades which rotates to generate a flow perpendicular to the rotor plane. Depending on the application considered, its size, the number of blades and the global complexity of the design varies. These differences characterize the vast range of operating regimes that a rotor can perform. The resulting list of applications is thus very rich: rotor systems are found in wind turbines, helicopters, marine propellers, pumps, vent systems and some aircrafts. Most of these applications (all except the wind turbines) rely on rotor systems to entrain a fluid motion by providing rotational kinetic energy to the latter. Conversely, wind turbines are conceived to extract electrical energy from the rotor rotations entrained by an incoming wind. In all these applications the rotor system sheds in its wake large helical vortex structures embedded in a shear layer. The wakes emanating from rotors are known as rotor wakes and the associated vortex structures are always considered to be nuisances as they induce noises, increased loads on blades and stress on the structures. For the past years, the research on the field have been mostly focused on the power conversion efficiency and the endurance of the rotor devices while little interest was shown to their wakes.

1.2.1 Wind turbine wakes: the near- and far-wake

In rotor-wake literature, the wake of a wind turbine is divided into two separated regions: the near- and the far-wake. The near-wake refers to the region directly downstream the rotor plane (up to, approximately, one rotor diameter) where the flow characteristics are

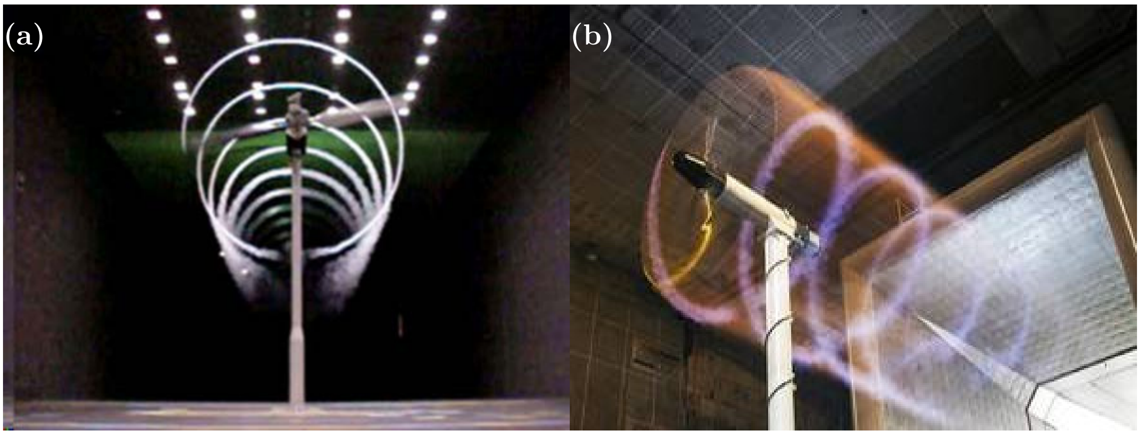

Figure 1.2 – Tip vortex visualisation on (a) the NREL wind turbine at NASA-AMES (Schreck, 2002) (b) the New-Mexico (Snel et al., 2007).

directly linked to the rotor's design and its aerodynamic properties. In this region, the flow field is principally constituted of large-scale and coherent vortical structures. The far-wake refers to the region beyond the near-wake, where the flow has transitioned and fully developed into turbulence. The far-wake region results from the convection and turbulent diffusion of coherent structures and is characterised by a momentum deficit and increased levels of turbulent intensity. The far-wake dynamics is mostly considered independent of the near-wake but results from its spatial evolution (Vermeer et al., 2003). Far-wake analyses are more oriented on wake-structure interactions, wake-atmospheric boundary layer interactions and mutual influence of multiple wind-turbine wakes when the turbines are placed in arrays as in wind farms (see figure 1.1). Near-wake studies focus on the creation, evolution and stability analysis of the coherent vortex structures emanating from the rotor blades.

1.2.2 Experiments and numerical computations

Helical vortices can be observed for instance in figures 1.2-a and 1.2-b, when revealed by the smoke released at the tip of the rotor blades. Most of the experimental results exposed in the literature about the near wake vortices are obtained from small scale experimental studies performed in controlled environments. The reasons for this are multiple. On one hand, field experiments with full scale wind turbines provide invaluable data, but due to the highly chaotic nature of the inflow conditions, clear exposure of the physical phenomena and analysis of the underlying mechanisms are challenging tasks. On the other hand, wind tunnel experiments on large-scale rotors would lead to the most relevant results but, due to the financial cost involved by such projects, only few documented sources exist in the literature (see Schreck (2002) and Snel et al. (2007) for detailed reviews see Vermeer et al. (2003) and Nemes (2015)). While restricted to a lower range of Reynolds numbers, the laboratory experiments provide a simplified but favourable approach that can help to elucidate the rather complex wake dynamics.

Numerical simulations are an efficient and complementary tool to understand the aerodynamics of rotor wakes. They are mainly divided into two categories. The numerical studies can be performed with or without the rotor present in the computational domain. The former is oriented mostly towards engineering problems such as rotorcraft aerodynamics, aeromechanic performance or noise reduction. An example of such simulation is presented in figure 1.3, where a snapshot of a rotor model and its near wake is plotted. The (purple colored) helical vortices are embedded within a turbulent flow with small scale structures (green colored). While providing insight into a, as much as possible, realistic flow dynam-

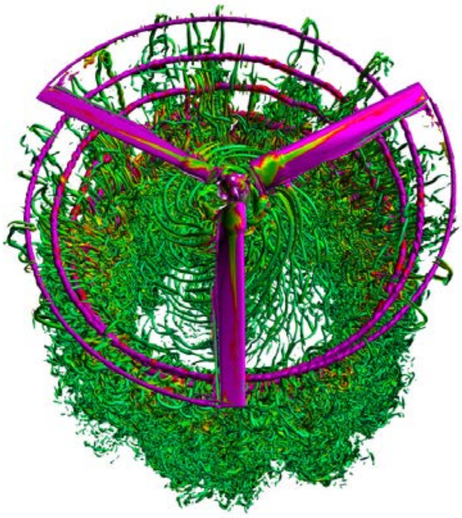

Figure 1.3 – Navier-Stokes simulation of a V-22 Osprey rotor in hover, using adaptive mesh refinement (AMR) and a Spalart-Allmaras/detached eddy simulation (DES) turbulence model. Vortices are rendered with the q-criterion. Magenta indicates high vorticity, blue indicates low vorticity. Neal Chaderjian, NASA/Ames. This study used 1,536 cores on NASA's Pleiades supercomputer

ics, the clear separation of the different physical phenomena remains difficult. With the rotor model in the computational domain, the computational cost is also increased due to the requirement that one has to resolve the boundary layer (1,536 cores in 1.3 with a supercomputer).

To overcome the latter difficulty, several techniques such as the actuator disc method (Sørensen and Myken, 1992) or the actuator line method (Ivanell et al., 2009) have been used. These methods represent rotors by equivalent forces distributed on a permeable disc or on lines in a flow domain. Such methods were applied for the prediction of a single wind turbine wake but also for the prediction of power extraction by a whole wind farm (Nilsson et al., 2015).

An additional possibility, although idealised, is to take advantage of an invariance of the problem. The rotor wakes shown in figures 1.2 and 1.3 all display in the near wake region, large vortex structures which have, at least locally, a helical symmetry i.e. the structures are invariant through a combined axial translation and a rotation about the same axis.

This thesis focuses on vortices with imposed helical symmetry. This reduces the fully three-dimensional problem to a two-dimensional one but still preserves three-dimensional effects (curvature and torsion). Such an approach necessarily filters out ingredients such as wake spatial development, fluid-rotor interaction and turbulence. On the contrary it focuses on the fundamental physical mechanisms (induction and diffusion).

1.3 Helically symmetric vortices and their instabilities

In the literature, theoretical studies used this idealised formulation to derive the dynamics of helical vortex systems in the inviscid framework: equilibrium states (Hardin, 1982), (Dritschel, 1991), (Ricca, 1994), (Kuibin and Okulov, 1998), (Wood and Boersma, 2001), (Fukumoto and Okulov, 2005), (Lucas and Dritschel, 2009) and their instabilities (Widnall, 1972), (Gupta and Loewy, 1974), (Okulov, 2004), (Okulov and Sørensen, 2007), (Hattori and Fukumoto, 2009), (Hattori and Fukumoto, 2014).

Among the studies devoted to equilibria, some concern thin-core helical vortices where the main problem is to remove the singular behaviour of curved filaments to deduce the actual dynamics (angular velocity, induced velocity). Lucas and Dritschel (2009) by contrast exhibit a family of helical vortex equilibria with arbitrary core size. Their approach is based on the helically symmetric Euler equations and consists in finding helical patch solutions steady in some rotating frame, imposing geometrical constraints on the centroid location and the vortex core size at fixed pitch. However all these studies pertain to inviscid flows, and one of the goals of the present work is to investigate and characterise viscous quasi-equilibrium that is reached by helical vortex systems.

Widnall (1972) first predicted the stability features of helical vortices. She performed the linear stability analysis of a helical vortex filament with respect to sinusoidal perturbations. She found that the system was subject to three types of unstable mode: a long wavelength mode, a mutual-inductance mode and a short wavelength mode. This work was extended by Gupta and Loewy (1974) to several helical vortices forming a regular array. He found modes analogous to those obtained for one single vortex and additional ones arising from the mutual interaction between distinct vortices. It is noteworthy that in the limit of infinite wavelengths, these latter modes are compatible with the helical symmetry constraint. Okulov (2004) focused specifically on these helically symmetrical modes in arrays of N vortices with circular cores and constant vorticity. He showed that such systems are unstable when the helical pitch is smaller than a threshold value. Later, in order to study the more realistic case of rotor wakes, Okulov and Sørensen (2007) investigated the effect of a central hub vortex. They found that the stability of such flows strongly depends on the vorticity profile in the core and that the central hub has a destabilizing effect.

They are very few experimental studies of instabilities in the literature.

The IRPHE partner (Bolnot, 2012), (Bolnot et al., 2014), (Quaranta et al., 2015) has an experimental facility with a water channel in which machined one- and two-bladed rotors can be exploited to generate carefully monitored helical wakes. Basic states are characterised using PIV measurements, and quantities such as velocity profile, circulation and core size are determined. The Widnall instability modes are forced by modulating the rotor angular velocity and their temporal growth rates are measured as a function of the imposed wavelength using dye visualisations. A very good agreement is obtained between the filamentary theory and the experiments. Felli et al. (2011) studied the spatial development of marine propeller wakes for two to four blades. They observed the growth of perturbations up to high amplitudes, which causes vortex groupings and eventually dissipation of the coherent structures. The vortices are observed by making the tip vortices cavitating by lowering the pressure in the test section. This also reveals the presence, at the axis, of the hub vortex which also takes part to the instability process.

A numerical code called HELIX has been developed at LIMSI-CNRS and d'Alembert-UPMC (Delbende et al., 2012). This code implements the helical formulation of the incompressible Navier-Stokes equations: it is quasi-two dimensional, based on a pseudo-spectral method in θ and finite differences in r. In a previous PhD work, Benjamin Piton (2011) performed the numerical analysis of the dynamics of some helical vortex systems. For a single helical vortex, he computed quasi-steady states for different helical pitches and Reynolds numbers, and analysed the angular rotation. He observed that for such vortices, the core diffuses according to a law close to that of classical two-dimension diffusion. He also focussed on the merging of two helical vortices. At large helical pitch, the merging was found very similar to that of two-dimensional vortices, however the helical geometry slows down the process. A criterion for merging was proposed. At medium pitch, the merging was found to become purely diffusive. At small pitch, a convective merging between successive coils was observed, resulting from the instability predicted by Okulov (2004). However, at low Reynolds numbers, this merging process becomes purely diffusive, as the instability is killed by viscosity.

1.4 Goal and personal contributions

The present work numerically investigates these instabilities using the Navier-Stokes equations linearised in the vicinity of imposed helically symmetric basic states: one, two and three tip vortices with and without the hub vortex. The time evolution of these vortex systems, when perturbed by unstable linear modes, are also computed in the nonlinear regime within the helical symmetry framework.
In order to achieve these objectives, numerous (mostly numerical) tasks were performed during these three years. The following paragraph summarizes my personal contributions to this PhD work. The numerical code HELIX was available and had been exploited by the previous PhD student Benjamin Piton using polar meshes with evenly spaced grid points in the radial direction. This code was first generalised for irregular grids, which implied to rewrite all the discretization matrices and nonlinear terms related to the Navier-Stokes and Poisson equations. This code was thereafter linearised in the vicinity of a frozen state and an Arnoldi algorithm within the helical framework was implemented in order to extract the dominant stability modes. The choice of implementing the algorithm from scratch rather than using libraries has been made for pedagogical reasons and also for a better control on the problem parameters. The structures of the solutions (such as the linear modes or nonlinear solutions) were analysed and investigated with the help of home-made tools (high order and accurate interpolations, optimisation procedures, integrations and spectral analysis). This handful of routines allowed for the successful comparisons of our numerical results with the theoretical ones obtained by our IRPHE partners with an asymptotic analysis (Blanco-Rodríguez et al., 2015). A particular attention was paid to the numerical implementation of Lagrangian particle tracking, for both passive and inertial particles. This tool enabled to highlight the complex trajectories prevailing in such vortex systems. The second linear code HELIKZ, aimed at investigating the stability of helical flows with respect to perturbations breaking the helical symmetry, has been available during the PhD. The Arnoldi algorithm was implemented for this general three-dimensional case using complex primitive variables. As the base flow in HELIKZ is provided by a preliminary run of the HELIX code, a whole battery of routines were also developed to automate and ease the management of the computations.

1.5 Outline

This manuscript is organised as follows. The first part (chapters 2 to 7) is dedicated to the numerical computation and characterisation of helically symmetric vortices. The second part (chapters 8 to 11) deals with the obtention of linear instability modes and their nonlinear evolution.

Chapter 2 introduces the framework of the helical symmetry and the governing equations for incompressible unbounded flows. Numerical aspects of the DNS code (HELIX) used in this work are presented in chapter 3. This includes the details on the numerical methods and the discretisation of the governing equations. An inviscid filamentary model is also derived using a cut-off technique. The equations of motion along with numerical validations are given in chapter 4. Chapter 5 presents the physical quantities (helix radius, angular velocity, vortex core size and ellipticity) which characterise the helical vortices obtained by DNS as well as their numerical computation. This characterisation is applied to the quasi-steady evolution of a single helical vortex 6. The streamline topology and the consequences for passive particle trajectories are analysed. The internal structure of the velocity field within the helical vortex core is studied in chapter 7: quasi-equilibrium solutions are decomposed into multipolar contributions and compared with the analytical predictions given by the IRPHE partner.

Chapter 8 tackles the principles linear stability analysis for helical flows, the Arnoldi method of mode extraction, its implementation and validation. This analysis is applied in chapter 9 to several vortex configurations: two and three helical vortices with/without a central hub vortex. The nonlinear dynamics of helical systems subject to these unstable modes is characterised in chapter 10. In chapter 11, the principles of the linear stability analysis are extended to perturbations breaking the helical symmetry. A new linear code HELIKZ is introduced and coupled to an Arnoldi procedure. Results obtained in this context are presented and analysed.

Chapter 12 summarises the results and discusses possible perspectives to this work.

Chapter 2

Navier-Stokes equations for helical flows

Contents

In the theory of shear flows, it is usual to assume local parallel flow approximation to study linear or nonlinear instability properties of jets, wakes, boundary layers... This local approach means that the slow streamwise variation is neglected. In rotor wakes, one may assume a similar type of approximation in which the base flow is assumed to satisfy a *helical symmetry* as illustrated in figure 2.1. For this particular symmetry, any vector

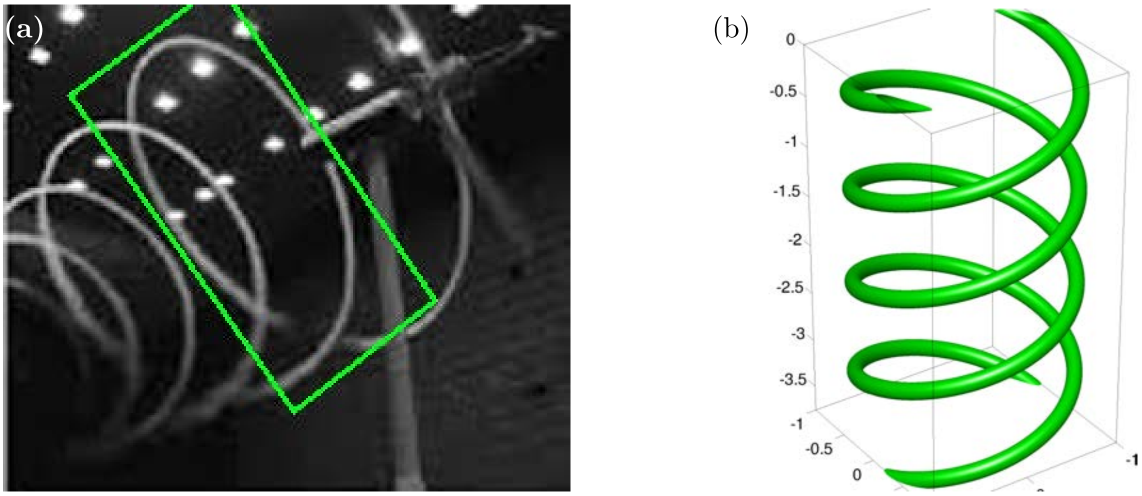

Figure 2.1 – (a) Near wake of the NREL wind turbine at NASA-AMES. (b) Numerical model: a vortex with enforced helical symmetry.

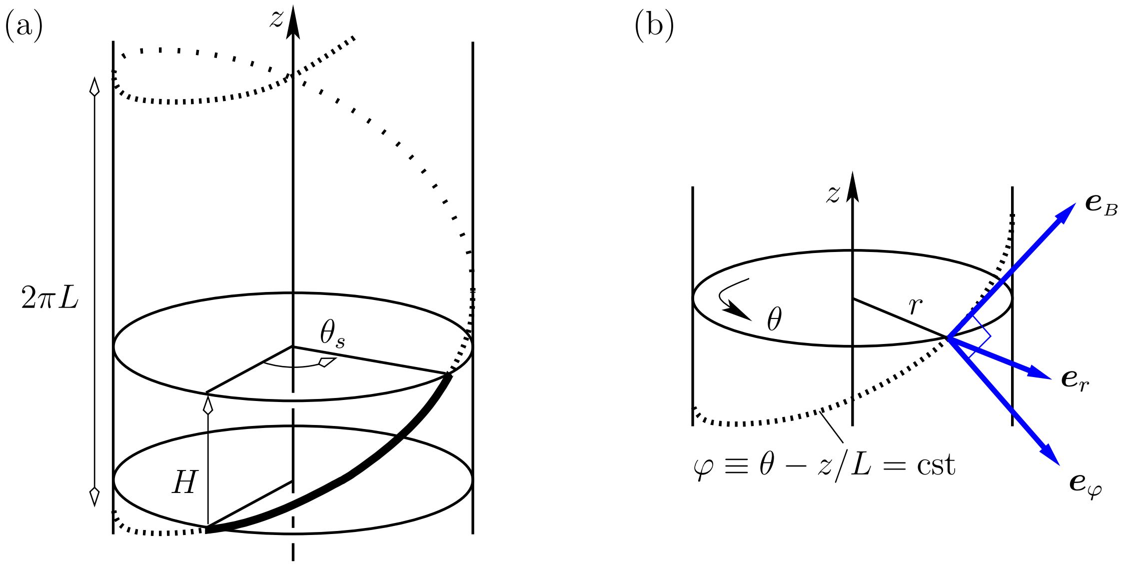

Figure 2.2 – (a) Geometrical parameters defining the helical symmetry. (b) Local orthonormal *helical* basis $(\boldsymbol{e_r}, \boldsymbol{e_B}, \boldsymbol{e_\varphi})$.

field remains unaffected by the combined actions of two continuous transformations: a translation along a given axis combined to a rotation about the same axis. Here, we present the helical symmetry (section 2.1), the equations governing the dynamics (section 2.2) and their spectral formulation (section 2.3), together with the boundary conditions at the centre and the edge of the circular domain (sections 2.4 and 2.5).

2.1 Helical symmetry

In the cylindrical coordinate basis $(\boldsymbol{e_r}, \boldsymbol{e_\theta}, \boldsymbol{e_z})$, the helical symmetry implies that the flow characteristics remain invariant though combined translation of magnitude H along the axis and a rotation of angle $\theta_s = H/L$ around the same axis (see figure 2.2-a) where $2\pi L$ is the *helix pitch*. The flow characteristics thus remain invariant along helical lines $\varphi = cst$ with

$$\varphi \equiv \theta - z/L, \tag{2.1}$$

and have a spatial periodicity of $2\pi L$ along the z-axis. The sign of the so-called *reduced pitch* L defines the direction of the helix, $L > 0$ corresponds to a right-handed helix while $L < 0$ corresponds to a left-handed one. For $L \to \pm\infty$, helical lines tend to be straight lines and the velocity field becomes two dimensional.

In order to implement the helical symmetry, we introduce an orthonormal *helical* basis $(\boldsymbol{e_B}, \boldsymbol{e_r}, \boldsymbol{e_\varphi})$ depicted in figure 2.2-b. It consists of a vector locally tangent to the helical lines called the *Beltrami* vector:

$$\boldsymbol{e_B} = \alpha\left(r\right)\left(\boldsymbol{e_z} + \frac{r}{L}\boldsymbol{e_\theta}\right) \tag{2.2}$$

with the r-dependent normalisation factor

$$\alpha(r) = \left(1 + \frac{r^2}{L^2}\right)^{-1/2}, \tag{2.3}$$

the unitary radial vector $\boldsymbol{e_r}$ and a third vector

$$\boldsymbol{e_\varphi} = \boldsymbol{e_B} \times \boldsymbol{e_r} = \alpha\left(r\right)\left(\boldsymbol{e_\theta} - \frac{z}{L}\boldsymbol{e_z}\right). \tag{2.4}$$

In this basis, any velocity field can be expressed as :

$$\boldsymbol{u} = u_r\, \boldsymbol{e_r} + u_B\, \boldsymbol{e_B} + u_\varphi\, \boldsymbol{e_\varphi} \tag{2.5}$$

with

$$\begin{aligned} u_r\,(r,\theta,z) &= \boldsymbol{u}\cdot\boldsymbol{e_r}, & (2.6)\\ u_B\,(r,\theta,z) &= \boldsymbol{u}\cdot\boldsymbol{e_B} = \alpha(r)\left(u_z + \frac{r}{L}u_\theta\right), & (2.7)\\ u_\varphi\,(r,\theta,z) &= \boldsymbol{u}\cdot\boldsymbol{e_\varphi} = \alpha(r)\left(u_\theta - \frac{r}{L}u_z\right). & (2.8)\end{aligned}$$

When the helical symmetry holds, the above components are constant along the helical lines

$$\boldsymbol{e_B}\cdot\boldsymbol{\nabla} u_r = \boldsymbol{e_B}\cdot\boldsymbol{\nabla} u_B = \boldsymbol{e_B}\cdot\boldsymbol{\nabla} u_\varphi = 0, \tag{2.9}$$

or, stated equivalently, solutions depend on two variables of space (r,φ) instead of the three variables (r,θ,z). A helically symmetric velocity field $\boldsymbol{u}$ is thus given by

$$\boldsymbol{u}\,(r,\varphi,t) = u_r\,(r,\varphi,t)\ \boldsymbol{e_r}\,(\theta) + u_B\,(r,\varphi,t)\ \boldsymbol{e_B}\,(r,\theta) + u_\varphi\,(r,\varphi,t)\ \boldsymbol{e_\varphi}\,(r,\theta)\,. \tag{2.10}$$

Note, however, that $\boldsymbol{e_B}$ and $\boldsymbol{e_\varphi}$ have a dependency with respect to (r,θ), not to (r,φ).

2.1.1 Expression of differential operators for helical fields

The expression of differential operators is derived from their definitions in cylindrical coordinates. First, partial derivatives are computed with the change of variable $(r,\theta,z)\to(r,\varphi)$:

$$\begin{aligned} \frac{\partial}{\partial\theta} &= \frac{\partial\varphi}{\partial\theta}\frac{\partial}{\partial\varphi} = \frac{\partial}{\partial\varphi}, & (2.11)\\ \frac{\partial}{\partial z} &= \frac{\partial\varphi}{\partial z}\frac{\partial}{\partial\varphi} = -\frac{1}{L}\frac{\partial}{\partial\varphi}. & (2.12)\end{aligned}$$

The gradient of a scalar field f is then given by:

$$\boldsymbol{\nabla} f = \frac{\partial f}{\partial r}\,\boldsymbol{e_r} + \frac{1}{r}\frac{\partial f}{\partial\theta}\,\boldsymbol{e_\theta} + \frac{\partial f}{\partial z}\,\boldsymbol{e_z} = \frac{\partial f}{\partial r}\,\boldsymbol{e_r} + \frac{1}{r\alpha}\frac{\partial f}{\partial\varphi}\,\boldsymbol{e_\varphi}. \tag{2.13}$$

As expected $\boldsymbol{\nabla} f$ has no component along $\boldsymbol{e_B}$, i.e. along helical lines. The divergence of a vector field $\boldsymbol{u}$ is given by:

$$\boldsymbol{\nabla}\cdot\boldsymbol{u} \equiv \frac{1}{r}\frac{\partial\,(ru_r)}{\partial r} + \frac{1}{r}\frac{\partial u_\theta}{\partial\theta} + \frac{\partial u_z}{\partial z} = \frac{1}{r}\frac{\partial\,(ru_r)}{\partial r} + \frac{1}{r\alpha}\frac{\partial u_\varphi}{\partial\varphi}, \tag{2.14}$$

which is up to the factor $\alpha(r)$ similar to the two-dimensional divergence operator in the cylindrical coordinate system (r,φ). Finally, the curl of $\boldsymbol{u}$ reads:

$$\boldsymbol{\nabla}\times\boldsymbol{u} = \frac{1}{r}\frac{\partial}{\partial\varphi}\left(\frac{u_B}{\alpha}\right)\boldsymbol{e_r} - \alpha\frac{\partial}{\partial r}\left(\frac{u_B}{\alpha}\right)\boldsymbol{e_\varphi} + \left\{\frac{1}{r\alpha}\frac{\partial}{\partial r}\,(r\alpha u_\varphi) - \frac{1}{r\alpha}\frac{\partial}{\partial\varphi}u_r + \frac{2}{L}\alpha^2 u_B\right\}\boldsymbol{e_B}. \tag{2.15}$$

2.1.2 Incompressibility for helical fields.

Flows studied in the present thesis are incompressible, that is

$$\boldsymbol{\nabla} \cdot \boldsymbol{u} = 0. \tag{2.16}$$

From expression (2.14), this condition implies the existence of a stream function $\Psi(r, \varphi, t)$ such that

$$u_r = \frac{1}{r}\frac{\partial \Psi}{\partial \varphi}, \tag{2.17}$$

$$u_\varphi = -\alpha \frac{\partial \Psi}{\partial r}. \tag{2.18}$$

The velocity field $\boldsymbol{u}$ of a general incompressible helical flow can then be reduced to only two scalar fields, namely its helical component $u_B(r, \varphi, t)$ along $\boldsymbol{e_B}$ and the stream function $\Psi(r, \varphi, t)$:

$$\boldsymbol{u}(r, \varphi, t) = u_B(r, \varphi, t)\, \boldsymbol{e_B} + \alpha(r) \boldsymbol{\nabla} \Psi(r, \varphi, t) \times \boldsymbol{e_B}. \tag{2.19}$$

From equations (2.15) and (2.17)-(2.18), the velocity component, u_B/α plays for vorticity $\boldsymbol{\omega} = \boldsymbol{\nabla} \times \boldsymbol{u}$ the role of the stream function for velocity

$$\omega_r = \frac{1}{r}\frac{\partial}{\partial \varphi}\left(\frac{u_B}{\alpha}\right), \tag{2.20}$$

$$\omega_\varphi = -\alpha \frac{\partial}{\partial r}\left(\frac{u_B}{\alpha}\right). \tag{2.21}$$

As a consequence, $\boldsymbol{\omega}$ can be expressed with only two scalar fields, namely its vorticity component ω_B and the velocity component u_B/α

$$\boldsymbol{\omega}(r, \varphi, t) = \omega_B(r, \varphi, t)\, \boldsymbol{e_B} + \alpha(r) \boldsymbol{\nabla}\left(\frac{u_B(r, \varphi, t)}{\alpha}\right) \times \boldsymbol{e_B}. \tag{2.22}$$

Using equations (2.15), (2.17) and (2.18), the helical component ω_B can be expressed as :

$$\omega_B = -\mathbb{L}\, \Psi + 2\frac{\alpha^2}{L} u_B \tag{2.23}$$

where the linear operator $\mathbb{L}$ stands for:

$$\mathbb{L}\,(.) \equiv \frac{1}{r\alpha}\frac{\partial}{\partial r}\left(r\alpha^2 \frac{\partial}{\partial r}(.)\right) + \frac{1}{r^2 \alpha}\frac{\partial^2}{\partial \varphi^2}(.)\,. \tag{2.24}$$

Equation (2.23) connects the stream function Ψ to vorticity component ω_B and velocity component u_B. This $\Psi - \omega_B - u_B$ relation turns out to be the generalisation of the two-dimensional stream function-vorticity ($\Psi - \omega$) formulation for helical flows. The direct consequence of (2.23) is that the knowledge of ω_B and u_B gives access to Ψ and thereafter to all other variables through equations (2.17)-(2.18) and (2.20)-(2.21). Since the dynamics has not been taken into account yet, the above relations can be used in any area of physics when helically symmetric and divergence-free fields are present (magneto-hydrodynamics, plasma physics, ...).

2.2 Governing equations for helically symmetric flows

Two dynamical equations, one for u_B and one for ω_B, are needed to obtain the time evolution of the full system. The starting point is the Navier-Stokes equations

$$\frac{\partial}{\partial t}\boldsymbol{u} + \boldsymbol{u} \cdot \boldsymbol{\nabla} \boldsymbol{u} = -\frac{1}{\rho}\boldsymbol{\nabla} p + \nu \boldsymbol{\nabla}^{\mathbf{2}} \boldsymbol{u}, \tag{2.25}$$

$$\boldsymbol{\nabla} \cdot \boldsymbol{u} = 0, \tag{2.26}$$

with p the pressure field, ρ the uniform density of the fluid and ν its kinematic viscosity. In the incompressible framework, the following vectorial relations can be used

$$\boldsymbol{u}\cdot\boldsymbol{\nabla}\boldsymbol{u}=\boldsymbol{\omega}\times\boldsymbol{u}+\boldsymbol{\nabla}\left(\frac{\boldsymbol{u}^2}{2}\right),$$
$$\boldsymbol{\nabla}^2\boldsymbol{u}=-\boldsymbol{\nabla}\times\boldsymbol{\omega}$$

to rewrite equation (2.25) as

$$\frac{\partial}{\partial t}\boldsymbol{u}+\boldsymbol{\omega}\times\boldsymbol{u}=-\boldsymbol{\nabla}\left(\frac{p}{\rho}+\frac{\boldsymbol{u}^2}{2}\right)-\nu\boldsymbol{\nabla}\times\boldsymbol{\omega}. \qquad (2.27)$$

Equation for vorticity is obtained by taking the curl of (2.27):

$$\frac{\partial}{\partial t}\boldsymbol{\omega}+\boldsymbol{\nabla}\times(\boldsymbol{\omega}\times\boldsymbol{u})=-\nu\boldsymbol{\nabla}\times(\boldsymbol{\nabla}\times\boldsymbol{\omega}). \qquad (2.28)$$

Projecting equations (2.27)-(2.28) on the *Beltrami* vector $\boldsymbol{e_B}$ leads to the two needed scalar equations. The first one for $u_B\,(r,\varphi,t)$ reads:

$$\frac{\partial}{\partial t}u_B+NL_u=VT_u \qquad (2.29)$$

where the viscous term is given by

$$VT_u\equiv\nu\left[\mathbb{L}\left(\frac{u_B}{\alpha}\right)-\frac{2\alpha^2}{L}\omega_B\right], \qquad (2.30)$$

and the nonlinear term by

$$NL_u\equiv\boldsymbol{e}_B\cdot[\boldsymbol{\omega}\times\boldsymbol{u}]=\omega_r\,u_\varphi-\omega_\varphi\,u_r\,. \qquad (2.31)$$

Thanks to relation (2.9), the pressure field p disappears from the equation for u_B. The second equation, for $\omega_B\,(r,\varphi,t)$, reads:

$$\frac{\partial}{\partial t}\omega_B+NL_\omega=VT_\omega \qquad (2.32)$$

where the viscous term is given by

$$VT_\omega\equiv-\nu\,\boldsymbol{e}_B\cdot\boldsymbol{\nabla}\times[\boldsymbol{\nabla}\times\boldsymbol{\omega}]=\nu\left[\mathbb{L}\left(\frac{\omega_B}{\alpha}\right)-\left(\frac{2\alpha^2}{L}\right)^2\omega_B\right]+\nu\,\frac{2\alpha^2}{L}\mathbb{L}\left(\frac{u_B}{\alpha}\right), \qquad (2.33)$$

and the nonlinear term by

$$NL_\omega\equiv\boldsymbol{e}_B\cdot\boldsymbol{\nabla}\times[\boldsymbol{\omega}\times\boldsymbol{u}]\,. \qquad (2.34)$$

This latter quantity can be reduced after some algebra to:

$$NL_\omega=\frac{1}{r\alpha}\left\{\frac{\partial}{\partial r}(r\alpha g_\varphi)-\frac{\partial}{\partial\varphi}g_r\right\}+\frac{2\alpha^2}{L}g_B+\frac{\alpha}{L^2}\frac{\partial}{\partial\varphi}\left(u_B^2\right), \qquad (2.35)$$

where

$$g_\varphi=\omega_B\,u_r,\quad g_r=-\omega_B\,u_\varphi,\quad g_B=\omega_r\,u_\varphi-\omega_\varphi\,u_r.$$

The dynamics of helically symmetric flows are obtained through the set of equations (2.29)-(2.35) along with (2.23) which completely define the problem. The periodicity of the variables along φ is exploited and a pseudo-spectral D.N.S. code is built on this formulation. In appendix A, the helical rate of strain tensor is given for the sake of completeness.

2.3 Spectral formulation of the governing equations.

In order to solve them, one formulates equations (2.29)-(2.35) in spectral space. Quantities $\omega_B(r,\varphi,t)$ and $u_B(r,\varphi,t)$ are 2π-periodic with respect the variable φ and these quantities can be expanded in Fourier series along φ:

$$u_B(r,\varphi,t) = \sum_{m=-\infty}^{+\infty} u_B^{(m)}(r,t)\, e^{\mathrm{i}m\varphi}, \tag{2.36}$$

$$\omega_B(r,\varphi,t) = \sum_{m=-\infty}^{+\infty} \omega_B^{(m)}(r,t)\, e^{\mathrm{i}m\varphi}, \tag{2.37}$$

where $u_B^{(m)}(r,t)$, and $\omega_B^{(m)}(r,t)$ are complex Fourier coefficients. Equations (2.29) and (2.32) are recast for each Fourier mode m. A distinction has to be made between the case $m \neq 0$ and the case $m = 0$, as their boundary conditions and numerical resolution strongly differ.

2.3.1 Modes $m \neq 0$

For mode $m \neq 0$, the pair $\left(\omega_B^{(m)}, u_B^{(m)}\right)$ is obtained by solving equations (2.29) and (2.32) projected on each mode m

$$\frac{\partial}{\partial t}\omega_B^{(m)} + NL_\omega^{(m)} = VT_\omega^{(m)}, \tag{2.38}$$

$$\frac{\partial}{\partial t}u_B^{(m)} + NL_u^{(m)} = VT_u^{(m)}. \tag{2.39}$$

The terms $NL_\omega^{(m)}, VT_\omega^{(m)}, NL_u^{(m)}$ and $VT_u^{(m)}$ are given by

$$NL_\omega^{(m)} = \frac{1}{r\alpha}\left\{\frac{\partial}{\partial r}\left(r\alpha g_\varphi^{(m)}\right) - \mathrm{i}m g_r^{(m)}\right\} + \frac{2\alpha^2}{L} g_B^{(m)} + \frac{\alpha}{L^2}\mathrm{i}m\left(u_B^2\right)^{(m)}, \tag{2.40}$$

$$VT_\omega^{(m)} = \nu\left[\mathbb{L}^{(m)}\left(\frac{\omega_B^{(m)}}{\alpha}\right) - \left(\frac{2\alpha^2}{L}\right)^2 \omega_B^{(m)}\right] + \nu\,\frac{2\alpha^2}{L}\mathbb{L}^{(m)}\left(\frac{u_B^{(m)}}{\alpha}\right), \tag{2.41}$$

$$NL_u^{(m)} = \left\{\omega_r\, u_\varphi - \omega_\varphi\, u_r\right\}^{(m)}, \tag{2.42}$$

$$VT_u^{(m)} = \nu\left[\mathbb{L}^{(m)}\left(\frac{u_B^{(m)}}{\alpha}\right) - \frac{2\alpha^2}{L}\omega_B^{(m)}\right]. \tag{2.43}$$

The stream function modes $\Psi^{(m)}$ are computed by inverting the generalised Poisson equation (2.24) written for each mode m:

$$\mathbb{L}^{(m)}\Psi^{(m)} = -\omega_B^{(m)} + \frac{2\alpha^2}{L}u_B^{(m)} \tag{2.44}$$

with the operator $\mathbb{L}^{(m)}$ defined by

$$\mathbb{L}^{(m)}(\cdot) = \frac{1}{r\alpha}\frac{\partial}{\partial r}\left(r\alpha^2\frac{\partial}{\partial r}(\cdot)\right) - \frac{m^2}{r^2\alpha}(\cdot)\,. \tag{2.45}$$

Velocity components $u_r^{(m)}(r,t)$, $u_\varphi^{(m)}(r,t)$ are obtained from $\Psi^{(m)}(r,t)$ through

$$u_r^{(m)}(r,t) = \frac{\mathrm{i}m}{r}\Psi^{(m)}\,, \qquad u_\varphi^{(m)}(r,t) = -\alpha(r)\frac{\partial}{\partial r}\Psi^{(m)}\,, \tag{2.46}$$

and the vorticity components from $u_B^{(m)}/\alpha$ through

$$\omega_r^{(m)}(r,t) = \frac{\mathrm{i}m}{r}\left(\frac{u_B^{(m)}}{\alpha}\right)\,, \qquad \omega_\varphi^{(m)}(r,t) = -\alpha(r)\frac{\partial}{\partial r}\left(\frac{u_B^{(m)}}{\alpha}\right)\,. \tag{2.47}$$

2.3.2 Modes $m = 0$

The treatment of mode $m = 0$ is different from modes $m \neq 0$. Using (2.23) for mode $m = 0$, the relation

$$\frac{\omega_B^{(0)}}{\alpha} = \frac{2}{L}\,\alpha\, u_B^{(0)} + \frac{1}{r\,\alpha^2}\,\frac{\partial}{\partial r}(r\,\alpha\, u_\varphi^{(0)}) \tag{2.48}$$

is obtained showing a direct link between $\omega_B^{(0)}$, $u_\varphi^{(0)}$ and $u_B^{(0)}$. For $m = 0$, the pair $(u_\varphi^{(0)}, u_B^{(0)})$ will be hence chosen as the problem unknowns rather than $(\omega_B^{(0)}, u_B^{(0)})$. The dynamical equation for ${u_\varphi}^{(0)}$ is obtained by projecting the momentum equation (2.27) on $\boldsymbol{e_\varphi}$:

$$\frac{\partial}{\partial t} u_\varphi^{(0)} = -\boldsymbol{e_\varphi} \cdot (\boldsymbol{\omega} \times \boldsymbol{u})^{(0)} - \boldsymbol{e_\varphi} \cdot \boldsymbol{\nabla}^{(0)} \left(\frac{p}{\rho} + \frac{\boldsymbol{u}^2}{2} \right) - \nu \boldsymbol{e_\varphi} \cdot (\boldsymbol{\nabla} \times \omega)^{(0)} . \tag{2.49}$$

Thanks to the gradient expression (2.13) written for mode $m = 0$, pressure disappears from equation (2.49). Finally, some algebra leads to:

$$\frac{\partial}{\partial t} u_\varphi^{(0)} = \{\omega_r u_B - \omega_B u_r\}^{(0)} + \nu\alpha \frac{\partial}{\partial r}\left(\frac{\omega_B^{(0)}}{\alpha} \right) . \tag{2.50}$$

Since

$$\omega_r u_B = \frac{1}{r}\frac{\partial}{\partial \varphi}\left(\frac{u_B}{\alpha}\right) u_B = \frac{1}{2r\alpha}\frac{\partial}{\partial \varphi} u_B^2, \tag{2.51}$$

one obtains $(\omega_r u_B)^{(0)} = 0$, reducing equation (2.50) to

$$\frac{\partial}{\partial t} u_\varphi^{(0)} = \{-\omega_B u_r\}^{(0)} + \nu\alpha \frac{\partial}{\partial r}\left(\frac{\omega_B^{(0)}}{\alpha} \right) . \tag{2.52}$$

To summarize, the set of equations needed for mode $m = 0$ are

$$\frac{\partial}{\partial t} u_\varphi^{(0)} + NL_{u_\varphi}^{(0)} = VT_{u_\varphi}^{(0)}, \tag{2.53}$$

$$\frac{\partial}{\partial t} u_B^{(0)} + NL_u^{(0)} = VT_u^{(0)}, \tag{2.54}$$

with

$$NL_{u_\varphi}^{(0)} = \{\omega_B u_r\}^{(0)} , \tag{2.55}$$

$$VT_{u_\varphi}^{(0)} = \nu\alpha \frac{\partial}{\partial r}\left(\frac{2}{L}\,\alpha\, u_B^{(0)} + \frac{1}{r\,\alpha^2}\,\frac{\partial}{\partial r}(r\,\alpha\, u_\varphi^{(0)}) \right), \tag{2.56}$$

$$NL_u^{(0)} = \{\omega_r\, u_\varphi - \omega_\varphi\, u_r\}^{(0)} , \tag{2.57}$$

$$VT_u^{(0)} = \nu \left\{ \frac{1}{r\alpha}\frac{\partial}{\partial r}\left(r\alpha^2 \frac{\partial}{\partial r}\left(\frac{u_B^{(0)}}{\alpha} \right) \right) - \frac{2\alpha^2}{L}\left(\frac{2}{L}\,\alpha^2\, u_B^{(0)} + \frac{1}{r\,\alpha}\,\frac{\partial}{\partial r}(r\,\alpha\, u_\varphi^{(0)}) \right) \right\} . \tag{2.58}$$

As far as other components are concerned, radial velocity and radial vorticity components vanish for $m = 0$

$$u_r^{(0)} = 0 \qquad \omega_r^{(0)} = 0 \tag{2.59}$$

as they are respectively derivatives of Ψ and u_B/α with respect to φ (equations (2.17) and (2.20)). In order to obtain $\Psi^{(0)}$, one integrates equation (2.18)

$$\Psi^{(0)}\,(r) = -\int_0^r \frac{u_\varphi^{(0)}(r')}{\alpha(r')} r' \,\mathrm{d}r'. \tag{2.60}$$

Finally, $\omega_\varphi^{(0)}$ is simply obtained from definition (2.21):

$$\omega_\varphi^{(0)} = -\alpha \frac{\partial}{\partial r}\left(\frac{u_B^{(0)}}{\alpha} \right) , \tag{2.61}$$

and $\omega_B^{(0)}$ is recovered from (2.48).

2.4 Boundary conditions at $r = 0$

A detailed analysis of the conditions at the axis $r = 0$ are described in the appendix B. In the numerical formulation, the imposed boundary conditions are deduced from equations (B.25)-(B.27) of appendix B. However a weaker form is used.

2.4.1 Boundary conditions at $r = 0$ for modes $m \neq 0$

For modes $m \neq 0$, we impose Dirichlet conditions at $r = 0$ on the components $\Psi^{(m)}$, ${\omega_B}^{(m)}$ and ${u_B}^{(m)}$:

$$\Psi^{(m)}(0) = 0\ , \quad {\omega_B}^{(m)}(0) = 0\ , \quad {u_B}^{(m)}(0) = 0\,, \quad \text{for} \quad m \neq 0. \tag{2.62}$$

For $m \geq 2$, one may also need the values of components $u_r^{(m)}$, $\omega_r^{(m)}$, $u_\varphi^{(m)}$ and $\omega_\varphi^{(m)}$ at the axis:

$$\begin{aligned} \omega_r^{(m)}(0) = 0, \quad & u_r^{(m)}(0) = 0 \quad \text{for} \quad m \geq 2 \\ \omega_\varphi^{(m)}(0) = 0, \quad & u_\varphi^{(m)}(0) = 0 \quad \text{for} \quad m \geq 2. \end{aligned} \tag{2.63}$$

The mode $m = 1$ is a particular case: the components $u_r^{(1)}$, $\omega_r^{(1)}$ and $u_\varphi^{(1)}$, $\omega_\varphi^{(1)}$ are finite at the axis and their values can be deduced from $\Psi^{(1)}$ and $u_B^{(1)}$. Using (2.46) and (2.47), ${u_r}^{(1)}$ and $\omega_r^{(1)}$ read

$${u_r}^{(1)} = \frac{\mathrm{i}}{r}\Psi^{(1)}\ , \qquad \omega_r^{(1)} = \frac{\mathrm{i}}{r}\left(\frac{u_B^{(1)}}{\alpha}\right). \tag{2.64}$$

Taking the limit as $r \to 0$ and using L'Hospital's rule leads to:

$$\lim_{r \to 0} {u_r}^{(1)} = \lim_{r \to 0} \frac{\mathrm{i}\Psi^{(1)}}{r} = \mathrm{i}\left.\frac{\partial \Psi^{(1)}}{\partial r}\right|_{r=0} \tag{2.65}$$

which evaluates the undetermined form in equation (2.64). For the vorticity condition, one obtains in a similar way

$$\omega_r^{(1)}(0) = \mathrm{i}\left.\frac{\partial}{\partial r}\left(\frac{u_B^{(1)}}{\alpha}\right)\right|_{r=0}, \quad u_\varphi^{(1)}(0) = -\left.\frac{\partial \Psi^{(1)}}{\partial r}\right|_{r=0}, \quad \omega_\varphi^{(1)}(0) = -\left.\frac{\partial}{\partial r}\left(\frac{u_B^{(1)}}{\alpha}\right)\right|_{r=0}. \tag{2.66}$$

2.4.2 Boundary conditions at $r = 0$ for mode $m = 0$

The boundary conditions for the axisymmetric contribution of the velocity components simply read

$$\left.\frac{\partial}{\partial r}\left(\frac{u_B^{(0)}}{\alpha}\right)\right|_{r=0} = 0, \qquad u_r^{(0)}(0) = 0, \qquad u_\varphi^{(0)}(0) = 0. \tag{2.67}$$

2.5 Boundary condition at $r = R_{ext}$

Conditions at the boundary of the computational domain depend on the physics (bounded flow, unbounded flow, flow subjected to shear, etc.). Here, the numerical solution is matched to an outer potential flow in order to mimic a fluid medium of infinite extent.

2.5.1 Modes $m \neq 0$

At the outer boundary $r = R_{ext}$ of the computational domain, the numerical solution is matched with an analytical potential flow solution. This condition translates, for the helical vorticity ${\omega_B}^{(m)}$ and the helical velocity ${u_B}^{(m)}$, into :

$$ {\omega_B}^{(m)}(r = R_{ext}) = 0, \qquad {u_B}^{(m)}(r = R_{ext}) = 0 \ \text{ for } \ m \neq 0. \tag{2.68} $$

For $r > R_{ext}$, the flow is purely potential: the stream function Ψ satisfies a Laplace equation $\boldsymbol{\nabla}^2\Psi = 0$. Using formulas (2.13)-(2.14), the Laplacian can be expressed in the helical framework as:

$$ \boldsymbol{\nabla}^2\Psi = \frac{1}{r}\frac{\partial}{\partial r}\left(r\frac{\partial}{\partial r}\Psi\right) + \frac{1}{r^2\alpha^2}\frac{\partial^2}{\partial\varphi^2}\Psi. \tag{2.69} $$

Let us expand the stream function in Fourier series along the periodical direction φ

$$ \Psi(r,\varphi) = \sum_{m=-\infty}^{+\infty} \Psi^{(m)}(r)\, e^{im\varphi}. \tag{2.70} $$

The Laplace equation for Ψ can be written for each mode m

$$ r^2\frac{\partial^2}{\partial r^2}\Psi^{(m)}(r) + r\frac{\partial}{\partial r}\Psi(r)^{(m)} - \Psi^{(m)}(r)\left(\frac{m^2r^2}{L^2} + m^2\right) = 0, \tag{2.71} $$

yielding a modified Bessel function of order m. The solution of this equation depends on the value of L. For the two-dimensional case where $L \to \infty$, the ratio r^2/L^2 vanishes and the solution is given by $\Psi(r)^{(m)} = A_m r^{-m} + B_m r^m$. The requirement that the solution remains finite imposes $B_m = 0$. For any finite value of L, equation (2.71) accepts two linearly independent solutions, the modified Bessel function of the first kind I_m and the modified Bessel function of the second kind K_m. Since I_m and K_m are respectively exponentially growing and decaying functions, only the modified Bessel function of the second kind is physically relevant. To summarize, for $r > R_{ext}$

$$ \Psi^{(m)}(r) = \begin{cases} A_m/r^m & \text{if } |L| = \infty \\ A_m K_m\left(|m/L|\, r\right) & \text{if } L \text{ finite} \end{cases} \tag{2.72} $$

The unknown coefficients A_m can be eliminated using relationships between Ψ and its first derivative. For $L \to \infty$ it directly reads

$$ \frac{\partial}{\partial r}\Psi^{(m)} = -\frac{m}{r}\Psi^{(m)} \tag{2.73} $$

while for finite value of L, by setting $\gamma = m/|L|$ and using the following recurrence relationship for K_m

$$ \frac{\mathrm{d}}{\mathrm{d}r}K_m(\gamma r) = -\gamma K_{m-1}(\gamma r) - \frac{m}{r}K_m(\gamma r)\ , \quad m \geq 1\,, \tag{2.74} $$

one obtains

$$ \frac{\partial}{\partial r}\Psi^{(m)} = -m\Psi^{(m)}\left(\frac{1}{r} - \frac{1}{|L|}\frac{K_{m-1}(\gamma r)}{K_m(\gamma r)}\right). \tag{2.75} $$

The matching conditions at $r = R_{ext}$ between the inner (numerical) solution and the outer (analytical) solution for Ψ and its radial derivative impose Robin boundary conditions for the numerical solution:

$$ \frac{\partial}{\partial r}\Psi^{(m)}(R_{\text{ext}}) = -mC_m\Psi^{(m)}(R_{\text{ext}}) \tag{2.76} $$

$$ \text{with } C_m = \frac{1}{R_{\text{ext}}} + \begin{cases} 0 & \text{if } |L| = \infty \\ \dfrac{1}{|L|}\dfrac{K_{m-1}(|m/L|R_{\text{ext}})}{K_m(|m/L|R_{\text{ext}})} & \text{if } L \text{ finite} \end{cases} $$

2.5.2 Modes $m = 0$

From equations (2.46) and (2.47) for $u_r^{(0)}$ and $\omega_r^{(0)}$, when expressed on the outer boundary at $r = R_{ext}$, one deduces

$$\omega_r^{(0)}\left(R_{ext}\right) = 0, \quad u_r^{(0)}\left(R_{ext}\right) = 0, \quad \omega_B^{(0)}(R_{ext}) = 0, \quad \omega_\varphi^{(0)}(R_{ext}) = 0. \tag{2.77}$$

The velocity component $u_B^{(0)}\left(r = R_{ext}\right)$ is obtained from the definition in (2.7) expressed on the boundary

$$u_B^{(0)}\left(R_{ext}\right) = \alpha\left(R_{ext}\right)\left(u_z^{(0)}\left(R_{ext}\right) + \frac{R_{ext}}{L}u_\theta^{(0)}\left(R_{ext}\right)\right). \tag{2.78}$$

The axial velocity $u_z^{(0)}\left(R_{ext}\right) \equiv U_z^\infty$ is a prescribed value and is chosen to be set to 0 as it requires an *a priori* knowledge on the dynamics for the case considered. The azimuthal counterpart is supposed to behave as $u_\theta^{(0)} \sim \Gamma/2\pi r$ for large r, where Γ is the total circulation. Injecting these into (2.78) yields

$$u_B^{(0)}\left(R_{ext}\right) = \alpha\left(R_{ext}\right)\left(U_z^\infty + \frac{\Gamma}{2\pi L}\right). \tag{2.79}$$

Finally, the same considerations for $u_\varphi^{(0)}$ leads to

$$u_\varphi^{(0)}\left(R_{ext}\right) = \alpha\left(R_{ext}\right)\left(\frac{\Gamma}{2\pi R_{ext}} - \frac{R_{ext}}{L}U_z^\infty\right). \tag{2.80}$$

Chapter 3

DNS code with enforced helical symmetry : HELIX

Contents

In this chapter, details on the temporal and spatial discretisation of the equations are provided. In the direction φ, a Fourier decomposition is performed. The equations recast for azimuthal modes m, are spatially discretised along the radial direction r. In the first version of the code, evenly spaced grid points were used for radial discretisation, which had the benefit of simplicity when discretising the derivatives up to 2nd order accuracy. The disadvantage is the very high total number of grid points to be used to mesh the whole computational domain if one wishes to finely capture the vortex core structures. In order to reduce the computational time while ensuring fair accuracy within the regions of interest, a mesh with unevenly spaced grid points in the radial direction is introduced. The temporal scheme is first presented (section 3.1), the spatial mesh (section 3.2) and the discretisation of the governing equations are then given (sections 3.3 and 3.4).

3.1 Temporal scheme for the dynamical equations

The two dynamical equations to be integrated in time are expressed for modes $m \neq 0$

$$\frac{\partial}{\partial t} u_{B}^{(m)} + NL_{u}^{(m)} = VT_{u}^{(m)}, \tag{3.1}$$

$$\frac{\partial}{\partial t} \omega_{B}^{(m)} + NL_{\omega}^{(m)} = VT_{\omega}^{(m)}, \tag{3.2}$$

while for mode $m = 0$ they read

$$\frac{\partial}{\partial t} u_{B}^{(0)} + NL_{u}^{(0)} = VT_{u}^{(0)}, \tag{3.3}$$

$$\frac{\partial}{\partial t} u_{\varphi}^{(0)} + NL_{u_\varphi}^{(0)} = VT_{u_\varphi}^{(0)}. \tag{3.4}$$

The viscous and nonlinear terms in equations (3.1)-(3.4) are given by (2.40)-(2.43) and (2.55)-(2.58). In order to present the temporal scheme in a compact form, one introduces the following quantities: for $m \neq 0$, $G^{(m)} = (u_{B}^{(m)}, \omega_{B}^{(m)})$, $NL^{(m)} = (NL_{u}^{(m)}, NL_{\omega}^{(m)})$ and $VT^{(m)} = (VT_{u}^{(m)}, VT_{\omega}^{(m)})$; similarly for $m = 0$, $G^{(0)} = (u_{B}^{(0)}, u_{\varphi}^{(0)})$, $NL^{(0)} = (NL_{u}^{(0)}, NL_{u_\varphi}^{(0)})$ and $VT^{(0)} = (VT_{u}^{(0)}, VT_{u_\varphi}^{(0)})$.

3.1.1 Temporal derivative: 2nd order backward Euler scheme

The time step Δt is assumed constant, and $G_{n}^{(m)}$ refers to the value of $G^{(m)}(t)$ at discrete time $t_n \equiv n\Delta t$. All the dynamical equations are temporally discretised at second order accuracy at time t_{n+1}. In this code, a second order backward discretisation is used for the temporal derivative:

$$\left.\frac{\partial}{\partial t} G^{(m)}\right|_{n+1} = \frac{3\, G_{n+1}^{(m)} - 4\, G_{n}^{(m)} + G_{n-1}^{(m)}}{2\,\Delta t} + \mathcal{O}(\Delta t^2). \tag{3.5}$$

3.1.2 Nonlinear terms: second order Adams-Bashforth extrapolation

The nonlinear terms have to be evaluated at instant t_{n+1}. Two main approaches can be considered. A first method would consist in writing the term $NL_{n+1}^{(m)}$ using variables $G_{n+1}^{(p)}$ relative to all mode p at time t_{n+1} (implicit nonlinear term). This would result in a fully coupled nonlinear system which could be solved using for instance Newton-Raphson iterations. The alternative used in the present code, Helix, is an explicit formulation for the nonlinear terms. It consists in writing the nonlinear term at time t_{n+1} using an extrapolation from its values at times t_n and t_{n-1}. This has the advantage that at each time step the system to be solved becomes linear. The extrapolation is obtained via second order Adams-Bashforth scheme:

$$NL_{n+1}^{(m)} = 2\, NL_{n}^{(m)} - NL_{n-1}^{(m)} + \mathcal{O}(\Delta t^2). \tag{3.6}$$

3.1.3 Viscous terms: implicit scheme

The viscous terms are treated implicitly: this stabilises the temporal scheme and allows for larger time-steps Δt. Since the viscous term

$$VT_{n+1}^{(m)} = \mathcal{L}_v G_{n+1}^{(m)}, \tag{3.7}$$

is linear in the variable $G_{n+1}^{(m)}$, the viscous operator $\mathcal{L}_v$ becomes part of the linear operator which is inverted at each time step (see below the l.h.s. of equation (3.9)).

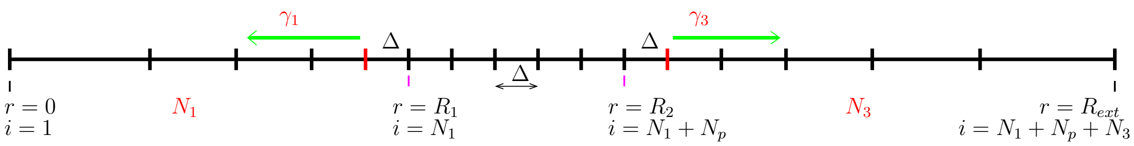

Figure 3.1 – Structure of the radial mesh used for the spatial discretisation. In the central section (indices $i = N_1, ..., N_1 + N_p$), the grid points are regularly spaced. Two regions of irregularly spaced points are represented with different contraction/expansion parameters γ_1 for $i = 1, ..., N_1 - 1$ and γ_2 for $i = N_1 + N_p, ..., N_r$.

3.1.4 General form

Using formulas (3.5),(3.6), (3.7), the time advance of quantity $G^{(m)}$ is governed by

$$\frac{3\,G^{(m)}_{n+1} - 4\,G^{(m)}_{n} + G^{(m)}_{n-1}}{2\,\Delta t} + \left(2\,NL^{(m)}_{n} - NL^{(m)}_{n-1}\right) = \mathcal{L}_v G^{(m)}_{n+1}\,, \tag{3.8}$$

Putting all unknown variables (relative to time step $n + 1$) to the l.h.s. and all known variables (relative to n and $n - 1$) to the r.h.s., equation (3.8) is recast as

$$\left(\sigma\mathcal{I} - \mathcal{L}_v\right) G^{(m)}_{n+1} = \left(-2\,NL^{(m)}_{n} + NL^{(m)}_{n-1}\right) + \frac{4\,G^{(m)}_{n} - G^{(m)}_{n-1}}{2\,\Delta t}, \tag{3.9}$$

with $\sigma = 3/\left(2\Delta t\right)$. The radial discretisation is presented in the next section.

3.2 Spatial discretisation

3.2.1 Fourier decomposition along φ

The Fourier series in equation (2.36) and (2.37) are truncated to a finite number of complex mode $|m| < M$. Since modes with negative m can be direclty obtained as complex conjugates, we consider only the positive m. The standard 2/3 dealiasing requires the computation of $3M/2$ modes. This is done by discretising φ at $N_\theta = 3M$ physical angles given by

$$\varphi_j = j\delta\theta \quad (j = 0, ..., N_\theta - 1), \quad \varphi_{N_\theta} = \varphi_0 = 0, \tag{3.10}$$

where $\delta\theta = 2\pi/N_\theta$. The first M first complex modes are effectively used, the higher modes $m = M, ..., 3M/2 - 1$ being dismissed at each time step.

3.2.2 Irregular meshes

We create a radial grid mesh where points are not necessarily evenly spaced. We aim at placing most of the grid points within the region where the vortices are supposed to be localised. In the present context such a region is either an annulus or a disk $0 \leq R_1 \leq r \leq R_2$, bound by the lower and upper radii R_1 and R_2. This ensures that the dynamics and the core structure of the vortices are accurately captured in that region. In order to reduce the total number of grid points, we connect the above refined region to regions with a coarser grid, corresponding to the regions where the flow is likely to be potential. A typical arrangement of the regions is depicted in figure 3.1. In the refined region (region 2), we use N_2 regularly spaced grid points, spaced by a distance $\Delta = \left(R_2 - R_1\right)/N_2$ set at $r_i = R_1 + \left(i - N_1\right)\Delta$ for $i = N_1, ..., N_1 + N_2$. In the coarse mesh regions (regions 1 and 3), we use N_1 and N_3 grid points. The cells next to the refined regions are imposed to be of size Δ (see red ticks in figure 3.1) while for the others we set fixed contraction/expansion rates γ_i: one chooses the grid spacings $h_i \equiv r_{i+1} - r_i$ such that

$$\gamma_1 = h_i/h_{i-1} \quad \text{for} \quad i < N_1 - 1 \tag{3.11}$$

$$\gamma_3 = h_i/h_{i-1} \quad \text{for} \quad i \geq N_1 + N_2 + 1. \tag{3.12}$$

We require the γ_i parameters to be close to 1 (we choose in practice $0.9 < \gamma_i < 1.1$) in order to control the discretisation errors (see section 3.2.3 below).
In practice, radii R_1, R_2, R_{ext} and the number N_2 of grid points in region 2 are first chosen, which fixes Δ. For region 3, the expansion rate γ_3 is then determined as the closest value below 1.1 which ensures that the outer boundary at $r = R_{ext}$ is a grid point. Similarly for region 1, when present, the contraction rate γ_1 is the closest value above 0.9 ensuring that the centre of the domain $r = 0$ is a grid point. The number of grid points N_1, N_3 of regions 1 and 3 are then an output of this procedure. Since in region 3, the following sequence holds

$$\begin{aligned}
&r\left(N_1 + N_p\right) = R_2 \\
&r\left(N_1 + N_p + 1\right) = R_2 + \Delta \\
&r\left(N_1 + N_p + 2\right) = R_2 + \Delta(1 + \gamma_3) \\
&r\left(N_1 + N_p + 3\right) = R_2 + \Delta(1 + \gamma_3 + \gamma_3^2) \\
&\vdots \\
&r\left(N_1 + N_p + N_3\right) = R_{ext} = R_2 + \Delta \sum_{p=0}^{N_3-1} \gamma_3^p = R_2 + \Delta \frac{1 - \gamma_3^{N_3}}{1 - \gamma_3},
\end{aligned}$$

the determination of γ_3 amounts to solve the equation

$$\left(R_2 - R_{ext}\right)\left(1 - \gamma_3\right) + \Delta\left(1 - \gamma_3^{N_3}\right) = 0, \tag{3.13}$$

for N_3 and γ_3. This is done in two steps: equation (3.13) is first solved for N_3 at fixed value of $\gamma_3 = 1.1$. N_3 is obtained as the closest integer value greater than

$$\frac{\log\left[1 - \dfrac{1}{(R_2 - R_{ext})(1 - \gamma_3)}\right]}{\log \gamma_3}. \tag{3.14}$$

Equation (3.13) is then solved for γ_3 using a Newton algorithm with $\gamma_3 = 1.1$ as initial guess. The iterations converge toward the closest solution below 1.1. A similar procedure is used for region 1. Some mesh examples are shown in figure 3.2.

3.2.3 Finite differences along the radial direction r

The first and second order derivatives with respect to r are discretized with the finite difference method. Such methods are well known for regular grids, we establish the derivative formulas when the spacing $h_i \equiv r_{i+1} - r_i$ is not constant. Let us define $u_i \equiv u\left(r_i\right)$. Using the Taylor expansions,

$$u_{i+1} = u_i + h_i \left.\frac{\partial u}{\partial r}\right|_i + \frac{h_i^2}{2} \left.\frac{\partial^2 u}{\partial r^2}\right|_i + \frac{h_i^3}{6} \left.\frac{\partial^3 u}{\partial r^3}\right|_i + \mathcal{O}(h_i^4), \tag{3.15}$$

$$u_{i-1} = u_i - h_{i-1} \left.\frac{\partial u}{\partial r}\right|_i + \frac{h_{i-1}^2}{2} \left.\frac{\partial^2 u}{\partial r^2}\right|_i - \frac{h_{i-1}^3}{6} \left.\frac{\partial^3 u}{\partial r^3}\right|_i + \mathcal{O}(h_{i-1}^4) \tag{3.16}$$

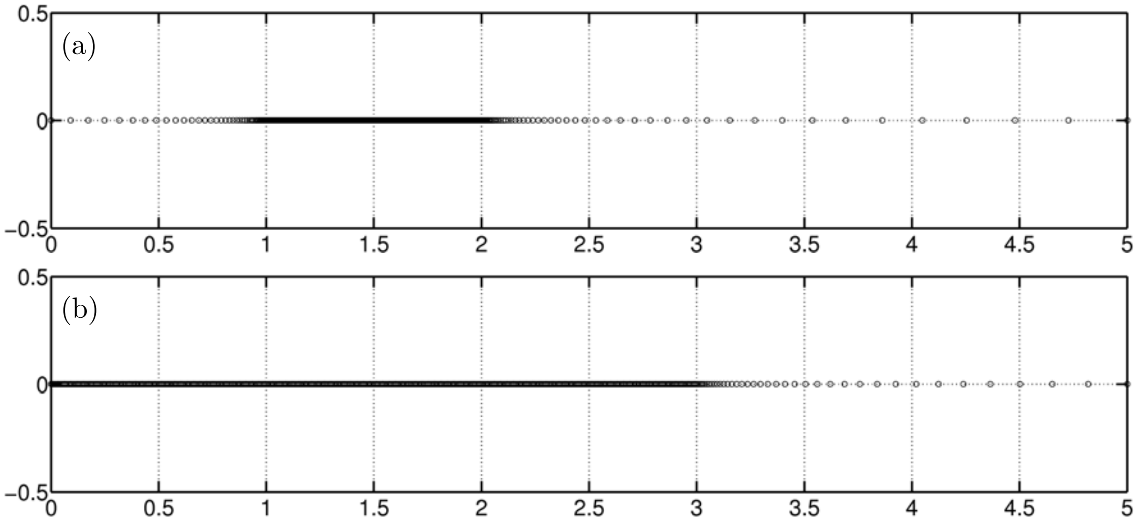

Figure 3.2 – Example of irregular meshes. (a) Mesh with irregular grid points for regions $0 \leq r \leq R_1$ and $R_2 \leq r \leq R_{ext}$ with $R_1 = 1, R_2 = 2, R_{ext} = 5$. The parameters obtained with the optimisation process are found to be $N_p = 500, \Delta = 0.002, N_1 = 43, N_3 = 53, \gamma_1 = 1.0975, \gamma_3 = 1.0991$. (b) Mesh with regularly spaced points for $0 \leq r \leq R_2$ with $R_2 = 3$ and $R_{ext} = 5$. The resulting parameters obtained with the optimisation process are found to be $N_1 = N_p = 384$, $N_3 = 38$ $\gamma_1 = \Delta = 0.006$ and $\gamma_3 = 1.0965$.

one obtains an approximation for the derivative of u at nodes r_i:

$$u_{i+1} - u_{i-1} = (h_i + h_{i-1}) \left.\frac{\partial u}{\partial r}\right|_i + \frac{1}{2}\left(h_i^2 - h_{i-1}^2\right) \left.\frac{\partial^2 u}{\partial r^2}\right|_i + \frac{1}{6}\left(h_i^3 + h_{i-1}^3\right) \left.\frac{\partial^3 u}{\partial r^3}\right|_i + \cdots$$

$$\left.\frac{\partial u}{\partial r}\right|_i = \frac{u_{i+1} - u_{i-1}}{h_i + h_{i+1}} - \frac{1}{2}(h_i - h_{i-1}) \left.\frac{\partial^2 u}{\partial r^2}\right|_i + \cdots \tag{3.17}$$

This approximation is accurate to first order and the leading error term is proportional to $(h_i - h_{i-1}) = h_i(1-\gamma)$. In the coarse regions where $\left.\frac{\partial^2 u}{\partial r^2}\right|_i$ is a priori small, taking $|1-\gamma| < 0.1$ as discussed previously, still leads to an acceptable accuracy. In the refined regions where $\gamma = 1$ the second order accuracy is ensured.
We further introduce the staggered points $r_{i+1/2}$ and $r_{i-1/2}$ such that

$$r_{i+1/2} = \frac{r_i + r_{i+1}}{2}, \tag{3.18}$$

$$r_{i-1/2} = \frac{r_i + r_{i-1}}{2} \tag{3.19}$$

and compute the first derivative at r_i using the values of u at the staggered points $r_{i+1/2}$ and $r_{i-1/2}$:

$$\left.\frac{\partial u}{\partial r}\right|_i = \frac{2}{h_i + h_{i-1}} u_{i+1/2} - \frac{2}{h_i + h_{i-1}} u_{i-1/2} - \frac{1}{4}(h_i - h_{i-1}) \left.\frac{\partial^2 u}{\partial r^2}\right|_i + \mathcal{O}\left(h^2\right). \tag{3.20}$$

This relation is useful to derive the second derivative. It is obtained by replacing u by $\frac{\partial u}{\partial r}$

in (3.20):

$$\frac{\partial}{\partial r}\left(\frac{\partial u}{\partial r}\right)\bigg|_i = \left(\frac{\partial u}{\partial r}\bigg|_{i+\frac{1}{2}} - \frac{\partial u}{\partial r}\bigg|_{i-\frac{1}{2}}\right)\frac{2}{h_i + h_{i-1}} + \mathcal{O}\left(h\right), \tag{3.21}$$

$$\frac{\partial^2 u}{\partial r^2}\bigg|_i = \frac{2}{h_{i-1}\left(h_i + h_{i-1}\right)}u_{i-1} - \frac{2}{h_i h_{i-1}}u_i + \frac{2}{h_i\left(h_i + h_{i-1}\right)}u_{i+1} + \mathcal{O}\left(h\right). \tag{3.22}$$

Note that for regularly spaced grid points with $h_i = h_{i-1} = h$, the equation (3.22) becomes the general well-known formula of the second derivative at second order accuracy for regular grid points.

3.3 Discrete system of equations for $m \neq 0$

For modes $m \neq 0$, all the unknowns of the problem are solved at grid points r_i.

3.3.1 Modified Poisson equation for $\Psi^{(m)}$

The discrete form of equation (2.44)

$$\mathbb{L}^{(m)}\Psi^{(m)}\Big|_i = -\omega_{B_i}^{(m)} + \frac{2\alpha_i^2}{L}u_{B_i}^{(m)} \tag{3.23}$$

is solved at each time step in order to obtain $\Psi^{(m)}$. The linear operator $\mathbb{L}^{(m)}$ (2.45) is discretised at each grid point r_i using formula (3.22):

$$\begin{aligned}\mathbb{L}^{(m)}\Psi^{(m)}\Big|_i =& \frac{2}{r_i\alpha_i\left(h_i + h_{i-1}\right)}\left\{r_{i+\frac{1}{2}}\alpha_{i+\frac{1}{2}}^2\frac{\left(\Psi_{i+1}^{(m)} - \Psi_i^{(m)}\right)}{h_i} - r_{i-\frac{1}{2}}\alpha_{i-\frac{1}{2}}^2\frac{\left(\Psi_i^{(m)} - \Psi_{i-1}^{(m)}\right)}{h_{i-1}}\right\}\\ &- \frac{m^2}{r_i^2\alpha_i}\Psi_i^{(m)}.\end{aligned} \tag{3.24}$$

Introducing the quantities $\eta_i^+ = \dfrac{h_i\left(h_i + h_{i-1}\right)}{2}$ and $\eta_i^- = \dfrac{h_{i-1}\left(h_i + h_{i-1}\right)}{2}$, the discretised operator $\mathbb{L}^{(m)}\Psi^{(m)}\Big|_i$ thus reads:

$$\begin{bmatrix}\dfrac{r_{i-1/2}\alpha_{i-1/2}^2}{r_i\alpha_i\eta_i^-} & -\left(\dfrac{r_{i+1/2}\alpha_{i+1/2}^2}{r_i\alpha_i\eta_i^+} + \dfrac{r_{i-1/2}\alpha_{i-1/2}^2}{r_i\alpha_i\eta_i^-} + \dfrac{m^2}{r_i^2\alpha_i}\right) & \dfrac{r_{i+1/2}\alpha_{i+1/2}^2}{r_i\alpha_i\eta_i^+}\end{bmatrix}\begin{bmatrix}\Psi_{i-1}^{(m)}\\ \\ \Psi_i^{(m)}\\ \\ \Psi_{i+1}^{(m)}\end{bmatrix}.$$

The resulting tridiagonal system has to be solved for $2 \leq i \leq N_r - 1$. It also contains the quantities $\Psi_1^{(m)}$ and $\Psi_{N_r}^{(m)}$. These terms are substituted for, using the boundary conditions given in (2.62) and (2.68). On the axis, at $r = r_1 = 0$, the regularity condition for $m \neq 0$ directly imposes:

$$\Psi_1^{(m)} = 0. \tag{3.25}$$

At the outer boundary of the domain, the condition is discretised using a second order backward formula

$$\begin{aligned}\Psi_{N_r}^{(m)} =& \frac{\left(h_{N_r-1} + h_{N_r-2}\right)^2}{mC_m h_{N_r-1}h_{N_r-2}\left(h_{N_r-1} + h_{N_r-2}\right) + h_{N_r-2}\left(h_{N_r-2} + 2h_{N_r-1}\right)}\Psi_{N_r-1}^{(m)}\\ &- \frac{h_{N_r-1}^2}{mC_m h_{N_r-1}h_{N_r-2}\left(h_{N_r-1} + h_{N_r-2}\right) + h_{N_r-2}^2 + 2h_{N_r-1}h_{N_r-2}}\Psi_{N_r-2}^{(m)}.\end{aligned} \tag{3.26}$$

$$\begin{bmatrix} \begin{pmatrix} \\ PZ^{(m)} \\ \\ \end{pmatrix} & \begin{pmatrix} \\ PD^{(m)} \\ \\ \end{pmatrix} \\ \begin{pmatrix} \\ PG^{(m)} \\ \\ \end{pmatrix} & \begin{pmatrix} \\ PU^{(m)} \\ \\ \end{pmatrix} \end{bmatrix} \begin{bmatrix} \begin{pmatrix} \\ \omega_{B_{n+1}}^{(m)} \\ \\ \end{pmatrix} \\ \begin{pmatrix} \\ u_{B_{n+1}}^{(m)} \\ \\ \end{pmatrix} \end{bmatrix} = \begin{bmatrix} \begin{pmatrix} \\ RHS_{\omega_B}^{(m)} \\ \\ \end{pmatrix} \\ \begin{pmatrix} \\ RHS_{u_B}^{(m)} \\ \\ \end{pmatrix} \end{bmatrix}$$

Figure 3.3 – Matrix bloc structure for mode $m \neq 0$ at instant t_{n+1}. PZ, PD, PU are tridiagonal matrix blocks while PG is diagonal.

The resulting tridiagonal $(N_r - 2) \times (N_r - 2)$ system is solved using a band LU factorisation of the LAPACK library. As each mode m can be treated independently, parallel OpenMP micro-tasking is implemented: different ranges of m values are assigned to different threads.

3.3.2 Modified Helmholtz equations for $\left(\omega_B^{(m)}, u_B^{(m)}\right)$

The system of equations for $\left(\omega_B^{(m)}, u_B^{(m)}\right)$ resulting from the temporal discretisation of (3.9) can be written in a matrix bloc form as depicted in figure 3.3. As ω_B and u_B are coupled through the dynamical equations, the resulting discretised system displays a 2×2 block structure: the bloc matrices PZ and PD contain the discretisation coefficients of modified Helmholtz equation for ω_B while the bloc matrices PG and PU refer to the modified Helmholtz equation for u_B. The viscous terms $VT_\omega^{(m)}$ and $VT_u^{(m)}$ discretised at nodes r_i are expressed as

$$\begin{aligned} VT_\omega^{(m)}\Big|_i &= \nu \left[\mathbb{L}^{(m)} \left(\frac{\omega_B^{(m)}}{\alpha} \right)\Bigg|_i - \left(\frac{2\alpha_i^2}{L} \right)^2 \omega_{B_i}^{(m)} \right] + \nu \frac{2\alpha_i^2}{L}\, \mathbb{L}^{(m)} \left(\frac{u_B^{(m)}}{\alpha} \right)\Bigg|_i , \\ VT_u^{(m)}\Big|_i &= \nu \left[\mathbb{L}^{(m)} \left(\frac{u_B^{(m)}}{\alpha} \right)\Bigg|_i - \frac{2\alpha_i^2}{L} \omega_{B_i^{(m)}} \right] . \end{aligned}$$

Using the discretisation of operator $\mathbb{L}^{(m)}$ (formula (3.24)), one obtains

$$PZ^{(m)} \cdot \omega_B^{(m)}\Big|_i = \sigma \omega_{B_i}^{(m)} - \nu \left[\mathbb{L}^{(m)} \left(\frac{\omega_B^{(m)}}{\alpha} \right)\Bigg|_i - \left(\frac{2\alpha_i^2}{L} \right)^2 \omega_{B_i}^{(m)} \right] \tag{3.27}$$

which reads

$$\left[-\nu \frac{r_{i-\frac{1}{2}} \alpha_{i-\frac{1}{2}}^2}{r_i \alpha_i \alpha_{i-1} \eta_i^-} \quad \sigma + \nu \left(\frac{r_{i+\frac{1}{2}} \alpha_{i+\frac{1}{2}}^2}{r_i \alpha_i^2 \eta_i^+} + \frac{r_{i-\frac{1}{2}} \alpha_{i-\frac{1}{2}}^2}{r_i \alpha_i^2 \eta_i^-} + \frac{m^2}{r_i^2 \alpha_i^2} + \frac{4\alpha_i^4}{L^2} \right) \quad -\nu \frac{r_{i+\frac{1}{2}} \alpha_{i+\frac{1}{2}}^2}{r_i \alpha_i \alpha_{i+1} \eta_i^+} \right] \begin{bmatrix} \omega_{B_{i-1}}^{(m)} \\ \\ \omega_{B_i}^{(m)} \\ \\ \omega_{B_{i+1}}^{(m)} \end{bmatrix} .$$

Similarly, the other matrix blocks are expressed as

$$PD^{(m)} \cdot u_B^{(m)}\Big|_i = -\frac{2\nu}{L} \alpha_i^2\, \mathbb{L}^{(m)} \left(\frac{u_B^{(m)}}{\alpha} \right)\Bigg|_i \tag{3.28}$$

$$= \frac{2\nu}{L}\begin{bmatrix} -\frac{r_{i-\frac{1}{2}}\alpha^2_{i-\frac{1}{2}}\alpha_i}{r_i\alpha_{i-1}\eta_i^-} & \frac{r_{i+\frac{1}{2}}\alpha^2_{i+\frac{1}{2}}}{r_i\eta_i^+}+\frac{r_{i-\frac{1}{2}}\alpha^2_{i-\frac{1}{2}}}{r_i\eta_i^-}+\frac{m^2}{r_i^2} & -\frac{\alpha_i r_{i+\frac{1}{2}}\alpha^2_{i+\frac{1}{2}}}{r_i\alpha_{i+1}\eta_i^+}\end{bmatrix}\begin{bmatrix} u^{(m)}_{B_{i-1}} \\ u^{(m)}_{B_i} \\ u^{(m)}_{B_{i+1}}\end{bmatrix}$$

$$PG^{(m)} \cdot \omega_B^{(m)}\Big|_i = \frac{2\nu}{L}\alpha_i^2\omega^{(m)}_{B_i} \tag{3.29}$$

$$PU^{(m)} \cdot u_B^{(m)}\Big|_i = \sigma u^{(m)}_{B_i} - \nu\,\mathbb{L}^{(m)}\left(\frac{u_B^{(m)}}{\alpha}\right)\Bigg|_i \tag{3.30}$$

$$= \begin{bmatrix} -\nu\frac{r_{i-\frac{1}{2}}\alpha^2_{i-\frac{1}{2}}}{r_i\alpha_i\alpha_{i-1}\eta_i^-} & \sigma+\nu\left(\frac{r_{i+\frac{1}{2}}\alpha^2_{i+\frac{1}{2}}}{r_i\alpha_i^2\eta_i^+}+\frac{r_{i-\frac{1}{2}}\alpha^2_{i-\frac{1}{2}}}{r_i\alpha_i^2\eta_i^-}+\frac{m^2}{r_i^2\alpha_i^2}\right) & -\nu\frac{r_{i+\frac{1}{2}}\alpha^2_{i+\frac{1}{2}}}{r_i\alpha_i\alpha_{i+1}\eta_i^+}\end{bmatrix}\begin{bmatrix} u^{(m)}_{Bi-1} \\ u^{(m)}_{Bi} \\ u^{(m)}_{Bi+1}\end{bmatrix}$$

The resulting system, for $2 \leq i \leq N_r - 1$, contains also the quantities $\omega_B^{(m)}(r_1)$ and $\omega_B^{(m)}(r_{N_r})$ which are substituted for by their expressions at the boundaries for $r_1 = 0$ (2.62) and $r_{N_r} = R_{ext}$ (2.68)

$$u_B^{(m)}(r_{N_r}) = 0, \tag{3.31}$$

$$\omega_B^{(m)}(r_{N_r}) = 0, \tag{3.32}$$

$$u_B^{(m)}(r_1) = 0, \tag{3.33}$$

$$\omega_B^{(m)}(r_1) = 0. \tag{3.34}$$

The nonlinear terms $NL_n^{(m)}$ appearing in the right hand side of (3.9) have to be also discretised at nodes r_i:

$$NL_\omega^{(m)}\Big|_i = \frac{1}{r_i\alpha_i}\frac{\partial}{\partial r}\left(r\alpha g_\varphi^{(m)}\right)\Big|_i - \frac{im}{r_i\alpha_i}\,g_r^{(m)}\Big|_i + \frac{2\alpha_i^2}{L}\,g_B^{(m)}\Big|_i + \frac{im\alpha_i}{L^2}(u^2_{B_i})^{(m)} \tag{3.35}$$

$$NL_u^{(m)}\Big|_i = g_B^{(m)}\Big|_i \tag{3.36}$$

where $g_B \equiv \omega_r u_\varphi - \omega_\varphi u_r$, $g_r \equiv \omega_B u_\varphi$ and $g_\varphi \equiv \omega_B u_r$.

In the *pseudo-spectral* approach, nonlinear terms are evaluated in the physical space. The evaluation of the radial derivative of g_φ at r_i requires the computation of $\omega_B u_r$ at the staggered grid points $r_{i+1/2}$. In order to address this problem, $g_\varphi\left(r_{i+1/2}, \varphi_j\right)$ is obtained by interpolation of $\omega_B u_r$ between points r_i and r_{i+1} in physical space:

$$\begin{aligned} g_\varphi\left(r_{i+1/2}, \varphi_j\right) &= [\omega_B u_r]\left(r_{i+1/2}, \varphi_j\right) \\ &= \frac{1}{2}\Big(\omega_B\left(r_i, \varphi_j\right)u_r\left(r_i, \varphi_j\right) + \omega_B\left(r_{i+1}, \varphi_j\right)u_r\left(r_{i+1}, \varphi_j\right)\Big). \end{aligned} \tag{3.37}$$

$$\left[\begin{array}{cc} \left(\quad PV^{(0)} \quad \right) & \left(\quad PD^{(0)} \quad \right) \\ \left(\quad PG^{(0)} \quad \right) & \left(\quad PU^{(0)} \quad \right) \end{array}\right] \left[\begin{array}{c} \left(u_{\varphi_{n+1}}^{(0)} \right) \\ \left(u_{B_{n+1}}^{(0)} \right) \end{array}\right] = \left[\begin{array}{c} \left(RHS_{u_\varphi}^{(0)} \right) \\ \left(RHS_{u_B}^{(0)} \right) \end{array}\right]$$

Figure 3.4 – Matrix bloc structure for mode $m = 0$ at discrete instant t_{n+1}. The matrix blocks $PV^{(0)}$ and $PU^{(0)}$ are tridiagonal while $PG^{(0)}$ and $PD^{(0)}$ are bidiagonal.

Moreover, g_r and g_B need to be evaluated at nodes r_i while the components u_φ and ω_φ are available at nodes $r_{i+1/2}$. The following interpolation formulas are used:

$$\begin{aligned} g_B\left(r_i, \varphi_j\right) &= \left[\omega_r u_\varphi\right]\left(r_i, \varphi_j\right) - \left[\omega_\varphi u_r\right]\left(r_i, \varphi_j\right) \qquad (3.38) \\ &= \omega_r\left(r_i, \varphi_j\right)\left(\frac{h_i}{h_i + h_{i-1}} u_\varphi\left(r_{i-1/2}, \varphi_j\right) + \frac{h_{i-1}}{h_i + h_{i-1}} u_\varphi\left(r_{i+1/2}, \varphi_j\right)\right) \\ &\quad - u_r\left(r_i, \varphi_j\right)\left(\frac{h_i}{h_i + h_{i-1}} \omega_\varphi\left(r_{i-1/2}, \varphi_j\right) + \frac{h_{i-1}}{h_i + h_{i-1}} \omega_\varphi\left(r_{i+1/2}, \varphi_j\right)\right), \\ g_r\left(r_i, \varphi_j\right) &= \left[\omega_B u_\varphi\right]\left(r_i, \varphi_j\right) \qquad (3.39) \\ &= \omega_B\left(r_i, \varphi_j\right)\left(\frac{h_i}{h_i + h_{i-1}} u_\varphi\left(r_{i-1/2}, \varphi_j\right) + \frac{h_{i-1}}{h_i + h_{i-1}} u_\varphi\left(r_{i+1/2}, \varphi_j\right)\right). \end{aligned}$$

The above components are then Fourier transformed to yield $g_\varphi^{(m)}$, $g_r^{(m)}$ and $g_B^{(m)}$ from which nonlinear terms $NL_\omega^{(m)}$ and $NL_u^{(m)}$ are deduced. The remaining terms in equation (3.9) are already known from the previous time steps so that the right hand side is completely determined.

The resulting linear system has dimension $2(N_r - 2) \times 2(N_r - 2)$ and the coupling between $\omega_B^{(m)}$ and $u_B^{(m)}$ would require solving the system blockwise. In order to avoid the block solving, we first reorder the variables according to $\omega_B^{(m)}(r_2), u_B^{(m)}(r_2), \omega_B^{(m)}(r_3), u_B^{(m)}(r_3), \ldots$. For each mode $m \neq 0$ this leads to a single band matrix with a left half-bandwidth 2 and right half-bandwidth 3 – a hexadiagonal matrix which is solved using band LU factorisation.

3.4 Discrete system of equations for $m = 0$

3.4.1 Computation of the streamfunction $\Psi^{(0)}$

For $m = 0$, there is no need to solve a linear system for the axisymmetric contribution $\Psi^{(0)}$, because it can obtained directly through a numerical integration of equation (2.18) along the radial direction.

3.4.2 Modified Helmholtz equations for $\left(u_\varphi^{(0)}, u_B^{(0)}\right)$

For the mode $m = 0$, the unknown functions are $u_\varphi^{(0)}$ et $u_B^{(0)}$. An important difference exists due to $u_\varphi^{(0)}$ being defined on the staggered points $r_{i+1/2}$. The coupled system that has to be solved for $\left(u_\varphi^{(0)}, u_B^{(0)}\right)$ has the 2×2 block structure depicted in figure 3.4.

The viscous terms $VT_{u_\varphi}^{(0)}$ and $VT_{u_B}^{(0)}$ are now discretised at nodes $r_{i+1/2}$ and r_i, respectively.

They are expressed with the block matrices $PV^{(0)}, PD^{(0)}, PG^{(0)}$ and $PU^{(0)}$ such that

$$VT^{(0)}_{u_\varphi}\Big|_{i+1/2} = \nu\left(\alpha_{i+1/2}\frac{\partial}{\partial r}\left(\frac{1}{r\alpha^2}\frac{\partial}{\partial r}\left(r\alpha u^{(0)}_\varphi\right)\right)\Big|_{i+1/2} + \frac{2\alpha_{i+1/2}}{L}\frac{\partial}{\partial r}\left(\alpha u^{(0)}_B\right)\Big|_{i+1/2}\right),$$

$$VT^{(0)}_{u_B}\Big|_i = \nu\left[-\frac{2\alpha_i}{r_i L}\frac{\partial}{\partial r}\left(r\alpha u^{(0)}_\varphi\right)\Big|_i - \frac{4\alpha_i^4}{L^2}u^{(0)}_{B_i} + \frac{1}{r_i\alpha}\frac{\partial}{\partial r}\left(r\alpha^2\frac{\partial}{\partial r}\left(\frac{u^{(0)}_B}{\alpha}\right)\right)\Big|_i\right].$$

These terms contain the discretisation coefficients obtained after injecting the formulas (3.22). For $i = 2, ..., N_r - 1$, one obtains

$$PV^{(0)}\cdot u^{(0)}_\varphi\Big|_{i+1/2} = \sigma u^{(0)}_{\varphi_{i+1/2}} - \nu\alpha_{i+1/2}\frac{\partial}{\partial r}\left(\frac{1}{r\alpha^2}\frac{\partial}{\partial r}\left(r\alpha u^0_\varphi\right)\right)\Big|_{i+1/2} \tag{3.40}$$

$$= \begin{bmatrix} -\nu\dfrac{r_{i-\frac{1}{2}}\alpha_{i+\frac{1}{2}}\alpha_{i-\frac{1}{2}}}{r_i\alpha_i^2\eta_i^+} & \sigma + \nu\left(\dfrac{r_{i+\frac{1}{2}}\alpha^2_{i+\frac{1}{2}}}{r_i\alpha_i^2\eta_i^+} + \dfrac{r_{i+\frac{1}{2}}\alpha^2_{i+\frac{1}{2}}}{r_{i+1}\alpha^2_{i+1}\eta_i^{++}}\right) & -\nu\dfrac{r_{i+\frac{3}{2}}\alpha_{i+\frac{1}{2}}\alpha_{i+\frac{3}{2}}}{r_{i+1}\alpha^2_{i+1}\eta_i^{++}}\end{bmatrix}\begin{bmatrix} u^{(0)}_{\varphi_{i-1/2}} \\ u^{(0)}_{\varphi_{i+1/2}} \\ u^{(0)}_{\varphi_{i+3/2}}\end{bmatrix}$$

$$PD^{(0)}\cdot u^{(0)}_B\Big|_{i+\frac{1}{2}} = -2\nu\frac{\alpha_{i+\frac{1}{2}}}{L}\frac{\partial}{\partial r}\left(\alpha u^{(0)}_B\right)\Big|_{i+\frac{1}{2}} = \begin{bmatrix} 0 & \dfrac{2\alpha_{i+\frac{1}{2}}\alpha_i}{Lh_i} & -\dfrac{2\alpha_{i+\frac{1}{2}}\alpha_{i+1}}{Lh_i}\end{bmatrix}\begin{bmatrix} u^{(0)}_{B_{i-1}} \\ u^{(0)}_{B_i} \\ u^{(0)}_{B_{i+1}}\end{bmatrix} \tag{3.41}$$

$$PG^{(0)}\cdot u^{(0)}_\varphi\Big|_i = \frac{2\alpha_i}{Lr_i}\frac{\partial}{\partial r}\left(r\alpha u^{(0)}_\varphi\right)\Big|_i \tag{3.42}$$

$$= \begin{bmatrix} \dfrac{4r_{i-\frac{1}{2}}\alpha_{i-\frac{1}{2}}\alpha_i}{Lr_i\left(h_i + h_{i-1}\right)} & \dfrac{4r_{i+\frac{1}{2}}\alpha_{i+\frac{1}{2}}\alpha_i}{Lr_i\left(h_i + h_{i-1}\right)} & 0\end{bmatrix}\begin{bmatrix} u^{(0)}_{\varphi_{i-1/2}} \\ u^{(0)}_{\varphi_{i+1/2}} \\ u^{(0)}_{\varphi_{i+3/2}}\end{bmatrix} \tag{3.43}$$

$$PU^{(0)}\cdot u^{(0)}_B\Big|_i = \left(\sigma + \frac{4\alpha_i^4}{L^2}\right)u^{(0)}_{B_i} - \frac{1}{r_i\alpha_i}\frac{\partial}{\partial r}\left(r\alpha^2\frac{\partial}{\partial r}\left(\frac{u^{(0)}_B}{\alpha}\right)\right)\Big|_i \tag{3.44}$$

$$= \begin{bmatrix} -\dfrac{r_{i-\frac{1}{2}}\alpha^2_{i-\frac{1}{2}}}{r_i\alpha_i\alpha_{i-1}\delta r_i{}^-} & \sigma + \dfrac{4\alpha_i^4}{L^2} + \dfrac{r_{i+\frac{1}{2}}\alpha^2_{i+\frac{1}{2}}}{r_i\alpha_i^2\delta r_i{}^+} + \dfrac{r_{i-\frac{1}{2}}\alpha^2_{i-\frac{1}{2}}}{r_i\alpha_i^2\delta r_i{}^-} & -\dfrac{r_{i+\frac{1}{2}}\alpha^2_{i+\frac{1}{2}}}{r_i\alpha_i\alpha_{i+1}\delta r_i{}^+}\end{bmatrix}\begin{bmatrix} u^{(0)}_{B_{i-1}} \\ u^{(0)}_{B_i} \\ u^{(0)}_{B_{i+1}}\end{bmatrix}$$

where η_i^{++} is given by $\eta_i^{++} = \dfrac{h_i\left(h_i + h_{i+1}\right)}{2}$. Matrices $PV^{(0)}$ and $PU^{(0)}$ are tridiagonal while $PD^{(0)}$ and $PG^{(0)}$ are bidiagonal. The system of equations for $u^{(0)}_B$ is written at grid points r_i for $2 \leq i \leq N_r - 1$ (as for modes $m \neq 0$). Wherever they appear, the values of $u_B^{(0)}(r_1)$ and $u_B^{(0)}(r_{N_r})$ are substituted for by their expression arising from the boundary conditions (2.67) and (2.78):

$$u_B^{(0)}(r_1) = \frac{(h_2+h_1)^2}{\alpha_2\left(h_2^2+2h_2h_1\right)} u_B^{(0)}(r_2) - \frac{h_1^2}{\alpha_3\left(h_2^2+2h_2h_1\right)} u_B^{(0)}(r_3)\,, \tag{3.45}$$

$$u_B^{(0)}(r_{N_r}) = \alpha(r_{N_r})\left(u_z^{\infty} + \frac{\Gamma}{2\pi L}\right). \tag{3.46}$$

As the first equation for u_{B_1} involves u_{B_2} and u_{B_3}, an extra diagonal term proportional to u_{B_3} arises in the matrix block $PV^{(0)}$. This term is unwanted as it breaks the band structure. Fortunately, it is removed by an appropriate linear combination of the equation for $u_\varphi^{(0)}\left(r_{3/2}\right)$ with the equation for $u_{B_2}^{(0)}$. This procedure preserves both the band structure of $PV^{(0)}$ and the second order accuracy.

By contrast, the system of equations for $u_\varphi^{(0)}$ should be written at staggered grid points $r_{i+1/2}$. The first value at $r_{3/2}$ is part of the unknowns of the system whereas the last value at $r_{N_r+1/2}$ is replaced by

$$u_\varphi^{(0)}(r_{N_r+1/2}) = \alpha(R_{\text{ext}}+h_{N_r}/2)\left(\frac{\Gamma}{2\,\pi\left(R_{\text{ext}}+h_{N_r}/2\right)} - \frac{R_{\text{ext}}+h_{N_r}/2}{L}U_z^{\infty}\right) \tag{3.47}$$

according to (2.80). It remains that for $i=1$, at radial distance $r = r_{3/2}$, we need an expression for the viscous term

$$VT_{u_\varphi}^{(0)}\Big|_{r_{3/2}} = \nu\,\alpha(r_{3/2})\,\frac{\partial}{\partial r}\left(\frac{\omega_B^{(0)}}{\alpha}\right)\Bigg|_{r_{3/2}} = \nu\frac{\alpha(r_{3/2})}{h_1}\left[\frac{\omega_B^{(0)}(r_2)}{\alpha(r_2)} - \frac{\omega_B^{(0)}(r_1)}{\alpha(r_1)}\right], \tag{3.48}$$

which should be written with the help of $u_\varphi^{(0)}$ and $u_B^{(0)}$. From equation (2.48), one gets

$$r\alpha\,\omega_B^{(0)} = \frac{2}{L}r\alpha^3\,u_B^{(0)} + \frac{\partial}{\partial r}\left(r\alpha\,u_\varphi^{(0)}\right). \tag{3.49}$$

Integration of (3.49) from $r=0$ to $r=r_{3/2}$ and discretisation of this integral yields the second-order accurate formula:

$$\omega_B^{(0)}(r_1) = \frac{2}{L}\,u_B^{(0)}(r_1) + \frac{4\alpha(r_{3/2})}{h_1}u_\varphi^{(0)}(r_{3/2}). \tag{3.50}$$

In addition, equation (3.49), when discretised with a centred finite difference scheme at $r = r_2$, yields

$$\omega_B^{(0)}(r_2) = \frac{2}{L}\,\alpha^2(r_2)\,u_B^{(0)}(r_2) + 2\frac{r_{5/2}\alpha(r_{5/2})\,u_\varphi^{(0)}(r_{5/2}) - r_{3/2}\alpha(r_{3/2})\,u_\varphi^{(0)}(r_{3/2})}{r_2\alpha(r_2)\,\left(h_1+h_2\right)}. \tag{3.51}$$

The expression of the viscous term thus consists of

$$PV^{(0)}\cdot u_\varphi^{(0)}\Big|_{r_{3/2}} = \begin{bmatrix} \sigma + \nu\left(-\dfrac{2r_{3/2}\alpha_{3/2}}{r_2\alpha_2h_1\left(h_1+h_2\right)} + \dfrac{4\alpha_{3/2}}{h_1^2}\right) & \nu\dfrac{-r_{5/2}\alpha_{5/2}}{r_2\alpha_2^2h_1\left(h_1+h_2\right)} & 0 \end{bmatrix} \begin{bmatrix} u_{\varphi_{3/2}}^{(0)} \\ u_{\varphi_{5/2}}^{(0)} \\ u_{\varphi_{7/2}}^{(0)} \end{bmatrix}$$

and the coupling terms

$$PD^{(0)} \cdot u_B^{(0)}\Big|_{r_{3/2}} = \begin{bmatrix} \dfrac{2\nu}{Lh_1} & \dfrac{-2\nu}{\alpha_2 h_1} & 0 \end{bmatrix} \begin{bmatrix} u_{B_1}^{(0)} \\ u_{B_2}^{(0)} \\ u_{B_3}^{(0)} \end{bmatrix}.$$

In the right hand side of (3.4), the nonlinear terms

$$NL_{u_B}^{(0)} = g_B^{(0)} = [\omega_r \, u_\varphi - \omega_\varphi \, u_r]^{(0)} \tag{3.52}$$

$$NL_{u_\varphi}^{(0)} = g_\varphi^{(0)} = [\omega_B u_r]^{(0)} \tag{3.53}$$

are respectively discretised at $r = r_i$ and $r = r_{i+1/2}$. As the nonlinear terms are computed in the physical space and then Fourier transformed, all Fourier modes m including the axisymmetric contribution $m = 0$ are readily available to compute the right hand side of the system. The unknown variables are reordered according to $u_\varphi^{(0)}(r_1)$, $u_B^{(0)}(r_2)$, $u_\varphi^{(0)}(r_2)$, $u_B^{(0)}(r_3)$,... This leads to a pentadiagonal matrix with left and right-half bandwidth 2. The reordered system is solved with the LAPACK library.

Chapter 4

Vortex filaments: cut-off theory

Contents

For two-dimensional flows, the analysis of the flow dynamics can be reduced to the study of ordinary differential equations (O.D.E.) describing a set of point vortices. For three-dimensional flows, a filamentary approach based on the cutoff theory exists in which the flow dynamics is described by the time evolution of lines. In the present chapter, this latter approach is adopted with the additional constraint of helical symmetry. In this context, the time evolution problem of a set of helical filaments (see figure 4.1) can be again written as an O.D.E. system. This chapter assumes an incompressible inviscid flow which is at rest at $r \to \infty$ and describes the ordinary differential equations (section 4.1), the numerical integration (section 4.2) and a validation (section 4.3) for a set of helical vortices.

This approach is used in chapter 6 to obtain an analytical approximation for the angular velocity of a quasi-equilibrium and in chapter 10 to obtain the nonlinear dynamics of an unstable set of helical vortices.

Let us consider a set of N helical filaments indexed by the subscript $j = 1, ..., N$. Each filament $\mathscr{H}_j$ is labelled by its vector position $\boldsymbol{r_j}$:

$$\boldsymbol{r}_j\left(r_j, \varphi_j, \theta, t\right) = \boldsymbol{i}\, r_j\left(t\right)\, \cos\Big(\theta + \varphi_j\left(t\right)\Big) + \boldsymbol{j}\, r_j\left(t\right)\, \sin\Big(\theta + \varphi_j\left(t\right)\Big) + \boldsymbol{k}\,\frac{\theta}{\gamma}, \tag{4.1}$$

where θ is a continuous parameter defining a particular point on the filament and γ is the inverse of the reduced pitch L introduced in chapter 2, so that $2\pi/\gamma = 2\pi L$ is the spatial period along the axial direction z. At time t, the helical filament $\mathscr{H}_j$ intersects the horizontal plane ($z = 0$ or $\theta = 0$) at

$$\boldsymbol{r_j^0}(t) \equiv \boldsymbol{r_j}\left(r_j, \varphi_j, 0, t\right) = \boldsymbol{i} r_j(t) \cos\left(\varphi_j(t)\right) + \boldsymbol{j} r_j(t) \sin\left(\varphi_j(t)\right) = r_j(t)\boldsymbol{e_r}\left(\varphi_j(t)\right). \tag{4.2}$$

Variables $r_j(t)$ and $\varphi_j(t)$ are thus respectively the radial and azimuthal positions of this intersecting point. Note that γ is kept constant in time and is identical for all filaments: all filaments are right-handed or else left-handed to comply with helical symmetry. Following Ricca (1994), it is adequate for computations to introduce on each filament $\mathscr{H}_j$, a Frenet-Serret basis $(\boldsymbol{t}_j, \boldsymbol{n}_j, \boldsymbol{b}_j)$. Vector $\boldsymbol{t_j}$ is the vector tangent to the filament

$$\boldsymbol{t}_j \equiv \boldsymbol{r_j}' = \frac{\gamma\, r_j}{\sqrt{1 + \gamma^2 r_j^2}} \left[-\boldsymbol{i}\, \sin(\theta + \varphi_j) + \boldsymbol{j}\, \cos(\theta + \varphi_j) + \frac{\boldsymbol{k}}{\gamma\, r_j} \right]. \tag{4.3}$$

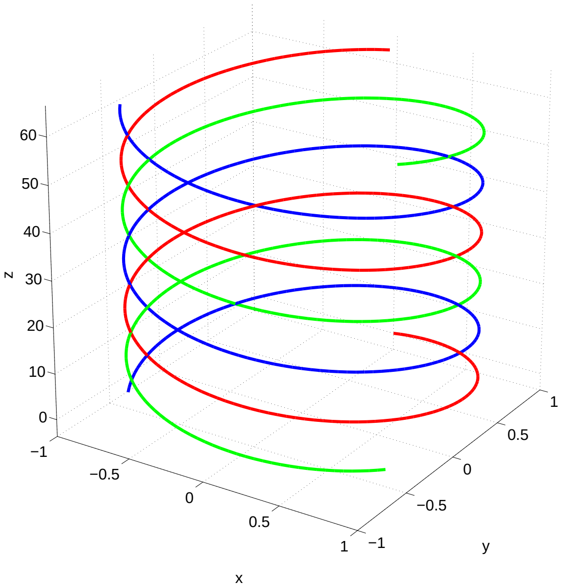

Figure 4.1 – $N = 3$ helical vortex filaments.

where the prime denotes the derivative with respect to the arclength $s_j \equiv \theta\left(1+\gamma^2 r_j^2\right)^{1/2}/\gamma$ of helix $\mathscr{H}_j$. The unit normal vector $\boldsymbol{n}_j$ is defined as

$$\boldsymbol{n}_j \equiv \frac{\boldsymbol{r}_j''}{\left\|\boldsymbol{r}_j''\right\|} = -\boldsymbol{i}\,\cos(\theta+\varphi_j) - \boldsymbol{j}\,\sin(\theta+\varphi_j), \tag{4.4}$$

and the binormal $\boldsymbol{b}_j \equiv \boldsymbol{t}_j \times \boldsymbol{n}_j$ reads

$$\boldsymbol{b}_j = \frac{1}{\sqrt{1+\gamma^2 r_j^2}}\left[\boldsymbol{i}\sin(\theta+\varphi_j) - \boldsymbol{j}\cos(\theta+\varphi_j) + \boldsymbol{k}\gamma\, r_j\right]. \tag{4.5}$$

It is recalled that the following equations are satisfied

$$\frac{\mathrm{d}\boldsymbol{t}_j}{\mathrm{d}s} = \kappa\,\boldsymbol{n}_j, \qquad \frac{\mathrm{d}\boldsymbol{b}_j}{\mathrm{d}s} = -\tau\,\boldsymbol{n}_j. \tag{4.6}$$

where κ stands for the curvature and τ for the torsion of the helix:

$$\kappa \equiv \left\|\boldsymbol{r}_j''\right\| = \frac{\gamma^2\, r_j}{1+\gamma^2\, r_j^2}, \qquad \tau = \frac{\gamma}{1+r_j^2\gamma^2}. \tag{4.7}$$

4.1 The ODE system governing the helical vortex filaments

If we determine the motion of the particular fluid particle located at time t at position $\boldsymbol{r}_i^0(t)$, we are able to recover the position and motion of the whole filament $\mathscr{H}_i$ because of the helical symmetry.

4.1.1 Computation of the velocity using the Biot-Savart law

Let us compute the Lagrangian velocity $\boldsymbol{u}_i\left(\boldsymbol{r}_i^0\right)$ of that particular point. It can be decomposed into two contributions: the induced motion of the filament $\mathscr{H}_i$ on itself and the velocity induced by the $N-1$ other filaments:

$$\boldsymbol{u}_i\left(\boldsymbol{r}_i^0\right) = \boldsymbol{u}_j^{\text{self}}\left(\boldsymbol{r}_i^0\right) + \sum_{j\neq i}^{N} \boldsymbol{u}_j\left(\boldsymbol{r}_i^0\right). \tag{4.8}$$

The velocity induced by the jth ($j \neq i$) filament $\mathscr{H}_j$ at a point $\boldsymbol{r_i^0} \in \mathscr{H}_i$ is given by the Biot-Savart law:

$$\boldsymbol{u_j}(\boldsymbol{r_i^0}) = \frac{\Gamma_j}{4\pi} \int_{-\infty}^{+\infty} \boldsymbol{t_j} \times \frac{\left(\boldsymbol{r_i^0} - \boldsymbol{r_j}\right)}{\left\|\left(\boldsymbol{r_i^0} - \boldsymbol{r_j}\right)\right\|^3} \mathrm{d}s_j \tag{4.9}$$

that can be evaluated by direct integration (see Appendix D). The self-induced velocity $\boldsymbol{u_i^{\text{self}}}\left(\boldsymbol{r_i^0}\right)$ of filament $\mathscr{H}_i$ at a point $\boldsymbol{r_i^0} \in \mathscr{H}_i$ is again given by the Biot-Savart law. However the integral is singular and should be regularized using the cutoff theory which introduces a vortex core size (see Appendix D).

4.1.2 Motion of the intersecting point

Let us consider a given fluid particle located on the filament $\mathscr{H}_i$. A parameter $\theta = \theta_p(t)$ defines its position *via*

$$\begin{aligned}\boldsymbol{r}_i(\theta_p, t) &= \boldsymbol{i}\, r_i(t)\, \cos(\theta_p + \varphi_i(t)) + \boldsymbol{j}\, r_i(t)\, \sin(\theta_p + \varphi_i(t)) + \boldsymbol{k}\, \frac{\theta_p}{\gamma} &(4.10)\\ &= r_i(t)\, \boldsymbol{e}_r(\theta_p + \varphi_i(t)) + \boldsymbol{k}\, \frac{\theta_p}{\gamma}. &(4.11)\end{aligned}$$

As $\theta = \theta_p(t)$ *a priori* varies in time, it follows that

$$\frac{D\boldsymbol{r}_i}{Dt} = \frac{\partial \mathbf{r}_i}{\partial s_i}\frac{ds_i}{d\theta}\frac{\mathrm{d}\theta_p}{\mathrm{dt}} + \frac{\partial \mathbf{r}_i}{\partial \varphi_i}\frac{\mathrm{d}\varphi_i}{\mathrm{dt}} + \frac{\partial \mathbf{r}_i}{\partial r_i}\frac{\mathrm{d}r_i}{\mathrm{dt}} \tag{4.12}$$

with

$$\frac{\partial \mathbf{r}_i}{\partial s_i} = \boldsymbol{t}_i, \quad \frac{\partial \mathbf{r}_i}{\partial \varphi_i} = r_i(t)\boldsymbol{e}_\theta(\theta_p + \varphi_i(t)) = r_i(t)\boldsymbol{k} \times \boldsymbol{e}_r(\theta_p + \varphi_i(t)), \quad \frac{\partial \mathbf{r}_i}{\partial r_i} = \boldsymbol{e}_r(\theta_p + \varphi_i(t)).$$

Within the framework of filament theory, only the velocity components orthogonal to the filament can be computed for velocity at a point located on the vortex itself. As a consequence, the condition

$$\frac{D\boldsymbol{r}_i}{Dt} = \boldsymbol{u_i}\left(\boldsymbol{r_i}\right) \tag{4.13}$$

is imposed only along $\boldsymbol{n}_i$ and $\boldsymbol{b}_i$:

$$\begin{aligned}\left(\boldsymbol{u_i}\left(\boldsymbol{r_i}\right) - \frac{D\boldsymbol{r}_i}{Dt}\right) \cdot \boldsymbol{n}_i &= \left(\boldsymbol{u_i}\left(\boldsymbol{r_i}\right) - \frac{\partial \mathbf{r}_i}{\partial \varphi_i}\frac{\mathrm{d}\varphi_i}{\mathrm{dt}} - \frac{\partial \mathbf{r}_i}{\partial r_i}\frac{\mathrm{d}r_i}{\mathrm{dt}}\right) \cdot \boldsymbol{n}_i = 0, &(4.14)\\ \left(\boldsymbol{u_i}\left(\boldsymbol{r_i}\right) - \frac{D\boldsymbol{r}_i}{Dt}\right) \cdot \boldsymbol{b}_i &= \left(\boldsymbol{u_i}\left(\boldsymbol{r_i}\right) - \frac{\partial \mathbf{r}_i}{\partial \varphi_i}\frac{\mathrm{d}\varphi_i}{\mathrm{dt}} - \frac{\partial \mathbf{r}_i}{\partial r_i}\frac{\mathrm{d}r_i}{\mathrm{dt}}\right) \cdot \boldsymbol{b}_i = 0. &(4.15)\end{aligned}$$

For a given time t, let us now impose the above equations to the particle located at $\boldsymbol{r_i^0} = r_i(t)\, \boldsymbol{e}_r(\varphi_i(t))$ that is at $z = 0$ or $\theta_p(t) = 0$. Since at point $\boldsymbol{r_i^0}$ one has

$$\boldsymbol{n}_i = -\boldsymbol{e}_r(\varphi_i(t)), \quad \boldsymbol{b}_i = \frac{1}{\sqrt{1 + \gamma^2 r_i^2}}\left[-\boldsymbol{e}_\theta(\varphi_i(t)) + \gamma\, r_i \boldsymbol{k}\right],$$

$$\frac{\partial \mathbf{r}_i}{\partial \varphi_i} = r_i(t)\boldsymbol{e}_\theta(\varphi_i(t)) = r_i(t)\boldsymbol{k} \times \boldsymbol{e}_r(\varphi_i(t)), \qquad \frac{\partial \mathbf{r}_i}{\partial r_i} = \boldsymbol{e}_r(\varphi_i(t)),$$

the following equations are obtained

$$\begin{aligned}\frac{\mathrm{d}r_i}{\mathrm{dt}} &= \boldsymbol{u_i}\left(\boldsymbol{r_i^0}\right) \cdot \boldsymbol{e}_r(\varphi_i(t)), &(4.16)\\ \frac{\mathrm{d}\varphi_i}{\mathrm{dt}} &= \boldsymbol{u_i}\left(\boldsymbol{r_i^0}\right) \cdot \left[\frac{\boldsymbol{e}_\theta(\varphi_i(t))}{r_i} - \gamma \boldsymbol{k}\right]. &(4.17)\end{aligned}$$

After introducing the expressions for $\boldsymbol{u_i}\left(\boldsymbol{r}_{\boldsymbol{i}}^{0}\right)$ computed in section 4.1.1 and after time-consuming computations, one gets a system of $2N$ O.D.E. for $r_i(t)$ and $\varphi_i(t)$:

$$\begin{aligned}
\frac{\mathrm{d}r_i}{\mathrm{d}t} &= \sum_{j\neq i}^{N} \frac{\Gamma_j}{4\,\pi\,|\gamma|}\, r_j[A_{ij}\cos(\varphi_j-\varphi_i)+B_{ij}\sin(\varphi_j-\varphi_i)], && (4.18)\\
\frac{\mathrm{d}\varphi_i}{\mathrm{d}t} &= \frac{\Gamma_i}{2\,\pi}\,\gamma^2\left\{[K_i\left(\gamma r_i,\gamma\delta\right)-I_i\left(\gamma r_i,\gamma\delta\right)]-\gamma^2\,r_i^2\,I_i\left(\gamma r_i,\gamma\delta\right)\right\}\\
&\quad+\sum_{j\neq i}^{N}\frac{\Gamma_j}{4\,\pi\,|\gamma|}\left[F_{ij}-\frac{r_j}{r_i}B_{ij}\cos(\varphi_j-\varphi_i)+\frac{r_j}{r_i}A_{ij}\sin(\varphi_j-\varphi_i)\right] && (4.19)\\
&\quad+\sum_{j\neq i}^{N}\frac{\Gamma_j\,|\gamma|}{4\,\pi}\left[(r_i\,r_j\,C_{ij}\cos(\varphi_j-\varphi_i)-r_i\,r_j\,D_{ij}\sin(\varphi_j-\varphi_i)-r_j^2\,F_{ij})\right]
\end{aligned}$$

where $\delta=\delta_1 a$ denotes the cut-off length with a the core size and δ_1 a dimensionless factor linked to the velocity profile in the vortex core (see Appendix D). The integrals

$$\begin{aligned}
A_{ij} &= \int_{-\infty}^{+\infty}[\sin(\theta)-\theta\,\cos(\theta)]Y_{ij}\,\mathrm{d}\theta, && (4.20)\\
B_{ij} &= \int_{-\infty}^{+\infty}[\cos(\theta)+\theta\,\sin(\theta)]Y_{ij}\,\mathrm{d}\theta,\\
C_{ij} &= \int_{-\infty}^{+\infty}[\cos(\theta)]Y_{ij}\,\mathrm{d}\theta,\\
D_{ij} &= \int_{-\infty}^{+\infty}[\sin(\theta)]Y_{ij}\,\mathrm{d}\theta,\\
F_{ij} &= \int_{-\infty}^{+\infty}Y_{ij}\,\mathrm{d}\theta,\\
Y_{ij} &= \frac{1}{Z_{ij}^{3/2}},\\
Z_{ij} &= \theta^2/\gamma^2+r_i^2+r_j^2-2r_jr_i\cos\theta\cos\left(\varphi_j-\varphi_i\right)+2r_jr_i\sin\theta\sin\left(\varphi_j-\varphi_i\right)
\end{aligned}$$

are related to the contributions of other vortices and the integrals

$$\begin{aligned}
I_i\left(\gamma r_i,\gamma\delta\right) &= \int_{\theta_{0i}}^{\infty}\frac{[1-\cos\theta]\,\mathrm{d}\theta}{\{\theta^2+2\,\gamma^2\,r_i^2\,[1-\cos\theta]\}^{3/2}},\\
K_i\left(\gamma r_i,\gamma\delta\right) &= \frac{1}{\gamma^2 r_i^2}\left\{1-\frac{\theta_{0i}}{[2\gamma^2 r_i^2\,[1-\cos\theta_{0i}]+\theta_{0i}^2]^{1/2}}\right\}
\end{aligned}$$

to the self-induced contribution. Note that $\theta_{0_i}=\dfrac{|\gamma|\,\delta}{\sqrt{1+\gamma^2 r_i^2}}$.

4.2 Numerical integration for the helical vortex system

This system takes the form of a general dynamical system

$$\frac{\mathrm{d}\boldsymbol{X}}{\mathrm{d}t}=\boldsymbol{F}\left(\boldsymbol{X}\right),\qquad \boldsymbol{X}(t=0)=\boldsymbol{X}_0 \tag{4.21}$$

where $\boldsymbol{F}$ is a nonlinear function of $\boldsymbol{X}=(r_1,r_2,.....r_{N-1},r_N,\varphi_1,\varphi_2,....,\varphi_{N-1},\varphi_N)^T$. This system is solved numerically using a second order Adams-Bashforth extrapolation for the r.h.s.

$$\frac{\boldsymbol{X}_{n+1}-\boldsymbol{X}_n}{\delta t}=\frac{3}{2}\boldsymbol{F}_n-\frac{1}{2}\boldsymbol{F}_{n-1} \tag{4.22}$$

with $F_n = F(\boldsymbol{X}_n)$ and δt the time step. The method is second order accurate at time $(t_n + t_{n+1})/2$. To start the simulation, one uses the initial condition $\boldsymbol{X}_0$ and

$$\boldsymbol{X}_1 = \boldsymbol{X}_0 + \delta t \boldsymbol{F}(\boldsymbol{X}_{1/2}), \qquad \text{where} \qquad \boldsymbol{X}_{\frac{1}{2}} = \boldsymbol{X}_0 + \frac{\delta t}{2}\boldsymbol{F}(\boldsymbol{X}_0).$$

Integrals A_{ij} to F_{ij} are decomposed into a sum of $2N_p$ integrals (the value of N_p is chosen to be large enough to ensure numerical convergence)

$$A_{ij} = \sum_{p=-N_p}^{N_p} \int_0^{2\pi} \frac{[\sin(\theta) - (\theta + 2p\pi)\,\cos(\theta)]}{[(\theta + 2p\pi)^2/\gamma^2 + r_i^2 + r_j^2 - 2r_j r_i \cos(\theta)\cos(\varphi_j - \varphi_i) + 2r_j r_i \sin(\theta)\sin(\varphi_j - \varphi_i)]^{3/2}}\,\mathrm{d}\theta,$$

$$B_{ij} = \sum_{p=-N_p}^{N_p} \int_0^{2\pi} \frac{[\cos(\theta) + (\theta + 2p\pi)\,\sin(\theta)]}{[(\theta + 2p\pi)^2/\gamma^2 + r_i^2 + r_j^2 - 2r_j r_i \cos(\theta)\cos(\varphi_j - \varphi_i) + 2r_j r_i \sin(\theta)\sin(\varphi_j - \varphi_i)]^{3/2}}\,\mathrm{d}\theta,$$

$$C_{ij} = \sum_{p=-N_p}^{N_p} \int_0^{2\pi} \frac{\cos(\theta)}{[(\theta + 2p\pi)^2/\gamma^2 + r_i^2 + r_j^2 - 2r_j r_i \cos(\theta)\cos(\varphi_j - \varphi_i) + 2r_j r_i \sin(\theta)\sin(\varphi_j - \varphi_i)]^{3/2}}\,\mathrm{d}\theta,$$

$$D_{ij} = \sum_{p=-N_p}^{N_p} \int_0^{2\pi} \frac{\sin(\theta)}{[(\theta + 2p\pi)^2/\gamma^2 + r_i^2 + r_j^2 - 2r_j r_i \cos(\theta)\cos(\varphi_j - \varphi_i) + 2r_j r_i \sin(\theta)\sin(\varphi_j - \varphi_i)]^{3/2}}\,\mathrm{d}\theta,$$

$$F_{ij} = \sum_{p=-N_p}^{N_p} \int_0^{2\pi} \frac{1}{[(\theta + 2p\pi)^2/\gamma^2 + r_i^2 + r_j^2 - 2r_j r_i \cos(\theta)\cos(\varphi_j - \varphi_i) + 2r_j r_i \sin(\theta)\sin(\varphi_j - \varphi_i)]^{3/2}}\,\mathrm{d}\theta.$$

The integral I_i is split into a sum of N_p integrals

$$I_i = \int_{\theta_{0i}}^{2\pi} \frac{[1 - \cos\theta]\,\mathrm{d}\theta}{\{\theta^2 + 2\,\gamma^2\,r_i^2\,[1 - \cos(\theta)]\}^{3/2}}\,\mathrm{d}\theta + \sum_{p=1}^{N_p - 1} \int_0^{2\pi} \frac{[1 - \cos(\theta)]}{\{(\theta + 2p\pi)^2 + 2\,\gamma^2\,r_i^2\,[1 - \cos(\theta)]\}^{3/2}}\,\mathrm{d}\theta.$$

Each such integral is then discretized into an even number $N_{Simpson}$ of sub-intervals in $[0, 2\pi]$ and evaluated using a composite Simpson method

$$\int_0^{2\pi} f(\theta)\,\mathrm{d}\theta \approx \frac{h}{3}\left[f(0) + 4\sum_{j=1}^{n/2} f(\theta_{2j-1}) + 2\sum_{j=1}^{n/2-1} f(\theta_{2j}) + f(2\pi)\right]$$

where

$$\theta_j = jh \;\text{ for } j = 0, 1, \cdots, N_{Simpson}, \;\text{ and } h = \frac{2\pi}{N_{Simpson}}.$$

4.3 Numerical validation

In order to validate the code, a comparison between two-dimensional theoretical results and numerical results for $\gamma \to 0$ is performed.

First, the angular velocity of a polygon of N point vortices with $\gamma \to 0$ is performed starting with an initial condition

$$\varphi_i(t = 0) = \frac{(i-1)\,2\pi}{N}, \qquad r_i(t = 0) = 1.$$

For $N < 7$, the pure two-dimensional polygonal configuration is known to be a stable equilibrium with angular velocity

$$\Omega_{2D}^{th} = \frac{\Gamma\,(N-1)}{4\pi r_0^2}. \tag{4.23}$$

Here the circulation Γ and r_0 are set to 1. Numerically one sets $\gamma = 0.00001$ and core size $a = 0.1$. The numerical parameters are the time step $\delta t = 0.1$ and $N_{Simpson} = 256 \times 10^4$. Once the simulation is performed, the angular velocity is evaluated by the formula $\Omega_{2D}^n = [\varphi(t_n) - \varphi(t_{n-1})]/\delta t$. Ω_{2D}^n is shown to be constant with time (it does not depend on n) and Table 4.1 indicates that its numerical value is close to the theoretical expectation.

N	Ω_{2D}	Ω_{2D}^{th}
2	0.079577	0.079577
3	0.159154	0.159154
4	0.238732	0.238732
5	0.318309	0.318309
6	0.397886	0.397887

Table 4.1 – Comparison of the numerical Ω_{2D} and theoretical Ω_{2D}^{th} results for a polygonal configurations with $N = 2$ to 6 vortices.

A second test consists in computing the angular velocity of a pair of point vortices with $\gamma \to 0$, however with an initial condition off-centred with respect to the origin:

$$\begin{aligned} &r_1(t=0) = r_0 + \delta r, \quad r_2(t=0) = r_0 - \delta r, \\ &\varphi_1(t=0) = \varphi_2(t=0) = \frac{\pi}{4}. \end{aligned}$$

This pattern is more demanding as far as numerics are concerned. In this configuration, the vortices are theoretically expected to rotate around a centroid which is located at ($r = r_0$, $\varphi = \frac{\pi}{4}$). This is indeed observed and parameters and results are shown in table 4.2. The comparison is very good for $\delta r > 0.1$. When $\delta r = 0.1$, the angular velocity increases and a smaller time step $\delta t < 0.01$ is necessary to reach convergence.

N	γ	δt	$N_{Simpson}$	N_p	δr	Ω_{2D}	Ω_{2D}^{th}	Err-relative %
2	0.00001	0.01	256×10^4	8	0.1	7.33074	7.95774	~ 8
2	0.00001	0.05	256×10^4	8	0.2	1.9827	1.9894	0.33
2	0.00001	0.05	256×10^4	8	0.3	0.88566	0.88419	0.16
2	0.00001	0.05	256×10^4	8	0.4	0.4971	0.4973	0.03

Table 4.2 – Comparison numerical Ω_{2D} and theoretical Ω_{2D}^{th} results for a vortex pair when the centroid is not centred at the origin.

Chapter 5

Characterization of helical vortices

Contents

In this chapter, the numerical tools and the physical quantities of interest needed to characterize one or multiple helical vortices are presented. Helix radius and angular velocity can be directly extracted from the DNS fields (section 5.1). However, the analysis of the vortex core structures necessitates the definition of a cut plane "orthogonal" to the vortex (section 5.2). The fields are separated into in-plane and orthogonal components and a multipolar decomposition is applied (section 5.3), leading to the definition of vortex core radius and ellipticity (section 5.4).

5.1 Vortex position and angular velocity

All quantities are obtained by DNS at discrete points (r_i, φ_j) or equivalently at points (r_i, θ_j) in the plane $z = 0$ thereafter denoted plane Π_0.

5.1.1 Helix radius r_A

In the plane Π_0, we determine the position of the vortices as being the centre A of the vortex or the various centres in the case of multiple vortices. Point A with coordinates (r_A, θ_A) corresponds to the location where the maximum of the helical vorticity ω_B is reached in the vortex region in plane Π_0. The precise value of the helix radius r_A is obtained using a local quadratic interpolation of ω_B around the discrete maximum location. Alternatively, A can also be defined as a stagnation point (see definition and procedure in chapter 7).

5.1.2 Angular velocity Ω

Configurations of one helical vortex or a regular array of identical vortices may be inviscid equilibria when considered in a frame rotating at some constant angular velocity Ω_0. This rotation is due to both the self-induced vortex velocity and the mutual induction between vortices. When viscous diffusion acts, it gives rise to a slowly evolving state that we call *quasi-equilibrium* with changing angular velocity and core size. A first method for evaluating the instantaneous angular velocity $\Omega(t)$ is to track the azimuthal location of the vortex center θ_- and θ_+ in the Π_0 plane for times t_- and t_+ and to set $\Omega(t) = (\theta_+ - \theta_-)/(t_+ - t_-)$ at time $t = \frac{1}{2}(t_- + t_+)$. Such a procedure is inaccurate because determining $\theta_\pm$ is quite sensitive to the actual position of the vortex center within the numerical cell. Instead we use the vorticity component ω_B in the whole plane Π_0 at times t_- and t_+. The rotation angle $\delta\theta$ along the azimuth is determined to achieve the best correlation between $\omega_B(r, \theta + \delta\theta, t_-)$ and $\omega_B(r, \theta, t_+)$. Technically, the integral

$$I(\delta\theta) \equiv \iint_S |\omega_B(r, \theta, t_+) - \omega_B(r, \theta + \delta\theta, t_-)|^2 \mathrm{d}S\,, \tag{5.1}$$

is optimized using an iterative procedure. $\omega_B(r, \theta{+}\delta\theta, t_-)$ is easily obtained from $\omega_B(r, \theta, t_-)$: Fourier azimuthal modes $\omega_B^{(m)}$ are simply multiplied by $\mathrm{e}^{im\delta\theta}$. This approach is justified since for inviscid equilibria, $I(\delta\theta)$ vanishes for $\delta\theta = \Omega_0 \times (t_+ - t_-)$. For viscous quasi-equilibria, $I(\delta\theta)$ is assumed to reach a minimum when $\delta\theta = \Omega(t) \times (t_+ - t_-)$ yielding $\Omega(t)$ at time $t = \frac{1}{2}(t_- + t_+)$.

5.2 Framework description

The plane Π_0 is not convenient to characterize the vortex core structures. For instance, let us consider a helical vortex with circular vorticity distribution in its core. When cut by the plane Π_0 orthogonal to the helix axis, its cross-section is not circular but takes a banana shape. This effect is only geometrical and it is amplified when the helical pitch $2\pi L$ is reduced. This can be visualised in figure 5.1 (left column), where the contours of the helical vorticity component ω_B are plotted for the case of a single helical vortex and various values of L. In order to characterize the structure of a helical vortex, it is convenient to slice it with a plane locally perpendicular to the vorticity tube. Note that strictly speaking it is not possible to define "a plane perpendicular to a helical vortex" as the orientation of the vector $\boldsymbol{e}_B$ tangent to a helical line changes with position. However, if the vorticity tube is small enough so that these variations can be neglected, a perpendicular plane thereafter denoted $\Pi_\perp$ can be introduced. Note that the $\Pi_\perp$ is associated to one given vortex, and it depends on time. Other vortices present in the fluid domain are associated to other such orthogonal planes. The following section is dedicated to the definition of this plane.

5.2.1 Definition of $\Pi_\perp$ and its associated basis

The plane $\Pi_\perp$ is defined as the plane which includes point A of maximum helical vorticity and which is perpendicular to the helical line passing through this point, i.e. perpendicular to the unit vector $\boldsymbol{e}_{\boldsymbol{B_A}} \equiv \boldsymbol{e}_B\,(r_A, \theta_A)$ given by

$$\boldsymbol{e}_{\boldsymbol{B_A}}\,(r_A, \theta_A) = \alpha_A \left[\boldsymbol{e}_z + \frac{r_A}{L}\,\boldsymbol{e}_\theta\,(\theta_A)\right] \quad \text{with} \quad \alpha_A \equiv \alpha\,(r_A) = \frac{1}{\sqrt{1 + (r_A/L)^2}}. \tag{5.2}$$

If the vortex core size is small compared to L, all helical lines of this vorticity tube intersect quasi perpendicularly the $\Pi_\perp$-plane and the cross section of the vortex is by far

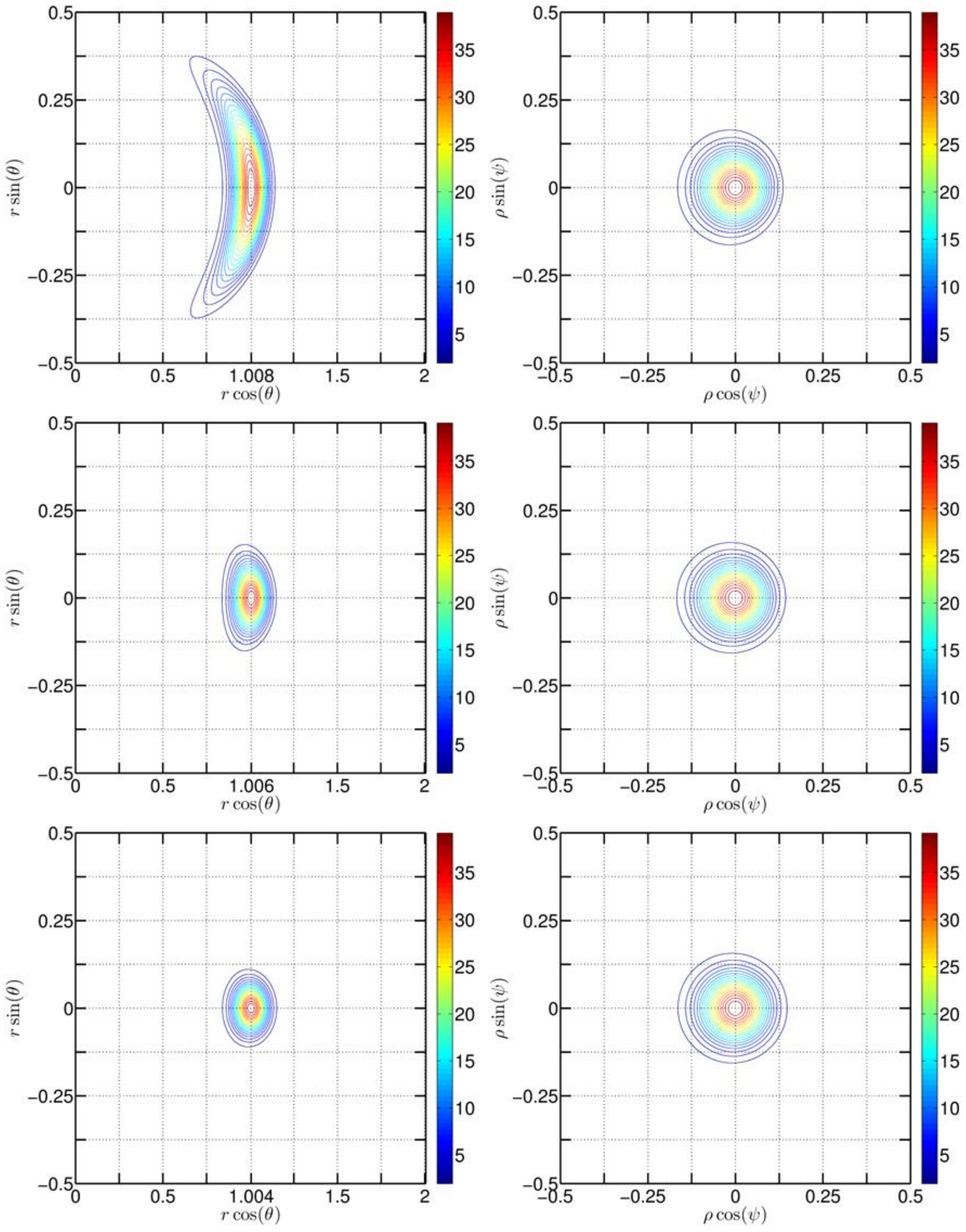

Figure 5.1 – Single vortex of core radius $a = 0.09$. Top: reduced pitch $L = 0.20$, middle: $L = 0.60$ and bottom: $L = 1$. Left column: contours of vorticity ω_B in the Π_0 plane. Right column: contours of vorticity ω_B in the $\Pi_\perp$ plane.

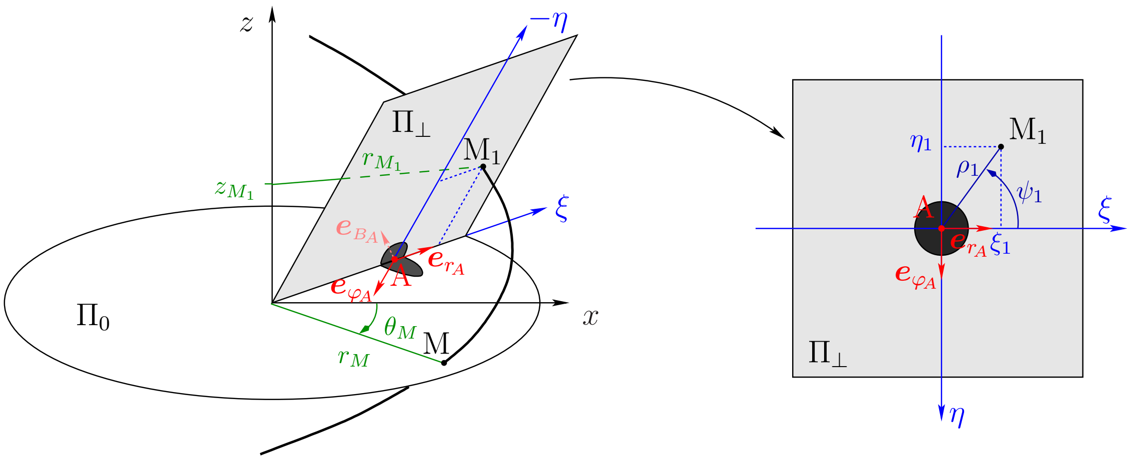

Figure 5.2 – Planes Π_0 and $\Pi_\perp$ with their associated coordinates systems. The black solid helical line intersects Π_0 at point M and $\Pi_\perp$ at point M_1.

more circular, as can be seen in figure 5.1 (right column). In the $\Pi_\perp$ plane, one may use a Cartesian basis $(\boldsymbol{e}_{\boldsymbol{r}_A}, \boldsymbol{e}_{\boldsymbol{\varphi}_A})$ defined as

$$\boldsymbol{e}_{\boldsymbol{\varphi}_A} \equiv \boldsymbol{e}_\varphi(r_A, \theta_A) = \alpha_A \left[\boldsymbol{e}_\theta(\theta_A) - \frac{r_A}{L}\,\boldsymbol{e}_z\right], \tag{5.3}$$

$$\boldsymbol{e}_{\boldsymbol{r}_A} \equiv \boldsymbol{e}_r(\theta_A) = \cos\theta_A\,\boldsymbol{e}_x + \sin\theta_A\,\boldsymbol{e}_y \tag{5.4}$$

or a local polar coordinate system centred at point A with local basis $\left(\boldsymbol{e}_{\boldsymbol{\rho}}, \boldsymbol{e}_\psi\right)$:

$$\boldsymbol{e}_{\boldsymbol{\rho}} = \cos\psi \boldsymbol{e}_{\boldsymbol{r}_A} + \sin\psi \boldsymbol{e}_{\boldsymbol{\varphi}_A}, \tag{5.5}$$

$$\boldsymbol{e}_\psi = \cos\psi \boldsymbol{e}_{\boldsymbol{\varphi}_A} - \sin\psi \boldsymbol{e}_{\boldsymbol{r}_A} \tag{5.6}$$

where ψ is the polar angle. A sketch of the different planes and their associated coordinate systems is shown in figure 5.2.

5.2.2 Relationships between planes Π_0 and $\Pi_\perp$

It is necessary to establish some connections between points in Π_0 and points in $\Pi_\perp$. Any point M in plane Π_0, is characterised by its Cartesian coordinates (x, y) or polar coordinates $(r_M, \theta_M = \varphi_M)$ given by

$$\overrightarrow{OM} = x_M\,\boldsymbol{e}_x + y_M\,\boldsymbol{e}_y, \quad \text{with} \quad x_M = r_M\,\cos\theta_M,\; y_M = r_M\,\sin\theta_M, \tag{5.7}$$

where $(\boldsymbol{e}_x, \boldsymbol{e}_y)$, are unitary vectors along x and y respectively.

Let us consider a point M_1 in the $\Pi_\perp$ plane. M_1 does not lie in plane Π_0 but sits on a helical line $\varphi = cst$ which intersects plane Π_0 at a given position M (see figure 5.2). Relations between the coordinates of M and M_1 can be now derived. The position vector $\overrightarrow{OM_1}$ can be expressed in the cylindrical coordinates associated to Π_0

$$\overrightarrow{OM_1} = z_{M_1}\,\boldsymbol{e}_z + r_M\,\cos\theta_{M_1}\,\boldsymbol{e}_x + r_M\,\sin\theta_{M_1}\,\boldsymbol{e}_y \tag{5.8}$$

with $\theta_{M_1} = \theta_M + z_{M_1}/L$, or it can be expressed in the Cartesian frame in the $\Pi_\perp$ plane

$$\overrightarrow{OM_1} = \overrightarrow{OA} + \xi_1\boldsymbol{e}_{\boldsymbol{r}_A} + \eta_1\boldsymbol{e}_{\boldsymbol{\varphi}_A} = (r_A + \xi_1)\boldsymbol{e}_{\boldsymbol{r}_A} + \eta_1\boldsymbol{e}_{\boldsymbol{\varphi}_A} \tag{5.9}$$

where (ξ_1, η_1) are the local Cartesian coordinates of M_1. Using expressions (5.8) and (5.9), the height z_{M_1} can be expressed as

$$z_{M_1} = \overrightarrow{OM_1} \cdot \boldsymbol{e_z} = -\alpha_A \frac{r_A}{L}\eta_1, \tag{5.10}$$

implying that vector

$$\overrightarrow{OM_1} - z_{M_1}\,\boldsymbol{e_z} = (r_A + \xi_1)\boldsymbol{e_{r_A}} + \eta_1\alpha_A^2\boldsymbol{e_{\varphi_A}} + \eta_1\alpha_A^2\frac{r_A}{L}\boldsymbol{e_{B_A}} \tag{5.11}$$

has no component along z. The norm of (5.11) yields

$$r_M^2 = r_{M_1}^2 = (r_A + \xi_1)^2 + \alpha_A^2\eta_1^2 \tag{5.12}$$

and computing the scalar products $\overrightarrow{OM_1} \cdot \boldsymbol{e_x}$ and $\overrightarrow{OM_1} \cdot \boldsymbol{e_y}$ leads to

$$r_M\ \cos(\theta_{M_1}) = (r_A + \xi_1)\cos\theta_A - \eta_1\alpha_A\sin\theta_A, \tag{5.13}$$
$$r_M\ \sin(\theta_{M_1}) = (r_A + \xi_1)\sin\theta_A + \eta_1\alpha_A\cos\theta_A, \tag{5.14}$$
$$\text{where } \theta_{M_1} = \theta_M - \alpha_A\frac{r_A}{L^2}\eta_1. \tag{5.15}$$

Equations (5.13)-(5.15) link the Cartesian coordinates (ξ_1, η_1) of a point M_1 in $\Pi_\perp$ to the coordinates (r_M, θ_M) of its "helically projected" image point M in Π_0. If, in the plane $\Pi_\perp$, the polar coordinates (ρ_1, ψ_1) of point M_1 are needed, the relations $\xi_1 = \rho_1\cos\psi_1, \eta_1 = \rho_1\sin\psi_1$ are used.

5.3 Multipolar decomposition of the fields in the $\Pi_\perp$ plane

In order to characterize a vortex in the $\Pi_\perp$ plane, the vorticity component ω_B is not sufficient, for instance, to evaluate the vortex circulation: except at point A, ω_B is *not* the vorticity component perpendicular to the plane $\Pi_\perp$. Consequently, it is preferable to separate the vorticity field into a component orthogonal to the plane $\Pi_\perp$, namely ω_{B_A}, and two in-plane polar components ω_ρ and ω_ψ defined by

$$\omega_{B_A}(M_1) \equiv \boldsymbol{\omega}(M_1)\cdot\boldsymbol{e_{B_A}}, \tag{5.16}$$
$$\omega_\rho\ (M_1) \equiv \boldsymbol{\omega}(M_1)\cdot\boldsymbol{e_\rho}, \tag{5.17}$$
$$\omega_\psi\ (M_1) \equiv \boldsymbol{\omega}(M_1)\cdot\boldsymbol{e_\psi}. \tag{5.18}$$

By using the following projections relations

$$\boldsymbol{e_B}(M_1)\cdot\boldsymbol{e_{B_A}} = \alpha_{M_1}\alpha_A\left[1 + \frac{r_{M_1}r_A}{L^2}\cos(\theta_{M_1} - \theta_A)\right], \tag{5.19}$$
$$\boldsymbol{e_\varphi}(M_1)\cdot\boldsymbol{e_{B_A}} = \alpha_{M_1}\alpha_A\left[\frac{r_A}{L}\cos(\theta_{M_1} - \theta_A) - \frac{r_{M_1}}{L}\right], \tag{5.20}$$
$$\boldsymbol{e_r}(M_1)\cdot\boldsymbol{e_{B_A}} = \alpha_A\frac{r_A}{L}\sin(\theta_{M_1} - \theta_A) \tag{5.21}$$

and some algebra, equations (5.16)-(5.18) turns into

$$\begin{aligned}\omega_{B_A}(M_1) = {} & \omega_B(M_1)\,\alpha_{M_1}\alpha_A\left[1 + \frac{r_{M_1}r_A}{L^2}\cos(\theta_{M_1} - \theta_A)\right] \\ & + \omega_\varphi(M_1)\,\alpha_{M_1}\alpha_A\left[\frac{r_A}{L}\cos(\theta_{M_1} - \theta_A) - \frac{r_{M_1}}{L}\right] + \omega_r(M_1)\,\alpha_A\frac{r_A}{L}\sin(\theta_{M_1} - \theta_A)\end{aligned} \tag{5.22}$$

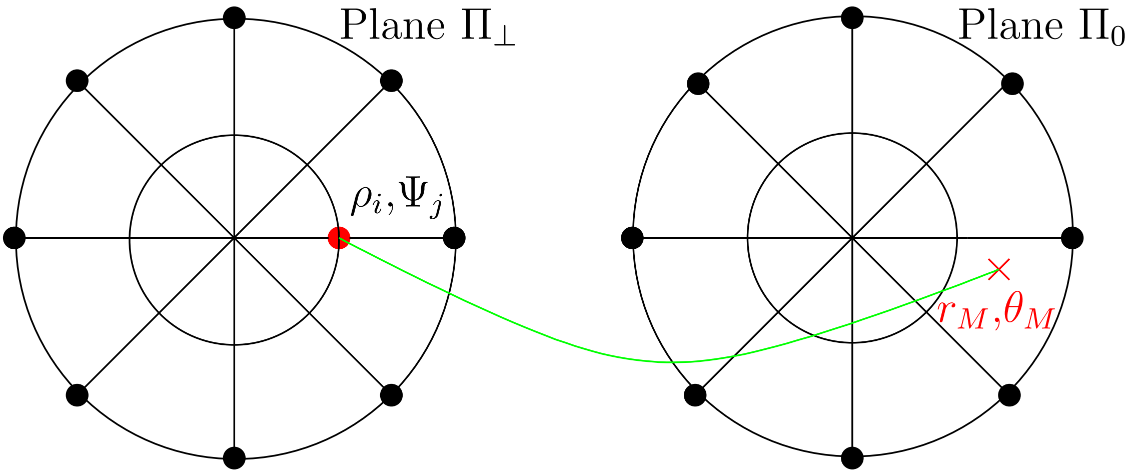

Figure 5.3 – Point M_1 located at grid node (ρ_i,ψ_j) in the $\Pi_\perp$ plane and corresponding point M with coordinates (r_M,θ_M) in the Π_0 plane.

$$\begin{aligned}\omega_\rho\left(M_1\right)=\omega_B\left(M_1\right)&\left[\frac{\alpha_{M_1}r_{M_1}}{L}\sin\left(\theta_A-\theta_{M_1}\right)\cos\psi\right.\\&\left.\qquad+\alpha_{M_1}\alpha_A\sin\psi\left(-\frac{r_A}{L}+\frac{r_{M_1}}{L}\cos\left(\theta_{M_1}-\theta_A\right)\right)\right]\\&+\omega_r\left(M_1\right)\left[\cos\left(\theta_{M_1}-\theta_A\right)\cos\psi+\alpha_A\sin\left(\theta_{M_1}-\theta_A\right)\sin\psi\right]\\&+\omega_\varphi\left(M_1\right)\left[\alpha_{M_1}\sin\left(\theta_A-\theta_{M_1}\right)\cos\psi+\alpha_{M_1}\alpha_A\frac{r_{M_1}r_A}{L^2}+\cos\left(\theta_{M_1}-\theta_A\right)\sin\psi\right]\end{aligned}\tag{5.23}$$

$$\begin{aligned}\omega_\psi\left(M_1\right)=\omega_B\left(M_1\right)&\left[-\frac{\alpha_{M_1}r_{M_1}}{L}\sin\left(\theta_A-\theta_{M_1}\right)\sin\psi\right.\\&\left.\qquad+\alpha_{M_1}\alpha_A\cos\psi\left(-\frac{r_A}{L}+\frac{r_{M_1}}{L}\cos\left(\theta_{M_1}-\theta_A\right)\right)\right]\\&+\omega_r\left(M_1\right)\left[-\cos\left(\theta_{M_1}-\theta_A\right)\sin\psi+\alpha_A\sin\left(\theta_{M_1}-\theta_A\right)\cos\psi\right]\\&+\omega_\varphi\left(M_1\right)\left[-\alpha_{M_1}\sin\left(\theta_A-\theta_{M_1}\right)\sin\psi+\alpha_{M_1}\alpha_A\frac{r_{M_1}r_A}{L^2}+\cos\left(\theta_{M_1}-\theta_A\right)\cos\psi\right].\end{aligned}\tag{5.24}$$

Velocity components have similar expressions, when $\boldsymbol{\omega}$ is replaced by $\boldsymbol{u}$ in the above equations.

The helical symmetry is used to retrieve the values of the flow field components in the $\Pi_\perp$ plane, namely vorticity $\omega_r(M_1)$, $\omega_\varphi(M_1)$, $\omega_B(M_1)$ and velocity $u_r(M_1)$, $u_\varphi(M_1)$, $u_B(M_1)$ components from the values $\omega_r(M)$, $\omega_\varphi(M)$, $\omega_B(M)$ and $u_r(M)$, $u_\varphi(M)$, $u_B(M)$ at point M "helically projected" on the Π_0 plane. In practice, we compute the above quantities on a regular grid (ρ_i,ψ_j) in $\Pi_\perp$ where the ρ_i are evenly spaced between 0 and a few typical vortex core sizes, and ψ_j is evenly spaced in $[0,2\pi[$: $\psi_j=2\pi j/N_\psi$ with $j=0,\cdots,N_\psi-1$ (this is needed for Fourier decomposition, see section below). However this grid becomes irregular when "projected" onto the computational domain Π_0 using relations (5.13)-(5.15) (see figure 5.3). Since *a priori* point M at (r_M,θ_M) does not correspond to any grid point of the computational domain in the Π_0 plane, an interpolation is needed to get the value at point M. To reach a good accuracy, a fifth order interpolation method based on Tchebychev polynomials is used (for more details, see the appendix E.1).

The core structure of the helical vortex can be studied by decomposing the quantities (5.16)-(5.18) and their respective velocity counterparts in the $\Pi_\perp$ plane in multipolar components. This is achieved by applying a discrete Fourier transform in the azimuthal direction ψ to yield the complex azimuthal modes with wavenumber m. For instance, on

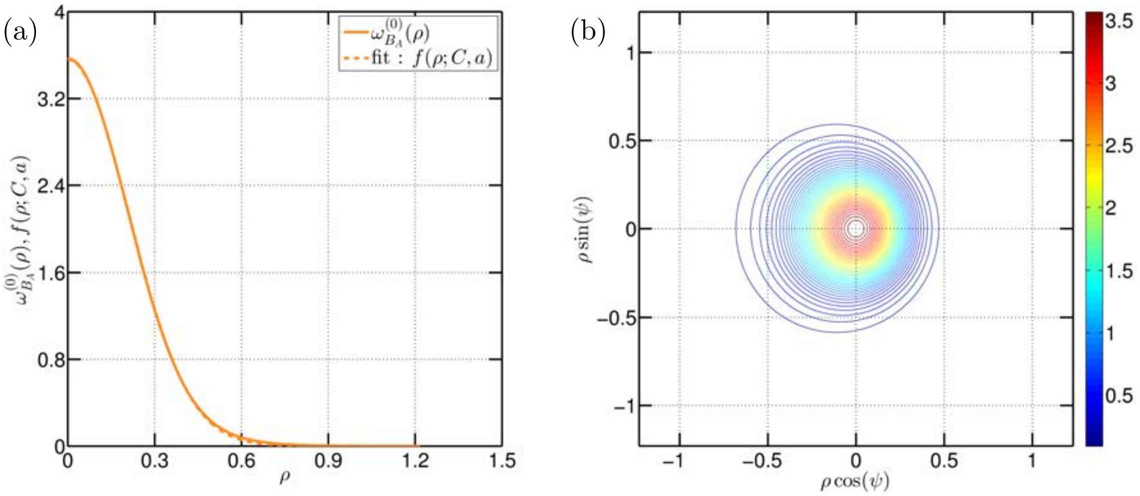

Figure 5.4 – A single vortex of reduced pitch $L = 1$. (a) Plot of the axisymmetric part of the helical vorticity $\omega^{(0)}_{B_A}(\rho)$ fitted with a Gaussian function $f(\rho; C, a)$. (b) Iso-contours of $\omega_{B_A}(\rho, \psi)$ on the $\Pi_\perp$ plane.

quantity $\omega_{B_A}(\rho_i, \psi_j)$, this means

$$\omega^{(m)}_{B_A}(\rho_i) = \frac{1}{N_\psi} \sum_{j=0}^{N_\psi - 1} \omega_{B_A}(\rho_i, \psi_j)\, \mathrm{e}^{-\mathrm{i}m\psi_j} \,. \tag{5.25}$$

The initial fields are recovered with the following inverse Fourier relation

$$\omega_{B_A}(\rho_i, \psi_j) = \sum_{m=0}^{N_\psi - 1} \omega^{(m)}_{B_A}(\rho_i)\, \mathrm{e}^{\mathrm{i}m\psi_j} \,. \tag{5.26}$$

5.4 Characterization of the vortex core structure

Examples of vortex core structures in the $\Pi_\perp$ plane are depicted for large and small pitch L in figures 5.4-b and 5.5-b respectively. For a vortex of large pitch (figure 5.4-b), the core structure is close to axisymmetric as for two-dimensional vortex. For small pitch, strong interactions between successive turns occur, causing the core structure to deviate from axisymmetry because of the self induced strain field (see figure 5.5-b). We introduce here the two most relevant quantities used to characterise the vortex core shape: the core size which can be quantified from the axisymmetric component, and the ellipticity from the quadripolar component.

5.4.1 Vortex core size a

Contrary to the two-dimensional case, there is no clear procedure to define the core size for a helical vortex. Here, we propose two different approaches.

First approach : least square fit of $\omega^{(0)}_{B_A}$ with a Gaussian function

A first approach is based on the assumption that the axisymmetric structure for such developed vortices is close to a Gaussian profile, which is a viscous self-similar solutions for two-dimensional flows. More precisely, the procedure consists in fitting the axisymmetric component $\omega^{(0)}_{B_A}(\rho)$ of the vorticity by the function

$$f(\rho; C, a) \equiv C \cdot e^{-(\rho/a)^2} \quad \text{for} \quad \rho \in [0, \rho_{cut}] \,. \tag{5.27}$$

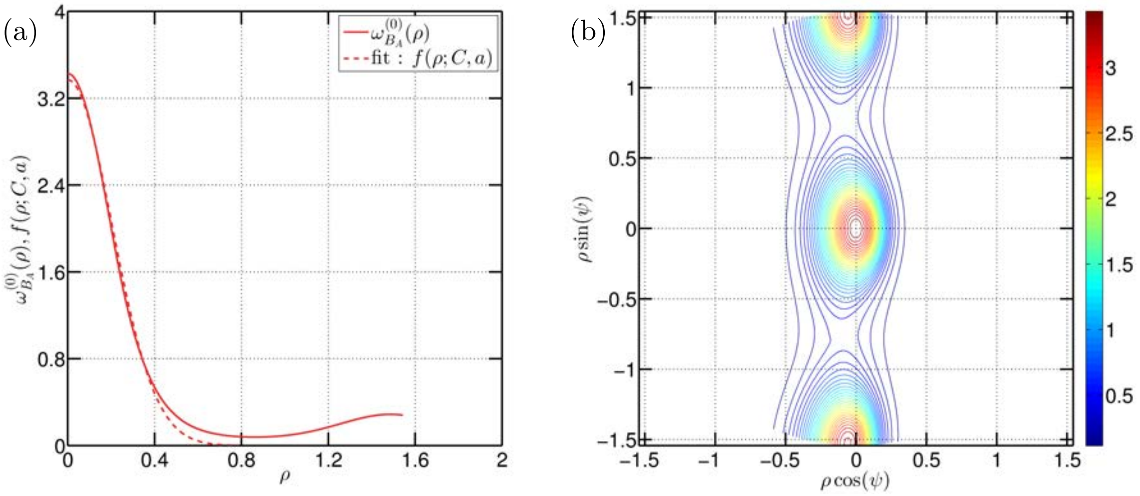

Figure 5.5 – One vortex of reduced pitch $L = 0.25$. (a) Plot of the axisymmetric part of the helical vorticity $\omega^{(0)}_{B_A}(\rho)$ and the fit function. (b) Iso-contours of $\omega_{B_A}(\rho, \psi)$ on the $\Pi_\perp$ plane.

The unknowns are quantities C, a and ρ_{cut}. The parameters C and a are chosen so that $f(\rho)$ is the optimal fit of $\omega^{(0)}_{B_A}(\rho)$ within the interval $\rho \in [0, \rho_{cut}]$. The appropriate value of ρ_{cut} is chosen so that vorticity is large enough in interval $[0, \rho_{cut}]$ in order to cover the pertinent part the vorticity profile. An example of a typical fit is shown figure 5.4-a for one vortex of reduced pitch $L = 1$ where the Gaussian profile is a good approximation for $\omega^{(0)}_{B_A}(\rho)$ (the two curves are almost undistinguishable). In the periphery of the vortex, however, the axisymmetry is somewhat broken as may be seen in figure 5.4-b. This feature due to vortex curvature does not significantly alter the evaluation of the core size (see the discussion below for the influence of and the choice of ρ_{cut}). For fixed ρ_{cut}, parameters C and a are computed with an iterative nonlinear least square method (see appendix E.2) with adequate initial guess values C^* and a^*. The amplitude guess value is set to $C^* = \omega^{(0)}_{B_A}(\rho = 0)$; since the fields are obtained by numerical simulation, the value of a^* for a given time t is initialized with the value computed at a previous time step.

Second approach: helical vorticity moments

The second approach computes the core size from vorticity moments. In a general two-dimensional flow, the vorticity moments read (Wu et al., 2007)

$$\iint_S \omega \prod_{i=1}^{2} x_i^{j_i} \mathrm{d}S \quad \text{with} \quad j_i \text{ positive integers,} \tag{5.28}$$

and some moments have a precise physical meaning: the zero moment is the circulation, the first moments are related to the vortex centroid and the total impulse while the second moments are related to the dispersion radius and to the angular momentum. Here, we extend these concepts to helical flows by considering the vorticity component ω_{B_A} in the plane $\Pi_\perp$. We thus introduce the moments of ω_{B_A}:

$$J_{mn} = \iint \xi^m \, \eta^n \, \omega_{B_A}(\xi, \eta) \, \mathrm{d}\xi \, \mathrm{d}\eta. \tag{5.29}$$

The vortex circulation Γ is obviously equal to J_{00} and one may define the centroid position of the vorticity in the $\Pi_\perp$ plane as

$$\xi_C = J_{10}/\Gamma, \qquad \eta_C = J_{01}/\Gamma. \tag{5.30}$$

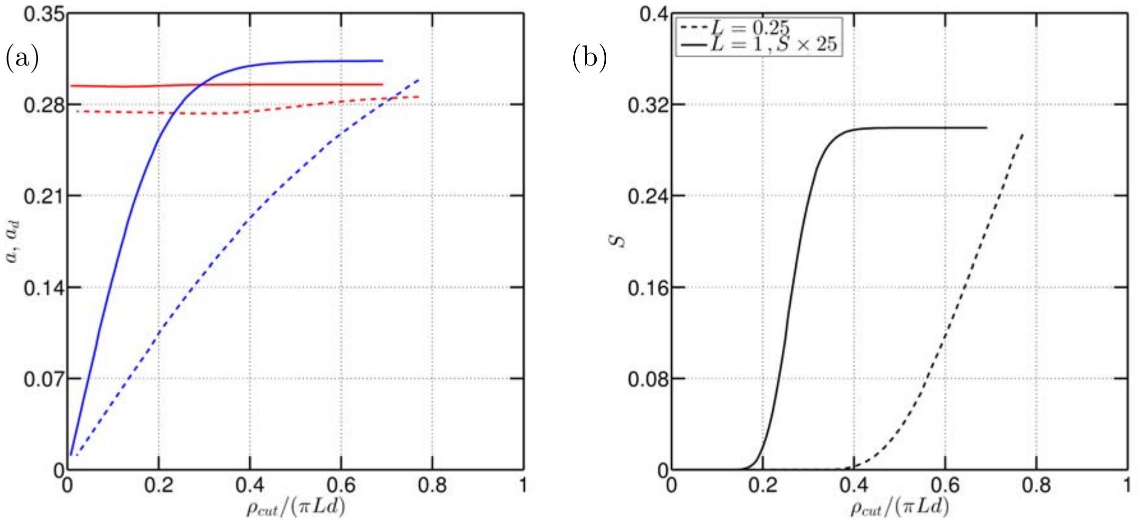

Figure 5.6 – One helical vortex for $L = 1$ (solid) and $L = 0.25$ (dashed). (a) Core sizes a (red) and a_d (blue) as a function of $\rho_{cut}/(\pi L d)$ (see definition of d in equation (5.33)). (b) Error S (equation (5.35)) as a function of $\rho_{cut}/(\pi L d)$. Note that for $L = 1$, the error S is multiplied by a factor of 25.

In our simulations, this point almost coincides with point A when chosen to be the vorticity maximum. The second-order moment

$$J_{20} + J_{02} = \iint \rho^2 \omega_{B_A}(\rho, \psi)\, \rho \, \mathrm{d}\rho \mathrm{d}\psi \tag{5.31}$$

defines the dispersion radius a_d:

$$a_d^2 = \frac{J_{20} + J_{02}}{J_{00}} = \frac{\displaystyle\int_0^{\rho_{cut}} \rho^2 \omega_{B_A}^{(0)} \rho \mathrm{d}\rho}{\displaystyle\int_0^{\rho_{cut}} \omega_{B_A}^{(0)} \rho \mathrm{d}\rho}. \tag{5.32}$$

The influence of the cutoff length ρ_{cut} on the core sizes a and a_d is now analysed. When choosing a value for ρ_{cut}, a difficulty arises due to its implicit link to the vortex structure. More precisely, it is related to the shortest distance separating two successive turns

$$D(a, L) \equiv 2(\pi L d - a), \qquad \text{with} \quad d = \frac{R}{\left(\sqrt{L^2 + R^2}\right)}. \tag{5.33}$$

The ratio d is a term arising from the angle between the $\Pi_\perp$ and the vertical (r, z)-plane. On a general basis, the successive turns of the vortex are considered to be well separated when $2a \ll 2\pi L d$. An example of such favourable configuration is shown in figure 5.4-a for $L = 1$ where the vorticity profile fully decays (to zero) around $\rho \sim 2a$. Based on the geometrical argument that ρ_{cut} cannot be larger than $\pi L d$ (otherwise a portion of the next coils would be included) and from the observation that ρ_{cut} needs to be at least twice the coresize value, the following constrain on ρ_{cut} can be constructed

$$2a \leq \rho_{cut} < \pi L d. \tag{5.34}$$

In equation (5.34), both a and ρ_{cut} are unknowns, but we expect a core size a to be largely independent of the choice of ρ_{cut}. For $L = 1$, the computation of the dispersion radius a_d as a function of ρ_{cut} is shown in figure 5.6-a (solid blue line). The core size increases from zero with ρ_{cut} until a plateau is reached at $a_d = 0.31$. For such configurations and despite

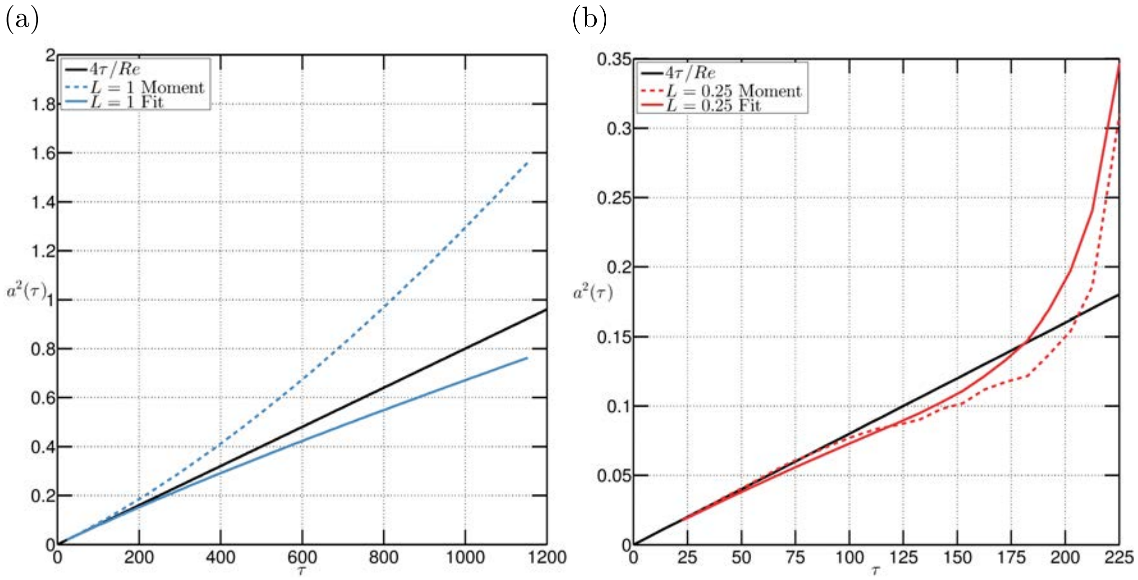

Figure 5.7 – Time evolution of the squared core size a^2 for one helical vortex at $Re = 5000$. (a) $L = 1$. (b) $L = 0.25$. Solid: fit of the axisymmetric mode of the helical vorticity $\omega_{BA}^{(0)}$. Dashed: a_d^2 obtained from the vorticity moments. In both graphs, the solid black line represents the two-dimensional diffusion law.

having a high sensitivity with respect to ρ_{cut} when small, this procedure can be well suited to compute the core size. The limit of this method appears when the condition (5.34) is no longer strictly satisfied i.e. for cases when $2a_d/\pi Ld \sim 1$. This occurs for example when the turns of the vortex are on the onset of merging as shown in figure 5.5-b for $L = 0.25$. For this case, the underlying axisymmetric vorticity profile does not completely reach zero (see figure 5.5-a). When a_d is obtained from the integration of such profile, one cannot obtain a unique value of a_d as it keeps increasing linearly within the whole range of authorised values for ρ_{cut}. It is thus preferable to use the method based on a Gaussian fit in order to estimate the core size a.

In order to check if the Gaussian fit method is sensitive to ρ_{cut}, we may also use different values of ρ_{cut}. The error S (relative to the vorticity maximum) for a choice of ρ_{cut} is defined by

$$S(\rho_{cut}) \equiv \frac{1}{\max \omega_{BA}^{(0)}} \sum_i \left(\omega_{BA}^{(0)}(\rho_i) - f(\rho_i; C, a) \right)^2 \quad \text{with} \quad \rho_i \in [0, \rho_{cut}] \,. \tag{5.35}$$

In figure 5.6-b, the error S is plotted when ρ_{cut} is varied for the two cases $L = 1$ (solid) and $L = 0.25$ (dashed). For $L = 0.25$, the error within the interval $0 \leq \rho_{cut}/\left(\pi L d\right) \leq 0.4$ remains close to zero and the vorticity profile is fitted accurately. The corresponding fitted core size a is plotted in figure 5.6-a (red dashed curve). It remains almost constant around the value $a = 0.275$. Further increasing ρ_{cut} leads to a drastic increase of the error S on the fit, because the vorticity profile deviates strongly from the Gaussian distribution due to the close neighbouring coils (see figure 5.5-a). The impact of this effect on the fitted coresize can be visualised in 5.6-b at $\rho_{cut}/\left(\pi L d\right) \sim 0.4$ as it increases by a small amount. For $L = 1$, the error S is almost nil for the range of values $0 \leq \rho_{cut}/\left(\pi L d\right) \leq 0.2$. It increases for greater values of ρ_{cut} but still remains very low of about 1% of the vorticity maximum (on figure 5.6-a, the corresponding curve is multiplied by a factor 25 for visualisation purpose). The fitted core size is not impacted since it remains roughly constant at value $a = 0.29$. Both methods are impacted by the presence of the neighbouring coils when they are too close, but the method based on the fit is less sensitive than the moment based method.

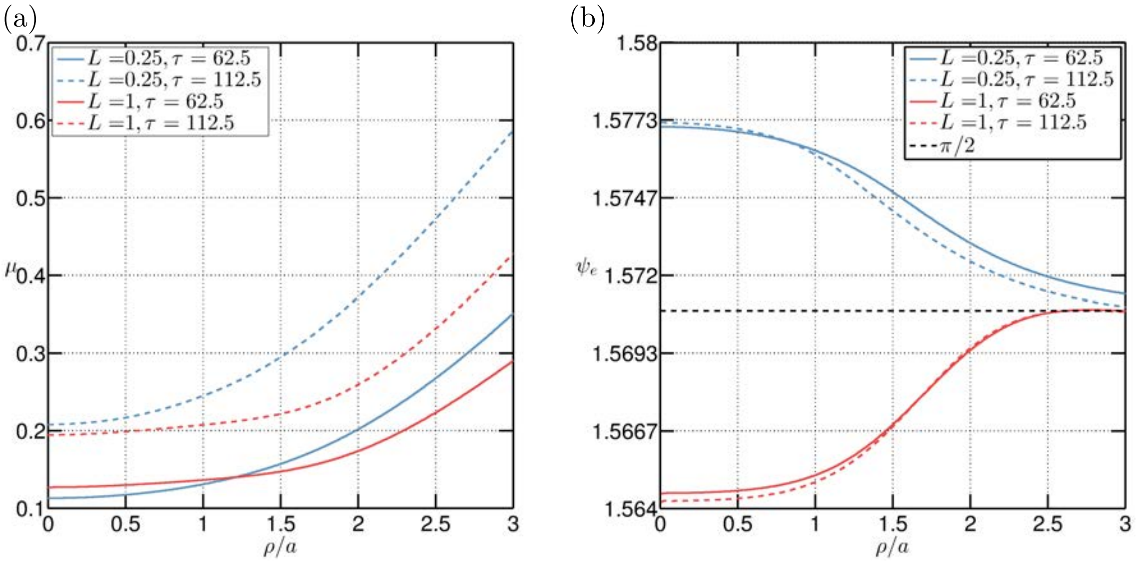

Figure 5.8 – One helical vortex of reduced pitch $L = 0.25$ and $L = 1$ at $Re = 5000$: (a) ellipticity μ at different instants $\tau = 62.5, 112.5$. (b) Angle ψ_e of the major axis of the ellipse at the same instants. On both plots, the radial coordinate is made dimensionless with the core size a.

In figure 5.7, the two methods are benchmarked for the two values of L considered. They both lead to comparable results during the very early evolution stages of the time evolution for $\tau \leq 50$, but diverge afterwards. For $L = 1$, the method based on vorticity moments yields larger values than the classical two-dimensional diffusion law, while the Gaussian fit provides smaller ones. Note that at $\tau \sim 1200$ the dispersion radius is about twice the fitted core size. For $L = 0.25$, both methods lead to similar results but the Gaussian fit method yields a smoother evolution curve for the core size. As vortex merging begins at $\tau \approx 220$, both methods are seen to depart from the two-dimensional diffusion law. From these observations and without a unique definition of the core size for a helical vortex, a choice has to be made: since the dispersion radius overestimates the core size and is strongly dependent on numerical parameters, we chose to characterise the core size using the fit of the axisymmetric component of the helical vorticity $\omega_{BA}^{(0)}$.

5.4.2 Ellipticity

The deformation of a vortex under the effect of strain introduces many azimuthal wavenumbers $m \neq 0$. In order to quantify the elliptical deformation, we use the quadripolar contributions of the computed fields (azimuthal mode $m = \pm 2$). More precisely, extending the work by (Jiménez et al., 1996) for helical flows, we study the geometry of streamlines in the frame rotating with the vortex. In that reference frame, the flow is steady and the stream function Ψ_R can be expanded as

$$\Psi_R(\rho, \psi) = \Psi_R^{(0)}(\rho) + {\Psi_R}^{(2)}(\rho)\, e^{\mathrm{i}2\psi} + c.c. + \ldots, \tag{5.36}$$

where $c.c.$ stands for the complex conjugate. We assume that the streamline of level Ψ_R is located at

$$\rho = \rho^{(0)} + \rho^{(2)} e^{\mathrm{i}2\psi} + c.c. \tag{5.37}$$

where $\rho^{(0)}$ and $\rho^{(2)}$ depend only on Ψ_R. The absence of a term in $e^{\mathrm{i}\psi}$ assumes that the streamline is centered at point A. If we discard higher multipolar contributions in (5.37), we get $\rho = \rho^{(0)} + 2|\rho^{(2)}|\cos(2\psi + \phi)$ where ϕ designates the phase of $\rho^{(2)}$. This corresponds to an ellipse with major and minor semi-axes of respective lengths $A(\rho^{(0)}) = \rho^{(0)} + 2|\rho^{(2)}|$

and $B(\rho^{(0)}) = \rho^{(0)} - 2|\rho^{(2)}|$, and ellipticity

$$\mu(\rho^{(0)}) = \frac{A-B}{A+B} = 2\,\frac{|\rho^{(2)}|}{\rho^{(0)}}\,. \tag{5.38}$$

Let us introduce (5.37) into (5.36) and use the Taylor expansion of (5.36) with respect to ρ:

$$\Psi_R\left(\rho,\psi\right) = \Psi_R^{(0)}\left(\rho^{(0)}\right) + \Psi_R^{(2)}\left(\rho^{(0)}\right)e^{\mathrm{i}2\psi} + \rho^{(2)}\left(\rho^{(0)}\right)e^{\mathrm{i}2\psi}\left.\frac{\partial\Psi_R^{(0)}}{\partial\rho}\right|_{\rho^{(0)}} + c.c + \ldots \tag{5.39}$$

Since Ψ_R is constant along streamlines, all orders in (5.39) are constant and, from first order terms, one gets the following relationship between $\rho^{(2)}$ and $\Psi_R^{(2)}$

$$\rho^{(2)}\left(\rho^{(0)}\right) = -\Psi_R^{(2)}\left(\rho^{(0)}\right)/\left.\frac{\partial\Psi^{(0)}}{\partial\rho}\right|_{\rho^{(0)}}\,. \tag{5.40}$$

Hence, one obtains the ellipticity :

$$\mu(\rho^{(0)}) = \frac{2}{\rho^{(0)}}\left|\Psi_R^{(2)}\right|\Big/\left|\frac{\partial\Psi^{(0)}}{\partial\rho}\right| \qquad \text{at } \rho=\rho^{(0)}. \tag{5.41}$$

The major axis of the ellipse is aligned at an angle $\psi_e = -\phi/2$ with respect to $\boldsymbol{e}_{\boldsymbol{r_A}}$, and with $\phi = \arctan\left(\Im\left\{\Psi^{(2)}\right\}/\Re\left\{\Psi^{(2)}\right\}\right)$. Finally, the value at the origin is finite and is computed through two successive uses of L'Hôpital's rule:

$$\lim_{\rho\to 0}\mu(\rho) = \left|\frac{\partial^2\Psi_R^{(2)}}{\partial\rho^2}\right|\Big/\left|\frac{\partial^2\Psi_R^{(0)}}{\partial\rho^2}\right| \qquad \text{at } \rho=0. \tag{5.42}$$

In figure 5.8-a-b, the ellipticity μ and the angle ψ_e are plotted for $L=0.25$ and $L=1$ at two different times. The ellipticity is found to increase with radial distance, as expected since vorticity levels gradually decrease. However, $\mu(\rho)$ remains almost constant up to a radial distance of one initial core size a. For this reason, we use $\mu_0 \equiv \mu(0)$ as a global measure of the core ellipticity in the following. For both cases the major axis of the ellipse is aligned at 90° with respect to $\boldsymbol{e}_{\boldsymbol{r_A}}$.

Note that the ellipticity could be also computed from the second moments of vorticity. Let consider X and Y the principal axes of the elliptical vortex in the $\Pi_\perp$ plane such that:

$$X = \xi\cos\psi_e + \eta\sin\psi_e \tag{5.43}$$

$$Y = -\xi\sin\psi_e + \eta\cos\psi_e, \tag{5.44}$$

with ψ_e the orientation angle of the ellipse with respect to the $\boldsymbol{e}_{\boldsymbol{r_A}}$-axis. Following (Le Dizès and Verga, 2002), A and B are related to the moments of vorticity (5.29):

$$\Gamma A^2 = \iint X^2\,\omega_{B_A}(\xi,\eta)\mathrm{d}\xi\,\mathrm{d}\eta = \left(J_{20}\cos^2\psi_e + 2J_{11}\cos\psi_e\sin\psi_e + J_{02}\sin^2\psi_e\right) \tag{5.45}$$

$$\Gamma B^2 = \iint Y^2\,\omega_{B_A}(\xi,\eta)\mathrm{d}\xi\,\mathrm{d}\eta = \left(J_{02}\cos^2\psi_e - 2J_{11}\cos\psi_e\sin\psi_e + J_{20}\sin^2\psi_e\right). \tag{5.46}$$

With the additional symmetry condition

$$\iint X\,Y\,\omega_{B_A}(\xi,\eta)\,\mathrm{d}\xi\,\mathrm{d}\eta = 0, \tag{5.47}$$

the angle of the major axis ψ_e is given by:

$$\psi_e = \arctan\left(\frac{J_{11}}{J_{20}-J_{02}}\right). \tag{5.48}$$

For reasons analogous to those given for the computation of the dispersion radius, such integral method is not used here.

Chapter 6

Quasi-equilibrium solutions for helical vortices

Contents

In this chapter, the time evolution of one helical vortex is analysed. Some invariance properties of helically symmetric systems are first presented in the inviscid as well as the viscous framework (section 6.1). We introduce specific initial conditions (section 6.2) aimed at ensuring a generic time evolution (section 6.3) of the system. After a rapid relaxation process (section 6.4), the system evolves to a generic quasi-equilibrium state (section 6.5). The streamline topology is investigated (section 6.6) and linked to particle transport (section 6.7). Finally we describe the late evolution towards an axisymmetric state which involves the merging of successive coils (section 6.8).

6.1 Invariant quantities

Instead of the helical vorticity u_B, we prefer to introduce quantity u_H

$$u_H \equiv \frac{u_B}{\alpha} - \left(U_z^\infty + \frac{\Gamma}{2\pi L} \right), \tag{6.1}$$

where U_z^∞ denotes the axial velocity far from the z-axis and Γ the total flow circulation. Indeed, quantity u_H vanishes far from the vorticity region since $u_B/\alpha = (u_z + ru_\theta/L)$ behaves as $U_z^\infty + \Gamma/(2\pi L)$ when $r \to \infty$. When u_H is uniform, it is bound by definition to be zero.

In the next section, some invariant quantities and conservation properties are derived from the viscous dynamics of helical flows (2.23)–(2.33).

6.1.1 Global Invariant quantities

Global quantities are obtained by integration in any (r, θ) plane over a disk S having a radius R_{ext} large enough to encompass the vorticity region. Quantities u_H, ω_B and ω_z are assumed to tend to zero rapidly enough as $r \to \infty$, so that the global quantities presented hereafter are indeed convergent integrals. The total circulation

$$\Gamma = \iint_S \omega_z \, r\mathrm{d}r\mathrm{d}\theta \tag{6.2}$$

is known to be a global invariant. Inserting the two equalities $\omega_z = \alpha(\omega_B - r\omega_\varphi/L)$ and $\omega_\varphi = -\alpha \partial u_H/\partial r$ which are valid in the helical symmetry context into equation (6.2), one gets after an integration by parts:

$$\Gamma = \mathcal{K}_1 - \frac{2}{L}\mathcal{K}_2 \quad \text{where} \quad \mathcal{K}_1 \equiv \iint_S \alpha\omega_B \, r\mathrm{d}r\mathrm{d}\theta, \quad \mathcal{K}_2 \equiv \iint_S \alpha^4 u_H \, r\mathrm{d}r\mathrm{d}\theta. \tag{6.3}$$

Another global invariant (Saffman, 1992; Kelbin et al., 2013) is the axial momentum $\mathcal{P}_z$ per axial length unit, given by

$$\mathcal{P}_z = \iint_S r\omega_\theta \, r\mathrm{d}r\mathrm{d}\theta \,. \tag{6.4}$$

In the context of helical symmetry, this global invariant reads:

$$\mathcal{P}_z = 2\mathcal{K}_2 + \frac{1}{L}\mathcal{K}_3 \quad \text{where} \quad \mathcal{K}_3 \equiv \iint_S r^2 \alpha\omega_B \, r\mathrm{d}r\mathrm{d}\theta. \tag{6.5}$$

Finally it can be shown from the Navier-Stokes equations that the global angular momentum $\mathcal{L}_z$ per axial length unit satisfies

$$\mathcal{L}_z(t) = \mathcal{L}_z(0) + 4\Gamma\nu t \,, \qquad \mathcal{L}_z = \iint_S r^2 \omega_z \, r\mathrm{d}r\mathrm{d}\theta \,. \tag{6.6}$$

In the context of helical symmetry, $\mathcal{L}_z$ can be written in terms of integrals of ω_B and u_H:

$$\mathcal{L}_z = 2L\mathcal{K}_2 + \mathcal{K}_3 - 2L\mathcal{K}_4 \,, \quad \text{where} \quad \mathcal{K}_4 \equiv \iint_S u_H \, r\mathrm{d}r\mathrm{d}\theta. \tag{6.7}$$

Relations (6.5), (6.6) and (6.7) can be combined to yield the following time evolution involving the integral of u_H:

$$\iint_S u_H \, r\mathrm{d}r\mathrm{d}\theta = \underbrace{\frac{1}{2}\left[\mathcal{P}_z - \frac{\mathcal{L}_z(0)}{L}\right]}_{\text{const.}} - \frac{2\Gamma}{L}\,\nu t \,. \tag{6.8}$$

For flows with zero total circulation ($\Gamma = 0$), the global angular momentum is conserved (Saffman, 1992), in which case the integral $\mathcal{K}_4$ of u_H becomes time-independent.

6.1.2 Local conservation laws for the inviscid case

Apart from global quantities, it is worth mentioning local conservation laws for helically symmetric flows. For inviscid flows (Lucas and Dritschel, 2009), quantity u_H is materially conserved (see equations (2.29) and (2.30)):

$$\frac{\partial}{\partial t} u_H + u_r \frac{\partial u_H}{\partial r} + \frac{u_\varphi}{\alpha r} \frac{\partial u_H}{\partial \varphi} = 0. \tag{6.9}$$

Using equation (2.19), the relation (6.9) can be expressed as

$$\frac{\partial}{\partial t} u_H + J(u_H, \psi) = 0, \quad \text{where} \quad J(f, g) \equiv \frac{1}{r} \left[\frac{\partial f}{\partial r} \frac{\partial g}{\partial \varphi} - \frac{\partial f}{\partial \varphi} \frac{\partial g}{\partial r} \right]. \tag{6.10}$$

This implies that, for $\nu = 0$, an initially uniform distribution $u_H = 0$ remains zero in time, and so do the vorticity components ω_r and ω_φ (see equations (2.22) and (6.1)). As a consequence, vorticity remains everywhere tangent to helical lines.
In the inviscid framework, it was further showed by (Lucas and Dritschel, 2009) that quantity $\alpha\omega_B$ evolves according to

$$\frac{\partial}{\partial t}(\alpha\omega_B) + J(\alpha\omega_B, \Psi) + \frac{2\alpha^4}{L} J(u_H, \Psi) + \frac{2\alpha^4}{L^2} u_H \frac{\partial u_H}{\partial \varphi} = 0. \tag{6.11}$$

Contrary to what happens for ω_z in the two-dimensional case (obtained in the limit $L = \infty$), quantity $\alpha\omega_B$ is not conserved on a general basis. However, when u_H is uniformly zero, $\alpha\omega_B$ is materially conserved:

$$\frac{\partial}{\partial t}(\alpha\omega_B) + J(\alpha\omega_B, \Psi) = 0 \qquad \text{with} \quad u_H = 0. \tag{6.12}$$

For *inviscid equilibrium solutions* rotating at angular velocity Ω_0, it is possible to say more. Such solutions are of the form $u_H(r, \varphi, t) = u_H(r, \varphi - \Omega_0 t)$, and, as a consequence,

$$\frac{\partial}{\partial t} u_H = -\Omega_0 \frac{\partial u_H}{\partial \varphi}. \tag{6.13}$$

Equation (6.10) then reduces to $J(u_H, \Psi_R) = 0$ where $\Psi_R \equiv \Psi + \frac{1}{2} r^2 \Omega_0$ denotes the streamfunction in the rotating frame of reference. This implies that u_H is a univoque function of Ψ_R:

$$u_H = F(\Psi_R). \tag{6.14}$$

For the specific case $u_H = 0$, the inviscid rotating equilibria satisfies $J(\alpha\omega_B, \Psi_R) = 0$, as implied by equation (6.12). This imposes $\alpha\omega_B$ to be a univoque function of Ψ_R:

$$\alpha\omega_B = G(\Psi_R) \quad \text{with} \quad u_H = 0. \tag{6.15}$$

For non-uniform u_H distribution, an equilibrium should satisfy equation (6.11) as well as equation (6.14) yielding

$$J(\alpha\omega_B, \Psi_R) + \frac{2\alpha^4}{L^2} {u_H}^{(R)} \frac{\partial u_H}{\partial \varphi} = 0, \tag{6.16}$$

where ${u_H}^{(R)} = u_H - L\Omega_0$ is the value of u_H in the rotating frame. If the second term in equation (6.16) is discarded, one recovers equation (6.15).

6.1.3 Local conservation laws in the viscous case

When viscosity is present, the equation for u_H and $\alpha\omega_B$ respectively read

$$\frac{\partial}{\partial t}u_H + J(u_H, \Psi) = \frac{\nu}{\alpha}\mathbb{L}(u_H) - \frac{2\nu}{L}\alpha\omega_B, \tag{6.17}$$

and

$$\begin{aligned}\frac{\partial}{\partial t}(\alpha\omega_B) + J(\alpha\omega_B, \Psi) + \frac{2\alpha^4}{L}J(u_H, \Psi) + \frac{2\alpha^4}{L^2}u_H\frac{\partial u_H}{\partial \varphi} \\ = \nu\left[\frac{1}{\alpha}\mathbb{L}(\alpha\omega_B) + \frac{4r\alpha^2}{L^2}\frac{\partial}{\partial r}(\alpha\omega_B) + \frac{2\alpha^3}{L}\mathbb{L}(u_H)\right].\end{aligned} \tag{6.18}$$

The last term in equation (6.17) couples u_H and $\alpha\omega_B$. This implies that, contrary to the inviscid case, u_H cannot remain null if $u_H(t=0) = 0$.

However it is possible to find an approximate time evolution in the viscous case. Indeed when $u_H(t=0) = 0$, equation (6.8) imposes $\mathcal{P}_z = \mathcal{L}_z/L$ and thus suggests that u_H might depend linearly on νt. Following this idea, we neglect for the initial time period the u_H terms in the dynamic equation (6.18) for $\alpha\omega_B$ leading to the approximation :

$$\frac{\partial}{\partial t}(\alpha\omega_B) + J(\alpha\omega_B, \Psi) = \nu\left[\frac{1}{\alpha}\mathbb{L}(\alpha\omega_B) + \frac{4r\alpha^2}{L^2}\frac{\partial}{\partial r}(\alpha\omega_B)\right].$$

If, in addition, we neglect the first radial derivative (second term in the rhs) with respect to second radial derivatives (first term in the rhs), then $\alpha\omega_B$ satisfies

$$\frac{\partial}{\partial t}(\alpha\omega_B) + J(\alpha\omega_B, \Psi) = \frac{\nu}{\alpha}\mathbb{L}(\alpha\omega_B). \tag{6.19}$$

Equations (6.17) and (6.19) as well as the initial condition are simultaneously satisfied if the following relationship holds between $\alpha\omega_B$ and u_H:

$$u_H = -\frac{2\nu t}{L}\alpha\omega_B(t)\,. \tag{6.20}$$

The above ansatz is presumably valid whenever u_H is small, and is fully consistent with the integral relation (6.8). We can extend this idea to a solution in which the initial condition reads as

$$u_H(r, \varphi, 0) = -\frac{\delta^2}{2L}\alpha\omega_B(r, \varphi, 0)\,, \tag{6.21}$$

where δ is a length such that $\delta/L \ll 1$. In that case, following the same approximations, the solution reads

$$u_H(r, \varphi, t) = -\frac{\delta^2 + 4\nu t}{2L}\alpha\omega_B(r, \varphi, t)\,. \tag{6.22}$$

We will show that this ansatz is validated by the numerical results (see section of section 6.5.1.

6.2 Initial conditions for a generic time evolution

For a two-dimensional vortex, it is known that the core size spreads in time according to $a(t) = (a_0^2 + 4\nu t)^{1/2}$. This classical diffusion law can be written as well as

$$a(\tau) = (4\nu\tau)^{1/2}\ , \quad \tau = t - t_\star\ , \quad t_\star = -\frac{1}{4}a_0^2/\nu < 0\,. \tag{6.23}$$

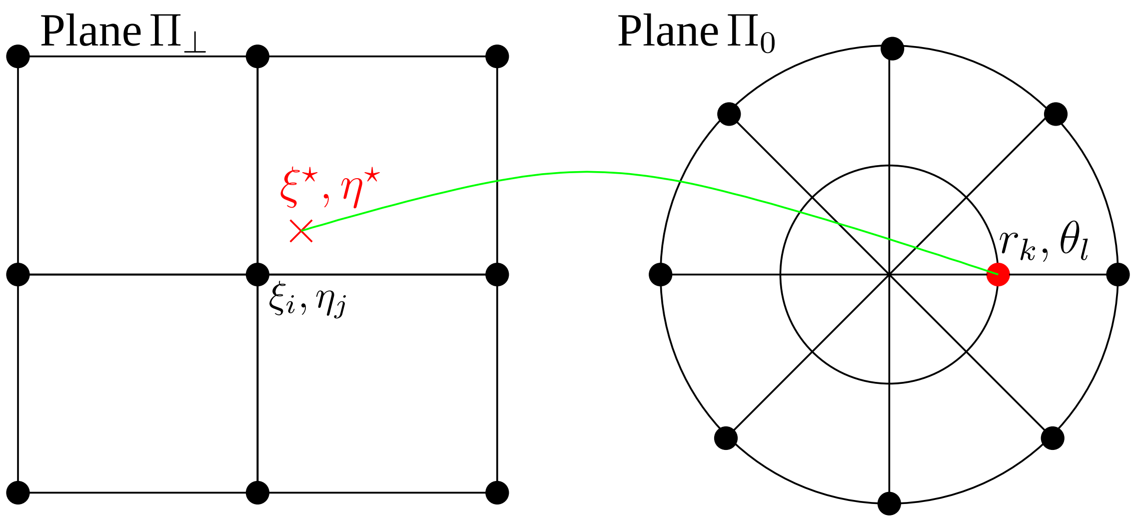

Figure 6.1 – Initial condition: image of the discrete position (r_k, θ_l) on the $\Pi_\perp$ plane with coordinate $\xi^\star, \eta^\star$.

Introducing the shifted time variable τ makes the diffusion law independant on the initial core size a_0. These basic considerations can be also used for an initial polygonal array of two-dimensional Gaussian vortices with identical core size a_0 when a_0 is small with respect to the distance between vortices. In that case, the system rotates as a polygonal array of point vortices while each vortex evolves in two stages (see for instance (Le Dizès and Verga, 2002)): a first rapid initial relaxation where Kelvin waves are observed, and a second phase in which a quasi-equilibrium is reached that slowly diffuses. In this latter stage, it is found that the time evolution of the array does not depend on a_0 if expressed as a function of τ.

Here we extend this procedure already used in the viscous two-dimensional setting ($L = \infty$ in our case) to the helical context. In the simulation, the initial condition consists of N identical vortices with a small core size $a_0 > 0$. The other geometrical parameters are the helical pitch $2\pi L$, and the location of the vorticity maximum at $(r_A, \theta_p = 2\pi p/N)$ for $p = 1, ...N$ in the Π_0 plane.

In order to ensure that the initial condition is close to an equilibrium solution, we choose to impose a Gaussian helical vorticity profile of amplitude C_0 and radius a_0 in the plane $\Pi_\perp$:

$$\widetilde{\omega_B}(\xi, \eta) = C_0 \exp\left(-\frac{\xi^2 + \eta^2}{a_0^2}\right). \tag{6.24}$$

This profile needs to be projected onto the polar mesh (r_k, θ_l) of plane Π_0. More precisely, it is necessary for each grid point M (r_k, θ_l) in Π_0 to locate the coordinates $(\xi^\star, \eta^\star)$ of the point M* in $\Pi_\perp$ belonging to the same helical line as M. Since the inverse process (from $\Pi_\perp$ to Π_0) is easier to tackle, a Cartesian grid is created in $\Pi_\perp$ with points $(\xi_i, \eta_j) \in [-5a_0, 5a_0]^2$, and mapped to the plane Π_0. The coord $(\xi^\star, \eta^\star)$ are then precisely located by minimising in the plane $\Pi_\perp$ a positive functional linked to the distance in Π_0 to point (r_k, θ_l), which is zero at $(\xi^\star, \eta^\star)$. Then $\tilde{\omega}_B$, is set in Π_0 at grid point (r_k, θ_l) using the value (6.24) at point $(\xi^\star, \eta^\star)$.

At the end of the process, the helical vorticity $\widetilde{\omega_B}\,(r, \theta)$, has been initialised in the computational domain Π_0 and the velocity component $\widetilde{u_H}\,(r, \theta)$ is deduced from $\widetilde{\omega_B}\,(r, \theta)$ by the ansatz (6.22) with $\delta = a_0$, namely:

$$\widetilde{u_H}\,(r, \theta) = -\alpha \frac{a_0^2}{2L} \tilde{\omega}_B(r, \theta). \tag{6.25}$$

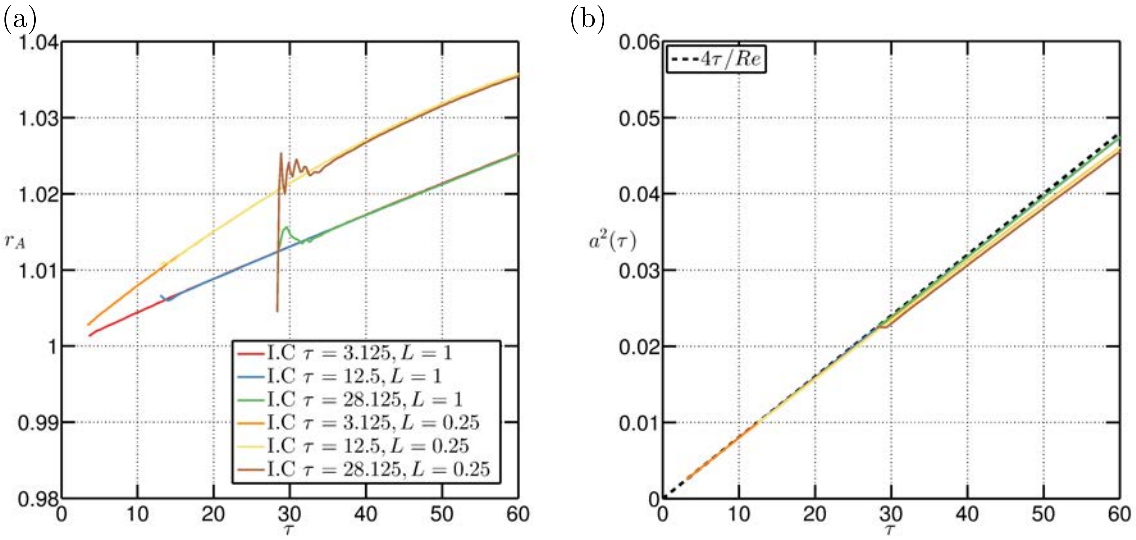

Figure 6.2 – One vortex of reduced pitch $L = 1$ and $L = 0.25$. Generic initial conditions at $Re = 5000$. For each plots, three initialisations at times: $\tau = 3.125$, $\tau = 12.5$ and $\tau = 28.125$. (a) Time evolution of the radial position r_{max} of the maximum of vorticity ω_B as a function of τ. (b) Time evolution of the quantity a^2, with a being the core size, as a function of τ, the black dashed line is the two dimension diffusion law $a^2(\tau) = 4\,\tau/Re$.

In these flows, circulation Γ and axial momentum $\mathcal{P}_z$ are conserved quantities. If both are prescribed, the normalisation constant C_0 in (6.24) and the helix radius r_A can be determined using formulas (6.3) and (6.5).

For these helical states, we have the same genericity requirement than in two dimensions concerning the initial core size a_0. Since no analytical solution exists for a viscous helical vortex, the vortex core size is assumed sufficiently small to satisfy the two-dimensional diffusion law in the $\Pi_\perp$ plane, which makes it possible to evaluate the virtual time origin $t_\star = -\frac{1}{4}a_0^2/\nu$. At $\tau = 0$, one thus assumes the existence of an array of helical filaments (zero core size). Because of conservation laws, each filament has circulation Γ, reduced pitch L and helix radius $R_\star = (\mathcal{P}_z L/\Gamma)^{1/2}$, which is close but distinct from r_A.

From now on, variables are made nondimensional using $R_\star$ as a lengthscale, and $\Gamma/R_\star$ as a timescale. Simulations now depend on three dimensionless parameters: the Reynolds number Γ/ν, the dimensionless helical pitch L and the dimensionless core size a_0.

The generic aspect of the time evolution with respect to the initial condition is illustrated figure 6.2. Computations are started with three different initial core sizes $a_0 = 0.05, 0.1, 0.15$, corresponding to the instants $\tau = 3.12, 12.5, 28.1$, for pitch $L = 0.25$ and $L = 1$. In figure 6.2-a, the time evolution of r_A is plotted. For a given L, all the curves end up collapsing after a short transient period (characterised by the wiggles). Note that, even if the initial oscillations tend to increase in amplitude and duration with the initial core size, they remain limited. This shows that the point vortex diffusion hypothesis coupled to the ansatz (6.22) for u_H holds even for small values of L. This is further confirmed in figure 6.2-b where the (squared) core size follows the two-dimensional diffusion law for short instants.

These features ensure that the long time dynamics do not depend on the initial core size a_0, which thus further reduces the number of control parameters to only two: the reduced pitch L and the Reynolds number Re.

6.3 Temporal evolution of a single helical vortex

In the following, we study the temporal evolution of a single generic helical vortex with enforced helical symmetry in an unbounded incompressible medium. The numerical domain is a disk of nondimensional radius $R_{\text{ext}} = 3$, meshed by $N_r \times N_\theta$ grid points where $N_r = 512$ and $N_\theta = 384$ typically. All the computations are run with the initial condition procedure described in section 6.2. The chosen values for the pitch are $L = 0.25, 0.5, 0.75, 1, 2, 3$ and the Reynolds number is fixed at $Re = 5000$.

The vortex evolution is mainly characterised by four stages of evolution. During the first stage the vortex goes through a rapid relaxation process where it adapts its structure to the strain field it is subject to (section 6.4). The second stage is a slow diffusion process where the vortex grows in size and rotates quasi steadily at angular velocity $\Omega\,(\tau)$, i.e. a quasi-equilibrium state (section 6.5). This generalises the inviscid equilibrium flow induced by one helical vortex (Kuibin and Okulov, 1998). At low pitch, a third stage occurs for large time: successive coils merge and the vortex progressively loses its helical structure and becomes a cylindrical vorticity layer. For all values of the pitch, the system finally evolves towards a columnar axisymmetric Gaussian vortex.

6.4 Relaxation towards quasi-equilibria for a single vortex

This section illustrates the first evolution stage, where the system rapidly relaxes towards a quasi-equilibrium state. This temporal evolution is only presented for a single helical vortex of pitch $L = 0.25$, of core size $a_0 = 0.06$, at $Re = 5000$. Results are similar for a single vortex at other pitch values and Reynolds numbers, as well as for a polygonal array of helical vortices.

The whole adaptation process of the helical vortex is the so-called relaxation process. For an array of vortices, the initial fields (6.24)–(6.25) are not an equilibrium of the Euler equations due to the presence of an external strain. For a single vortex, this also holds since a self-induced strain is present, originating from local curvature as well as induction due to remote vorticity. The vortex thus adapts its structure to this self-induced strain field: snapshots in figure 6.3 show how the initial axisymmetric vorticity distribution evolves towards an elliptic one within the core, while the very weak peripheral vorticity region displays a more complex evolution which is associated to the damping of inertial waves by viscosity. This relaxation process is thus very similar to what is observed in two dimensions for co-rotative vortices (Le Dizès and Verga, 2002) and counter rotatives vortices (Sipp et al., 2000).

6.5 Quasi equilibrium stage

6.5.1 Relationship between Ψ_R, u_H and $\alpha\omega_B$

After the short relaxation process depicted in figure 6.3, the vortex diffuses and rotates at an angular velocity Ω slowly varying with time. Snapshots of $\alpha\omega_B$ and u_H in figure 6.4 show that isovalues of these quantities are closely related to streamlines. This indicates that the flow is close to an Euler equilibrium: in the inviscid framework, functional relationships $u_H = F\,(\Psi_R)$ and, whenever u_H is weak, $\alpha\omega_B = G(\Psi_R)$ hold for equilibrium solutions (see section 6.1.2). This is further confirmed by the scatterplots in figure 6.5-a and b: the points $(\alpha\omega_B, \Psi_R)$ and $(u_H, \alpha\omega_B)$ are aligned on a single curve for any fixed time. For an Euler flow, the functional relationship would be steady. Here, this state is called quasi-equilibrium since it evolves in time because of viscous diffusion, leading to a slow

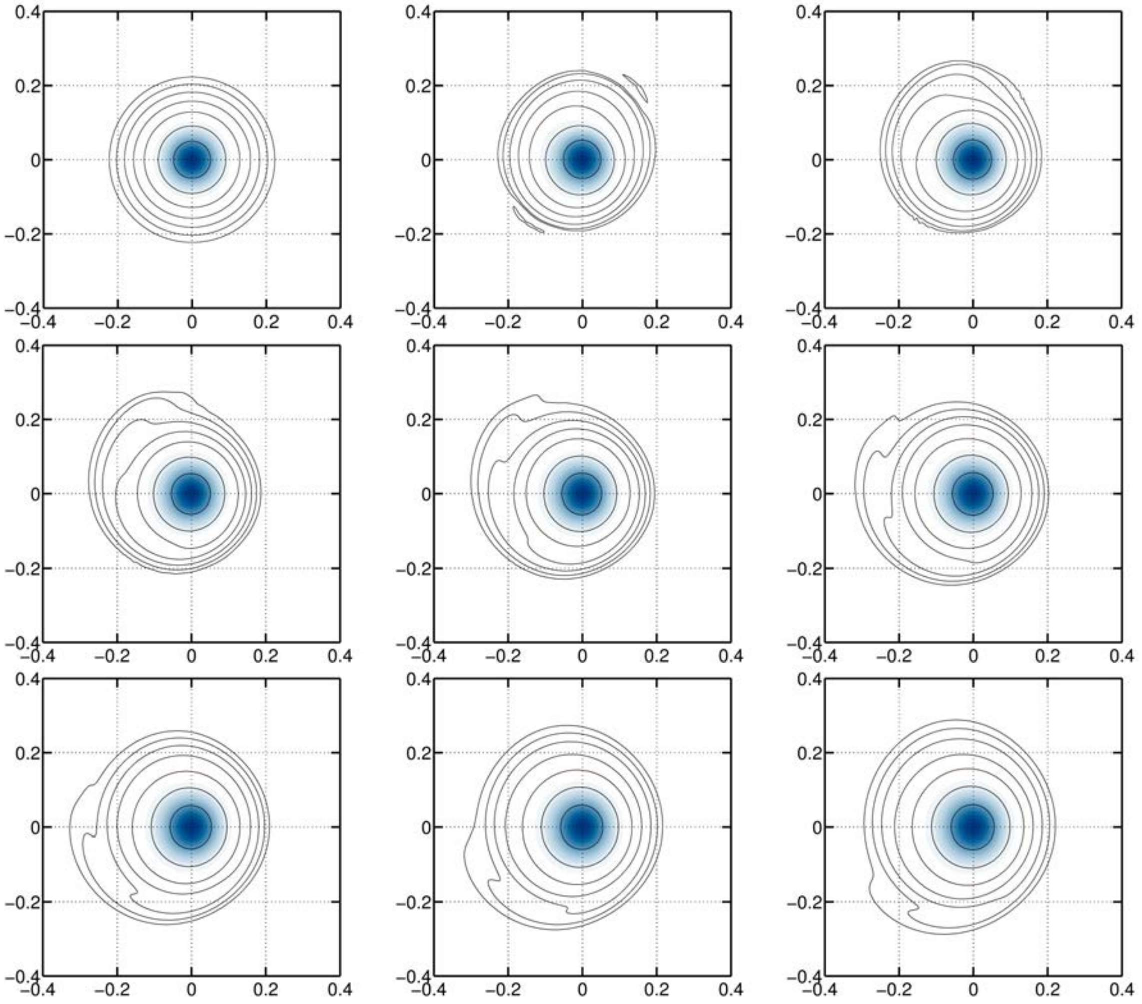

Figure 6.3 – One vortex of reduced pitch $L = 0.25$ and initial core size $a = 0.06$ at $Re = 5000$. Vorticity contours in the $\Pi_\perp$ plane during the relaxation process. From left to right, top to bottom $t\Gamma / \left(2\pi a_0^2\right) = 0, 10, ..., 80$. Contours levels are $\omega_{B_A} / \omega_{B_A}^{(0)}(0) = 0.5, 0.1, 0.01, 0.001, 10^{-4}, 10^{-5}, 10^{-6}$.

time dependance of the functional relationship as well. Figure 6.5-b confirms the linear dependence between u_H and $\alpha\omega_B$ predicted by equation (6.20).

6.5.2 Core size of a helical vortex

The core size a of the helical vortex is computed using the technique based on the Gaussian fit of the axisymmetric part of the helical vorticity (see section 5.4.1). When $L > 1$, the two-dimensional diffusion law is a fair approximation for the core size evolution, as can be seen in figure 6.6. When $L < 1$, the core size increases less than its two-dimensional counterpart. The strong increase of a observed for $L = 0.25$ around $\tau = 130$ corresponds to a core size as large as $a \sim 0.32$, where the notion of core size becomes questionable.

6.5.3 Self-similar solutions

On figure 6.7-a, the axisymmetric part of the helical vorticity $\omega_{B_A}^{(0)}$ (see 5.3) is plotted for a set of equally spaced times. A self-similar behaviour is identified: while the Gaussian's amplitude decreases in time, the radial spreading increases accordingly. When rescaled as

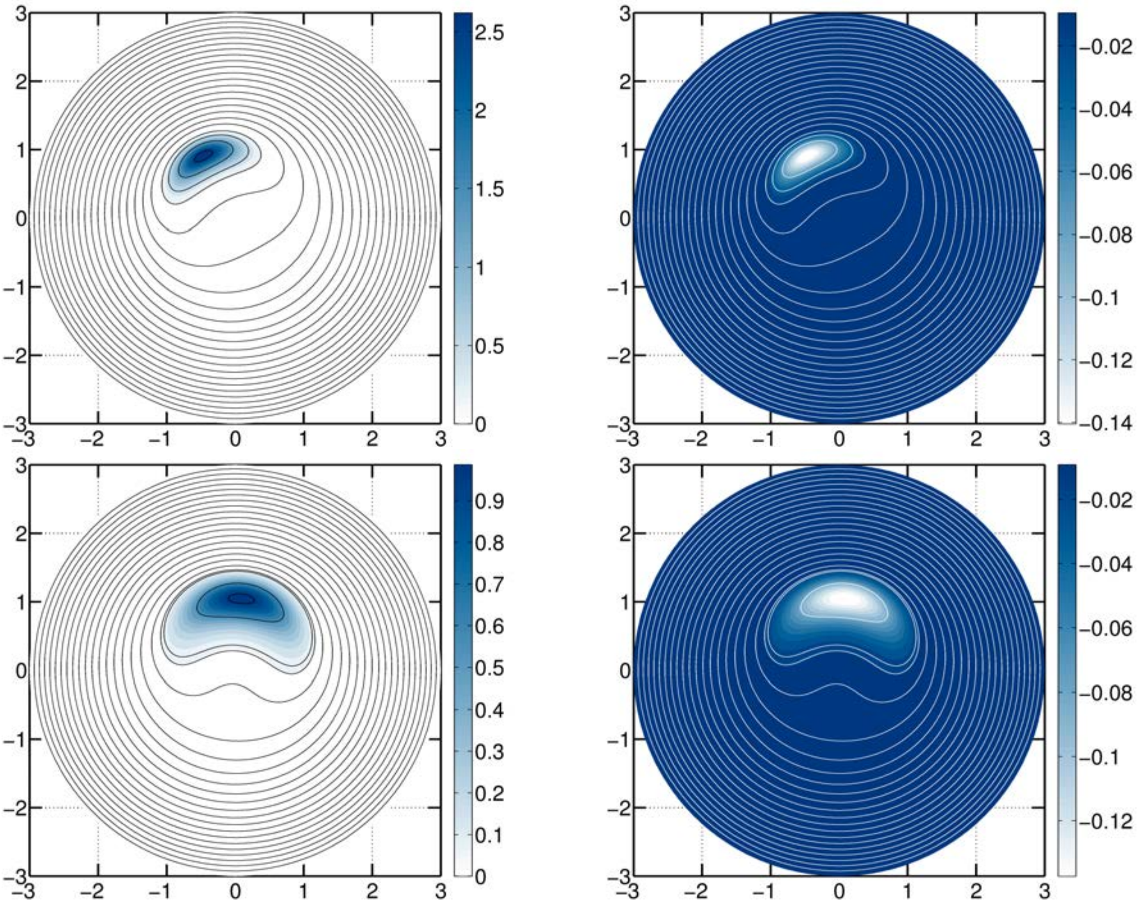

Figure 6.4 – One helical vortex of reduced pitch $L = 0.5$ at $Re = 5000$. Left column: isocontours of the stream function in the rotating frame ψ_R (black lines) superimposed on top of the quantity $\alpha\omega_B$ with ω_B being the helical vorticity . Right column: same isocontours of Ψ_R (white lines) superimposed on top of the helical velocity (jet) u_H. The chosen instants are $\tau = 62.5$ (top) and $\tau = 162.5$ (bottom).

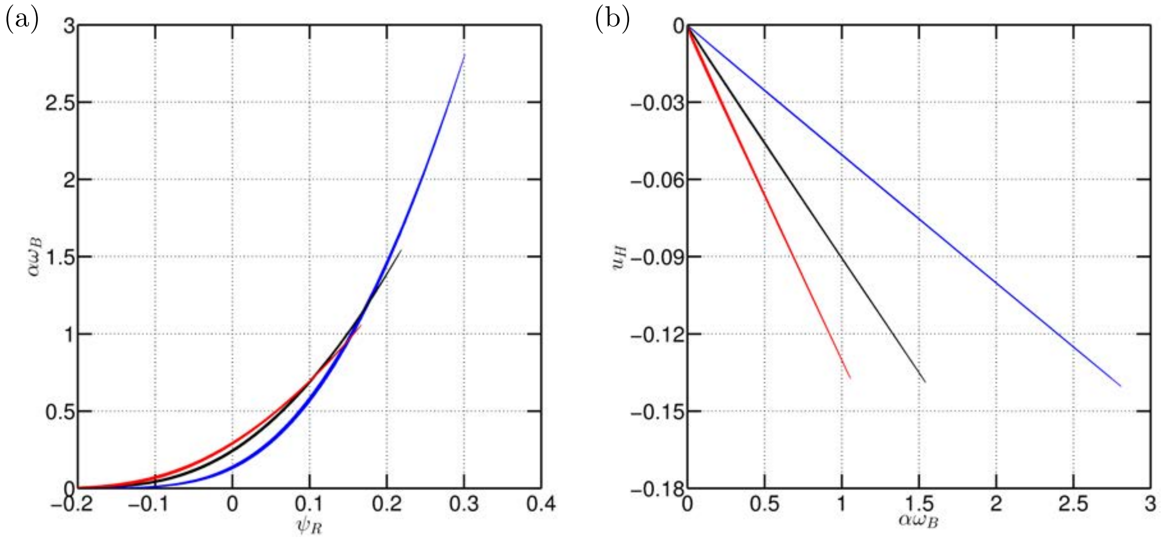

Figure 6.5 – One helical vortex of reduced pitch $L = 0.5$ at $Re = 5000$. Scatter plots of the quantities $(\alpha\omega_B, \Psi_R)$ and $(u_H, \alpha\omega_B)$ at instants $\tau = 62.5$ (blue), 112.5 (black), 162.5 (red). During the diffusing stage, all the (vorticity, streamfunction) points on (a) and (velocity, vorticity) points on (b) are aligned in a single curve for a given time τ, illustrating the functional relationship between these quantities.

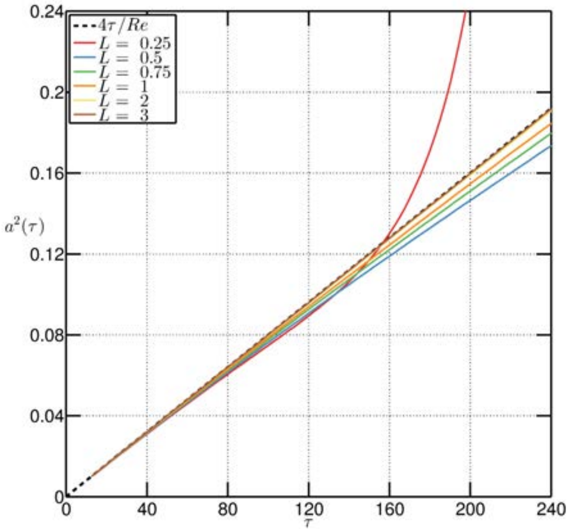

Figure 6.6 – Time evolution of the squared core size a^2 for a single helical vortex at $Re = 5000$ and different values of L. The black dashed line shows the two-dimensional diffusion law $a^2(\tau) = 4\,\tau/Re$.

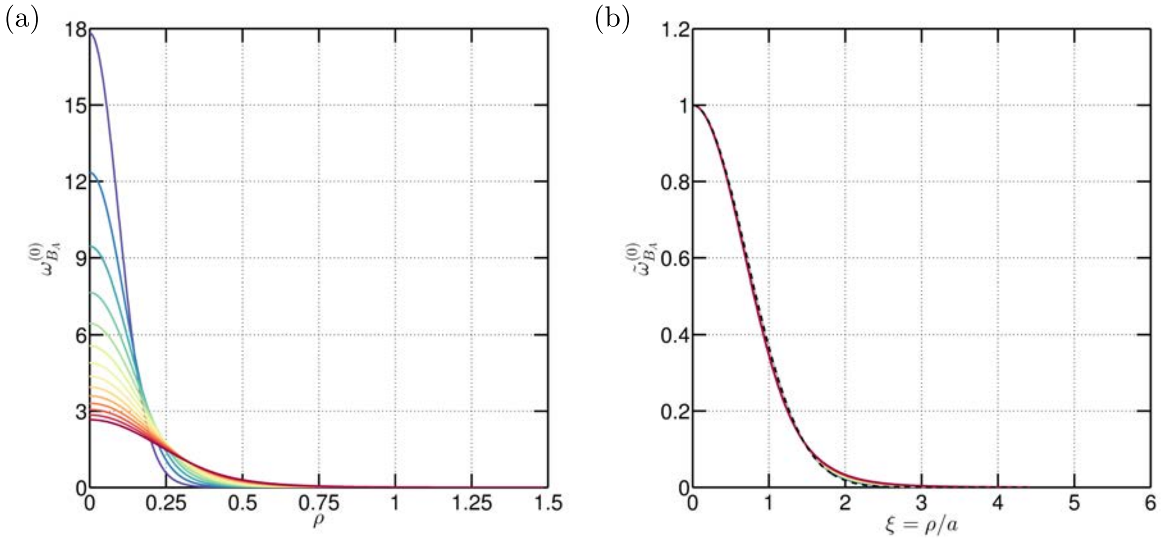

Figure 6.7 – One helical vortex of reduced pitch $L = 0.5$ at $Re = 5000$. (a) Axisymmetric part of $\omega_{B_A}^{(0)}(\rho)$ at instants $\tau = 22.5, 32.5, ..., 172.5$ (time increases from top to bottom). (b) Scaled profiles of the axisymmetric part of the helical vorticity as a function of the similarity variable ξ (6.26) for the same instants.

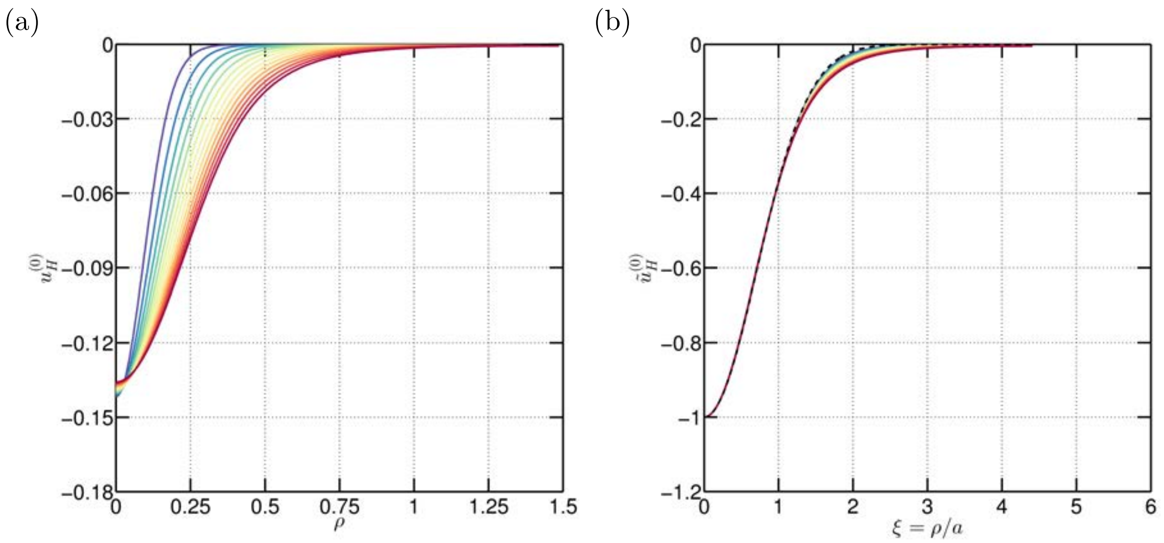

Figure 6.8 – One helical vortex of reduced pitch $L = 0.5$ at $Re = 5000$. (a) Axisymmetric part of the helical jet $u_H^{(0)}(\rho)$ at instants $\tau = 22.5 : 10 : 172.5$ (time increases from left to right). (b) Scaled profiles of the axisymmetric part of the helical jet as a function of the similarity variable ξ (6.26) for the same instants.

follows:

$$\tilde{\omega}_{B_A}^{(0)} = \frac{\omega_{B_A}^{(0)}(\xi,\tau)}{\omega_{B_A}^{(0)}(0,\tau)} \;, \qquad \xi = \frac{\rho}{a(\tau)} \;, \tag{6.26}$$

the profiles collapse (figure 6.7-b) onto the Gaussian curve $\tilde{\omega}_{B_A}^{(0)}(\xi) = \exp(-\xi^2)$. This self-similarity was already observed on numerically computed rotor wakes by Ali and Abid (2014). The profiles of $u_H^{(0)}$, the axisymmetric part of quantity u_H, are presented in figure 6.8-a. These profiles are also spreading in time (figure 6.8-b). However, as evidenced in figure 6.8-a, the amplitude of the velocity deficit remains approximately constant in time: based on equation (6.20) this implies that the maximum of vorticity varies as $1/\tau$. When plotted as a function of with the same variable ξ and normalised by its absolute maximum value, the curves collapse on a single one close to $\tilde{u}_H^{(0)}(\xi) = -e^{-\xi^2}$ (figure 6.8-b).

6.5.4 Helix radius r_A and angular velocity Ω

Let us characterize the global dynamics by tracking point A $(r_A(\tau), \theta_A(\tau))$ in the Π_0-plane where ω_B is maximum and by providing the angular velocity of the vortex $\Omega(\tau)$. The temporal evolution of the helix radius r_A is plotted in figure 6.9-a for different values of L at $Re = 5000$. For all values of L considered, the helix radius first increases. The explanation of this radial drift is not clear at the moment and is believed to be related to the conservation of the angular momentum with a core size increasing in time. However, for larger times, r_A reaches a maximum and then decreases (see figure 6.9-c). For small L, the maximum is reached at a critical time where the vortex successive coils are about to merge, as depicted in figure 6.10. For larger L, this mechanism is no more active, but since r_A should asymptotically be zero, a maximum is still reached. As seen in figure 6.11, the same argument about the successive coils about to come into contact does not hold to explain this maximum of r_A.

The angular velocity Ω of the vortex is plotted as a function of time in figures 6.9-b and d. It is compared to the values obtained with the corresponding temporal simulation using vortex filaments along with the cut-off theory introduced in chapter 4.

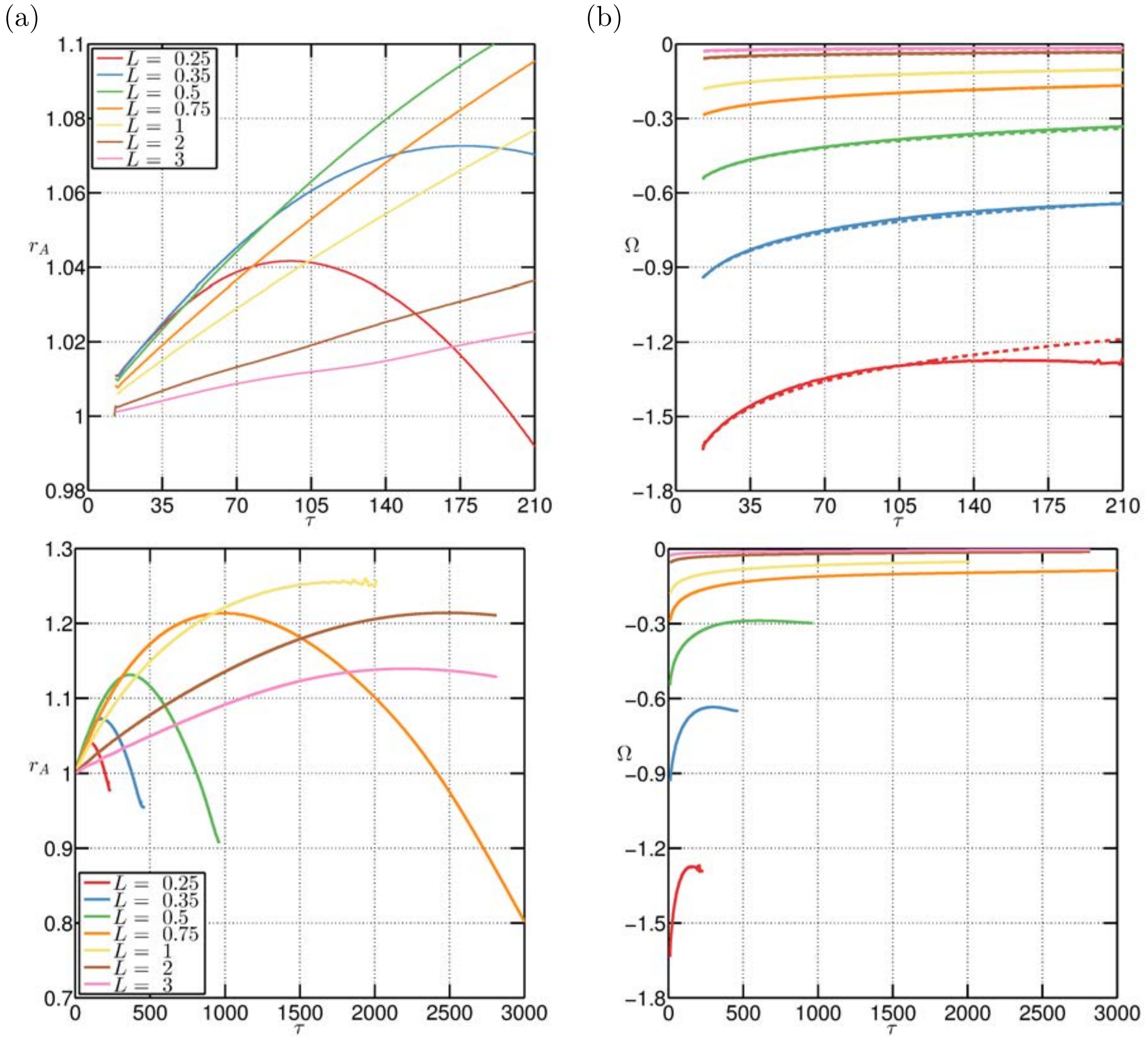

Figure 6.9 – One helical vortex at $Re = 5000$. (a) Time evolution of the helix radii r_A, for different values of L. (b) Time evolution of the angular velocity Ω for the same range of parameters. The dotted lines are the predicted values by the cutoff theory coupled to a 2D diffusion law for the vortex core size.

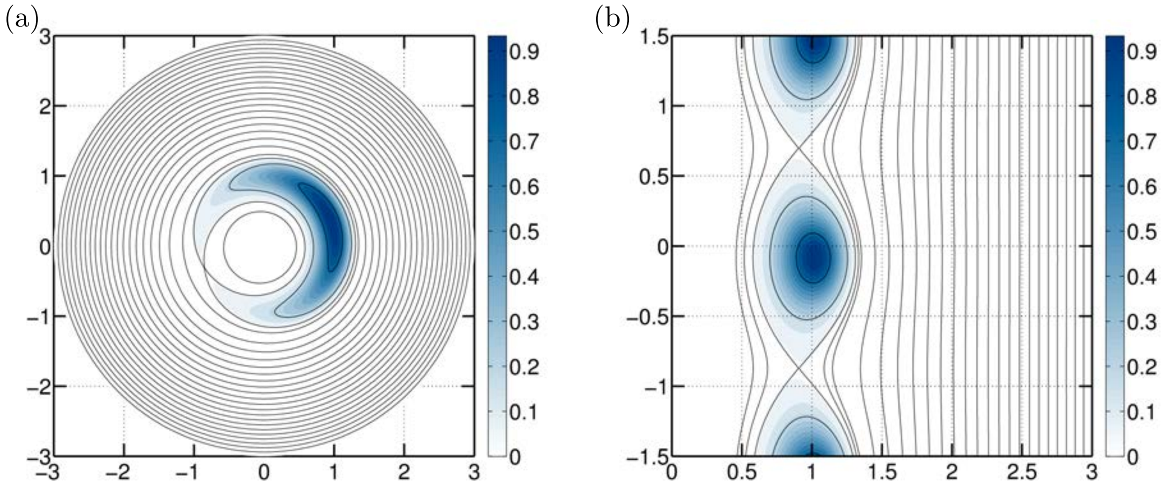

Figure 6.10 – One helical vortex of reduced pitch $L = 0.25$ for $Re = 5000$ at $\tau = 92.5$. (a) Isocontours of the stream function in the rotating frame Ψ_R (black lines) superimposed on top of the quantity $\alpha\omega_B$. (b) Representation in the meridian $r - z$ plane (two coils are represented).

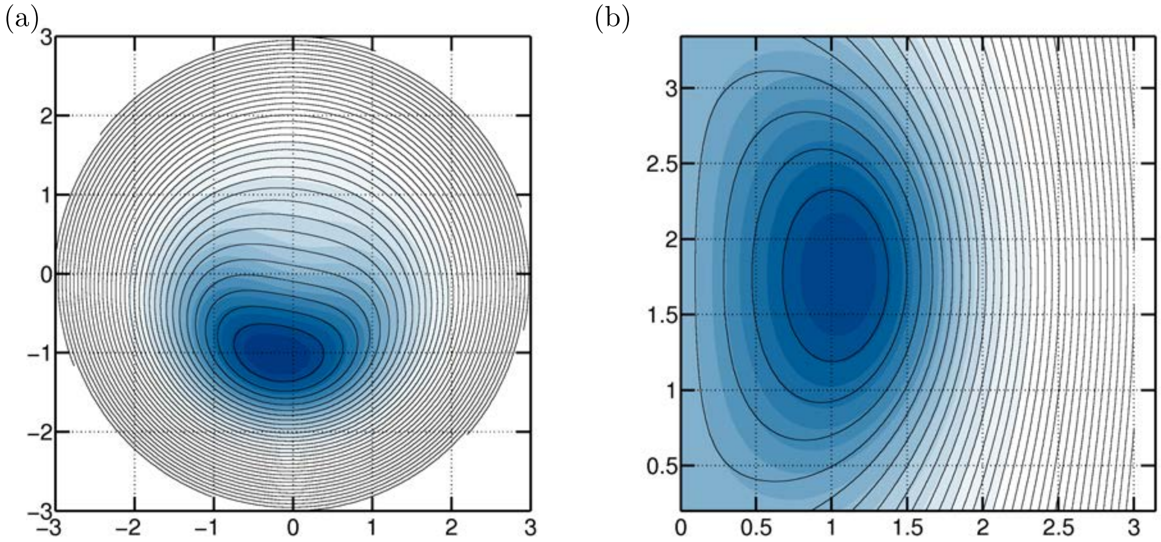

Figure 6.11 – One helical vortex of reduced pitch $L = 1$ for $Re = 5000$ at $\tau = 1750$. (a) Isocontours of the stream function in the rotating frame Ψ_R (black lines) superimposed on top of the quantity $\alpha\omega_B$. (b) Representation in the meridian $r - z$ plane.

6.5.5 Ellipticity μ and major axis angle ψ_e

We focus on the evolution of the ellipticity μ_0 in the center of the vortex core. In figure 6.12-a, the time evolution of the measured ellipticity μ_0 is plotted for various values of L. As L is decreased, it is found that the ellipticity increases, due to the increase of the self-induced strain rate γ acting on the vortex. This is reminiscent of a two-dimensional vortex in an external strain field. For a two-dimensional uniform elliptic patch of vorticity ω_p subjected to a plane strain at rates $\pm\gamma$, the ellipticity μ_0 is related to the ratio γ/ω_p according to Kida (1981):

$$\frac{\gamma}{\omega_p} = \frac{\mu_0\,(1-\mu_0^2)\,(1-\mu_0)}{2\,(1+\mu_0^2)}. \tag{6.27}$$

For small values of μ_0, the above expression can be linearised into

$$\frac{\gamma}{\omega_p} \sim \frac{\mu_0}{2}. \tag{6.28}$$

The above relationships hold for a patch, but have been shown to hold also for smooth vorticity profiles (Delbende and Rossi, 2009), if ω_p is chosen as $\omega_p = \Gamma/(2\pi a^2)$.
One may tentatively use (6.27) or (6.28) to estimate μ_0 in the three-dimensional context. For a single helical vortex, the strain rate γ is not externally imposed: it is self-induced and has been obtained through an asymptotic analysis (Blanco-Rodríguez et al., 2015):

$$\gamma = -2S\epsilon^2\ , \quad \epsilon = a\kappa = \frac{a/r_A}{1 + L^2/r_A^2} \tag{6.29}$$

where S is given in Blanco-Rodríguez et al. (2015) and ϵ is the expansion parameter of the asymptotic analysis which is assumed small. These considerations lead to a semi-analytical prediction for $\mu_0(\tau)$, which is plotted in figure 6.12-a (dashed lines) for various values of L. For large L, the auto-induced strain field is almost null and so is the ellipticity. At short instants, the agreement is very good at all L values. For small L, the agreement deteriorates at large times, as the expansion parameter ϵ increases. Indeed, as shown in figure 6.12-b, ϵ does not remain small for large times and/or small pitch L. At large pitch $L \geq 1$ however, the linear relation (6.28) is sufficient to predict μ_0 (see circles in figure 6.12-a).

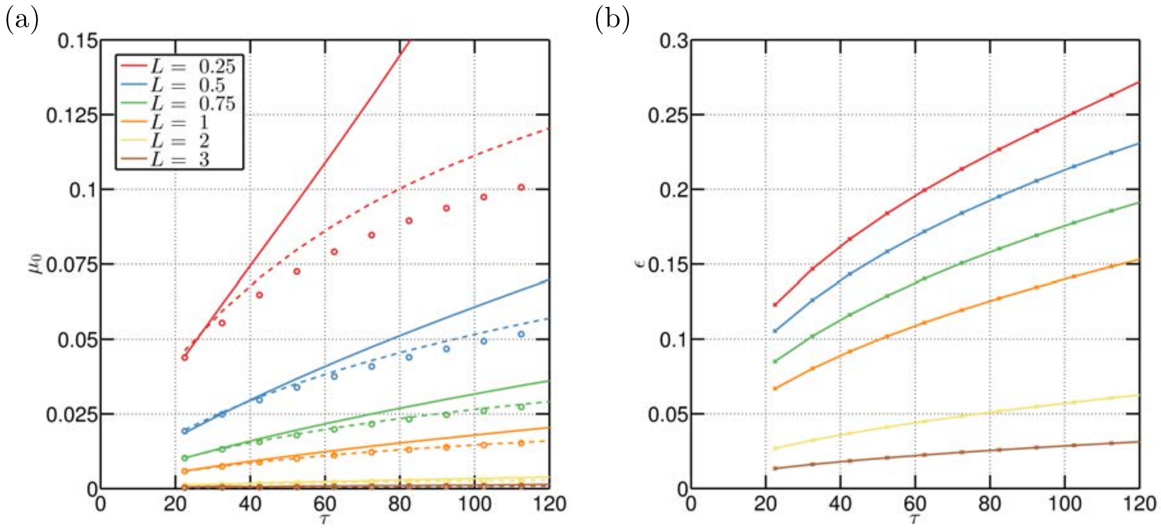

Figure 6.12 – One helical vortex at $Re = 5000$. (a) Time evolution of the ellipticity $\mu(\rho = 0) \equiv \mu_0$ at the center of the vortex for different values of L. Solid line : measured values, dashed line: ellipticity predicted from equation (6.27) with the strain γ obtained from the asymptotic analysis and the two-dimensional equivalent vortex patch. The circles are the prediction when the relation (6.27) is linearised into (6.28). (b) Time evolution of $\epsilon = a\kappa$ used in the asymptotic analysis with a and κ being the vortex core size and the curvature respectively.

The major axis is always found aligned with the vector $\boldsymbol{e}_{\varphi_A}$, hence orthogonal to the r-direction.

6.6 Streamline topology

The flow is further characterised by the streamline topology, first in the laboratory frame and then in the frame rotating with the vortex.

6.6.1 Streamline topology in the laboratory frame

In this section, the streamline topology induced by a single helical vortex in the laboratory frame is presented and compared to the topology predicted by an inviscid filamentary theory. In figure 6.13, the streamlines for several values of L are presented in plane Π_0. These states are characterised by the same core size $a = 0.06$. For large L, the structure is composed of smooth streamlines that all encircle the helical vortex centre-line (as in figure 6.13-a for $L = 1$). Below a critical value close to $L = 0.815$ (see figure 6.13-b), a new region with closed streamline structure appears outside the vortex region (see figure 6.13-c). This region grows when L is decreased, as shown in figure 6.13-d for $L = 0.5$ where the region now includes the helix axis.

In the inviscid framework, the topology of the streamlines associated to a helical vortex filament has been extensively studied by Andersen and Brøns (2014). These authors derived a closed formulation of the stream function from the solution by Hardin (1982), this formulation is briefly recalled below. Let $\xi = r/L$ and $\lambda = 1/L$. The stream function reads

$$\Psi_H(\xi,\varphi) = \frac{1}{2}\begin{cases} \dfrac{\xi^2}{2} - \dfrac{1}{2}\left(\left(1+\lambda^2\right)\left(1+\xi^2\right)^{1/4}\right)\Re\left(\ln\left(1-e^{+\delta_f+\mathrm{i}\varphi}\right)\right) \\ -\ln(\xi) + \ln(\lambda) - \dfrac{1}{2}\left(\left(1+\lambda^2\right)\left(1+\xi^2\right)^{1/4}\right)\Re\left(\ln\left(1-e^{-\delta_f+\mathrm{i}\varphi}\right)\right) \end{cases} \tag{6.30}$$

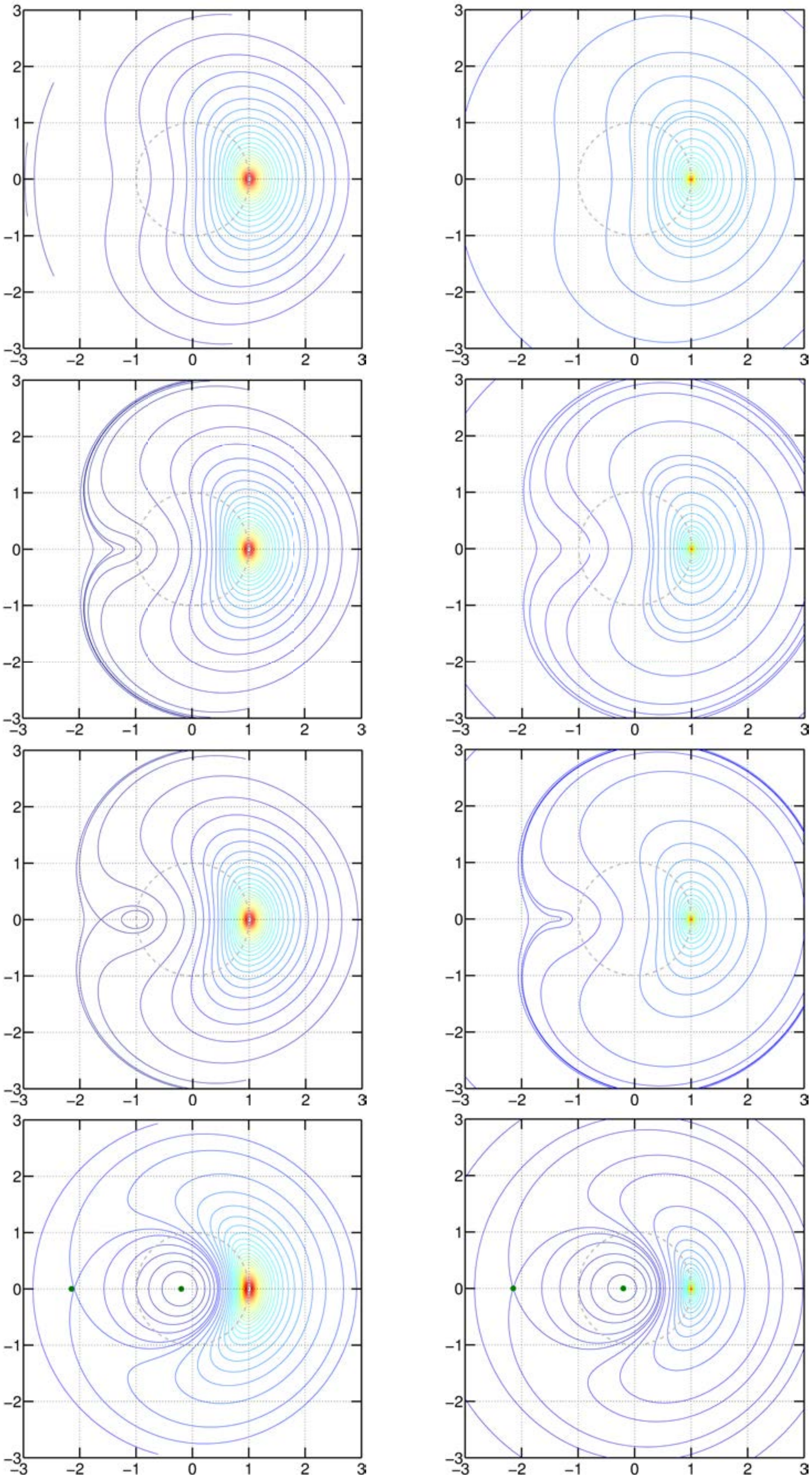

Figure 6.13 – Streamline topology in the laboratory frame for a helical vortex of reduced pitch $L = 1$ (top), $L = 0.815$ (second row), $L = 0.791$ (third row) and $L = 0.5$ (bottom). Left: Contours of Ψ from the DNS for a vortex with finite core size $a = 0.06$. Right: contours of Ψ_H from analytical formula (6.30). On both bottom graphs, the green dots correspond to the critical points of Ψ_H.

where the top line refers to the inner solution ($r < 1$) and the bottom line to the outer solution ($r > 1$). Variable δ_f is given by

$$\delta_f = \delta_f(\xi, \lambda) = f(\xi) - f(\lambda), \quad \text{where } f(x) = \sqrt{1+x^2} + \ln\left(\frac{x}{1+\sqrt{1+x^2}}\right). \tag{6.31}$$

Note that equation (6.30) diverges on the filament at $(\xi, \varphi) = (\lambda, 0)$.

On figure 6.13 (right column) the streamlines obtained through 6.30 are plotted for the same pitch values as the DNS. It is found that, the streamline structure globally reproduces that obtained by DNS in most of the flow. Unsurprisingly, some differences occur in the vortex core. As the core size in the DNS is reduced, the agreement improves (not shown). There are also local differences associated to the appearance of critical points of the stream function, which we discuss now.

In Andersen and Brøns (2014), the critical points of the stream function Ψ_H were analysed using equation (6.30). It was first demonstrated that the points at ($r \neq 1, \varphi = 0$) cannot be critical points whatever the pitch value. The critical points occur on the line ($r, \varphi = \pi$) and are found to be the zeros of the function F defined as:

$$\begin{aligned} F(\xi;\lambda) &\equiv \frac{\partial}{\partial \xi}\Psi_H(\xi,\pi) \\ &= \begin{cases} \dfrac{\xi}{2} - \dfrac{1}{2}\left(1+\lambda^2\right)^{1/4}\left(\dfrac{1}{2}\dfrac{\xi}{(1+\xi^2)^{3/4}}\ln\left(1+e^{\delta_f}\right) + \dfrac{(1+\xi^2)^{3/4}}{\xi}\dfrac{e^{\delta_f}}{1+e^{\delta_f}}\right) \\ -\dfrac{1}{2\xi} - \dfrac{1}{2}\left(1+\lambda^2\right)^{1/4}\left(\dfrac{1}{2}\dfrac{\xi}{(1+\xi^2)^{3/4}}\ln\left(1+e^{-\delta_f}\right) - \dfrac{(1+\xi^2)^{3/4}}{\xi}\dfrac{e^{-\delta_f}}{1+e^{-\delta_f}}\right) \end{cases}. \end{aligned} \tag{6.32}$$

In figure 6.13 (bottom right) the critical points are represented in filled green dots. When plotted on the DNS streamlines (bottom left), a very good agreement is found, even if a small discrepancy is observed on the location of critical points due to the finite core size. The theory shows that critical points occur through a saddle-node bifurcation when L is decreased below the critical value $L_{C1} = 0.7905$ (figure 6.13-c). At this precise value, the D.N.S. fields already show a small pocket of closed streamlines. Indeed the critical threshold we obtained by DNS is rather $L_{C1}^{DNS} \approx 0.815$ which is slightly off $L_{C1} = 0.7905$ due to the finite core size.

6.6.2 Streamline topology in the rotating frame

In previous section, we analysed the streamline structure in the laboratory frame and highlighted the topology modifications of the helical flow when the pitch L is varied. However, physical interpretations in the laboratory frame remain limited: since the flow is not stationary in this frame, trajectories differ from streamlines. It is thus more instructive to study the streamline structure in the frame rotating with the vortex system. Such a study gives valuable informations on Lagrangian dynamics of particles for example.

Influence of L

The influence of the pitch L on the flow topology is analysed. In figure 6.14, the isovalues of Ψ_R are plotted for $L = 0.5, 0.35, 0.25$ with the core size being fixed at $a = 0.25$. For this core size at $L = 0.5$, there is no critical point in the flow field aside from the vortex centre. At $L = 0.35$ and $L = 0.25$, a centre and a saddle point exist on the radial line located at the opposite of the vortex centre with respect to the origin.

When L decreases, the radial distance separating these critical points increases. The centre critical point shifts radially inwards while the saddle shifts outwards. The streamlines passing between these two critical points thus form a region where fluid particles do not travel around the vortex core but move along/around the z axis. This behaviour is associated to the velocity excess or deficit inside a helical vortex at small L. Indeed, the resulting flow field tends to be equivalent to that of a cylindrical vortex sheet with a jet or wake component inside the cylinder.

Influence of a

We now focus on the streamline topology obtained by DNS in the rotating frame when a is varied at fixed pitch L. In figure 6.15 the iso-contours of Ψ_R are plotted for $L = 0.5$ and different core sizes $a = 0.26, 0.485, 0.603$, again showing different topologies. For $a = 0.26$, no critical point is present in the flow field aside from the vortex centre. It is observed that the same scenario occurs when a is increased at fixed L as we had before when L is decreased at fixed a. Here, a pair of critical points arise at $a = 0.485$, which progressively shift apart radially when a is increased. Indeed, with a increasing, the vorticity tends to spread around the axis to form a cylindrical layer similar to the previous case. This explains why similar topologies are observed here.

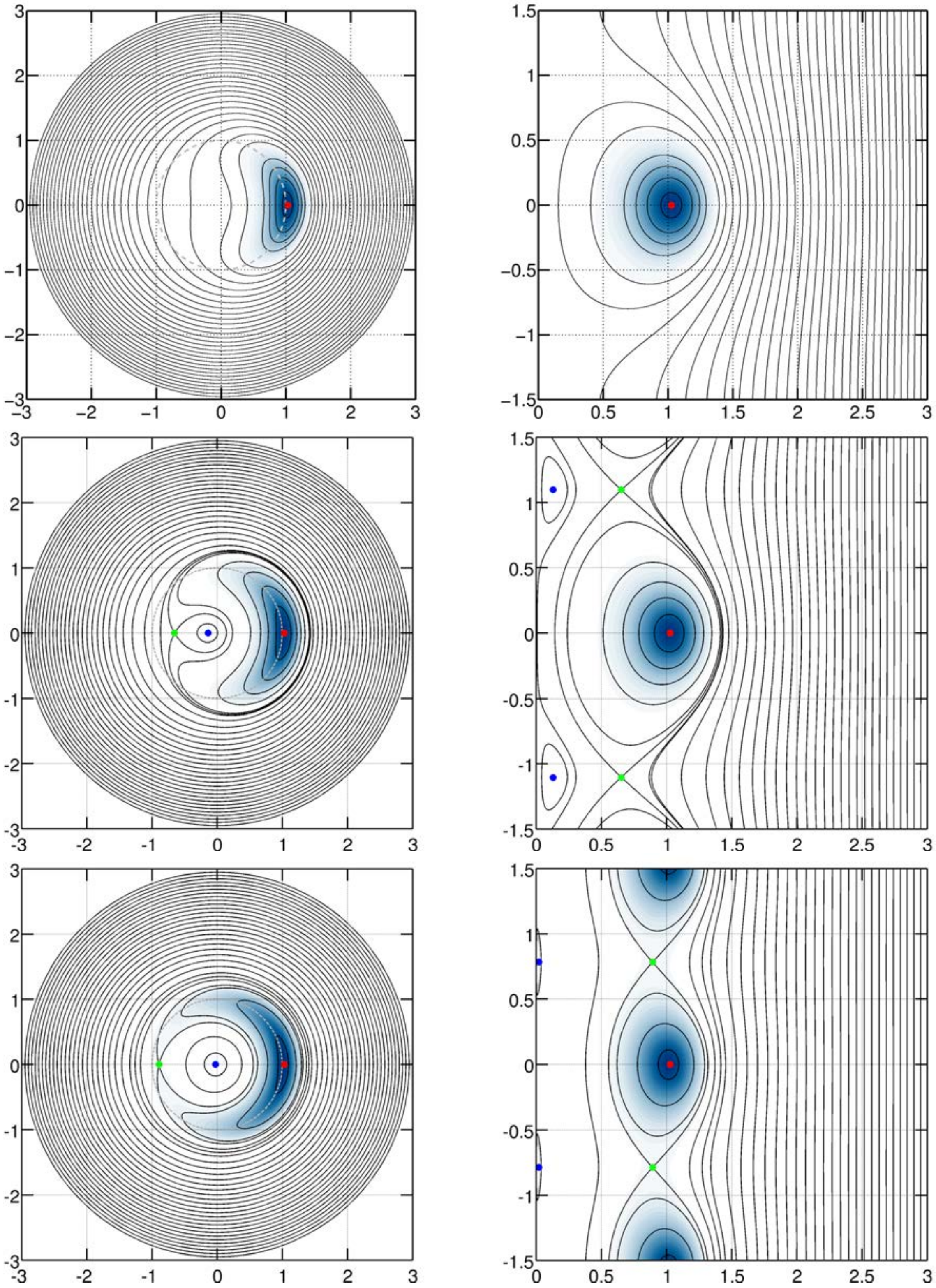

Figure 6.14 – Rotating frame: streamline topology obtained by DNS, for one helical vortex of core size $a = 0.25$ and for different L. Top row: $L = 0.5$. Middle row: $L = 0.35$. Bottom row: $L = 0.25$. First column: representation in Π_0. Second column: representation in the meridian plane $(r - z)$. The green dots represent the locations of the hyperbolic points. The blue and red dots represent the centre points: the blue dot is created in the inner region while the red one is located within the vortex centre.

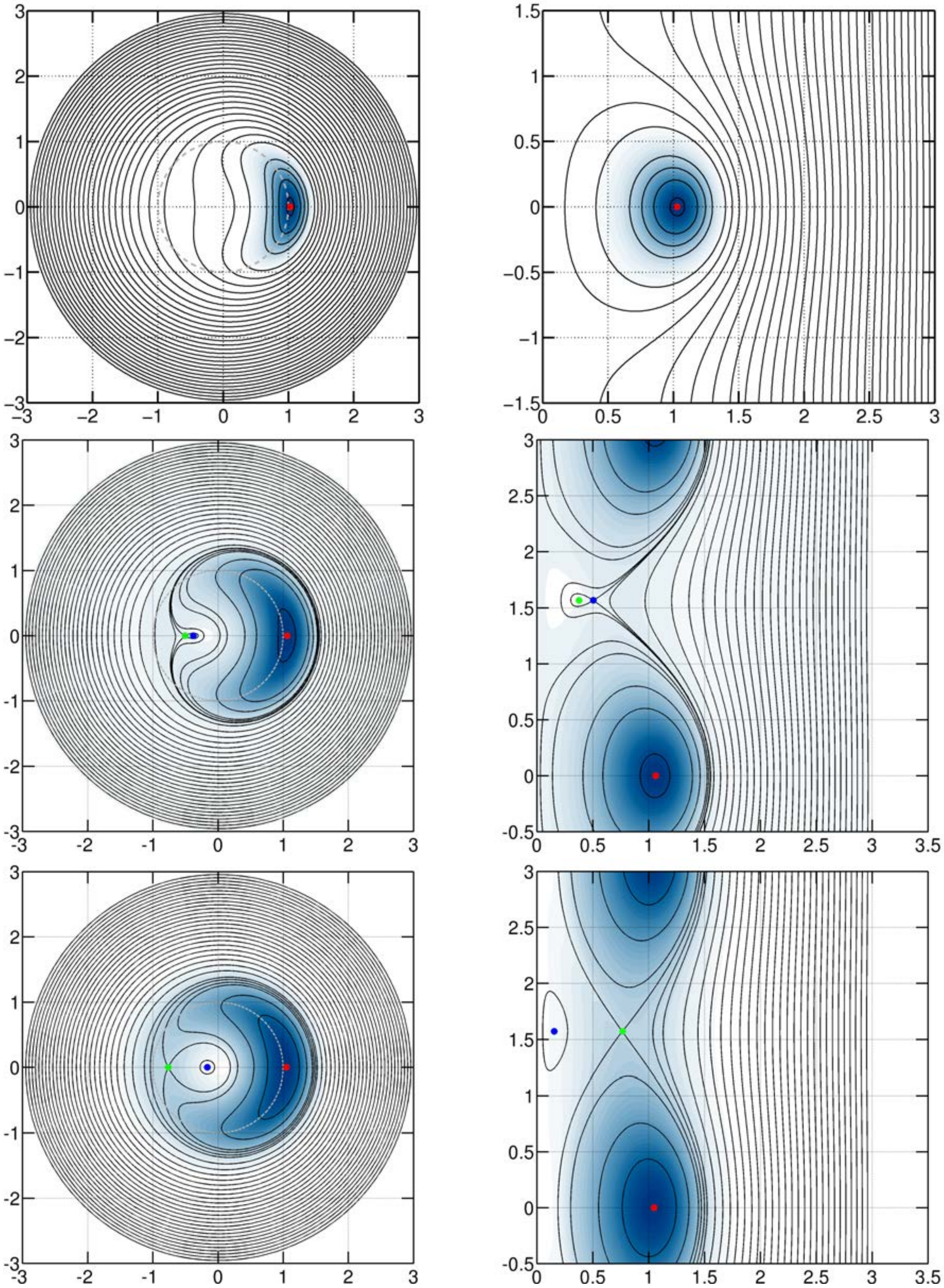

Figure 6.15 – Rotating frame: streamline topology obtained by DNS for one helical vortex $L = 0.5$ and for different core sizes a. Top row: $a = 0.26$. Middle row: $a = 0.485$. Bottom row: $a = 0.603$. First column: representation in Π_0. Second column: representation in the meridian plane $(r - z)$. The green dots represent the locations of the hyperbolic points. The blue and red dots represent the centre points: the blue dot is created in the inner region while the red one is located within the vortex centre.

6.7 Particle transport by a helical vortex

In this section, we study the motion of particles in presence of a helical vortex with frozen finite core size. This is done in the framework rotating with the vortex since the flow being stationary, the trajectories of fluid particles follow the streamlines.

6.7.1 Equations for the particle motion in the rotating frame

In an inertial frame, we define the velocity of a particle as the time derivative of its position vector $\boldsymbol{x_p}$:

$$\boldsymbol{u_p} \equiv \frac{\mathrm{d}\boldsymbol{x_p}}{\mathrm{d}t}, \tag{6.33}$$

where $\mathrm{d}/\mathrm{d}t$ denotes the time derivative in the inertial reference frame. Passive particles act as perfect tracers in the flow: their velocity equals that of the fluid particles $\boldsymbol{u}_{\boldsymbol{flow}}$. Hoverer, it is possible to take inertial effects into account by writing the momentum equation as:

$$\frac{\mathrm{d}\boldsymbol{u_p}}{\mathrm{d}t} = \frac{1}{St}\left(\boldsymbol{u_{flow}} - \boldsymbol{u_p}\right), \tag{6.34}$$

where the Stokes number St is given by

$$St \equiv \frac{\Gamma t_p}{R^2} = \frac{2\rho_p r_p^2 \Gamma}{9\rho\nu R^2}, \tag{6.35}$$

with the density ρ_p and the radius r_p of the particle, and the density ρ and the viscosity ν of the carrier flow, respectively. This number represents the ratio between the particle relaxation time t_p and a typical time scale of the flow (for passive particles, $St = 0$).
We now consider a non-inertial frame rotating with respect to the inertial frame at an angular velocity Ω around the vertical axis $\boldsymbol{e_z}$. Let $\mathrm{d}/\mathrm{d}t'$ denote the time derivative in this rotating frame of reference and consider a particle of position vector $\boldsymbol{x_p}$: if this particle is stationary in the rotating reference frame, it appears to move in the inertial frame. Hence it is clear that $\mathrm{d}/\mathrm{d}t \neq \mathrm{d}/\mathrm{d}t'$, more precisely

$$\frac{\mathrm{d}\boldsymbol{x_p}}{\mathrm{d}t} = \frac{\mathrm{d}\boldsymbol{x_p}}{\mathrm{d}t'} + \Omega\boldsymbol{e_z} \times \boldsymbol{x_p}. \tag{6.36}$$

In the rotating frame, we define:

$$\boldsymbol{u_p'} \equiv \frac{\mathrm{d}\boldsymbol{x_p}}{\mathrm{d}t'}. \tag{6.37}$$

Using definitions (6.33) and (6.37), equation (6.36) relates the velocity, $\boldsymbol{u_p} = \mathrm{d}\boldsymbol{x_p}/\mathrm{d}t$ of an object at position $\boldsymbol{x_p}$ in the inertial reference frame to its velocity, $\boldsymbol{u_p'} = \mathrm{d}\boldsymbol{x_p}/\mathrm{d}t'$, in the rotating reference frame

$$\boldsymbol{u_p} = \boldsymbol{u_p'} + \Omega\boldsymbol{e_z} \times \boldsymbol{x_p}. \tag{6.38}$$

In order to compute the acceleration, the operation is applied twice to $\boldsymbol{x_p}$:

$$\frac{\mathrm{d}\boldsymbol{u_p}}{\mathrm{d}t} \equiv \frac{\mathrm{d}^2\boldsymbol{x_p}}{\mathrm{d}t^2} = \left(\frac{\mathrm{d}}{\mathrm{d}t'} + \Omega\boldsymbol{e_z}\times\right)\left(\boldsymbol{u_p'} + \Omega\boldsymbol{e_z} \times \boldsymbol{x_p}\right) \tag{6.39}$$

yielding

$$\frac{\mathrm{d}\boldsymbol{u_p}}{\mathrm{d}t} = \frac{\mathrm{d}^2\boldsymbol{x_p}}{\mathrm{d}t'^2} + \Omega\boldsymbol{e_z} \times \frac{\mathrm{d}\boldsymbol{x_p}}{\mathrm{d}t'} + \frac{\mathrm{d}\left(\Omega\boldsymbol{e_z} \times \boldsymbol{x_p}\right)}{\mathrm{d}t'} + \Omega\boldsymbol{e_z} \times \left(\Omega\boldsymbol{e_z} \times \boldsymbol{x_p}\right). \tag{6.40}$$

If we assume that Ω is constant (frozen vortex), this yields:

$$\frac{\mathrm{d}\boldsymbol{u_p}}{\mathrm{d}t} = \frac{\mathrm{d}\boldsymbol{u_p'}}{\mathrm{d}t'} + 2\Omega\boldsymbol{e_z} \times \boldsymbol{u_p'} + \Omega\boldsymbol{e_z} \times \left(\Omega\boldsymbol{e_z} \times \boldsymbol{x_p}\right). \tag{6.41}$$

Finally, the acceleration in the rotating frame reads

$$\frac{\mathrm{d}\boldsymbol{u}'_{\boldsymbol{p}}}{\mathrm{d}t'} = \frac{\mathrm{d}\boldsymbol{u}_{\boldsymbol{p}}}{\mathrm{d}t} - 2\Omega\boldsymbol{e}_{\boldsymbol{z}} \times \boldsymbol{u}'_{\boldsymbol{p}} - \Omega\boldsymbol{e}_{\boldsymbol{z}} \times (\Omega\boldsymbol{e}_{\boldsymbol{z}} \times \boldsymbol{x}_{\boldsymbol{p}}) \tag{6.42}$$

and since $\boldsymbol{u}'_{\boldsymbol{flow}} - \boldsymbol{u}'_{\boldsymbol{p}} = \boldsymbol{u}_{\boldsymbol{flow}} - \boldsymbol{u}_{\boldsymbol{p}}$, equation (6.42) becomes

$$\frac{\mathrm{d}\boldsymbol{u}'_{\boldsymbol{p}}}{\mathrm{d}t'} = \frac{1}{St}\left(\boldsymbol{u}'_{\boldsymbol{flow}} - \boldsymbol{u}'_{\boldsymbol{p}}\right) - 2\Omega\boldsymbol{e}_{\boldsymbol{z}} \times \boldsymbol{u}'_{\boldsymbol{p}} - \Omega\boldsymbol{e}_{\boldsymbol{z}} \times (\Omega\boldsymbol{e}_{\boldsymbol{z}} \times \boldsymbol{x}_{\boldsymbol{p}})\,. \tag{6.43}$$

6.7.2 Particle initialisation and simulation

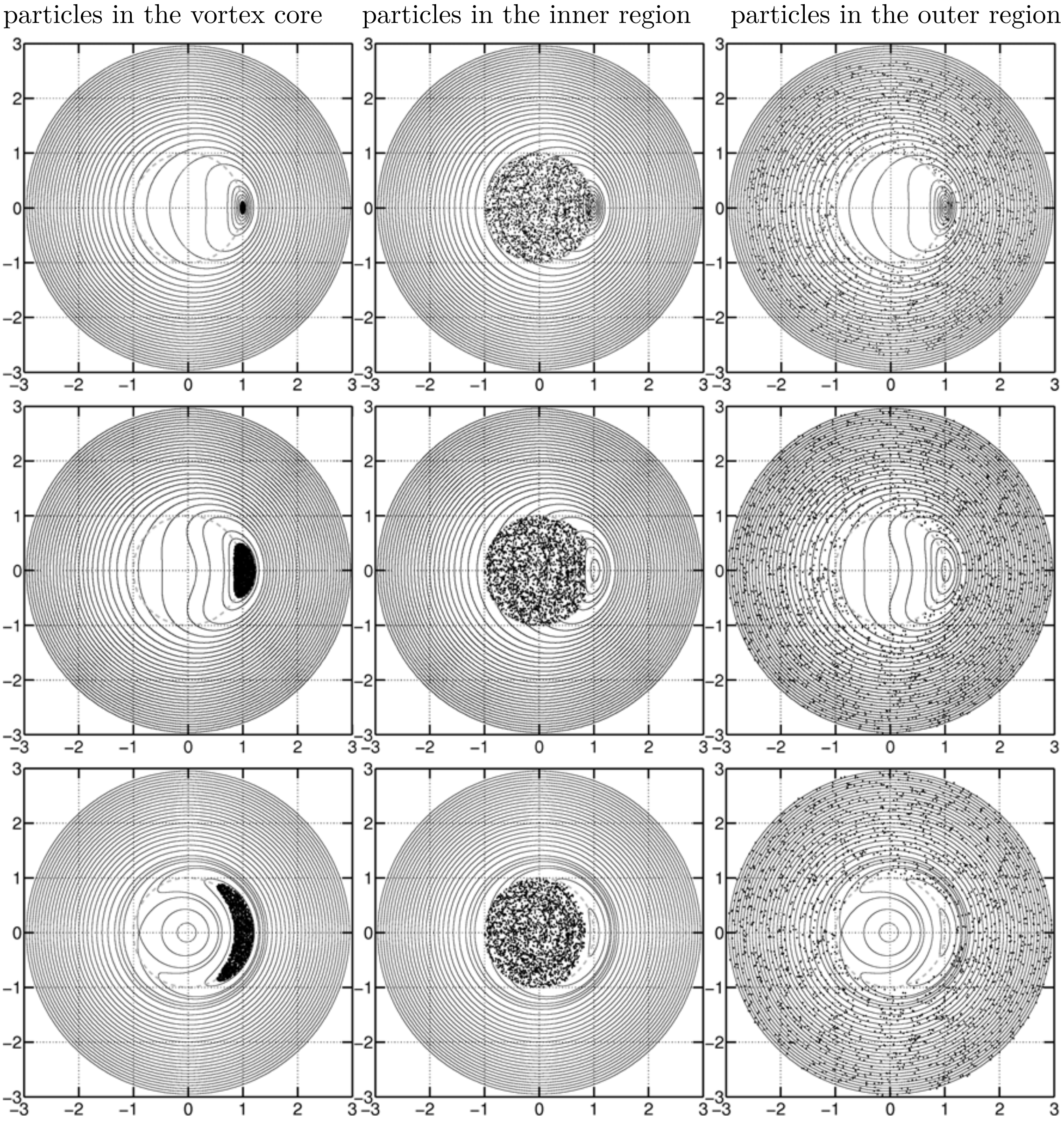

Figure 6.16 – Particle initialisations in the Π_0 plane on top of the streamlines in the rotating frame. Particles are set in the vortex core (left column), in the inner region (central column) and in the outer region (right column). Top row: case 1, middle row: case 2 and bottom row: case 3.

The fluid domain is virtually split into three different regions in Π_0:

— a first area called vortex core defined as the region (r, θ) where $\omega_B(r, \theta) > \frac{1}{2}\max(\omega_B)$;

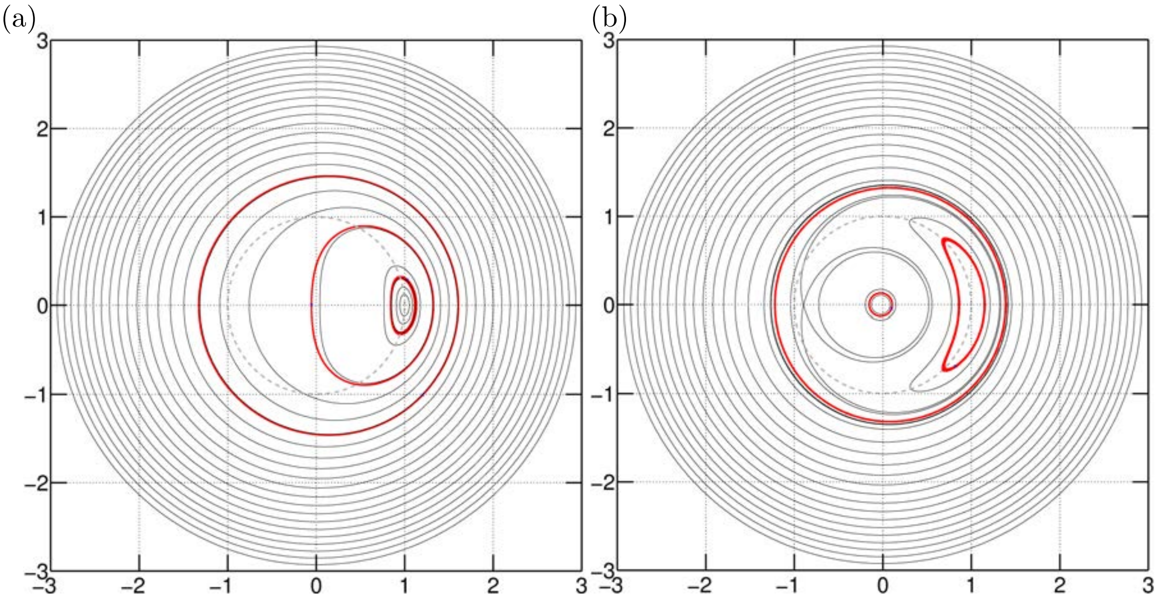

Figure 6.17 – Rotating frame: streamlines obtained by DNS for a single helical vortex. (a) Case 1. (b) Case 3. The trajectories of three particles are shown in red thick lines. Case 2, very similar to case 1, is not plotted.

— a second area called the inner region where $r < 1$ but which excludes the vortex core region;

— a third area called the outer region where $r > 1$ but which also excludes the vortex core region.

In each area, $N_p = 2000$ particles are randomly set and the corresponding trajectories are then integrated using equation (6.43) or, if $St = 0$, equation (6.37) with $\boldsymbol{u}'_p = \boldsymbol{u}'_{flow}$. Three different cases are investigated:

— case 1: $L = 0.5,\ \ a = 0.06$,

— case 2: $L = 0.5,\ \ a = 0.25$,

— case 3: $L = 0.25, a = 0.25$.

For cases 1 and 2, the streamlines have no critical points. For case 3, one centre and one saddle critical point are present in the inner region of the flow field. In figure 6.16, typical initialisations of the particles in each of the three areas are shown on top of the streamlines $\Psi_R = cst$ for the three cases under investigation.

6.7.3 Results for the passive case: $St = 0$

The trajectories of three particles emanating from each area are represented in figure 6.17 on top of the streamlines. In plane Π_0, the trajectories necessarily follow closed paths. The corresponding three-dimensional trajectories are shown for the three cases in figure 6.18.

When a particle is initially set within the vortex core, it is advected along the helical vortex tube (see left column of figure 6.18). It loops around the vortex centreline with a spatial and temporal periodicity which depends on the core size, the pitch and its distance to the centreline. As a consequence, there exist a wide diversity of geometries for such trajectories.

When a particle is initially set in the outer region, it follows trajectories close to a helix of large radius and small pitch (see right column of figure 6.18). This class of trajectories is weakly influenced by the geometrical parameters of the vortex.

When the particle is initially set in the inner region, two scenarios occur depending on the flow topology (see central column of figure 6.18). For case 1 and 2 (top and middle

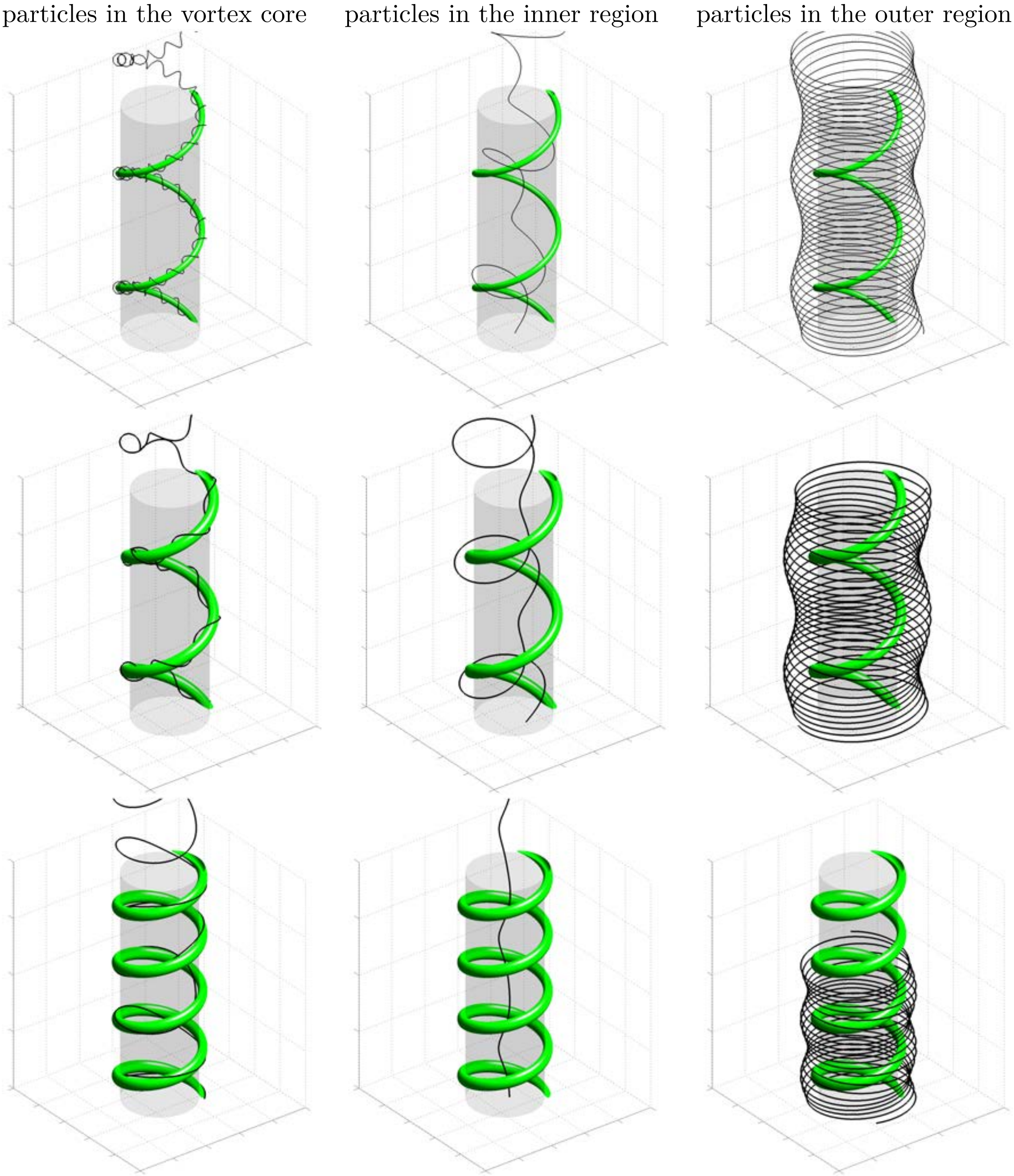

Figure 6.18 – Representation in the rotating frame of particle trajectories (solid black line) around a helical vortex of reduced pitch $L = 0.5$ with core size $a = 0.06$ (case 1, top row), core size $a = 0.25$ (case 2, middle row) and pitch $L = 0.25$ with core size $a = 0.25$ (case 3, bottom row). The particles are initially located within the vortex core (left figures), in the circle of radius $r < 1$ in Π_0 without being in the vortex core (central figures) and outside the circle of radius $r > 1$ without being in the vortex core (right figures). The trajectories correspond to the black curves shown in figure 6.17.

figures, without critical points), it progresses alternatively by looping around the vortex core and by moving along a path in the vicinity of the $z-$axis. For case 3 (bottom figure), if the particle follows a trajectory situated between the critical points it does not loop around the vortex core but rather travel along the axial direction. Again, this behaviour is associated to the velocity excess or deficit inside a helical vortex at small L or large a. The temporal aspect, in particular the advection velocity along the axis cannot be analysed from the above snapshots. We now present the time evolution of a large number of particles being released in each area in the plane $z = 0$. The dispersion of particles along the axial direction z is quantified by the probability density functions of the axial position z.

Probability density functions of the axial position z

At a given time t, the probability density function $f(z)$ of the particle axial position is such that $f(z)\delta z$ is the probability for particles to be present within the interval $[z, z+\delta z]$. This quantity is evaluated numerically by first defining a partition of the z axis in sub-intervals $[z_i, z_{i+1}]$, each one containing a prescribed number of particles chosen as $2\sqrt{N_p}$ (for regions where the particles are sparse, a maximum extent $z_{i+1}-z_i = 2\Delta z/\sqrt{N_p}$ is enforced instead, where Δz is the axial separation between the most distant particles at that time). The density function $f(z)$ is then computed at middle points $z_{i+1/2} = (z_i + z_{i+1})/2$ as:

$$f(z_{i+1/2}) = \frac{1}{\delta z_i}\frac{\delta N_i}{N_p}, \tag{6.44}$$

where δN_i is the number of particles located in $[z_i, z_i + \delta z_i]$ and $\delta z_i = z_{i+1} - z_i$.
We first analyse the evolution of particles initially situated in the vortex core (figure 6.19 left column). It is seen that the particles remain tightly clustered as far as the axial position z is concerned. It is observed that reducing the core size at fixed L or reducing L at fixed a both lead to higher axial velocities.
When the particles are initialised within the outer region (figure 6.19 right column), it is observed for the three cases that the particles all remain in the vicinity of the plane $z = 0$, which indicate a weak axial velocity. This is linked to the fact that in the present simulations the axial velocity far from the axis is set to zero.
When particles are initially set in the inner region, their distribution along the z axis presents a large scattering (figure 6.19 middle column). At large pitch (case 1 and 2), this scattering is particularly wide: the area contains particles which are close to the vortex core and propagate rapidly (see above) as well as particles more remote which propagate at reduced velocity. At smaller pitch (figure 6.19 bottom row, middle column) however, the scatter is reduced and the particles are found to travel along z at high speed, much higher than the particles in the vortex core. Again this corresponds to the excess velocity present inside the helical vortex at small pitch: when L is reduced, there are more coils hence more azimuthal vorticity per unit length along z and thus a large axial velocity gradient between the outer and the inner region.

6.7.4 Preliminary results for the inertial cases $St \neq 0$.

In order to illustrate the effect of inertia on particle motion, the trajectory of a particle with inertia is plotted in plane Π_0 and in three dimensions (figure 6.20).
While initially located within the inner region, the particle does not remain in that region as before. It thus progressively shift towards the outer region and leaves the computational domain. Due to lack of time, we could not analyse the dependency of the particle trajectories with respect to the Stokes number and to the geometrical vortex properties.

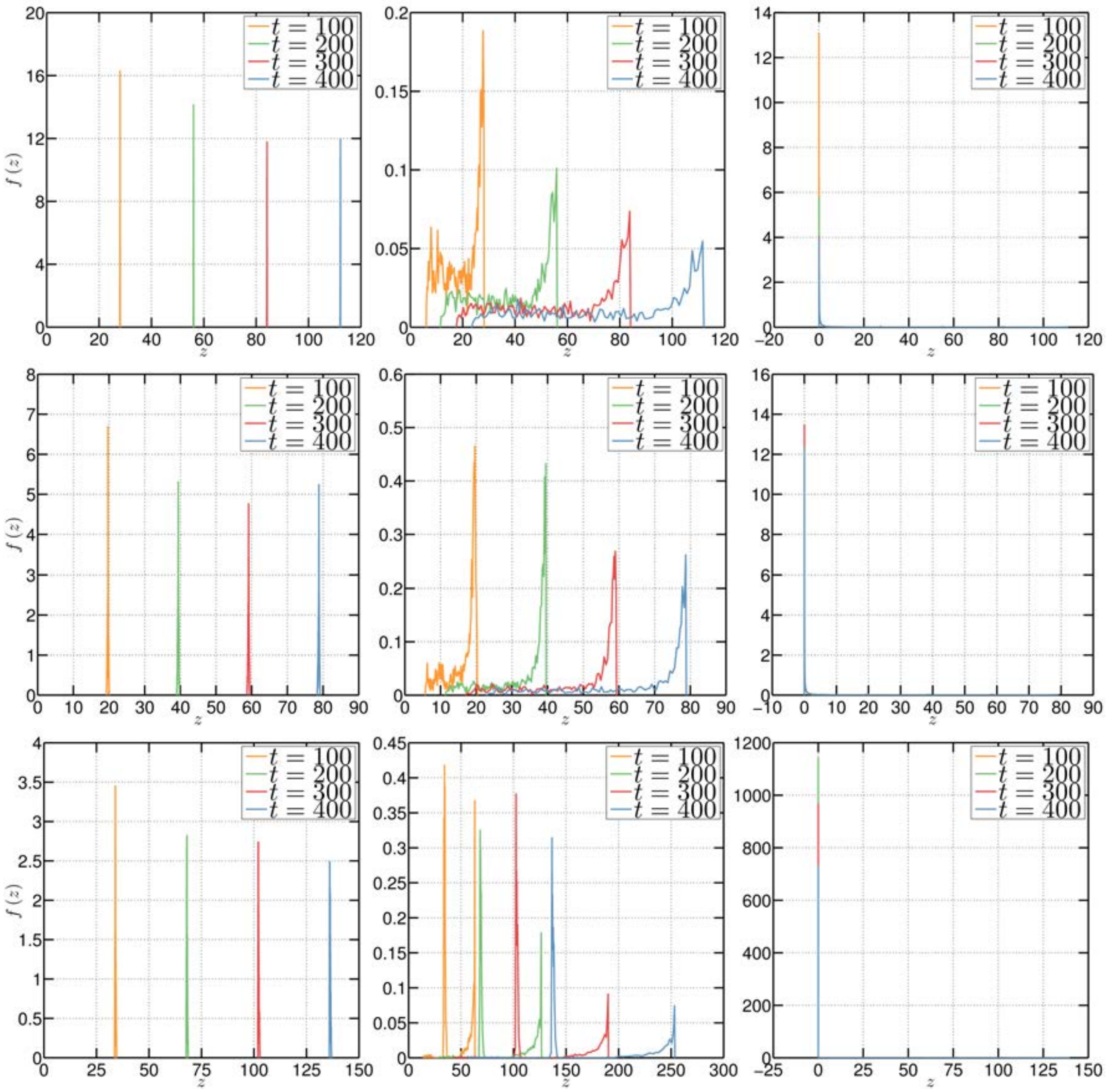

particles in the vortex core particles in the inner region particles in the outer region

Figure 6.19 – Passive particles ($St = 0$): time evolution of the probability density functions of the axial position z at $t = 100$ (orange), $t = 200$ (green), $t = 300$ (red) and $t = 400$ (blue). First row: case 1; second row: case 2; bottom row: case 3. The N_p particles are initially set at $z = 0$ in the vortex core (left column), or in the inner region (central column) or in the outer region (right column).

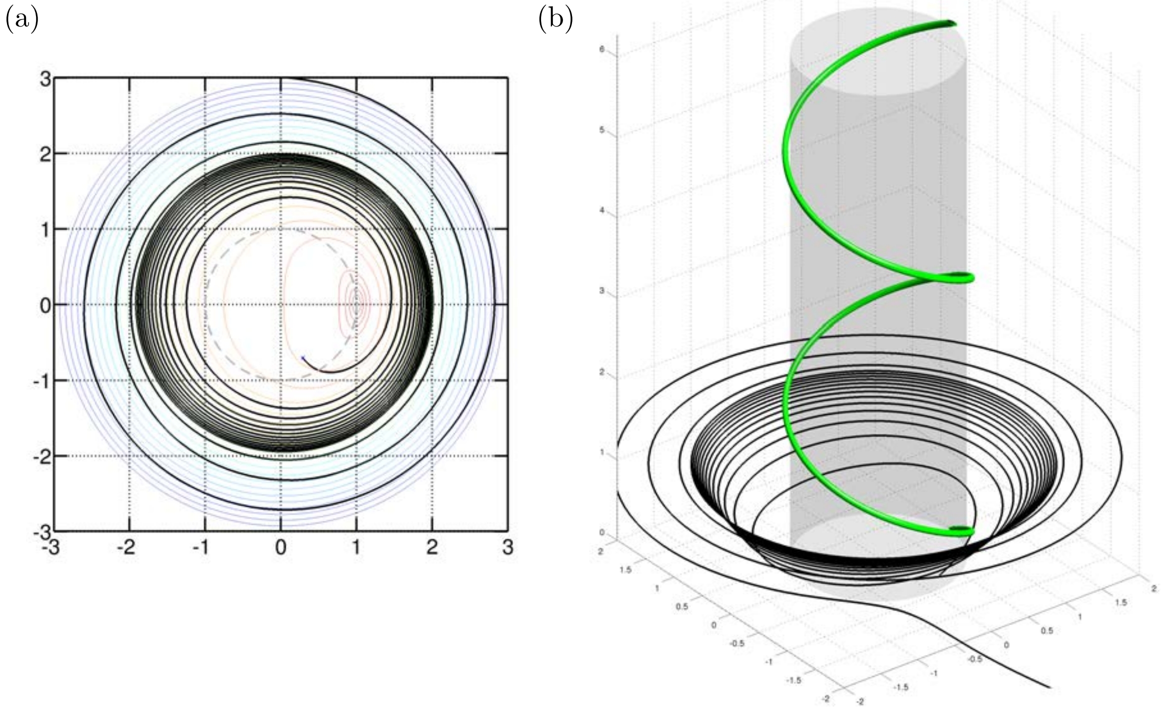

Figure 6.20 – Particle with inertia at Stokes number $St = 0.5$. Trajectory of a particle initially locate in the inner region represented (a) in plane Π_0, (b) in three dimensions.

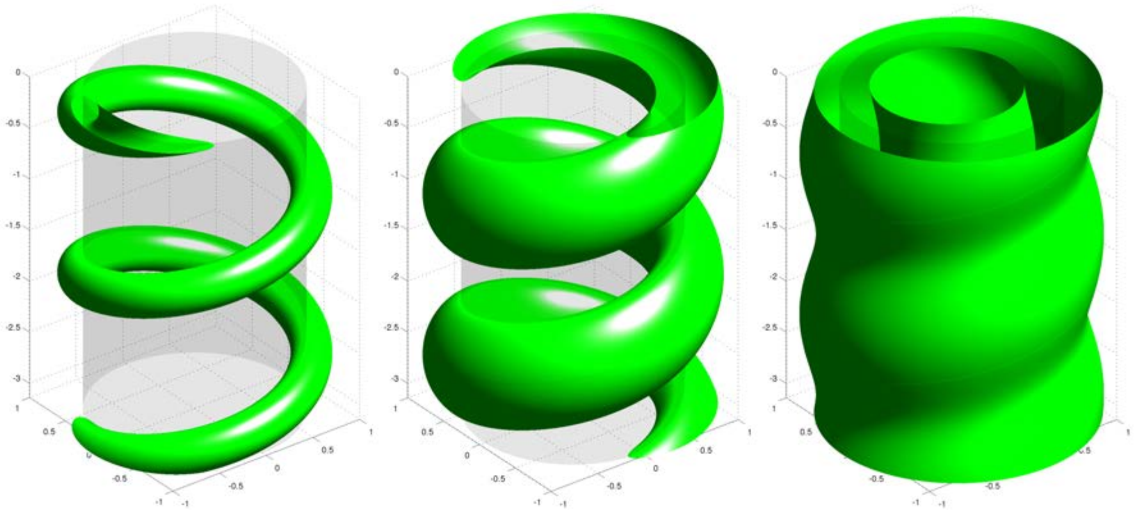

Figure 6.21 – One helical vortex of reduced pitch $L = 0.25$ and $Re = 5000$. Isosurfaces of $\alpha\omega_B$ at instants $\tau = 22.5, 92.5, 142.5$. The chosen isosurface value is $\alpha\omega_B(\tau) = 0.15 \max(\alpha\omega_B)$.

6.8 Late evolution: coil merging and axisymmetrisation

The late evolution of a single helical vortex at small pitch is a merging phase between the coils, as illustrated in figure 6.21 for $L = 0.25$. The helical vorticity field evolves towards a cylindrical layer of helical vorticity. At $L = 0.25$, the merging starts at roughly $\tau = 92.5$ which corresponds to the state plotted in figure 6.10. This is also the time at which the functional relation between the stream function and the quantity $\alpha\omega_B$ breaks. This is shown on the scatter plots in figure 6.22 for instants $\tau = 112.5$ and $\tau = 202.5$ where two branches are now observed (black and red curves). The splitting concerns regions of weak vorticity which include the vicinity of the hyperbolic point of the stream function, as seen in figure 6.23. This indicates that the evolution is not quasi-stationary during the merging.

Once the successive coils of the vortex have merged to yield a cylindrical sheet, the resulting structure continues to evolves on a slow diffusing time scale. The radial position r_A of the vortex center decreases in time until reaching the origin of the domain. At this moment the cylindrical vortex sheet becomes a centred axisymmetric vortex.

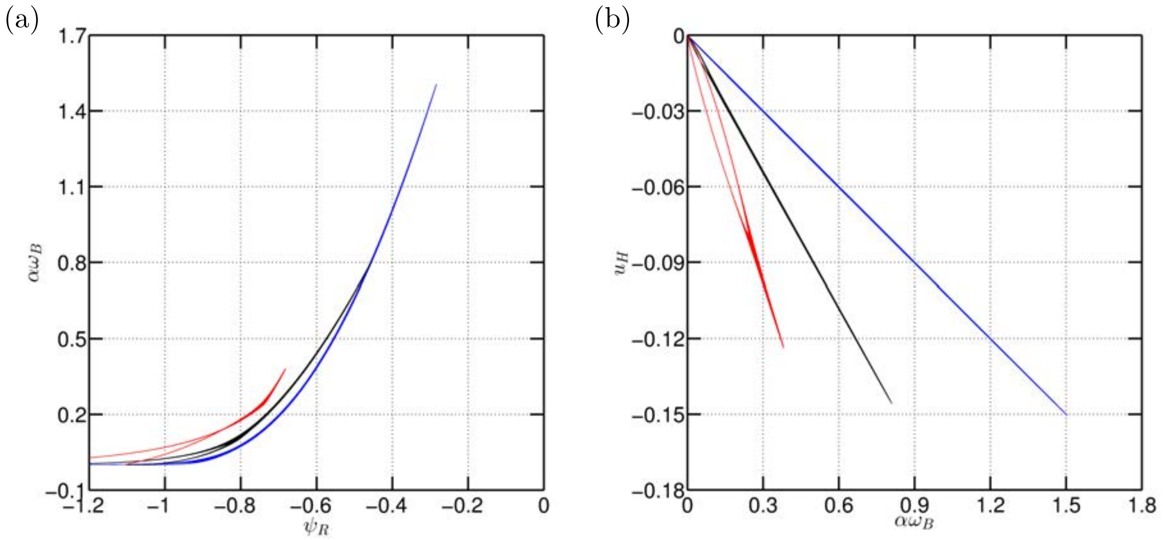

Figure 6.22 – One helical vortex of reduced pitch $L = 0.25$ and $Re = 5000$. Scatter plots of the quantities $(\alpha\omega_B, \Psi_R)$ and $(u_H, \alpha\omega_B)$ for instant $\tau = 62.5$ (blue), 112.5 (black), 202.5 (red).

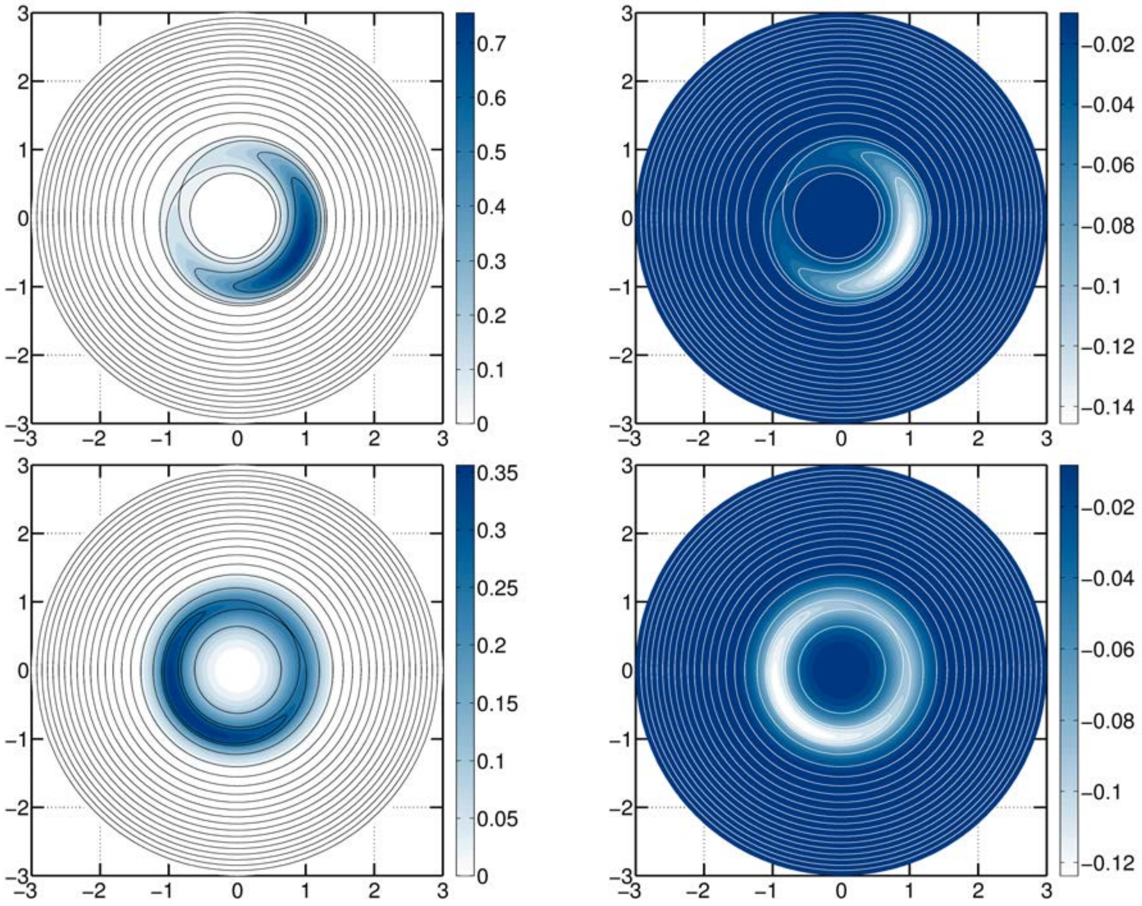

Figure 6.23 – One helical vortex of reduced pitch $L = 0.25$ and $Re = 5000$. Snapshots at $\tau = 112.5$ (top) and $\tau = 202.5$ (bottom). Left column: contours of the stream function in the rotating frame Ψ_R (black lines) superimposed on top of the quantity $\alpha\omega_B$. Right column: same streamlines (white lines) superimposed on top of the quantity u_H.

Chapter 7

Modal decomposition of the core structure: comparisons with asymptotic theory

Contents

In the present chapter, quasi-equilibrium solutions previously obtained are used to analyse the internal structure of the helical vortex and to compare them with analytical predictions. This work led to a publication (Blanco-Rodríguez et al., 2015) between the team at IRPHE Marseille who performed the theoretical analysis and our team at LIMSI Orsay and d'Alembert Paris who provided numerical results and performed comparisons between analytical and numerical results. This chapter includes the JFM paper (section 7.2). In section 7.1, however, additional details are provided about methods used for comparisons.

In the asymptotic analysis, the multipolar internal structure of vortex rings and helical vortices are predicted. Equations are expanded in powers of a small parameter ϵ defined in equation (6.29)

$$\epsilon = \frac{a}{r_A}\frac{1}{1+L^2/r_A^2} \tag{7.1}$$

representing the ratio between the vortex core size a and the radius of curvature. The leading order is chosen to be an axisymmetric columnar vortex with an axial jet/wake modeled by a Batchelor vortex profile $\boldsymbol{V} = \left(0, u^{(0)}, w^{(0)}\right)$ given in dimensionless cylindrical coordinates by

$$u^{(0)} = \frac{1}{r}\left(1-e^{-r^2}\right) \qquad\qquad w^{(0)} = W_0 e^{-r^2} + W_{0_0}. \tag{7.2}$$

This leading order is characterised by zero curvature and torsion. When curvature and torsion are introduced, the core structure is modified through local and non-local effects. The asymptotic analysis aims at predicting the associated corrections. At first order, a dipolar correction (azimuthal mode $m = 1$) arises and is shown to depend only on the local vortex curvature. This correction is thus identical for a ring, an array of rings, a helix and an array of N helices provided they have the same radius of curvature. At second order, a quadrupolar (azimuthal mode $m = 2$) correction arises and is shown to be composed of two contributions, one associated with the local curvature and another one arising from a two-dimensional strain field due to distant vortex parts and/or distant vortices.

7.1 Extraction of the multipolar profile from the DNS data.

In order to compare DNS results to theoretical predictions, we use numerical fields obtained at a fixed time τ chosen such that a quasi-equilibrium state in the frame rotating with the helical structure is reached. The rotation rate $\Omega(\tau)$ of the vortex structure is first computed using the method described in 5.1.2. The velocity field in the frame rotating at rate $\Omega(\tau)$ has then to be analysed in plane $\Pi_\perp$ in order to extract the monopolar, dipolar and quadrupolar contributions.

First, this necessitates to define how the plane $\Pi_\perp$ is chosen in the numerics (see subsection 7.1.1). Second the velocity and vorticity field can be expressed in three different reference frames:

- the laboratory frame (L) in which the vortex rotates
- the frame (T) in axial translation at velocity V_{frame} used in the theory in which the vortex is steady
- the frame (Ro) rotating at angular velocity $\hat{\Omega}_{frame}$ used for DNS post-treatment in which the vortex is also steady.

In order to compare our results to the theory, one has first to express the analytical velocity field $\boldsymbol{V}^{(Ro)}$ in the rotating frame of reference in adequate dimensionless form (see subsection 7.1.2). Third, one should provide the parameters of the monopolar fields (see subsection 7.1.3).

7.1.1 Choice of plane $\Pi_\perp$

In Blanco-Rodríguez et al. (2015), the centre line of the helical vortex of radius R ($R \equiv r_A$ in our notation) is a filament with imposed helical symmetry represented by a helix $\mathcal{S}$. The curve $\mathcal{S}$ is parametrized by the arc length s, such that in a general Cartesian frame, a point on $\mathcal{S}$ is located by $C(s) = (R\cos\theta, R\sin\theta, L\theta)$ with $\theta = s/\sqrt{R^2 + L^2}$. The Serret Frenet frame attached to $\mathcal{S}$ is defined by the tangent $\boldsymbol{t}$, the normal $\boldsymbol{n}$ and the bi-normal vector $\boldsymbol{b}$. The plane $(\boldsymbol{n}, \boldsymbol{b})$ generates the orthogonal plane $\Pi_\perp$ where a local polar coordinate system is constructed such that

$$\boldsymbol{e}_r = \boldsymbol{n}\cos\varphi + \boldsymbol{b}\sin\varphi, \tag{7.3}$$
$$\boldsymbol{e}_\varphi = -\boldsymbol{n}\sin\varphi + \boldsymbol{b}\cos\varphi. \tag{7.4}$$

With our notations this is equivalent to

$$\boldsymbol{e_\rho} = \boldsymbol{e_{r_A}}\cos(\psi) + \boldsymbol{e_{\varphi_A}}\sin(\psi) \tag{7.5}$$
$$\boldsymbol{e_\psi} = -\boldsymbol{e_{r_A}}\sin(\psi) + \boldsymbol{e_{\varphi_A}}\cos(\psi). \tag{7.6}$$

In this work, the origin of the local polar coordinate system (hence the vortex centre) is defined as the stagnation point of the velocity field in $\Pi_\perp$ such that:

$$\|\boldsymbol{v}_\perp(\rho,\psi)\| = \|u_\rho(\rho,\psi)\,\boldsymbol{e}_\rho + u_\psi(\rho,\psi)\,\boldsymbol{e}_\psi\| = 0 \text{ at the origin } \rho = 0. \tag{7.7}$$

Hence, the curve $\mathcal{S}$ crosses the plane Π_0 at a point A with coordinates (r_A, θ_A) such that (7.7) is satisfied. The location of point A is unknown and is found numerically with an iterative procedure. First, as initial guess value, one finds in Π_0, the position M_0 where

the helical vorticity ω_B reaches its maximum. Second, the plane $\Pi_\perp(M_0)$ normal to the local helical vector $\mathbf{e}_B(M_0)$ passing through this point M_0 is constructed. The velocity components u_ρ and u_ψ in (7.7) are computed in $\Pi_\perp(M_0)$ with the set of relations (5.17)-(5.18) derived in section 5.16. Third one determines the location of the point (ρ_0, ψ_0) in $\Pi_\perp(M_0)$ where the quantity $\|\boldsymbol{v}_\perp(\rho_0, \psi_0)\|$ (equation (7.7)) is minimum. The intersection of the helical line passing through this point, with local polar coordinate (ρ_0, ψ_0) in $\Pi_\perp(M_0)$, with the plane Π_0 defines the new stagnation point M_1.
At this stagnation point M_1, the local helical vector $\mathbf{e}_B(M_1)$ is oriented in a slightly different direction than $\mathbf{e}_B(M_0)$, so a new plane $\Pi_\perp(M_1)$ can be defined in which we can get another stagnation point M_2 by locating the position (ρ_1, ψ_1) in $\Pi_\perp(M_1)$ where (7.7) is minimum.
This operation is repeated until convergence (when $\|\boldsymbol{v}_\perp(0, \psi)\| < 10^{-11}$). In practice, around 100 iterations are necessary. At the end of the process, the stagnation point A (M_{st} with the notations of the paper) has been located, providing a helical centre line $\mathcal{S}$. The radial coordinate of A defines the value of R. The local frame is $(\boldsymbol{e_{r_A}}, \boldsymbol{e_{\varphi_A}}, \boldsymbol{e_{B_A}})$ which corresponds to the frame $(\boldsymbol{n}, \boldsymbol{b}, \boldsymbol{t})$ in the paper.

Velocity and vorticity fields can be easily expressed in the cylindrical coordinates attached to this plane and thereafter Fourier decomposed in the azimuthal direction using equations (5.25). This yields the monopolar, dipolar and quadripolar components needed for comparisons.

7.1.2 Expression of the theoretical velocity field in the rotating frame

In the laboratory frame (L), the vorticity field obtained by the D.N.S. has been shown (see chapter 6) to possess a structure close to that of the Batchelor vortex. This means that the monopolar component of the velocity in the laboratory frame (L) reads

$$\boldsymbol{V}^{(L)}_{\text{mono}} = \frac{\Gamma}{2\pi r}\left(1 - e^{-(\frac{r}{a})^2}\right)\mathbf{e}_\varphi + \hat{W}_0\, e^{-(\frac{r}{a})^2}\,\mathbf{e}_s + \hat{\boldsymbol{V}}_0$$

where $\hat{\boldsymbol{V}}_0$ is a constant velocity with a part $\hat{W}^{(L)}_{0_0}\mathbf{e}_s$ oriented along $\mathbf{e}_s$ and a part perpendicular to $\mathbf{e}_s$. In the rotating frame (Ro) in which the vortex is steady, the velocity reads

$$\begin{aligned}\boldsymbol{V}^{(Ro)} &= \boldsymbol{V}^{(L)}_{\text{mono}} - \hat{\Omega}_{frame}\,\mathbf{e}_z \times \rho\mathbf{e}_\rho \\ &= \boldsymbol{V}^{(L)}_{\text{mono}} - \hat{\Omega}_{frame}\,\mathbf{e}_z \times [\rho\mathbf{e}_\rho - R\mathbf{e}_\rho(M_{\text{st}})] - \hat{\Omega}_{frame}\,\mathbf{e}_z \times [R\mathbf{e}_\rho(M_{\text{st}})]\end{aligned}$$

or

$$\boldsymbol{V}^{(Ro)} = \boldsymbol{V}^{(L)}_{\text{mono}} - r\hat{\Omega}_{frame}\,\mathbf{e}_z \times \mathbf{e}_r - R\hat{\Omega}_{frame}\,\mathbf{e}_\phi(M_{\text{st}}).$$

Since

$$\mathbf{e}_z \times \mathbf{e}_r = -(\mathbf{e}_\varphi \cdot \mathbf{e_z})\mathbf{e}_s + (\mathbf{e_s} \cdot \mathbf{e_z})\mathbf{e}_\varphi = -\frac{1}{\sqrt{1+\alpha^2}}\cos\varphi\mathbf{e}_s + \frac{\alpha}{\sqrt{1+\alpha^2}}\mathbf{e}_\varphi\,,$$

one has

$$\boldsymbol{V}^{(Ro)} = \boldsymbol{V}^{(L)}_{\text{mono}} - r\hat{\Omega}_{frame}\frac{\alpha}{\sqrt{1+\alpha^2}}\mathbf{e}_\varphi + r\hat{\Omega}_{frame}\frac{1}{\sqrt{1+\alpha^2}}\cos\varphi\mathbf{e}_s - R\hat{\Omega}_{frame}\,\mathbf{e}_\phi(M_{\text{st}}).$$

Note that the component perpendicular to $\mathbf{e}_s$ for the term $-R\Omega_{frame}\,\mathbf{e}_\phi(M_{\text{st}})$ and the term $\hat{\boldsymbol{V}}_0$ cancel out by definition of the stagnation point. There remains only the term along $\mathbf{e}_s$ that is

$$-R\hat{\Omega}_{frame}\,\mathbf{e}_\phi(M_{\text{st}}) \cdot \mathbf{e_s} + \hat{\boldsymbol{V}}_0 \cdot \mathbf{e_s} = -R\hat{\Omega}_{frame}\,\frac{1}{\sqrt{1+\alpha^2}} + \hat{W}^{(L)}_{0_0} \equiv \hat{W}^{(Ro)}_{0_0}.$$

In the rotating frame (Ro), we thus assume a profile of the form

$$\begin{aligned} \boldsymbol{V}^{(Ro)} &= \left[\frac{\Gamma}{2\pi r}\left(1-e^{-(\frac{r}{a})^2}\right) - r\hat{\Omega}_{frame}\frac{\alpha}{\sqrt{1+\alpha^2}}\right]\mathbf{e}_\varphi \\ &\quad + \left[\hat{W}_{0_0}^{(Ro)} + \hat{W}_0\, e^{-(\frac{r}{a})^2} + r\hat{\Omega}_{frame}\frac{1}{\sqrt{1+\alpha^2}}\cos\varphi\right]\mathbf{e}_s\ . \end{aligned} \tag{7.8}$$

7.1.3 Getting the parameters of the monopolar contribution

We determine the values of parameters a, Γ, $\hat{W}_{0_0}^{(Ro)}$ and $\hat{W}_0$ present in equation (7.8) by fitting the monopolar component of the velocity obtained by D.N.S. Quantities a and $\Gamma/2\pi$ are then used to make velocity dimensionless as in the theory. For the monopolar component, this reads

$$\left[\frac{1}{r}\left(1-e^{-r^2}\right) - r\Omega_{frame}\frac{\alpha}{\sqrt{1+\alpha^2}}\right]\mathbf{e}_\varphi + [W_{0_0}^{(Ro)} + W_0\, e^{-r^2}]\,\mathbf{e}_s.$$

The parameter W_0 is identical in all reference frames. By contrast, the constant jet value W_{0_0} in the translation frame (T) is linked to $W_{0_0}^{(Ro)}$ by:

$$W_{0_0} = W_{0_0}^{(Ro)} - \frac{\sqrt{1+\alpha^2}}{\alpha}V_f\ .$$

This allows us to compute the two parameters W_0 and W_{0_0} necessitated by the asymptotic analysis, and to perform the comparison.

7.2 Paper: Internal structure of vortex rings and helical vortices

J. Fluid Mech. (2015), *vol.* 785, *pp.* 219–247. © Cambridge University Press 2015
doi:10.1017/jfm.2015.631

Internal structure of vortex rings and helical vortices

Francisco J. Blanco-Rodríguez[1], **Stéphane Le Dizès**[1,†], **Can Selçuk**[2,3], **Ivan Delbende**[2,3] **and Maurice Rossi**[4,5]

[1]Aix Marseille Université, CNRS, Centrale Marseille, IRPHE, UMR 7342, 13384 Marseille, France

[2]LIMSI, CNRS, Université Paris-Saclay, 91405 Orsay CEDEX, France

[3]Sorbonne Universités, UPMC Univ Paris 06, UFR d'Ingénierie, 75252 Paris CEDEX 05, France

[4]Sorbonne Universités, UPMC Univ Paris 06, UMR 7190, Institut Jean Le Rond d'Alembert, 75005, Paris, France

[5]CNRS, UMR 7190, Institut Jean Le Rond d'Alembert, 75005, Paris, France

(Received 10 April 2015; revised 10 August 2015; accepted 22 October 2015)

The internal structure of vortex rings and helical vortices is studied using asymptotic analysis and numerical simulations in cases where the core size of the vortex is small compared to its radius of curvature, or to the distance to other vortices. Several configurations are considered: a single vortex ring, an array of equally-spaced rings, a single helix and a regular array of helices. For such cases, the internal structure is assumed to be at leading order an axisymmetric concentrated vortex with an internal jet. A dipolar correction arises at first order and is shown to be the same for all cases, depending only on the local vortex curvature. A quadrupolar correction arises at second order. It is composed of two contributions, one associated with local curvature and another one arising from a non-local external 2-D strain field. This strain field itself is obtained by performing an asymptotic matching of the local internal solution with the external solution obtained from the Biot–Savart law. Only the amplitude of this strain field varies from one case to another. These asymptotic results are thereafter confronted with flow solutions obtained by direct numerical simulation (DNS) of the Navier–Stokes equations. Two different codes are used: for vortex rings, the simulations are performed in the axisymmetric framework; for helices, simulations are run using a dedicated code with built-in helical symmetry. Quantitative agreement is obtained. How these results can be used to theoretically predict the occurrence of both the elliptic instability and the curvature instability is finally addressed.

Key words: vortex flows, vortex interactions

1. Introduction

Most vortices observed in nature are curved and interact with nearby vortices. Although they can often be considered locally as axisymmetric (with possibly a jet component), their internal structure is actually azimuthally deformed by local

---

[†] Email address for correspondence: ledizes@irphe.univ-mrs.fr

effects (curvature, torsion) and non-local effects (remote vorticity). These azimuthal corrections are known to be the source of short-wavelength instabilities. The description of these corrections is therefore an important necessary step for the understanding and modelling of these instabilities. In this work, the first dipolar and quadrupolar corrections to a prescribed monopolar structure are computed for a single vortex ring, an array of rings, a helical vortex and an array of helices using two methods: an asymptotic analysis in the limit of small core size and dedicated numerical simulations.

Vortex rings are simple invariant vortical states that have been studied for more than a hundred years. In an inviscid framework, vortex rings are expected to propagate at a constant speed without changing their form. Many works have aimed at determining the ring propagation speed when the ring core size is small compared to its radius (see Saffman 1992). In this limit, the most recent work is by Fukumoto & Moffatt (2000) who also includes viscous effects and computes the internal structure of a vortex ring up to third order. This analysis clearly shows that dipolar corrections are generated at first order, while quadrupolar corrections only appear at second order. The link between dipolar corrections and local curvature has been known for a long time (Ting & Tung 1965; Widnall, Bliss & Zalay 1971; Moore & Saffman 1972). In a general setting, Callegari & Ting (1978) showed how dipolar corrections depend on the local vortex curvature. These results were extended by Fukumoto & Miyazaki (1991) to account for an axial jet component within the vortex. In the present study, these asymptotic predictions are retrieved and compared for the first time to numerical simulations of finite core size vortices.

Helical vortices are more complicated than rings; in addition to their translation motion they also rotate. Many works are devoted to the rotation and translation speeds of such invariant structures (Moore & Saffman 1972; Widnall 1972; Ricca 1994; Kuibin & Okulov 1998; Boersma & Wood 1999). In particular Kuibin & Okulov (1998) and Boersma & Wood (1999) used the expression of the velocity field in terms of Kapteyn series derived by Hardin (1982) for helical filaments. These results were further extended for multiple helices by Okulov (2004) and to higher-order corrections by Fukumoto & Okulov (2005). The effect of torsion is not present in the rings. It was first characterized by Ricca (1994) for helices. Torsion also generates a dipolar correction, as does curvature, but this effect is weaker since it is of second order (see Fukumoto & Okulov 2005). Quadrupolar corrections responsible for the elliptic deformation of the inner core are also expected at second order (see for instance Fukumoto & Moffatt 2000). Such corrections are known to be generated when a vortex is subjected to an external strain field (Moffatt, Kida & Ohkitani 1994), or is exposed to the influence of other vortices (see Le Dizès & Verga 2002) or to distant parts of the same vortex, as for a ring. This quadrupolar correction has been fully computed for a single vortex ring (without jet) by Fukumoto & Moffatt (2000). In the present work, this correction is also provided for an array of rings, a single helix and an array of helices. The effect of axial jet within the vortex core is also analysed.

These asymptotic results are then compared with numerical results obtained by DNS. For rings, the spectral DNS code developed by Bolnot (2012) is used, in which axisymmetry is enforced as well as axial periodicity, allowing short-wavelength instabilities (Widnall, Bliss & Tsai 1974; Hattori & Fukumoto 2003) and the pairing instability (Levy & Forsdyke 1927; Bolnot, Le Dizès & Leweke 2014) to be filtered out. For helical vortices, the DNS code developed by Delbende, Rossi & Daube (2012*a*) and restricted to the simulation of helically symmetrical flows is used.

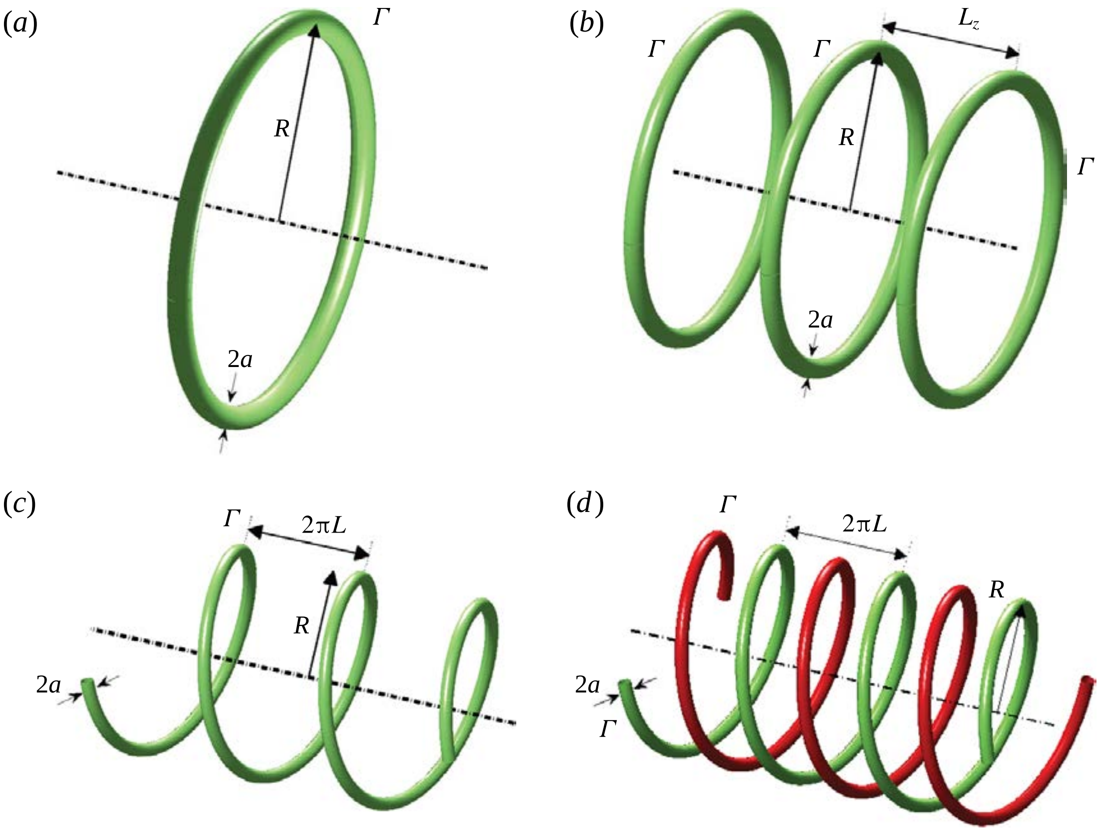

FIGURE 1. (Colour online) Vortex configurations studied in the present paper: (*a*) vortex ring, (*b*) array of rings, (*c*) helical vortex, (*d*) N helical vortices (here plotted for $N = 2$).

The paper is organized as follows. In § 2, the framework of the analysis is presented. The configurations under study are introduced, as well as the different parameters and the local reference frame in which the internal structure of the vortex is analysed. The asymptotic analysis of the inner structure is performed in § 3. Both the leading-order dipolar correction and quadrupolar corrections are obtained. The quadrupolar contribution is shown to depend on a single constant, which varies from one configuration to another. This constant is related to the external strain field experienced locally by the vortex and is computed in § 4 for each configuration. In § 5, asymptotic results are compared to DNS results. Section 6 provides a summary of the main results and a discussion of their implications concerning short-wavelength instabilities.

2. Presentation of the framework

Four vortex configurations are considered, where the vorticity field (longitudinal and transverse) is confined in a region of radius a around the curve $\mathscr{S}$, as illustrated in figure 1. Depending on the configuration, the curve $\mathscr{S}$ is

(i) a circle of radius R (figure 1*a*);
(ii) an infinite array of circles of radius R separated by a distance L_z (figure 1*b*);
(iii) an helix of radius R and pitch L (figure 1*c*);
(iv) a regular array of N helices of radius R and pitch L (figure 1*d*).

Such a curve $\mathscr{S}$ possesses a symmetry axis called the Oz axis and is parametrized by the arc length s. This means that in a global Cartesian frame, the point $C(s)$ is given by $C(s)=(R\cos\phi, R\sin\phi, L\phi)$ with $\phi=s/\sqrt{R^2+L^2}$ (for rings, L is taken to be zero). In this Cartesian frame, the Serret–Frenet frame can be expressed as

$$\boldsymbol{t}\equiv\frac{\dfrac{\mathrm{d}C}{\mathrm{d}s}}{\left|\dfrac{\mathrm{d}C}{\mathrm{d}s}\right|}=\frac{R(-\boldsymbol{e}_x\sin\phi+\boldsymbol{e}_y\cos\phi)+L\boldsymbol{e}_z}{\sqrt{R^2+L^2}}, \tag{2.1a}$$

$$\boldsymbol{n}\equiv\frac{\mathrm{d}\boldsymbol{t}}{\mathrm{d}s}=-(\boldsymbol{e}_x\cos\phi+\boldsymbol{e}_y\sin\phi), \tag{2.1b}$$

$$\boldsymbol{b}\equiv\boldsymbol{t}\times\boldsymbol{n}=\frac{R\boldsymbol{e}_z+L(\boldsymbol{e}_x\sin\phi-\boldsymbol{e}_y\cos\phi)}{\sqrt{R^2+L^2}}. \tag{2.1c}$$

Note that the curvature κ and torsion τ of this curve are given by

$$\kappa=\frac{R}{R^2+L^2}, \quad \tau=\frac{L}{R^2+L^2}. \tag{2.2a,b}$$

The vorticity field is assumed to be uniform along the curve $\mathscr{S}$, with a constant longitudinal circulation Γ. The vorticity field is also assumed to possess a transverse component associated with a localized jet along $\mathscr{S}$. This will be further defined below. The radius a is assumed to be small compared to the other length scales i.e. R and L_z for rings, and R and L/N for helices. In this context, we are studying the internal structure within the region of radius a around $\mathscr{S}$. It is therefore useful to define a local frame centred on a point $C(s)$ of $\mathscr{S}$. Following Callegari & Ting (1978), we introduce the local polar frame

$$\boldsymbol{e}_r=\boldsymbol{n}\cos\varphi+\boldsymbol{b}\sin\varphi, \tag{2.3a}$$

$$\boldsymbol{e}_\varphi=-\boldsymbol{n}\sin\varphi+\boldsymbol{b}\cos\varphi, \tag{2.3b}$$

$$\boldsymbol{e}_s=\boldsymbol{t}, \tag{2.3c}$$

associated with the local coordinate system (r, φ, s). The coordinate system is illustrated in figure 2 for ring and helix configurations. This non-orthogonal coordinate system is related to an orthogonal coordinate system (r, θ, s) where

$$\theta=\varphi+\theta_0(s), \quad \text{with } \frac{\partial\theta_0}{\partial s}=\tau, \tag{2.4}$$

which can be used to derive the governing equations in the local frame (see Callegari & Ting 1978, for details). In the following, the velocity vector field will be written $\boldsymbol{V}=v_\rho\boldsymbol{e}_\rho+v_\phi\boldsymbol{e}_\phi+v_z\boldsymbol{e}_z$ in the global cylindrical frame and $\boldsymbol{V}=u\boldsymbol{e}_r+v\boldsymbol{e}_\varphi+w\boldsymbol{e}_s$ in the local polar frame. The formulae that connect one representation to the other are provided in appendix A.

In the local frame, the vortex structure is assumed, at leading order, to be a columnar axisymmetrical vortex, independent of s and φ. Our goal is to determine the corrections to this axisymmetrical structure induced by the curvature and torsion of vortex lines, and the presence of distant vortices or vortical parts of the same vortex.

We introduce the following parameters

$$\varepsilon=\frac{Ra}{R^2+L^2}=\kappa a, \quad \alpha=\frac{L}{R}=\frac{\tau}{\kappa}, \quad \lambda=\frac{L_z}{R}. \tag{2.5a–c}$$

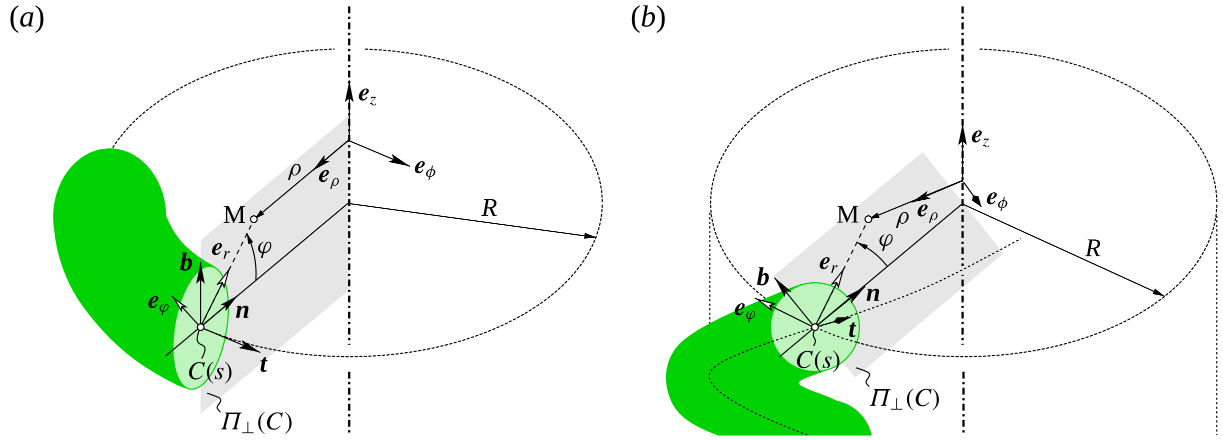

FIGURE 2. (Colour online) Illustration of the coordinate system for a ring (*a*) and a helix (*b*). The point M can be localized using the global cylindrical frame $(\boldsymbol{e}_\rho, \boldsymbol{e}_\phi, \boldsymbol{e}_z)$, or the local frames: the Serret–Frenet frame $(\boldsymbol{n}, \boldsymbol{b}, \boldsymbol{t})$ and the frame $(\boldsymbol{e}_r, \boldsymbol{e}_\varphi, \boldsymbol{t})$. Note that vectors $\boldsymbol{e}_r$ and $\boldsymbol{e}_\varphi$ are in the plane $(\boldsymbol{n}, \boldsymbol{b})$. Point $C(s)$ is defined as the point on the curve $\mathscr{S}$ which is the closest to point M.

The asymptotic analysis is performed in the limit $a \ll R$ and $a \ll L_z$ for rings, and $a \ll R$ and $a \ll L$ for helical vortices. The parameter ε is thus assumed to be small, whereas the parameters α and λ are $O(1)$. In the present study, we do not consider compressible and buoyancy effects and assume that the density is uniform and constant. Viscous effects are also neglected by assuming that the Reynolds number Γ/ν (ν is the kinematic viscosity) is sufficiently large. This hypothesis means that we consider vortex structures on time scales which are short compared to the viscous diffusion time scale a^2/ν. This allows us to consider vortical structures that translate and rotate steadily without changing their shapes. Here, we shall assume that there exists a frame translating at the velocity $V_{frame}\boldsymbol{e}_z$ where the solution is steady.

The computation of the displacement speed of helical vortices or rings has been the subject of numerous works (see for instance Saffman (1992) for rings and Alekseenko, Kuibin & Okulov (2007) for helices). In each case, there is a dominant local velocity contribution which is proportional to $-\varepsilon\,\log(\varepsilon)$ and oriented along the binormal vector $\boldsymbol{b}$, as predicted by the local induction approximation (Saffman 1992). This local contribution is corrected by $O(\varepsilon)$ non-local effects associated with distant vortex parts or other vortices. In all cases, the vortex structure displacement speed remains asymptotically small. The frame velocity V_{frame} is related to the vortex structure displacement speed in the manner illustrated in figure 3. For rings, the binormal vector is aligned along with the vertical axis, so the frame velocity correspond to the displacement speed $\boldsymbol{V}_{ring} = V_{ring}\boldsymbol{b} = V_{frame}\boldsymbol{e}_z$. For helices, the displacement speed can be decomposed as $\boldsymbol{V}_{helix} = V_{helix}\boldsymbol{b} = V_{frame}\boldsymbol{e}_z + W_{0_0}\boldsymbol{t}$, where $V_{frame} = \sqrt{1+\alpha^2}V_{helix}$ and $W_{0_0} = -\alpha V_{helix}$ because $\boldsymbol{e}_z \boldsymbol{\cdot} \boldsymbol{b} = 1/\sqrt{1+\alpha^2}$ and $\boldsymbol{e}_z \boldsymbol{\cdot} \boldsymbol{t} = \alpha/\sqrt{1+\alpha^2}$. The component W_{0_0} represents a uniform jet contribution along the vortex axis. It is only present in helices. Though small, we shall take this effect into account in our analysis.

In the uniformly translating frame, the solution satisfies the steady Euler equations. If, in the local frame, the velocity field (u, v, w) and pressure p are assumed to be independent of s, the steady Euler equations become (Callegari & Ting 1978)

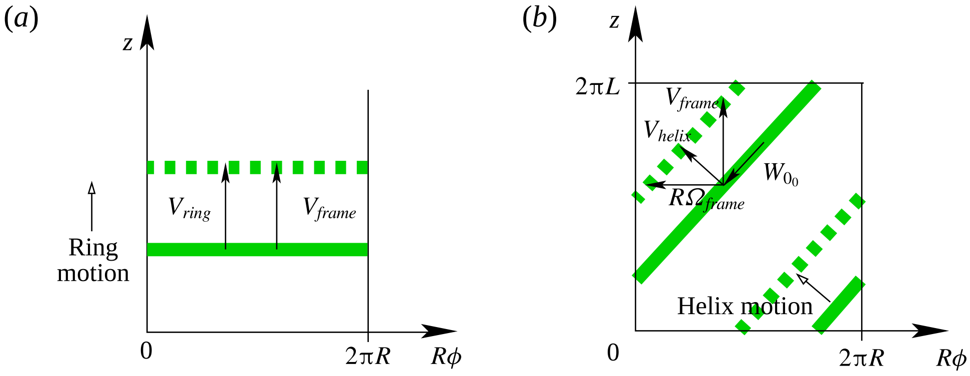

FIGURE 3. (Colour online) Definition of V_{frame} for a ring (*a*) and of a helix (*b*). The velocities $V_{frame}\boldsymbol{e}_z$ and $R\Omega_{frame}\boldsymbol{e}_\phi$ are such that their projection on the binormal vector $\boldsymbol{b}$ is equal to vortex structure displacement speed.

$$\frac{\varepsilon(-\alpha u_\varphi + w\cos\varphi)w}{h} + uu_r + \frac{v(u_\varphi - v)}{r} + p_r = 0, \tag{2.6a}$$

$$\frac{\varepsilon(-\alpha v_\varphi - w\sin\varphi)w}{h} + uv_r + \frac{v(v_\varphi + u)}{r} + \frac{p_\varphi}{r} = 0, \tag{2.6b}$$

$$\frac{\varepsilon[(-\alpha w_\varphi - (u\cos\varphi - v\sin\varphi))w - \alpha p_\varphi]}{h} + uw_r + \frac{vw_\varphi}{r} = 0, \tag{2.6c}$$

$$\frac{\varepsilon[-\alpha w_\varphi - (u\cos\varphi - v\sin\varphi)]}{h} + \left[u_r + \frac{u}{r} + \frac{v_\varphi}{r}\right] = 0, \tag{2.6d}$$

with $h = 1 - \varepsilon r\cos\varphi$. Note that, in the text, v_ρ, v_ϕ and v_z indicate the components in the global cylindrical frame, whereas the subscript indices for other variables such as the local components u, v, w refer to derivatives (e.g. $u_\varphi = \partial u/\partial\varphi$).

3. Internal vortex structure

In this section, we calculate the main dipolar and quadrupolar corrections to the local columnar axisymmetrical vortex. The velocity and pressure fields are expanded in powers of ε

$$u = \qquad + \varepsilon u^{(1)}(r,\varphi) + \varepsilon^2 u^{(2)}(r,\varphi) + \cdots, \tag{3.1a}$$

$$v = v^{(0)}(r) + \varepsilon v^{(1)}(r,\varphi) + \varepsilon^2 v^{(2)}(r,\varphi) + \cdots, \tag{3.1b}$$

$$w = w^{(0)}(r) + \varepsilon w^{(1)}(r,\varphi) + \varepsilon^2 w^{(2)}(r,\varphi) + \cdots, \tag{3.1c}$$

$$p = p^{(0)}(r) + \varepsilon p^{(1)}(r,\varphi) + \varepsilon^2 p^{(2)}(r,\varphi) + \cdots. \tag{3.1d}$$

3.1. *Monopolar structure*

At leading order, the solution is a straight vortex of azimuthal velocity $v^{(0)}(r)$ and axial velocity $w^{(0)}(r)$. The pressure $p^{(0)}$ is related to $v^{(0)}$ by

$$p^{(0)}(r) = \int_0^r \frac{[v^{(0)}(\eta)]^2}{\eta}\,\mathrm{d}\eta. \tag{3.2}$$

The longitudinal (axial) and transverse (azimuthal) distributions of vorticity are defined respectively from $v^{(0)}$ and $w^{(0)}$ by the following expressions

$$\zeta^{(0)} = \frac{1}{r}\frac{\partial}{\partial r}(rv^{(0)}), \tag{3.3a}$$

$$\Upsilon^{(0)} = -\frac{\partial w^{(0)}}{\partial r}. \tag{3.3b}$$

The asymptotic analysis can be performed for any axisymmetrical vortex with jet but for computations and numerical comparisons we use the Batchelor family of profiles

$$v^{(0)}(r) = \frac{1}{r}(1 - \mathrm{e}^{-r^2}), \tag{3.4a}$$

$$w^{(0)}(r) = W_0\mathrm{e}^{-r^2} + W_{0_0}. \tag{3.4b}$$

This vortex model is often used because it corresponds to profiles of fully viscous self-similar solutions; viscosity is then expected to modify the core size and the jet strength but not the profiles. In expressions (3.4*a*,*b*), the velocity is made dimensionless using the vortex core size, a, as a characteristic length and $\Gamma/(2\pi a)$ as characteristic velocity. The constant W_0 characterizes the jet strength and the constant W_{0_0} corresponds to a uniform flow component along the vortex axis. As explained above, such a component is present in helices. It is created by the change of reference frame, because the frame velocity does not correspond to the direction of propagation of the helix (see figure 3). If we take into account only this effect, it is related to the speed V_{frame} of the comoving frame by

$$W_{0_0} = -\frac{\alpha V_{frame}}{\sqrt{1+\alpha^2}}. \tag{3.5}$$

This term is null for vortex rings ($\alpha = 0$), and is $O(\varepsilon \log \varepsilon)$ for helices. Although this term is a higher-order term, it is convenient to introduce it here. We shall see below that it improves the predictions of the axial flow component.

3.2. *Dipolar correction*

The problem at first order provides the main dipolar correction to the axisymmetric vortex. This problem was first solved in a general setting by Callegari & Ting (1978). They showed that the first order corrections satisfy the system

$$\frac{v^{(0)}}{r}(u^{(1)}_{\varphi} - 2v^{(1)}) + p^{(1)}_r = -[w^{(0)}]^2 \cos\varphi, \tag{3.6a}$$

$$ru^{(1)}v^{(0)}_r + v^{(0)}(v^{(1)}_{\varphi} + u^{(1)}) + p^{(1)}_{\varphi} = r[w^{(0)}]^2 \sin\varphi, \tag{3.6b}$$

$$u^{(1)}w^{(0)}_r + \frac{v^{(0)}}{r}w^{(1)}_{\varphi} = -[w^{(0)}v^{(0)}]\sin\varphi, \tag{3.6c}$$

$$\frac{1}{r}(ru^{(1)})_r + \frac{1}{r}v^{(1)}_{\varphi} = -v^{(0)}\sin\varphi. \tag{3.6d}$$

This system possesses a solution of the form

$$u^{(1)} = \hat{u}^{(1)}(r)\sin\varphi = -\frac{\hat{\psi}^{(1)}}{r}\sin\varphi, \tag{3.7a}$$

$$v^{(1)} = \hat{v}^{(1)}(r)\cos\varphi = (-\hat{\psi}^{(1)}_r + rv^{(0)})\cos\varphi, \tag{3.7b}$$

$$w^{(1)} = \hat{w}^{(1)}(r)\cos\varphi = \left(-\frac{w_r^{(0)}}{v^{(0)}}\hat{\psi}^{(1)} + rw^{(0)}\right)\cos\varphi, \tag{3.7c}$$

$$p^{(1)} = \hat{p}^{(1)}(r)\cos\varphi = (-\zeta^{(0)}\hat{\psi}^{(1)} + v^{(0)}\hat{\psi}_r^{(1)} - r[v^{(0)}]^2 - r[w^{(0)}]^2)\cos\varphi, \tag{3.7d}$$

where the streamfunction amplitude $\hat{\psi}^{(1)}(r)$ satisfies

$$\mathscr{L}^{(1)}(\hat{\psi}^{(1)}) = 2r\zeta^{(0)} + v^{(0)} + 2r\frac{w^{(0)}w_r^{(0)}}{v^{(0)}}, \tag{3.8}$$

with the operator $\mathscr{L}^{(k)}$ for $k = 1, 2, \ldots$ defined as

$$\mathscr{L}^{(k)} \equiv \left[\frac{\partial^2}{\partial r^2} + \frac{1}{r}\frac{\partial}{\partial r} - \left(\frac{k^2}{r^2} + \frac{\zeta_r^{(0)}}{v^{(0)}}\right)\right]. \tag{3.9}$$

Using the method of variation of constants, (3.8) can be integrated in closed form as it possesses $v^{(0)}$ as an exact homogeneous solution. If the centre of the local frame is chosen such that the velocity in the $(\boldsymbol{n}, \boldsymbol{b})$ plane vanishes at the origin (up to $O(\varepsilon^2)$), $\hat{\psi}_r^{(1)}(0) = 0$ and $\hat{\psi}^{(1)}(0) = 0$ must be imposed, hence

$$\hat{\psi}^{(1)}(r) = v^{(0)}(r)\int_0^r \frac{\displaystyle\int_0^z v^{(0)}(\eta)\left[2\eta\zeta^{(0)}(\eta) + v^{(0)}(\eta) + 2\eta\frac{w^{(0)}(\eta)w_r^{(0)}(\eta)}{v^{(0)}(\eta)}\right]\eta\,\mathrm{d}\eta}{z[v^{(0)}(z)]^2}\,\mathrm{d}z. \tag{3.10}$$

As explained in Fukumoto & Moffatt (2000), adding a homogeneous solution $c_1 v^{(0)}$ to $\hat{\psi}^{(1)}$ corresponds to a change of frame centre. In the present work, the frame centre has been selected as the stagnation point of the flow, and this corresponds to $c_1 = 0$. As soon as the frame centre is fixed, there are no free parameters: streamfunction, velocity and pressure are given at first order by (3.7*a–d*) and (3.10).

The first-order correction is thus a pure dipolar correction which depends on the local curvature only. This correction is thus identical for a ring, an array of rings, a helix and an array of N helices. It is easy to show that $\hat{\psi}^{(1)}$ expands for large r (Fukumoto & Miyazaki 1991) as follows

$$\hat{\psi}^{(1)} \sim \frac{1}{2}r\log r + rA + O\left(\frac{1}{r}\right), \tag{3.11}$$

with

$$\begin{aligned} A &= \frac{1}{2}\lim_{r\to\infty}\left(\int_0^r \eta(v^{(0)}(\eta))^2\,\mathrm{d}\eta - \log r\right) + \frac{1}{4} - \int_0^\infty \eta((w^{(0)}(\eta))^2 - W_{0_0}^2)\,\mathrm{d}\eta \\ &= \frac{1}{4}(1 - W_0(W_0 + 2W_{0_0}) + \gamma - \log 2) \end{aligned} \tag{3.12}$$

and $\gamma \approx 0.577$ being Euler's constant. As $W_0 W_{0_0}$ is always small, we shall use the approximation $A \approx 0.22 - W_0^2/4$. In figure 4, the streamfunction, $\hat{\psi}^{(1)}/r$ is plotted together with its asymptotic behaviour for the Batchelor vortex for two jet parameters ($W_0 = 0$, $W_0 = 1$) and $W_{0_0} = 0$. When $W_0 = 0$, the dipolar component of the axial velocity follows the simple linear expression $\hat{w}^{(1)}(r) = rW_{0_0}$.

As shown by Fukumoto & Okulov (2005), dipolar corrections are modified by torsion at second order. Thus, rings and helices generate a different dipolar correction only if we consider higher-order terms.

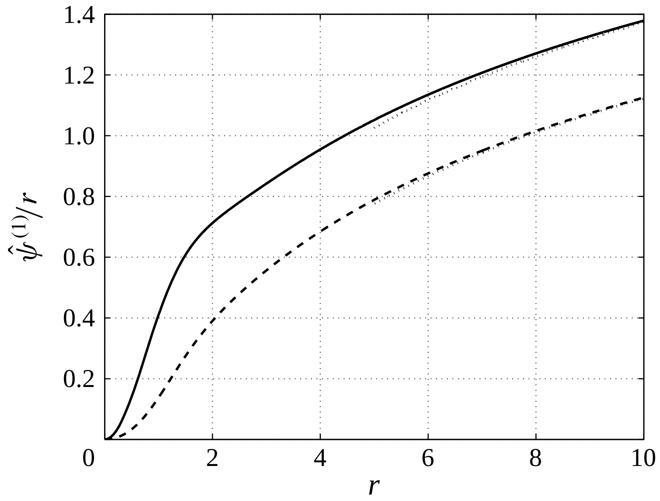

FIGURE 4. Characteristics of the dipolar correction for the Batchelor vortex. $\hat{\psi}^{(1)}/r$ versus r (solid line: $W_0 = 0$; dashed line: $W_0 = 1$. $W_{0_0} = 0$ for both cases) The dotted lines correspond to the asymptotic behaviour (3.11).

3.3. *Quadrupolar correction*

Quadrupolar corrections do not appear at first order but they are generated at second order. At second order, dipolar and monopolar corrections are also generated but we focus here on quadrupolar corrections, as monopolar and dipolar fields were already obtained at lower order. The perturbation equations for the second-order corrections are given by

$$\begin{aligned}\frac{v^{(0)}}{r}(u^{(2)}_{\varphi} - 2v^{(2)}) + p^{(2)}_{r} &= \left[\frac{v^{(1)}}{r}(v^{(1)} - u^{(1)}_{\varphi}) - u^{(1)}u^{(1)}_{r}\right] \\ &\quad - w^{(0)}(2w^{(1)}\cos\varphi + w^{(0)} r\cos^{2}\varphi),\end{aligned} \tag{3.13a}$$

$$\begin{aligned}ru^{(2)}v^{(0)}_{r} + v^{(0)}(v^{(2)}_{\varphi} + u^{(2)}) + p^{(2)}_{\varphi} &= -[ru^{(1)}v^{(1)}_{r} + v^{(1)}(v^{(1)}_{\varphi} + u^{(1)})] \\ &\quad + rw^{(0)}(2w^{(1)}\sin\varphi + w^{(0)} r\cos\varphi\sin\varphi),\end{aligned} \tag{3.13b}$$

$$\begin{aligned}u^{(2)}w^{(0)}_{r} + \frac{v^{(0)}}{r}w^{(2)}_{\varphi} &= -\left[u^{(1)}w^{(1)}_{r} + \frac{v^{(1)}}{r}w^{(1)}_{\varphi}\right] - v^{(0)}w^{(1)}\sin\varphi \\ &\quad + w^{(0)}(u^{(1)}\cos\varphi - v^{(1)}\sin\varphi - rv^{(0)}\cos\varphi\sin\varphi),\end{aligned} \tag{3.13c}$$

$$\frac{1}{r}(ru^{(2)})_{r} + \frac{1}{r}v^{(2)}_{\varphi} = u^{(1)}\cos\varphi - v^{(1)}\sin\varphi - rv^{(0)}\cos\varphi\sin\varphi. \tag{3.13d}$$

The quadrupolar field satisfying these equations is found to be of the form

$$u^{(2)}_{quad} = \hat{u}^{(2)}(r)\sin 2\varphi = -\frac{2}{r}\hat{\psi}^{(2)}\sin 2\varphi, \tag{3.14a}$$

$$v^{(2)}_{quad} = \hat{v}^{(2)}(r)\cos 2\varphi = (-\hat{\psi}^{(2)}_{r} + V_F)\cos 2\varphi, \tag{3.14b}$$

$$w^{(2)}_{quad} = \hat{w}^{(2)}(r)\cos 2\varphi = \left(-\frac{w^{(0)}_{r}}{v^{(0)}}\hat{\psi}^{(2)} + W_F\right)\cos 2\varphi, \tag{3.14c}$$

$$p^{(2)}_{quad} = \hat{p}^{(2)}(r)\cos 2\varphi = (-\zeta^{(0)}\hat{\psi}^{(2)} + v^{(0)}\hat{\psi}^{(2)}_{r} + P_F)\cos 2\varphi, \tag{3.14d}$$

with

$$V_F = \frac{r^2}{4}(\hat{u}_r^{(1)} + 2v^{(0)}), \tag{3.15a}$$

$$W_F = \frac{r}{4v^{(0)}}\left[-\frac{\hat{w}^{(1)}\hat{v}^{(1)}}{r} + \hat{w}_r^{(1)}\hat{u}^{(1)} + v^{(0)}(\hat{w}^{(1)} + rw^{(0)}) + w^{(0)}(\hat{v}^{(1)} - \hat{u}^{(1)})\right], \tag{3.15b}$$

$$P_F = \frac{r}{4}\hat{u}^{(1)}\hat{v}_r^{(1)} - \frac{\hat{v}^{(1)}}{4}(\hat{v}^{(1)} - \hat{u}^{(1)}) - \frac{r}{2}w^{(0)}\left(\hat{w}^{(1)} + \frac{r}{2}w^{(0)}\right) - v^{(0)}V_F. \tag{3.15c}$$

The streamfunction amplitude $\hat{\psi}^{(2)}$ satisfies

$$\mathscr{L}^{(2)}(\hat{\psi}^{(2)}) = \mathscr{F}, \tag{3.16}$$

with

$$\mathscr{F} = \frac{3rv^{(0)}}{4} - \frac{r\hat{\psi}^{(1)}\zeta_r^{(0)}}{v^{(0)}} - \frac{(\hat{\psi}^{(1)})^2}{4v^{(0)}}\left(\frac{\zeta_r^{(0)}}{v^{(0)}}\right)_r + \frac{r\hat{\psi}^{(1)}}{[v^{(0)}]^2}\left[\frac{w^{(0)}w_r^{(0)}v_r^{(0)}}{v^{(0)}} - (w^{(0)}w_r^{(0)})_r\right]. \tag{3.17}$$

The general solution to (3.16) which is finite at the origin, can be written as

$$\hat{\psi}^{(2)} = S\Psi^{(2)}(r) + \Psi_{NH}^{(2)}(r), \tag{3.18}$$

where $\Psi^{(2)}$ denotes the homogeneous function such that

$$\mathscr{L}^{(2)}(\Psi^{(2)}) = 0, \quad \Psi^{(2)} \underset{r\to 0}{\sim} s_0 r^2, \quad \Psi^{(2)} \underset{r\to+\infty}{\sim} r^2, \tag{3.19a-c}$$

and $\Psi_{NH}^{(2)}$ denotes a particular solution to the non-homogeneous problem (3.16). Finally, S is an arbitrary constant.

It is worth mentioning that another homogeneous solution of (3.13*a–d*) corresponding to a radial velocity proportional to $(2/r)\Psi^{(2)}(r)\cos 2\varphi$ could have been added in principle in (3.14*a*). This solution turns out not to be present for rings and helices, as will be seen in the expressions of the outer solution given in the next section.

The function $\Psi^{(2)}$ describes how a strain field is transmitted within a vortex. It was first introduced by Moffatt *et al.* (1994) for the asymptotic analysis of a vortex in a strain field. Eloy & Le Dizès (1999) showed that $s_0 \approx 2.525$ for a Gaussian vorticity profile. Function $\Psi_{NH}^{(2)}$ (and consequently $\hat{\psi}^{(2)}$) is expected to behave as $3/16r^2\log r$ for large r (see figure 5) because $\mathscr{F} \sim 3/4$ as $r \to +\infty$. Using the method of variation of constants and the fact that $\Psi^{(2)}$ is an exact solution of the homogeneous problem, $\Psi_{NH}^{(2)}$ is given by

$$\Psi_{NH}^{(2)} = \Psi^{(2)}(r)\left[\frac{3}{16}\log r - \int_r^{+\infty}\left(\frac{\displaystyle\int_0^s \eta\mathscr{F}(\eta)\Psi^{(2)}(\eta)\,\mathrm{d}\eta}{s[\Psi^{(2)}]^2} - \frac{3}{16s}\right)\mathrm{d}s\right]. \tag{3.20}$$

The strain rate $S_{NH}^{(2)} = \lim_{r\to 0}\Psi_{NH}^{(2)}/r^2$, which is associated with local curvature effects (it is not present for straight vortices (see, for instance, Le Dizès & Verga 2002)), strongly varies with respect to the jet parameter W_0 (see figure 6). Finally, the function $\Psi^{(2)}$ only depends on $v^{(0)}$ and the function $\Psi_{NH}^{(2)}$ only on $v^{(0)}$ and $w^{(0)}$, that is, they

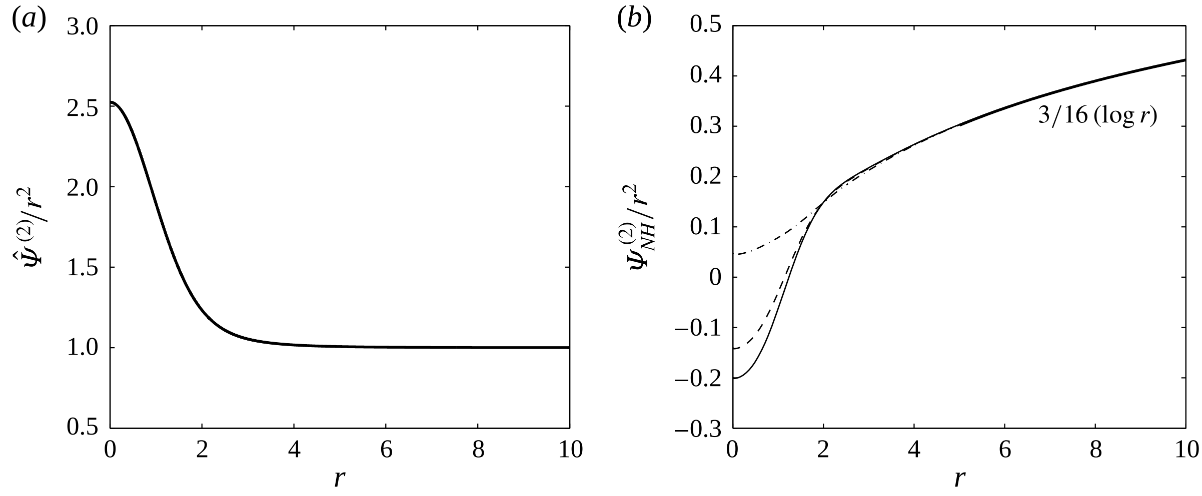

FIGURE 5. Characteristics of the quadrupolar correction for a Batchelor vortex. (*a*) $\Psi^{(2)}/r^2$ versus r; (*b*) $\Psi_{NH}^{(2)}/r^2$ versus r (solid line: $W_0 = 0$, dashed line: $W_0 = 0.4$, dash-dot line: $W_0 = 1$). For all cases, $W_{0_0} = 0$.

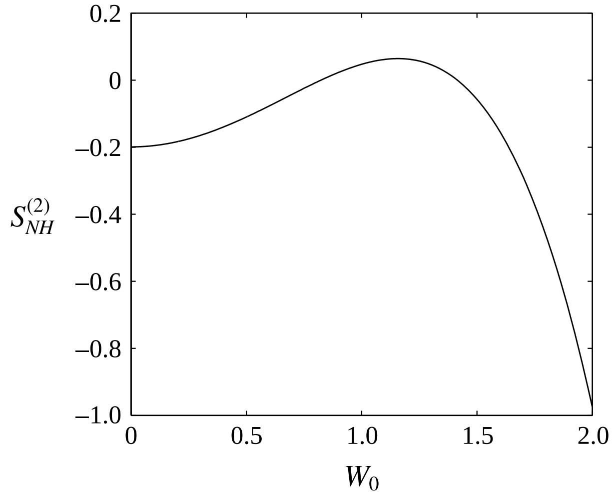

FIGURE 6. Variation of $S_{NH}^{(2)}$ with respect to W_0 for $W_{0_0} = 0$.

only depend on the local properties of the underlying axisymmetrical vortex. These two functions are plotted in figure 5 for the Batchelor vortex for three values of the jet parameter.

The constant S is not determined from the above inner analysis but from matching with an outer solution. It is hence expected to be different for each case; S is actually related to the external strain field experienced by the vortex (see the following section). Contrary to the dipolar correction, the quadrupolar correction is dependent on non-local effects. Yet this dependence comes about through a single constant! Near the origin, the function $\hat{\psi}^{(2)}$ represents a pure strain field

$$\hat{\psi}^{(2)} \sim S^{(2)} r^2, \tag{3.21}$$

where $S^{(2)} = s_0 S + S_{NH}^{(2)}$. The principal directions of this strain field are $\varphi = \pm\pi/4$.

The choice of the frame centre selected at first order does not affect the constant S, but has an impact on the forcing term $\mathscr{F}$, and thus on the function $\Psi_{NH}^{(2)}$. When

$W_0 = 0$, the axial flow component is particularly simple $\hat{w}^{(2)} = r^2 W_{0_0}/2$ and the other velocity components become independent of W_{0_0}.

4. External strain field

The constant S depends on the strain field induced by the background flow. It comes about through an asymptotic matching of the inner solution previously obtained with the outer solution obtained by the Biot–Savart law.

Let us consider the velocity $\boldsymbol{u}^{(out)}$ induced by the vortex system in a reference frame where the system is steady. Such a frame is chosen here as the frame uniformly translating with a velocity $V_{frame}\boldsymbol{e}_z$.

To get the outer solution, we assume that the vorticity is a monopolar field concentrated on the curve $\mathscr{S}$ corresponding to one of the configurations shown in figure 1. The velocity is then such that

$$\boldsymbol{u}^{(out)}(\boldsymbol{x}) = \boldsymbol{u}^{(BS)}(\boldsymbol{x}) - V_{frame}\boldsymbol{e}_z, \quad \text{with } \boldsymbol{u}^{(BS)}(\boldsymbol{x}) = -\frac{1}{4\pi}\int_{\mathscr{S}} \Gamma' \frac{(\boldsymbol{x}-\boldsymbol{x}')\times \boldsymbol{t}'}{|\boldsymbol{x}-\boldsymbol{x}'|^3}\,\mathrm{d}s'. \tag{4.1}$$

All vortices have a constant circulation $\Gamma' = 2\pi$. Note that we do not consider the transverse distribution of vorticity on $\mathscr{S}$ associated with the axial flow within the vortex. Indeed, this vorticity distribution is not expected to contribute to the external flow, as proved by Fukumoto & Miyazaki (1991). We also disregard higher-order corrections to (4.1) corresponding to multipolar vorticity concentration on $\mathscr{S}$; these corrections would be needed to perform a full matching of inner and outer solutions up to $O(\varepsilon^2)$ (see for instance Fukumoto & Moffatt 2000) but are not required for the computation of S. Here, we simply match the quadrupolar field of one component of the velocity field at leading-order only. More precisely, we impose that the local radial velocity of the outer solution possesses a quadrupolar part $u^{(out)}_{quad}$ of the form

$$u^{(out)}_{quad} = u^{(BS)}_{quad} \sim \varepsilon^2[(-2Sr - \tfrac{3}{8} r \log r)\sin 2\varphi] \quad \text{for } 1 \ll r \ll 1/\varepsilon. \tag{4.2}$$

4.1. *A single vortex ring*

The asymptotic description of a single ring was first considered by Widnall & Tsai (1977). It was recently re-examined by Fukumoto & Moffatt (2000) and Fukumoto (2002). Fukumoto & Moffatt (2000) obtained an asymptotic solution up to ε^3 which can be used for the present analysis. Their expression (3.7) of the outer solution in the regime $(1 \ll r \ll R)$ leads to the radial velocity

$$u^{(BS)} \sim \frac{1}{2R}\left(\log\left(\frac{8R}{r}\right) - 1\right)\sin\varphi + \frac{3r}{8R^2}\left(\log\left(\frac{8R}{r}\right) - \frac{4}{3}\right)\sin 2\varphi. \tag{4.3}$$

Since $\varepsilon = 1/R$ for the ring, the matching of their quadrupolar field with the inner quadrupolar part (4.2) requires that

$$S^{Ri} = -\frac{3}{16}\left[\log\left(\frac{8}{\varepsilon}\right) - \frac{4}{3}\right]. \tag{4.4}$$

Note that such a formula could have also been obtained from expression (4.21) of Widnall & Tsai (1977).

4.2. *An array of vortex rings*

The velocity field of an array of vortex rings is equal to the field of a single ring plus the field generated by distant rings. The first contribution has been calculated in the previous section. The contribution from distant rings can be obtained directly from the Biot–Savart integral. The velocity field of the ring placed at position $z=2\pi n L_z$ can be written using the global cylindrical coordinate system (see appendix A) as

$$v_{n,\rho}^{(BS)}(\rho, z) = -\frac{1}{2}\int_0^{2\pi} \frac{R(z-2\pi n L_z)\cos s}{(\rho^2 - 2R\rho\cos s + R^2 + (z-2\pi n L_z)^2)^{3/2}}\,\mathrm{d}s, \tag{4.5a}$$

$$v_{n,z}^{(BS)}(\rho, z) = -\frac{1}{2}\int_0^{2\pi} \frac{R(R^2 - \rho R\cos s + (z-2\pi n L_z)^2)\cos s}{(\rho^2 - 2R\rho\cos s + R^2 + (z-2\pi n L_z)^2)^{3/2}}\,\mathrm{d}s. \tag{4.5b}$$

Using the expression for the local radial velocity (see appendix A), one obtains ($L=\alpha=0$)

$$u(r, \varphi) = -v_\rho \cos\varphi + v_z \sin\varphi \tag{4.6}$$

$$\rho = R - r\cos\varphi, \quad z = r\sin\varphi \tag{4.7a,b}$$

Finally, the dipolar and quadrupolar terms are for $r \ll R$

$$u^{BS} \sim \sum_{n\neq 0}\left[v_{n,z}^{(BS)}(R, 0)\sin\varphi - \frac{r}{2}(\partial_z v_{n,\rho}^{(BS)}(R, 0) + \partial_\rho v_{n,z}^{(BS)}(R, 0))\sin 2\varphi\right]. \tag{4.8}$$

The quadrupolar velocity contribution from distant rings becomes ($\varepsilon = 1/R$)

$$u_{quad}^{BS} \sim -2S^{DRi}\varepsilon^2 r, \quad \text{with } S^{DRi} = \frac{R^2}{2}\sum_{n=1}^{\infty}(\partial_z v_{n,\rho}^{(BS)}(R, 0) + \partial_\rho v_{n,z}^{(BS)}(R, 0)). \tag{4.9}$$

As shown by Levy & Forsdyke (1927), S^{DRi} can also be expressed in terms of the complete elliptic integrals of the first and second kind, $\boldsymbol{K}(Z)$ and $\boldsymbol{E}(Z)$, (Abramowitz & Stegun 1965, p. 590)

$$S^{DRi} = \frac{1}{4}\sum_{n=1}^{\infty} \Lambda_n^{3/2}\left(\left(1 - \frac{4}{n^2\lambda^2}\right)\boldsymbol{E}(\Lambda_n) - \boldsymbol{K}(\Lambda_n)\right), \tag{4.10}$$

with

$$\Lambda_n = \frac{1}{1 + n^2\lambda^2/4}. \tag{4.11}$$

The function S^{DRi} is plotted in figure 7 as a function of the parameter $\lambda = L_z/R$. The constant S for an array of vortex rings is

$$S^{ARi} = S^{DRi} + S^{Ri}. \tag{4.12}$$

Both contributions are negative, and tend to elongate the vortex core along the z direction. In figure 8, the total contribution is plotted as a function of λ for a few values of ε.

Note that because

$$S^{DRi} \sim -\frac{\pi^2}{6\lambda^2} \quad \text{as } \lambda \to 0, \tag{4.13}$$

the complete external strain rate is equal to $S_{ext} \equiv 2S^{DRi}\varepsilon^2 \sim -\pi^2/(3L_z^2)$ which is equal to the external strain rate generated by an array of point vortices of circulation 2π separated by a distance L_z (Lamb 1932).

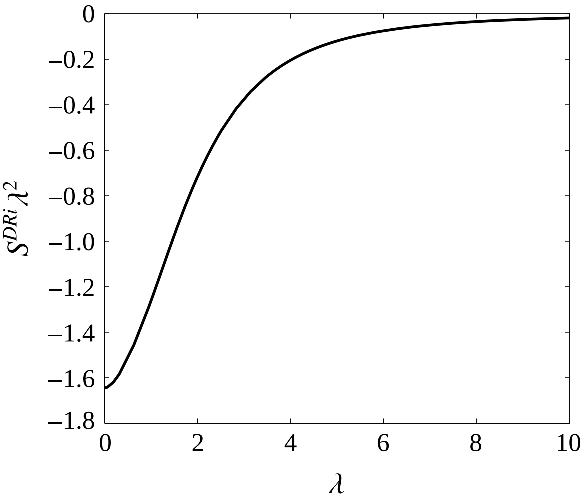

FIGURE 7. Strain rate parameter S^{DRi} generated by distant rings in an array of rings as a function of the aspect ratio $\lambda = L_z/R$.

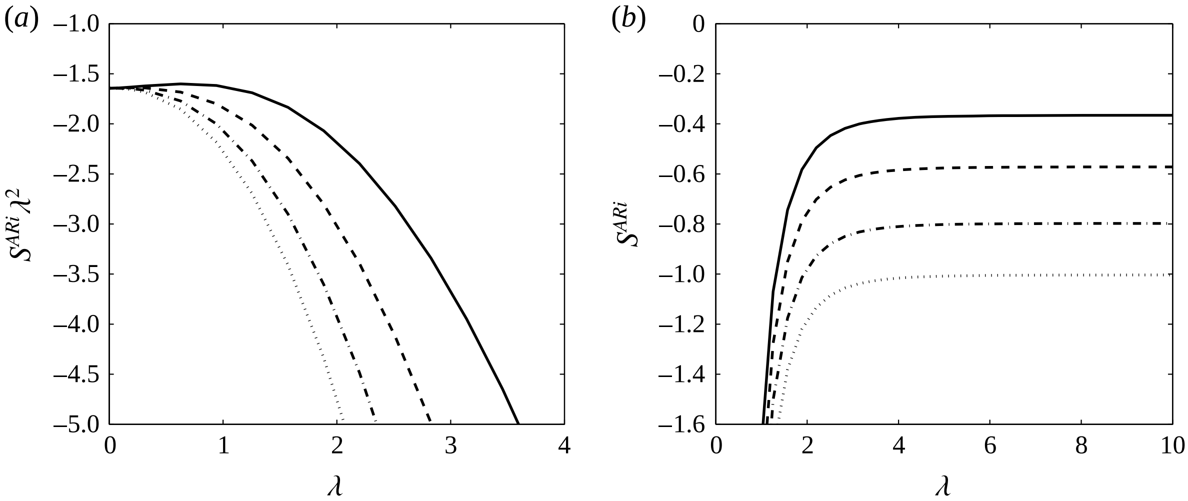

FIGURE 8. Strain rate parameter S^{ARi} for an array of vortex rings as a function of $\lambda = L_z/R$ for various $\varepsilon = a/R$. Solid line: $\varepsilon = 0.33$; dashed line: $\varepsilon = 0.1$; dash-dot line: $\varepsilon = 0.033$; dotted line: $\varepsilon = 0.01$.

4.3. *A single helix*

As shown by Hardin (1982), the velocity field induced by a helical vortex filament can be expressed in cylindrical coordinates for $\rho < R$ (with our normalization) as

$$v_\rho^{(BS)}(\rho, \chi) = \frac{2}{R\alpha^2} \operatorname{Im}\left[H_1^{1,1}\left(\frac{\rho}{R\alpha}, \frac{1}{\alpha}, \chi\right)\right], \tag{4.14a}$$

$$v_\phi^{(BS)}(\rho, \chi) = \frac{2}{\rho\alpha} \operatorname{Re}\left[H_1^{0,1}\left(\frac{\rho}{R\alpha}, \frac{1}{\alpha}, \chi\right)\right], \tag{4.14b}$$

$$v_z^{(BS)}(\rho, \chi) = \frac{1}{R\alpha} - \frac{2}{R\alpha^2} \operatorname{Re}\left[H_1^{0,1}\left(\frac{\rho}{R\alpha}, \frac{1}{\alpha}, \chi\right)\right], \tag{4.14c}$$

where $\chi = \phi - z/L$ and Re[ ] (respectively Im[ ]) indicates the real (respectively imaginary) part of a complex expression, and

$$H_M^{I,J}(x, y, \chi) = \sum_{m=1}^{\infty} m^M I_m^{(I)}(mx) K_m^{(J)}(my) \exp(im\chi), \tag{4.15}$$

where we used the notation introduced by Okulov (2004) for the Kapteyn series. $I_m^{(I)}$ and $K_m^{(J)}$ denote the Ith and Jth derivative of modified Bessel functions. Other expressions for the velocity field can be obtained for $\rho > R$, but we only need the above expressions valid for $\rho < R$ to compute the value of S.

The value $\chi = 0$ defines the angular position of the helix. Without restriction, we can consider a local frame centred on the point in cylindrical coordinates $(\rho, \phi, z) = (R, 0, 0)$. The local radial velocity u can be deduced from (4.14*a–c*) using (A 4*a*) and (A 5*a–c*) given in appendix A. We are interested in the expansion of u as r/R goes to zero. As shown by Okulov (2004), it is convenient to isolate the singularity of the Kapteyn series to obtain such an expansion (see appendix B). The derivation, which should be carried up to $O(r/R)^2$ terms, is tedious but straightforward. It can be facilitated by using a symbolic software. The final result is expression (B 12) for u with the following expression for S:

$$\begin{aligned} S^{He} &= -\frac{3}{16}\log\left(\frac{\alpha}{(\alpha^2+1)^{3/2}\varepsilon}\right) - \frac{(\alpha^2+1)^2}{24\alpha^2} - \frac{1}{4}(\alpha^2+1)^2 + \frac{1}{4}\alpha(\alpha^2+1)^{3/2} \\ &\quad + \frac{1}{96}(28\alpha^2+11) + \sum_{m=1}^{\infty} R_m(\alpha), \end{aligned} \tag{4.16}$$

with

$$\begin{aligned} R_m(\alpha) &= \frac{\alpha(\alpha^2+1)^{3/2}}{2} + \frac{3}{16m} - \frac{(1+\alpha^2)^3 m}{2\alpha^2} \\ &\quad + \frac{m^2(\alpha^2+1)^{5/2}}{\alpha^3}\left(-I_{m-1}\left(\frac{m}{\alpha}\right) + \alpha I_m\left(\frac{m}{\alpha}\right)\right)\left(K_{m-1}\left(\frac{m}{\alpha}\right) + \alpha K_m\left(\frac{m}{\alpha}\right)\right) \\ &\quad + m(\alpha^2+1)^{3/2} I_m\left(\frac{m}{\alpha}\right)\left(K_{m-1}\left(\frac{m}{\alpha}\right) + \alpha K_m\left(\frac{m}{\alpha}\right)\right). \end{aligned} \tag{4.17}$$

The function S^{He} is plotted in figure 9 for various values of ε.

Note that when $\alpha \to 0$, we have $S^{He} \sim -1/(24\alpha^2)$, which corresponds to the value (4.13) for an array of rings for small λ since we have the relation $\lambda = 2\pi\alpha$. From figure 9, we can also guess that $S^{He} \sim O(\alpha^2)$ as $\alpha \to \infty$, which implies that the self-external strain of a helix does vanish when its pitch L/R goes to infinity with a fixed a/R.

4.4. *Multiple helices*

When there are several helices, we must add to the previous contribution of a single helix, the contribution from the other distant helices. Expressions (4.14*a–c*) for the velocity field can still be used. For the helix located in the horizontal plane $(0xy)$ at $\phi_k = 2\pi k/N$, we have to change $\chi = \phi - z/L$ into $\chi = (\phi - \phi_k) - z/L$. Summing the contribution from each helix for $k = 1, \ldots, N-1$ and expanding every quantity

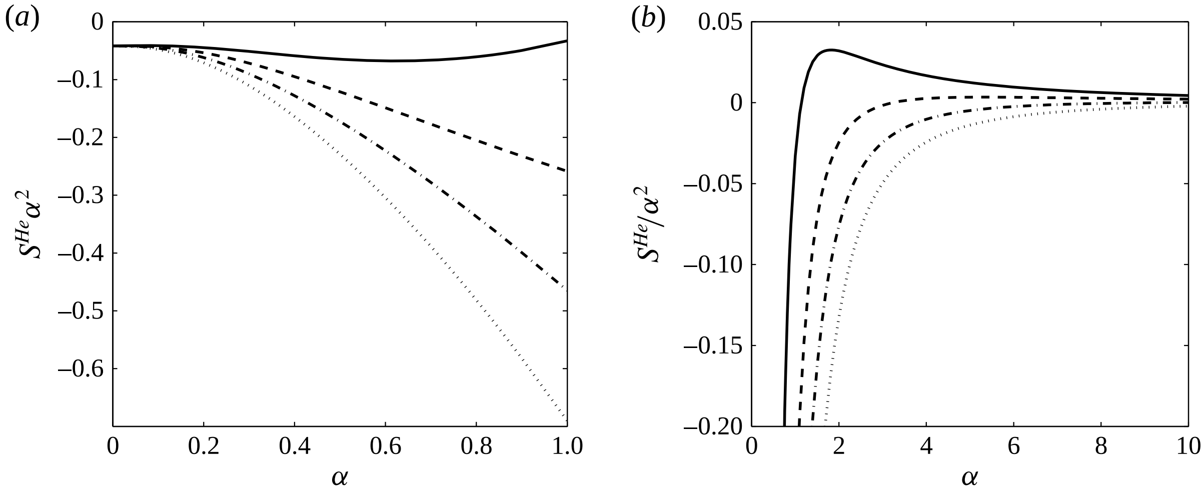

FIGURE 9. Strain rate parameter S^{He} as a function of $\alpha = L/R$ for various ε. Solid line: $\varepsilon = 0.33$; dashed line: $\varepsilon = 0.1$; dash-dot line: $\varepsilon = 0.033$; dotted line: $\varepsilon = 0.01$.

as $r/R \to 0$ leads to expression (B 15) for the local radial velocity (see appendix B) where S is given by

$$\begin{aligned} S^{DHe} &= \frac{3\log(N)}{16} - \frac{(\alpha^2+1)^3(N^2-1)}{24\alpha^2} \\ &\quad + \frac{\alpha(\alpha^2+1)^{3/2}(N-1)}{4} + \sum_{m=1}^{\infty} R_m(\alpha)\varrho\left(\frac{m}{N}\right), \end{aligned} \tag{4.18}$$

with $R_m(\alpha)$ given by (4.17) and

$$\varrho\left(\frac{m}{N}\right) = \sum_{k=1}^{N-1} \cos\left(2\pi k\frac{m}{N}\right) = \begin{cases} -1 & \dfrac{m}{N} \notin \mathbb{N}, \\ N-1 & \dfrac{m}{N} \in \mathbb{N}. \end{cases} \tag{4.19}$$

We obtain for multiple helices $S^{MHe} = S^{He} + S^{DHe}$, that is

$$\begin{aligned} S^{MHe} &= -\frac{3}{16}\log\left(\frac{\alpha}{(\alpha^2+1)^{3/2}N\varepsilon}\right) - \frac{4(\alpha^2+1)^3N^2 + \alpha^2(20\alpha^4+12\alpha^2+9)}{96\alpha^2} \\ &\quad + \frac{\alpha(\alpha^2+1)^{3/2}N}{4} + N\sum_{n=1}^{\infty} R_{nN}(\alpha). \end{aligned} \tag{4.20}$$

The function S^{MHe} is plotted in figure 10 for $N = 1, 2, 3, 5$ and $\varepsilon = 1$. Plots for other values of ε are obtained by adding $(3/16)\log\varepsilon$ as $S^{MHe}(\varepsilon) = S^{MHe}(1) + (3/16)\log\varepsilon$.

Note that we have

$$S^{MHe} \sim -\frac{N^2}{24\alpha^2} \quad \text{as } \alpha \to 0, \tag{4.21}$$

$$S^{MHe} \sim -\frac{(N-1)(N-5)}{24}\alpha^4 \quad \text{as } \alpha \to \infty. \tag{4.22}$$

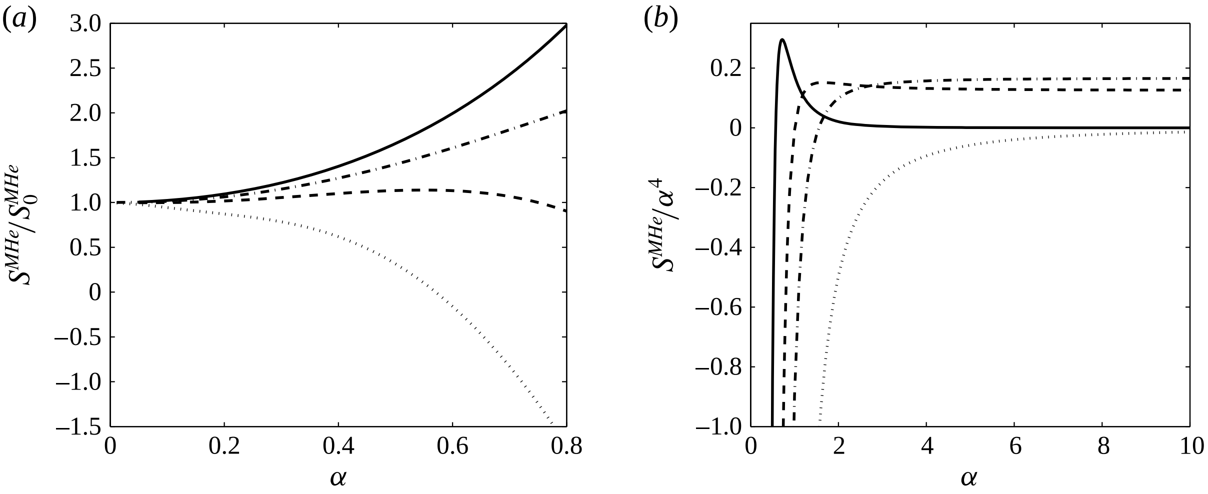

FIGURE 10. Strain rate parameter S^{MHe} versus $\alpha = L/R$ for N helices with $N = 1, 2, 3, 5$ (solid, dash, dash-dot, dotted lines) for $\varepsilon = 1$. (*a*) S^{MHe} is normalized by its expression at the origin $S_0^{MHe} = -N^2/(24\alpha^2)$; (*b*) S^{MHe} is normalized by α^4.

For large α, the problem becomes a configuration of 2-D straight vortices on a polygon. This can be used to check (4.22). For $N = 2$, the calculation is straightforward as the strain field at $(x, y) = (R, 0)$ is due to a vortex of circulation 2π located at $(-R, 0)$. We immediately obtain a strain rate $S_{ext} = 1/(4R^2) = (1/4)\varepsilon^2(1 + \alpha^2)^2 = 2S\varepsilon^2$ which gives $S = (1/8)\alpha^4$ for large α in accordance with (4.22) for $N = 2$.

For large N, we obtain

$$S^{MHe} \sim -\frac{(1+\alpha^2)^3 N^2}{24\alpha^2}, \tag{4.23}$$

which corresponds to the external strain rate generated by an array of straight vortices of circulation 2π and separated by the shortest distance between the helices: $L_z = 2\pi L/(N\sqrt{1+\alpha^2})$.

Note that although S^{MHe} diverges for small and large α, the external strain rate defined by $S_{ext} = 2S^{MHe}\varepsilon^2 = 2S^{MHe}(a/R)^2/(1 + \alpha^2)^2$ remains always small when the core size, a, remains small compared to the shortest distance to the other parts of the vortex structure.

5. Comparison with numerical results

In this section, the asymptotic solution is compared to direct numerical simulations.

5.1. *Simulation of a ring array*

For an array of vortex rings, the pseudo-spectral code developed by Bolnot (2012) is used. This code has been validated and run to analyse the stability of vortex rings with respect to the pairing instability in Bolnot *et al.* (2014). The system is assumed axisymmetric and periodic in the axial direction. The numerical formulation is based on Chebyshev and Fourier decompositions in the radial and axial directions, and on an extrapolation Adams–Bashforth scheme for time evolution. The simulation is initialized by a normalized Gaussian profile for the azimuthal vorticity and velocity centred at $(\rho, z) = (R_0, 0)$ in a box of axial length L_z with a prescribed jet parameter. At $t = 0$, circulation and core radius of the vortex ring and Reynolds number are fixed to $\Gamma_0 = 2\pi$, $a_0 = 1$ and $Re = \Gamma_0/\nu = 2000$.

After a short relaxation process, the solution reaches a quasi-steady state in the frame moving with the vortex ring (Bolnot *et al.* 2014). The core size and jet parameter have slightly evolved during the relaxation process but are adequately predicted using the viscous expansion factor $\sqrt{1+4t/Re}$ (Bolnot *et al.* 2014). It is this quasi-equilibrium state (frozen at a time t_r) that is compared to the asymptotic solution. In order to agree with the definition used in the asymptotic analysis, the radius R of the ring should correspond to a radial and axial velocity stagnation point. As the plane of symmetry of the solution is fixed in the centre $z = 0$ of the box, the radius R is obtained from the condition $u_z(R, 0) = 0$ which leads to a value slightly different from R_0.

As soon as the centre of the local frame is obtained, the local velocity field (u, v, w) can be computed using (A 4*a–c*), (A 5*a–i*) and (A 1*a–c*). An azimuthal decomposition is then performed to get the monopolar, dipolar and quadrupolar contributions that we compare to the theory.

Figure 11 shows a comparison between asymptotic and DNS results for an array of vortex rings for the parameters $\varepsilon = 0.11$, $\lambda = L_z/R = 3$, $W_0 = 0.1$ and $Re = 2000$. In these figures, we plotted the monopolar, dipolar and quadrupolar contributions of each velocity component in the local frame, using the same normalisation as in the theory. The core size, circulation and jet parameter have been evaluated by comparing the monopolar part (*a*,*d*,*g*) of the numerical velocity fields with the Gaussian model used. It is found that the theoretical profile selected at zero order is appropriate (see comparison figure 11*a*,*d*,*g*). A good agreement between numerical and theoretical curves is also found for all dipolar and quadrupolar components. Other configurations have been tested, and a similar agreement has always been observed. This constitutes a strong validation for both theory and code.

5.2. *Simulation of helices*

The simulations of helix systems have been carried out using the helical code developed in Delbende *et al.* (2012*a*), which implements a generalisation of the vorticity-streamfunction formulation in a circular domain, with finite differences in the radial direction and spectral decomposition along the azimuth. The helical symmetry is explicitly enforced in such a way that the 3-D Navier–Stokes equations are reduced to a 2-D unsteady problem. The code has also been validated and used in Delbende, Rossi & Piton (2012*b*), Delbende, Piton & Rossi (2015).

Similarly to vortex ring simulations, we start the simulation with Gaussian profiles for the axial velocity and axial vorticity around one or several helical curves (see figure 1) with prescribed a_0, R_0, W_0, Γ and L. The Reynolds number is always fixed at $Re = \Gamma/\nu = 10\,000$. After a relaxation process, the system reaches a quasi-equilibrium state in the frame rotating at the rotation rate Ω_{frame} of the helical structure. The rotation rate Ω_{frame} is related to the displacement speed of the helical structure as sketched in figure 3. It can then also be expressed as a function of V_{frame} using $\Omega_{frame} = -V_{frame}/(\alpha R)$.

The difficulty concerning the treatment of the numerical data is the prescription of the local frame. Such a frame is not naturally defined from the DNS, and is obtained here by an iterative procedure. Let us define the helical vorticity ω_B by $\boldsymbol{\omega} \boldsymbol{\cdot} \boldsymbol{e}_B$ where $\boldsymbol{e}_B$ is a unit vector tangent to any helical line (for details see Delbende *et al.* (2012*a*)).

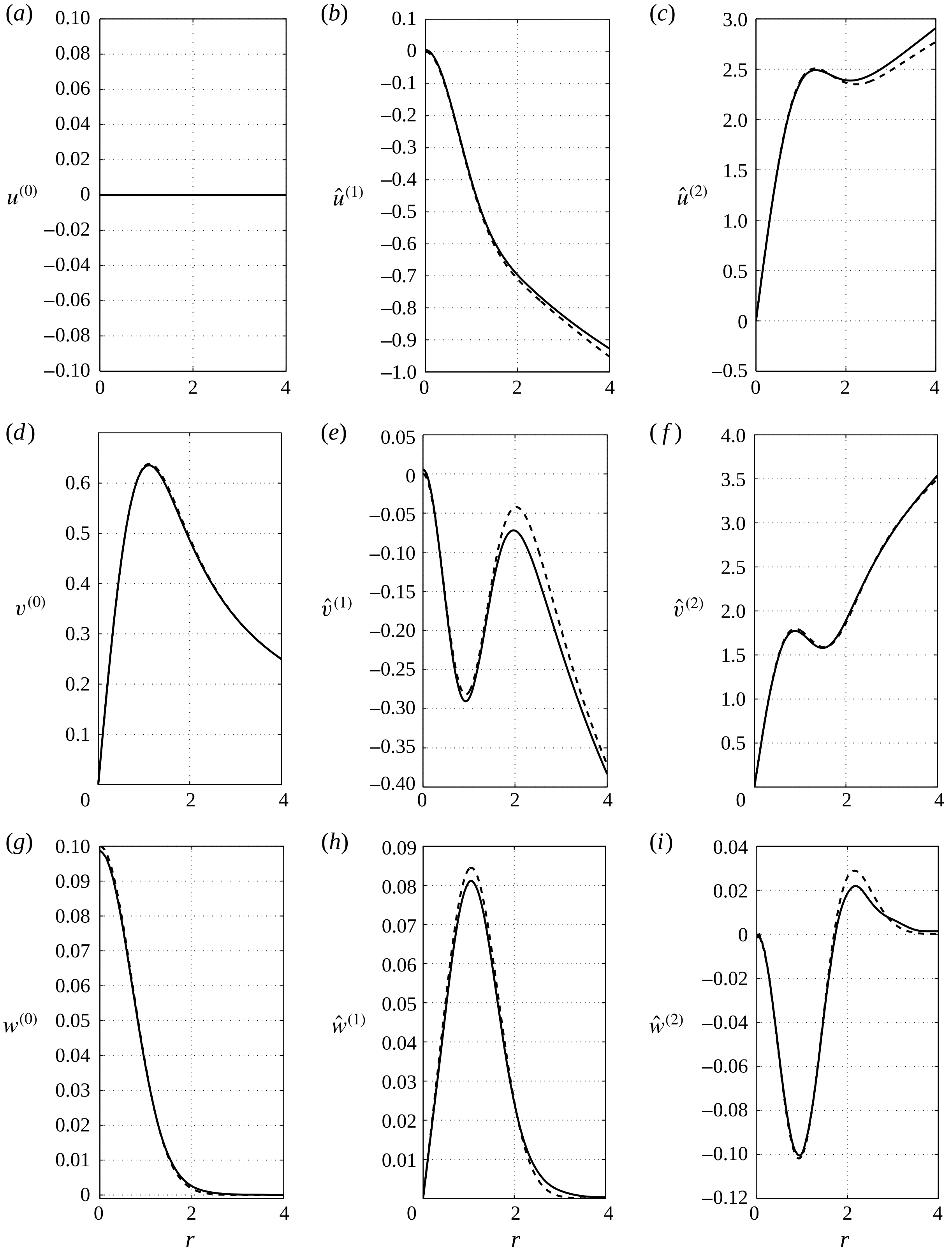

FIGURE 11. Array of swirling vortex rings with jet strength $W_0 = 0.1$, at $L_z/R = 3$, $\varepsilon = 0.11$, $Re = 2000$: comparison between asymptotic results (dashed lines) and DNS results (solid lines). (*a*,*d*,*g*) Monopolar component; (*b*,*e*,*h*): dipolar component; (*c*,*f*,*i*) quadrupolar component. (*a*–*c*) Radial velocity, (*d*–*f*) azimuthal velocity, (*g*–*i*) axial velocity.

This quantity is directly provided by the helical code. First, one finds the position M_0 where the helical vorticity ω_B reaches its maximum in a global horizontal plane. Second, one defines the plane $\Pi_\perp(M_0)$ normal to the local helical vector $\boldsymbol{e}_B(M_0)$ passing through this point M_0. Third, one determines the stagnation point M_1 of the velocity components normal to $\boldsymbol{e}_B(M_0)$ in $\Pi_\perp(M_0)$. At this stagnation point, M_1, the local helical vector $\boldsymbol{e}_B(M_1)$ is oriented in a slightly different direction than $\boldsymbol{e}_B(M_0)$, so a new plane $\Pi_\perp(M_1)$ can be defined in which we can obtain another stagnation point M_2 of the velocity components normal to $\boldsymbol{e}_B(M_1)$ in $\Pi_\perp(M_1)$. This operation is repeated until it has converged to the point that will be the centre of the local frame. In practice, around 100 iterations are necessary. At the end of the process, the stagnation point C has been located, providing a helical line $\mathscr{S}$. The radial coordinate of C defines the value of R. The local frame is such that $\boldsymbol{e}_B(C)$ corresponds to the vector $\boldsymbol{e}_s$ of the theory.

Velocity and vorticity fields are expressed in the cylindrical coordinates attached to this local frame and thereafter Fourier decomposed in the azimuthal direction to obtain the monopolar, dipolar and quadrupolar components. The monopolar components are used to correct the value of the parameters a, Γ and W_0, by fitting axial vorticity and axial velocity with Gaussian profiles, after subtracting the uniform vorticity associated with the rotation of the frame. At the end of this procedure, all theoretical parameters have been obtained and each component can be adequately renormalized for comparison. Note that the frame used in the theory to obtain a steady vortex system is different; it is translating rather than rotating. To express the theoretical results in the rotating frame, one simply subtracts velocity $-V_{frame}\boldsymbol{e}_z + \Omega_{frame}\rho\boldsymbol{e}_\phi$ from the theoretical solution. Using (A 6), this amounts to performing the following modifications on the theoretical fields:

$$v^{(0)} \rightarrow v^{(0)} + \varepsilon\sqrt{1+\alpha^2}V_{frame}r, \tag{5.1a}$$

$$w^{(0)} \rightarrow w^{(0)} + \frac{\sqrt{1+\alpha^2}}{\alpha}V_{frame}, \tag{5.1b}$$

$$w^{(1)} \rightarrow w^{(1)} - \frac{\sqrt{1+\alpha^2}}{\alpha}V_{frame}r. \tag{5.1c}$$

Since V_{frame} is $O(\varepsilon \log \varepsilon)$ for helices, these changes are higher-order terms. Nevertheless, it is convenient to introduce them here because they improve the predictions of the axial flow component, as shown below.

In figure 12 (respectively figure 13), theoretical and numerical results are compared for a single helix with axial flow $W_0 = 0.54$ (respectively for a system of two helices without axial jet $W_0 = 0$). For radial and azimuthal velocity components, a fair agreement is found between theory and DNS results. Despite a smaller value of ε, the agreement is found to be less convincing than for an array of rings. It is also seen that the change (5.1*a–c*) of reference frame has to be taken into account. However, a small mismatch between DNS and theory remains for the monopolar component. This is probably at the origin of the deteriorated agreement for the dipolar and quadrupolar components (see bottom figures in figures 12 and 13).

As for the ring arrays, other configurations have been tested for helical vortex systems and we always observed a good agreement with the asymptotic theory. The values obtained from the numerical simulations for the internal strain rate $S^{(2)}$ and for the frame rotation rate Ω_{frame} have also been compared to the theory and we have systematically found a good agreement. This provides a validation of expressions (4.20) and (B 17) for the external strain field and translation speed of multiple helices.

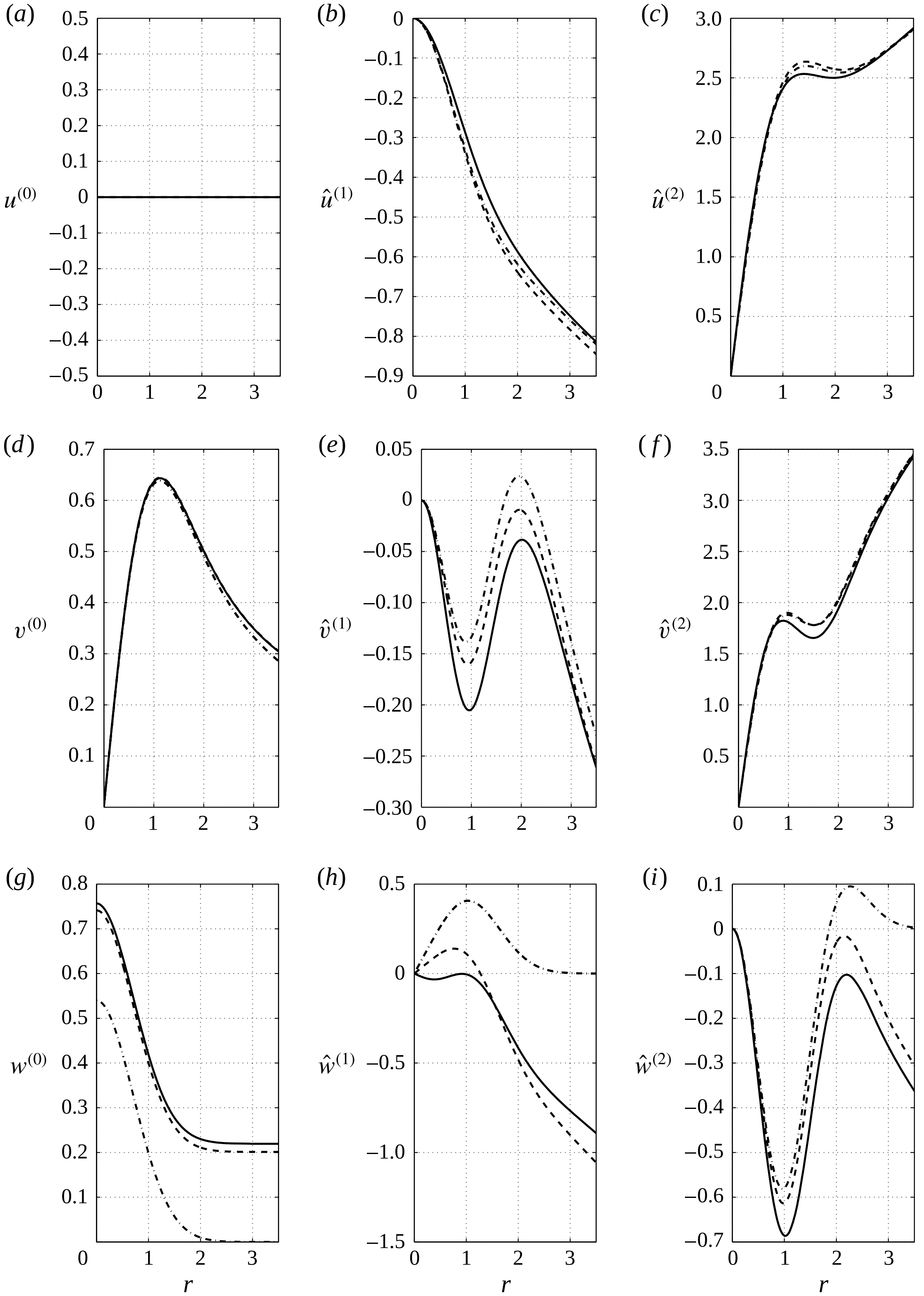

FIGURE 12. Single helix with $W_0 = 0.54$, $L/R = 0.5$, $\varepsilon = 0.045$, $Re = 10^4$: comparison between asymptotic (dashed lines) and DNS (solid lines). (*a*,*d*,*g*) Monopolar component; (*b*,*e*,*h*) dipolar component; (*c*,*f*,*i*) quadrupolar component. (*a*–*c*) Radial velocity, (*d*–*f*) azimuthal velocity, (*g*–*i*) axial velocity. The dash-dotted lines correspond to the theory without taking into account the effect of the change of frame ($W_{0_0} = 0$). For these parameters, the theory gives $\Omega_{frame} = -0.0120$ and $S = -0.6341$, which gives a strain rate in the vortex centre $S^{(2)} = -1.699$ (defined in (3.21)). The numerical values are $\Omega_{frame} = -0.0110$ and $S^{(2)} = -1.803$.

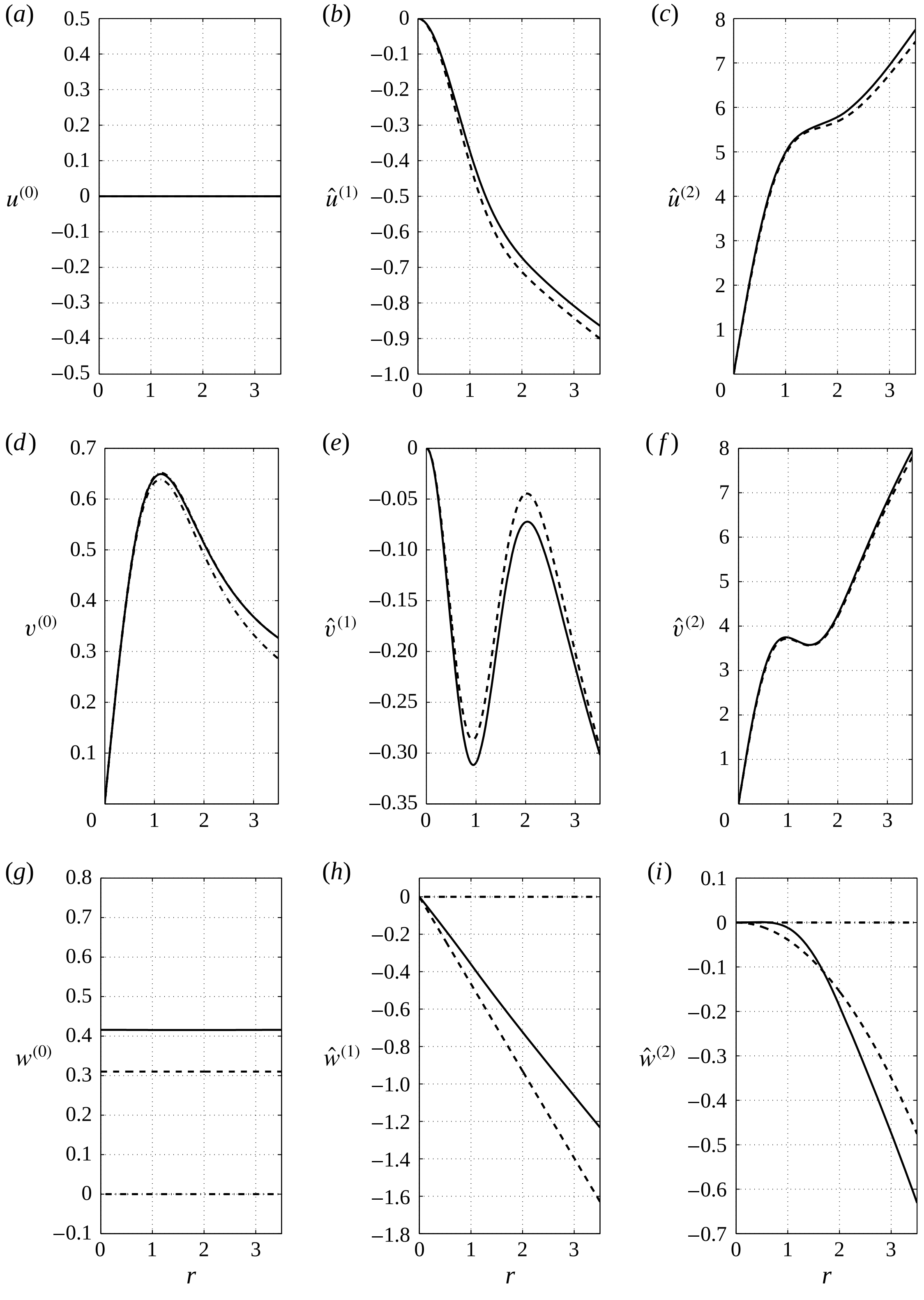

FIGURE 13. System of two helical vortices with $W_0 = 0$, $L/R = 0.5$, $\varepsilon = 0.06$, $Re = 10^4$: comparison between asymptotic (dashed lines) and DNS (solid lines). (*a*,*d*,*g*) Monopolar component; (*b*,*e*,*h*) dipolar component; (*c*,*f*,*i*) quadrupolar component. (*a*–*c*) Radial velocity, (*d*–*f*) azimuthal velocity, (*g*–*i*) axial velocity. The dash-dotted lines correspond to the theory without taking into account the effect of the change of frame ($W_{0_0} = 0$). For these parameters, the theory predicts $\varOmega_{frame} = -0.0258$ and $S = -1.2832$, which gives a strain rate in the centre $S^{(2)} = -3.441$ (defined in (3.21)). The numerical values are $\varOmega_{frame} = -0.0261$ and $S^{(2)} = -3.496$.

6. Conclusions

We analysed the internal structure of vortex rings and helical vortices showing that they can be described using an asymptotic theory where the core size is considered small compared to the other scales of the vortex structure. At leading order, the vortex structure was assumed locally an axisymmetric vortex with axial flow. The asymptotic theory was used to determine dipolar and quadrupolar corrections associated with this structure. It was shown that dipolar corrections which appear at first order depend in a dominant way on the local curvature of the vortex. As a consequence, we expect rings, arrays of rings, helices and multiples helices to all exhibit the same dipolar correction if they possess the same curvature. We also computed the quadrupolar corrections which appear at second order. Contrary to the dipolar corrections, such corrections depend on the global geometry. To be more precise, quadrupolar corrections are composed of a contribution which depends on the local curvature and a non-local contribution associated with the strain field generated by distant part of the vortex structure. The non-local contribution has been calculated for a vortex ring, an array of rings, a helix and multiple helices by considering the flow field obtained from Biot–Savart law for vortex filaments.

The asymptotic results have been compared to numerical solutions obtained by DNS for both rings and helices. A good agreement has been observed for rings. For helices, a fair agreement has also been demonstrated. In practice, this case is more involved because of the necessity to define a plane orthogonal to the vortex core structure.

The present results are important to model the short-wavelength instabilities that can develop in rings or helices. Both dipolar and quadrupolar correction terms are expected to couple modes of the underlying vortex and be a source of instability. The dipolar correction term is known to be responsible of the so-called curvature instability. This instability has been theoretically predicted for rings (Hattori & Fukumoto 2003; Fukumoto & Hattori 2005) and helices (Hattori & Fukumoto 2009, 2014). However, the analysis has only been performed for particular vortices with uniform vorticity. It would be interesting to extend the analysis to more realistic vortices such as those considered in the present study. The quadrupolar correction is associated with the so-called elliptic instability (see for instance Kerswell 2002). Widnall & Tsai (1977) provided a growth rate estimate for the elliptic instability in a single ring with a Rankine vorticity profile. No person however has so far provided any prediction for helices or rings with a realistic vorticity profile. Yet, we expect this instability to be present as the quadrupolar field contained a strain field part which is also present in straight vortices. An interesting study would then be to compute the effects of the additional quadrupolar field which is generated by curvature.

Both curvature and elliptic instabilities are also expected to be strongly affected by the presence of axial flow, as this parameter modifies the form of vortex modes involved in the instabilities (Lacaze, Ryan & Le Dizès 2007; Roy *et al.* 2011). We suspect that this parameter is crucial to an understanding of the competition between both instabilities and associate recent observations in helices (Leweke *et al.* 2014) with one instability or another.

Acknowledgements

This work received support from the French Agence Nationale de la Recherche under the A*MIDEX grant ANR-11-IDEX-0001-02, the LABEX MEC project ANR-11-LABX-0092 and the ANR HELIX project ANR-12-BS09-0023-01. HPC resources from GENCI–IDRIS (grant 2015-2a1386) are also acknowledged.

Appendix A. Change of coordinate systems

In this section, we provide the formulae which can be used to obtain the velocity field in the local frame from its expression in the global cylindrical frame. Consider a point of coordinates (ρ, ϕ, z) in the global cylindrical coordinate system and assume that this point has the coordinates (r, φ, s) in the local frame defined by (2.1) and (2.3) centred on the point $C(s)$ of cylindrical coordinates $(R, \phi_0, L\phi_0)$ (see figure 2). We obtain the following relation between the coordinates:

$$\rho^2 = (R - r\cos\varphi)^2 + \frac{\alpha^2}{1+\alpha^2} r^2 \sin^2\varphi, \tag{A 1a}$$

$$\rho \sin\phi = (R - r\cos\varphi)\sin\phi_0 - \frac{\alpha}{\sqrt{1+\alpha^2}} r \sin\varphi \cos\phi_0, \tag{A 1b}$$

$$z = L\phi_0 + \frac{1}{\sqrt{1+\alpha^2}} r\sin\varphi, \tag{A 1c}$$

$$s = \phi_0 \sqrt{R^2 + L^2}. \tag{A 1d}$$

If the velocity field can be written in the global cylindrical frame as

$$\boldsymbol{V} = \boldsymbol{V}(\rho, \phi, z) = v_\rho \boldsymbol{e}_\rho + v_\phi \boldsymbol{e}_\phi + v_z \boldsymbol{e}_z \tag{A 2}$$

and

$$\boldsymbol{V} = u\boldsymbol{e_r} + v\boldsymbol{e}_\varphi + w\boldsymbol{e_s} \tag{A 3}$$

in the local frame, we derive the relation between (u, v, w) and (v_ρ, v_ϕ, v_z):

$$u(r, \varphi, s) = v_\rho(\rho, \phi, z)\boldsymbol{e_r}\cdot\boldsymbol{e}_\rho + v_\phi(\rho, \phi, z)\boldsymbol{e_r}\cdot\boldsymbol{e}_\phi + v_z(\rho, \phi, z)\boldsymbol{e_r}\cdot\boldsymbol{e}_z, \tag{A 4a}$$

$$v(r, \varphi, s) = v_\rho(\rho, \phi, z)\boldsymbol{e}_\varphi\cdot\boldsymbol{e}_\rho + v_\phi(\rho, \phi, z)\boldsymbol{e}_\varphi\cdot\boldsymbol{e}_\phi + v_z(\rho, \phi, z)\boldsymbol{e}_\varphi\cdot\boldsymbol{e}_z, \tag{A 4b}$$

$$w(r, \varphi, s) = v_\rho(\rho, \phi, z)\boldsymbol{e_s}\cdot\boldsymbol{e}_\rho + v_\phi(\rho, \phi, z)\boldsymbol{e_s}\cdot\boldsymbol{e}_\phi + v_z(\rho, \phi, z)\boldsymbol{e_s}\cdot\boldsymbol{e}_z, \tag{A 4c}$$

where

$$\boldsymbol{e_r}\cdot\boldsymbol{e}_\rho = -\left(\frac{R}{\rho} - \frac{r}{\rho}\cos\varphi\right)\cos\varphi + \frac{\alpha^2}{(1+\alpha^2)}\frac{r}{\rho}\sin^2\varphi, \tag{A 5a}$$

$$\boldsymbol{e_r}\cdot\boldsymbol{e}_\phi = -\frac{\alpha}{\sqrt{1+\alpha^2}}\frac{R}{\rho}\sin\varphi, \tag{A 5b}$$

$$\boldsymbol{e_r}\cdot\boldsymbol{e}_z = \frac{1}{\sqrt{1+\alpha^2}}\sin\varphi, \tag{A 5c}$$

$$\boldsymbol{e}_\varphi\cdot\boldsymbol{e}_\rho = \left(\frac{R}{\rho} - \frac{r}{\rho}\cos\varphi\right)\sin\varphi + \frac{\alpha^2}{(1+\alpha^2)}\frac{r}{\rho}\sin\varphi\cos\varphi, \tag{A 5d}$$

$$\boldsymbol{e}_\varphi\cdot\boldsymbol{e}_\phi = \frac{\alpha}{\sqrt{1+\alpha^2}}\left(\frac{r}{\rho} - \frac{R}{\rho}\cos\varphi\right), \tag{A 5e}$$

$$\boldsymbol{e}_\varphi\cdot\boldsymbol{e}_z = \frac{1}{\sqrt{1+\alpha^2}}\cos\varphi, \tag{A 5f}$$

$$\boldsymbol{e}_s \cdot \boldsymbol{e}_\rho = -\frac{\alpha}{(1+\alpha^2)} \frac{r}{\rho} \sin\varphi, \tag{A 5g}$$

$$\boldsymbol{e}_s \cdot \boldsymbol{e}_\phi = \frac{1}{\sqrt{1+\alpha^2}} \left(\frac{R}{\rho} - \frac{r}{\rho} \cos\varphi \right), \tag{A 5h}$$

$$\boldsymbol{e}_s \cdot \boldsymbol{e}_z = \frac{\alpha}{\sqrt{1+\alpha^2}}. \tag{A 5i}$$

These expressions can be used to express in the local frame with the local coordinates the vector $\boldsymbol{U} = -V_{frame}\boldsymbol{e}_z + \Omega_{frame}\rho\boldsymbol{e}_\phi$ associated with the change of frame in § 5.2. Using $\Omega_{frame} = -V_{frame}/(\alpha R)$, we obtain

$$\boldsymbol{U} = V_{frame} \left(-\frac{r}{R\sqrt{1+\alpha^2}} \boldsymbol{e}_\varphi + \left(-\frac{\sqrt{1+\alpha^2}}{\alpha} + \frac{r\cos\varphi}{R\alpha\sqrt{1+\alpha^2}} \right) \boldsymbol{e}_s \right). \tag{A 6}$$

Appendix B. Inner expansion of Hardin solution for helices

To derive the inner expansion of Hardin solution, it is convenient to isolate the singularity of the Kapteyn series using the technique introduced by Okulov (2004). We have in particular used the expressions (valid for $\rho < R$) given by Fukumoto & Okulov (2005):

$$v_\rho^{(BS)} = \frac{2}{R\alpha^2} \mathrm{Im} \left[\lambda^{1,1} \left(\frac{\mathrm{e}^{\xi+\mathrm{i}\chi}}{1-\mathrm{e}^{\xi+\mathrm{i}\chi}} + \alpha^{1,1} \log(1-\mathrm{e}^{\xi+\mathrm{i}\chi}) + \beta^{1,1} \mathrm{Li}_2(\mathrm{e}^{\xi+\mathrm{i}\chi}) \right) + R_1^{1,1} \right], \tag{B 1a}$$

$$v_\phi^{(BS)} = \frac{2}{\rho\alpha} \mathrm{Re} \left[\lambda^{0,1} \left(\frac{\mathrm{e}^{\xi+\mathrm{i}\chi}}{1-\mathrm{e}^{\xi+\mathrm{i}\chi}} + \alpha^{0,1} \log(1-\mathrm{e}^{\xi+\mathrm{i}\chi}) + \beta^{0,1} \mathrm{Li}_2(\mathrm{e}^{\xi+\mathrm{i}\chi}) \right) + R_1^{0,1} \right], \tag{B 1b}$$

$$v_z^{(BS)} = \frac{1}{2\alpha} - \frac{2}{R\alpha^2} \mathrm{Re} \left[\lambda^{0,1} \left(\frac{\mathrm{e}^{\xi+\mathrm{i}\chi}}{1-\mathrm{e}^{\xi+\mathrm{i}\chi}} + \alpha^{0,1} \log(1-\mathrm{e}^{\xi+\mathrm{i}\chi}) + \beta^{0,1} \mathrm{Li}_2(\mathrm{e}^{\xi+\mathrm{i}\chi}) \right) + R_1^{0,1} \right], \tag{B 1c}$$

where

$$\chi = \phi - z/(R\alpha), \quad \mathrm{e}^\xi = \frac{x(1+\sqrt{1+y^2})\exp(\sqrt{1+x^2})}{y(1+\sqrt{1+x^2})\exp(\sqrt{1+y^2})}, \tag{B 2a,b}$$

$$\lambda^{1,1} = -\frac{((1+x^2)(1+y^2))^{1/4}}{2xy}, \quad \lambda^{0,1} = -\frac{1}{2y} \left(\frac{1+y^2}{1+x^2} \right)^{1/4}, \tag{B 3a,b}$$

$$\alpha^{1,1} = \upsilon_1(t_x) - \upsilon_1(t_y), \quad \beta^{1,1} = \upsilon_2(t_x) + \upsilon_2(t_y) - \upsilon_1(t_x)\upsilon_1(t_y), \tag{B 4a,b}$$

$$\alpha^{0,1} = \vartheta_1(t_x) - \upsilon_1(t_y), \quad \beta^{0,1} = \vartheta_2(t_x) + \upsilon_2(t_y) - \vartheta_1(t_x)\upsilon_1(t_y), \tag{B 4c,d}$$

with

$$x = \frac{\rho}{R\alpha}, \quad y = \frac{1}{\alpha}, \quad t_x = \frac{1}{\sqrt{1+x^2}}, \quad t_y = \frac{1}{\sqrt{1+y^2}}, \tag{B 5a–d}$$

and

$$\upsilon_1(t) = (-9t + 7t^3)/24, \tag{B.6a}$$

$$\vartheta_1(t) = (3t - 5t^3)/24, \tag{B.6b}$$

$$\upsilon_2(t) = (-135t^2 + 594t^4 - 455t^6)/1152, \tag{B.6c}$$

$$\vartheta_2(t) = (81t^2 - 462t^4 + 385t^6)/1152. \tag{B.6d}$$

The functions $R_1^{1,1}$ and $R_1^{0,1}$ are defined by

$$R_1^{1,1} = \sum_{m=1}^{\infty} ri_m^{1,1}(x, y)\mathrm{e}^{\mathrm{i}m\chi}, \quad R_1^{0,1} = \sum_{m=1}^{\infty} ri_m^{0,1}(x, y)\mathrm{e}^{\mathrm{i}m\chi}, \tag{B 7a,b}$$

with

$$ri_m^{1,1}(x, y) = mI'_m(mx)K'_m(my) - \lambda^{1,1}\mathrm{e}^{m\xi}\left(1 + \frac{\alpha^{1,1}}{m} + \frac{\beta^{1,1}}{m^2}\right), \tag{B.8a}$$

$$ri_m^{0,1}(x, y) = mI_m(mx)K'_m(my) - \lambda^{0,1}\mathrm{e}^{m\xi}\left(1 + \frac{\alpha^{0,1}}{m} + \frac{\beta^{0,1}}{m^2}\right). \tag{B.8b}$$

An expression for u in terms of the local coordinates is obtained using (A 4a) and (A 1a–c) with $\phi_0 = 0$. Expanding all the quantities as $r/R \to 0$, we find an expression for a single helix of the form

$$u^{(BS)} \sim [C^{He} - \tfrac{1}{2}\log r]\varepsilon \sin\varphi + [-2S^{He} - \tfrac{3}{8}\log r]\varepsilon^2 r \sin 2\varphi, \tag{B.9}$$

where S^{He} is given by (4.16) and

$$C^{He} = \frac{1 - \alpha^4 + \alpha^3\sqrt{1+\alpha^2}}{2\alpha\sqrt{1+\alpha^2}} + \frac{1}{2}\log\left(\frac{\alpha}{\varepsilon(1+\alpha^2)^{3/2}}\right) + \sum_{m=1}^{\infty} c_m(\alpha), \tag{B.10}$$

with

$$c_m(\alpha) = -\frac{(1+\alpha^2)^{3/2}}{\alpha}\left(\frac{2m}{\alpha}I_m\left(\frac{m}{\alpha}\right)K'_m\left(\frac{m}{\alpha}\right) + 1\right) - \frac{1}{2m}. \tag{B.11}$$

Both $R_m(\alpha)$ and $c_m(\alpha)$ are $O(1/m^3)$ for large m, which guarantees that the sums in (4.16) and (B 10) are absolutely convergent.

If we now add the contribution from the displacement of the frame (which is $-V_{frame}^{He}\boldsymbol{e}_z$) we obtain from (4.1) for a single helix

$$u^{(out)} \sim \left[-\frac{V_{frame}^{He}}{\sqrt{1+\alpha^2}} + C^{He} - \frac{1}{2}\log r\right]\varepsilon \sin\varphi + \left[-2S^{He} - \frac{3}{8}\log r\right]\varepsilon^2 r \sin 2\varphi. \tag{B.12}$$

The matching of this expression with the inner expansions provides the strain rate S^{He} and the frame velocity V_{frame}^{He}:

$$V_{frame}^{He} = \sqrt{1+\alpha^2}(C^{He} + A)\varepsilon, \tag{B.13}$$

where A is defined by (3.12). This expression is analogue to an expression already given in Alekseenko *et al.* (2007), p. 250.

The velocity field induced by the distant helices is obtained by summing the $N-1$ contributions taken at $\phi_k = 2\pi k/N$, $k = 1, \ldots, N-1$. There are many simplifications thanks to the relations

$$\sum_{k=1}^{N-1} \frac{\exp(\mathrm{i}\phi_k)}{1-\exp(\mathrm{i}\phi_k)} = \frac{1-N}{2}, \tag{B.14a}$$

$$\sum_{k=1}^{N-1} \log(1-\exp(\mathrm{i}\phi_k)) = \log N, \tag{B.14b}$$

$$\sum_{k=1}^{N-1} \mathrm{Li}_2(\exp(\mathrm{i}\phi_k)) = \frac{\pi^2}{6}\frac{1-N}{N}. \tag{B.14c}$$

After a long but straightforward calculation, we obtain for the contribution from distant helices

$$u^{(BS)} \sim C^{DHe}\varepsilon \sin\varphi - 2S^{DHe}\varepsilon^2 r \sin 2\varphi, \tag{B.15}$$

where S^{DHe} is given by (4.18) and

$$C^{DHe} = -\frac{\sqrt{1+\alpha^2}(\alpha^2-1)(N-1)}{2\alpha} - \frac{1}{2}\log N + \sum_{m=1}^{\infty} c_m(\alpha)\varrho\left(\frac{m}{N}\right), \tag{B.16}$$

with $\varrho(x)$ defined in (4.19).

The velocity field obtained by multiple helices is the sum of the contributions from a single helix and distant helices. From the complete matching of the dipolar component, we obtain using (B 12) and (B 15), an expression for the velocity V_{frame}^{MHe} of the frame for multiple helices:

$$V_{frame}^{MHe} = \sqrt{1+\alpha^2}(C^{MHe} + A)\varepsilon, \tag{B.17}$$

where $C^{MHe} = C^{He} + C^{DHe}$ reduces to

$$C^{MHe} = \frac{\alpha^2}{2} - \frac{\sqrt{1+\alpha^2}(\alpha^2-1)N}{2\alpha} + \frac{1}{2}\log\left(\frac{\alpha}{\varepsilon(1+\alpha^2)^{3/2}N}\right) + N\sum_{k=1}^{\infty} c_{Nk}(\alpha). \tag{B.18}$$

It is this expression of V_{frame}, with $A \approx 0.22 - W_0^2/4$ which has been used in expression (3.5) for W_{0_0} and in (5.1*a–c*).

Note finally that the expressions (B 9) and (B 15), and (4.3) and (4.8) for rings, contain no $\cos 2\phi$ terms. This property validates the hypothesis made in § 3.3 that there is no homogeneous solution proportional to $\cos 2\phi$ in the inner expression (3.14*a*) of the quadrupolar contribution to the radial velocity.

REFERENCES

ABRAMOWITZ, M. & STEGUN, I. A. 1965 *Handbook of Mathematical Functions*. Dover.

ALEKSEENKO, S. V., KUIBIN, P. A. & OKULOV, V. L. 2007 *Theory of Concentrated Vortices: An Introduction*. Springer.

BOERSMA, J. & WOOD, D. H. 1999 On the self-induced motion of a helical vortex. *J. Fluid Mech.* **384**, 263–280.

BOLNOT, H. 2012 Instabilités des tourbillons hélicoïdaux: application au sillage des rotors. PhD thesis, Aix Marseille University.

BOLNOT, H., LE DIZÈS, S. & LEWEKE, T. 2014 Spatio-temporal development of the pairing instability in an infinite array of vortex rings. *Fluid Dyn. Res.* **46**, 061405.

CALLEGARI, A. J. & TING, L. 1978 Motion of a curved vortex filament with decaying vortical core and axial velocity. *SIAM J. Appl. Maths* **35**, 148–175.

DELBENDE, I., PITON, B. & ROSSI, M. 2015 Merging of two helical vortices. *Eur. J. Mech.* (*B/Fluids*) **49**, 363–372.

DELBENDE, I., ROSSI, M. & DAUBE, O. 2012*a* DNS of flows with helical symmetry. *J. Theor. Comput. Fluid Dyn.* **26**, 141–160.

DELBENDE, I., ROSSI, M. & PITON, B. 2012*b* Direct numerical simulation of helical vortices. *Intl J. Engng Systems Model. Simul.* **4**, 94–101.

ELOY, C. & LE DIZÈS, S. 1999 Three-dimensional instability of Burgers and Lamb-Oseen vortices in a strain field. *J. Fluid Mech.* **378**, 145–166.

FUKUMOTO, Y. 2002 Higher-order asymptotic theory for the velocity field induced by an inviscid vortex ring. *Fluid Dyn. Res.* **30**, 67–95.

FUKUMOTO, Y. & HATTORI, Y. 2005 Curvature instability of a vortex ring. *J. Fluid Mech.* **526**, 77–115.

FUKUMOTO, Y. & MIYAZAKI, T. 1991 Three-dimensional distorsions of a vortex filament with axial velocity. *J. Fluid Mech.* **222**, 369–416.

FUKUMOTO, Y. & MOFFATT, H. K. 2000 Motion and expansion of a viscous vortex ring. Part 1. A higher-order asymptotic formula for the velocity. *J. Fluid Mech.* **417**, 1–45.

FUKUMOTO, Y. & OKULOV, V. L. 2005 The velocity induced by a helical vortex tube. *Phys. Fluids* **17**, 107101.

HARDIN, J. C. 1982 The velocity field induced by a helical vortex filament. *Phys. Fluids* **25** (11), 1949–1952.

HATTORI, Y. & FUKUMOTO, Y. 2003 Short-wavelength stability analysis of thin vortex rings. *Phys. Fluids* **15**, 3151–3163.

HATTORI, Y. & FUKUMOTO, Y. 2009 Short-wavelength stability analysis of a helical vortex tube. *Phys. Fluids* **21**, 014104.

HATTORI, Y. & FUKUMOTO, Y. 2014 Modal stability analysis of a helical vortex tube with axial flow. *J. Fluid Mech.* **738**, 222–249.

KERSWELL, R. R. 2002 Elliptical instability. *Annu. Rev. Fluid Mech.* **34**, 83–113.

KUIBIN, P. A. & OKULOV, V. L. 1998 Self-induced motion and asymptotic expansion of the velocity field in the vicinity of a helical vortex filament. *Phys. Fluids* **10**, 607–614.

LACAZE, L., RYAN, K. & LE DIZÈS, S. 2007 Elliptic instability in a strained batchelor vortex. *J. Fluid Mech.* **577**, 341–361.

LAMB, H. 1932 *Hydrodynamics*, 6th edn. Cambridge University Press.

LE DIZÈS, S. & VERGA, A. 2002 Viscous interaction of two co-rotating vortices before merging. *J. Fluid Mech.* **467**, 389–410.

LEVY, H. & FORSDYKE, A. G. 1927 The stability of an infinite system of circular vortices. *Proc. R. Soc. Lond.* A **114**, 594–604.

LEWEKE, T., QUARANTA, H. U., BOLNOT, H., BLANCO-RODRIGUEZ, F. J. & LE DIZÈS, S. 2014 Long- and short-wave instabilities in helical vortices. *J. Phys.: Conf. Ser.* **524**, 012154.

MOFFATT, H. K., KIDA, S. & OHKITANI, K. 1994 Stretched vortices – the sinews of turbulence; large-Reynolds-number asymptotics. *J. Fluid Mech.* **259**, 241–264.

MOORE, D. W. & SAFFMAN, P. G. 1972 The motion of a vortex filament with axial flow. *Phil. Trans. R. Soc. Lond.* A **272**, 403–429.

OKULOV, V. L. 2004 On the stability of multiple helical vortices. *J. Fluid Mech.* **521**, 319–342.

RICCA, R. L. 1994 The effect of torsion on the motion of a helical vortex filament. *J. Fluid Mech.* **273**, 241–259.

ROY, C., LEWEKE, T., THOMPSON, M. C. & HOURIGAN, K. 2011 Experiments on the elliptic instability in vortex pairs with axial core flow. *J. Fluid Mech.* **677**, 383–416.

SAFFMAN, P. G. 1992 *Vortex Dynamics*. Cambridge University Press.

TING, L. & TUNG, C. 1965 Motion and decay of a vortex in a nonuniform stream. *Phys. Fluids* **8**, 1039.

WIDNALL, S. E. 1972 The stability of a helical vortex filament. *J. Fluid Mech.* **54**, 641–663.

WIDNALL, S. E., BLISS, D. & TSAI, C.-Y. 1974 The instability of short waves on a vortex ring. *J. Fluid Mech.* **66**, 35–47.

WIDNALL, S. E., BLISS, D. B. & ZALAY, Y. 1971 Theoretical and experimental study of the stability of a vortex pair. In *Aircraft Wake Turbulence and Its Detection* (ed. J. H. Olsen, A. Goldburg & M. Rogers), pp. 305–338. Springer.

WIDNALL, S. E. & TSAI, C.-Y. 1977 The instability of the thin vortex ring of constant vorticity. *Phil. Trans. R. Soc. Lond.* A **287**, 273–305.

Chapter 8

Linear Stability analysis in the helical framework

Contents

In this chapter, the linear stability analysis within the helical framework is presented. In section 8.1, the base flow $\boldsymbol{u}$ is described. The perturbation equations for $\boldsymbol{u'}$ and $\boldsymbol{\omega'}$, in the helical framework, are provided in 8.2. The Arnoldi method used to extract the eigenvalues and the associated eigenvectors is detailed in 8.3. The method is then validated in the laboratory frame with two well documented cases in section 8.4. Finally an analysis is provided for the cases requiring a rotating frame of reference (section 8.5), highlighting the need of a very high accuracy on the computed angular velocity Ω.

8.1 Basic state solutions in the rotating frame: frozen quasi-equilibrium solutions

Let us consider quasi-equilibrium solutions of one or an array of N identical helical vortices which were presented in chapter 6. These solutions are obtained numerically and are unsteady since their core size and angular velocity are slowly changing with time. In this chapter, we define a basic state solution as follows. First, we consider the flow structure corresponding to the quasi-equilibrium solution at a given time τ_b. This flow structure is characterized by a set of parameters: the core size $a = a\,(\tau_b)$, the helix radius $r_A\,(\tau_b)$, the angular velocity $\Omega\,(\tau_b)$ at time τ_b and the reduced pitch L. Second, the basic state solution is defined as being this flow structure (velocity $\boldsymbol{u}(\tau_b)$, vorticity $\boldsymbol{\omega}(\tau_b)$) in steady

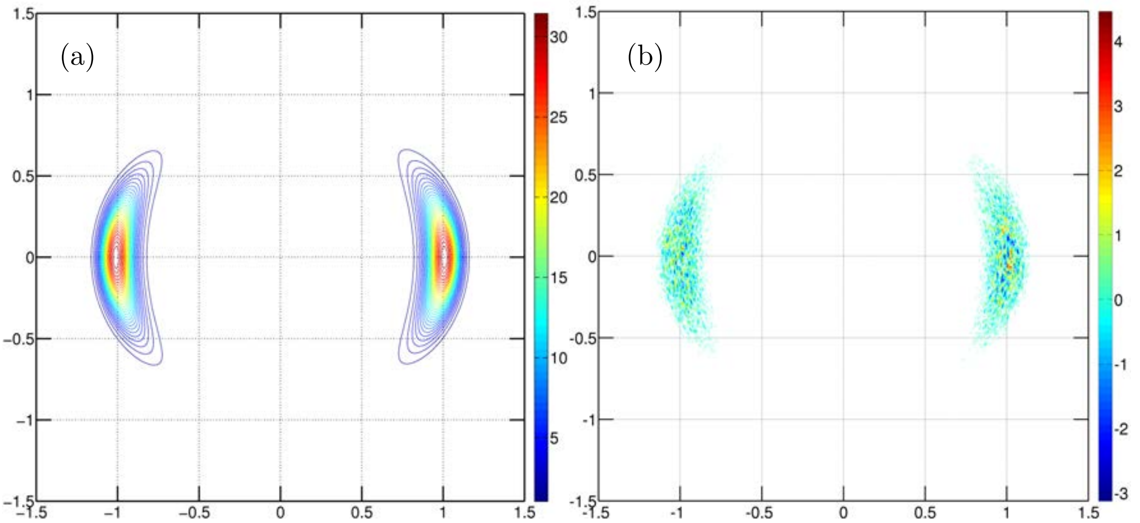

Figure 8.1 – Stability analysis of $N = 2$ helical vortices of reduced pitch $L = 0.3$ with core size $a_b = 0.09$. (a) Frozen base flow : contours of the helical vorticity component ω_B in the Π_0 plane. Note that the x and y are chosen such that vortex centres are aligned at $y = 0$. (b) Initial helical vorticity perturbations ω'_B in Π_0.

rotation at angular velocity $\Omega(\tau_b)$. Such a solution is clearly not a strict Navier-Stokes solution. In a way we introduce a body force term to counterbalance the viscous diffusion. This is justified for the range of flows we consider which are typically at high Reynolds number, similarly to what is current practice for shear flow stability analysis. To perform the stability analysis, it is preferable to be in the frame of reference rotating with the vortices at $\Omega(\tau_b)$. This is performed by removing the solid body rotation from the helical vorticity and velocity components as:

$$u_B^R = u_B - \frac{r^2}{L}\alpha\Omega(\tau_b), \tag{8.1}$$

$$u_\varphi^R = u_\varphi - r\alpha\Omega(\tau_b), \tag{8.2}$$

$$\omega_B^R = \omega_B - 2\alpha\Omega(\tau_b), \tag{8.3}$$

$$\omega_\varphi^R = \omega_\varphi + \frac{2r}{L}\alpha\Omega(\tau_b). \tag{8.4}$$

In this frame, the basic flow is steady and standard temporal stability analysis can be performed. By freezing the basic state, the associated diffusion process is neglected. However the viscous diffusion acts on perturbations. A typical frozen basic state is depicted in figure 8.1-a.

8.2 Perturbation equations in the helical and rotating framework

The velocity and vorticity in the rotating frame of reference are written as a superposition of the basic state $\boldsymbol{u^R}, \boldsymbol{\omega^R}$ and perturbations $\boldsymbol{u'}, \boldsymbol{\omega'}$:

$$\boldsymbol{u^R_{tot}} = \boldsymbol{u^R} + \boldsymbol{u'} \tag{8.5}$$

$$\boldsymbol{\omega^R_{tot}} = \boldsymbol{\omega^R} + \boldsymbol{\omega'} \tag{8.6}$$

In the framework of helical symmetry, the equations for the perturbations are first written in the rotating frame of reference. This introduces a Coriolis force into the equations (2.29) and (2.32) (see appendix F for additional details). By linearising these equations in the rotating frame of reference, the dynamical equation for the velocity perturbation u'_B is obtained

$$\frac{\partial}{\partial t}u'_B + \omega^R_r u'_\varphi + u^R_\varphi \omega'_r - (\omega^R_\varphi u'_r + u^R_r \omega'_\varphi) + \frac{2\Omega}{L}\alpha r u'_r = \nu\left[\mathbb{L}\left(\frac{u'_B}{\alpha}\right) - 2\frac{\alpha^2}{L}\omega'_B\right]. \tag{8.7}$$

And the dynamical equation for the vorticity perturbation ω'_B, which has a rather more complicated form, becomes :

$$\begin{aligned}&\frac{\partial}{\partial t}\omega'_B + \frac{1}{r\alpha}\frac{\partial}{\partial r}\left(r\alpha\left(\omega^R_B u'_r + u^R_r \omega'_B\right)\right) + \frac{1}{r\alpha}\frac{\partial}{\partial \varphi}\left(\omega^R_B u'_\varphi + u^R_\varphi \omega'_B\right)\\ &+ \frac{2\alpha^2}{L}\left[\omega^R_r u'_\varphi + u^R_\varphi \omega'_r - \left(\omega^R_\varphi u'_r + u^R_r \omega'_\varphi\right)\right] + \frac{\alpha}{L^2}\frac{\partial}{\partial \varphi}\left(2u^R_B u'_B\right) + \frac{2\Omega}{L}\frac{\partial u'_B}{\partial \varphi}\\ &= \nu\left[\mathbb{L}\left(\frac{\omega'_B}{\alpha}\right) - \left(2\frac{\alpha^2}{L}\right)^2\omega'_B\right] + \nu\frac{2\alpha^2}{L}\mathbb{L}\left(\frac{u'_B}{\alpha}\right).\end{aligned} \tag{8.8}$$

As the modified Laplace operator $\mathbb{L}$ is linear, the third equation linking the streamfunction perturbation Ψ' to ω'_B and u'_B directly reads:

$$\mathbb{L}\,\Psi' = 2\frac{\alpha^2}{L}u'_B - \omega'_B. \tag{8.9}$$

In the system of dynamical equations (8.7)-(8.8), the other perturbation components $u'_r, u'_\varphi, \omega'_r$ and ω'_φ also appear. These components can be expressed from u'_B, ω'_B and Ψ' using formulas (2.17)-(2.18) and (2.20)-(2.21). At this point, by introducing the perturbation vector $\boldsymbol{p'} = (u'_B, \omega'_B, \Psi')^T$, the whole linear system can be rewritten as

$$\mathbf{B}\frac{\partial \boldsymbol{p'}}{\partial t} = \mathbf{J}\boldsymbol{p'}, \tag{8.10}$$

where a mass matrix $\mathbf{B}$ and the Jacobian matrix $\mathbf{J}$ have been introduced:

$$\mathbf{B} = \begin{pmatrix}1 & 0 & 0\\ 0 & 1 & 0\\ 0 & 0 & 0\end{pmatrix}, \quad \mathbf{J} = \begin{pmatrix}J_{11} & J_{12} & J_{13}\\ J_{21} & J_{22} & J_{23}\\ 2\frac{\alpha^2}{L} & -1 & -\mathbb{L}\end{pmatrix}. \tag{8.11}$$

The system (8.10) can be further reduced with the help of equation (8.9) which implies that Ψ' can be also formally expressed from u'_B and ω'_B as:

$$\Psi' = \mathbb{L}^{-1}\left\{2\frac{\alpha^2}{L}u'_B - \omega'_B\right\}. \tag{8.12}$$

Upon introducing the reduced perturbation vector $\boldsymbol{q'} = (u'_B\ , \omega'_B)^T$ of length $2N$ with $N = N_r \times N_\theta$, the total number of grid points, we rewrite the linearised Navier-Stokes system as :

$$\frac{\partial}{\partial t}\boldsymbol{q'} = \mathbf{A}\,\boldsymbol{q'} \tag{8.13}$$

where $\mathbf{A}$ is a linear operator and $\boldsymbol{q'}(t_0) = \boldsymbol{q'_0}$ is a given initial condition.

8.3 The Arnoldi method

8.3.1 Initial condition: random noise

The algorithm we use requires to start the linear simulation from a perturbation consisting in synthetic noise for $\boldsymbol{q'_0}$. This perturbation is computed in the Π_0 plane as follows. In a

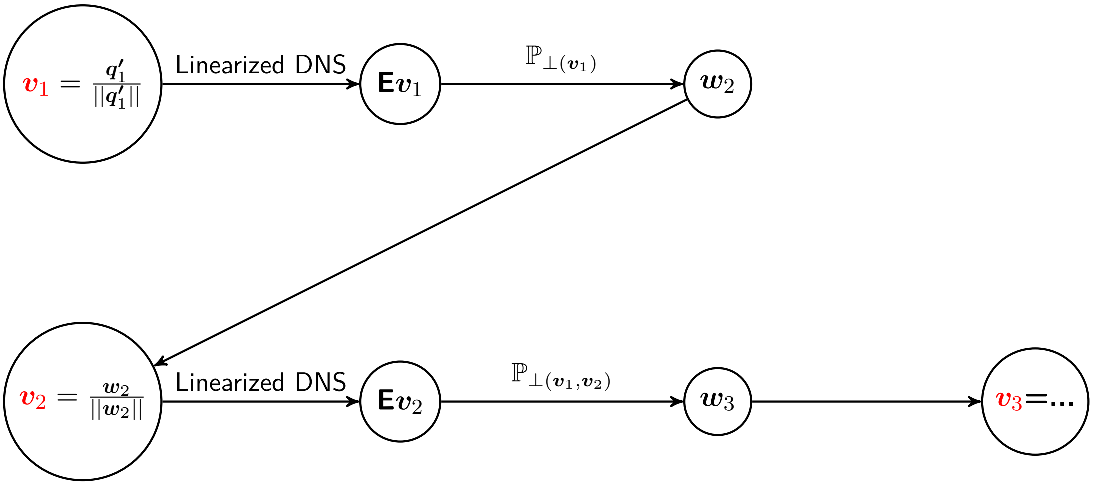

Figure 8.2 – Sketch of the first two iterations of the Arnoldi algorithm.

first step, one initiates the helical components

$$\omega_B'^{(m)} = n_w'^{(m)}(r)\, g_m(r, r_1, r_2), \quad u_B'^{(m)} = n_u'^{(m)}(r)\, g_m(r, r_1, r_2) \tag{8.14}$$

in Fourier space using random distributions $n_w^{(m)\prime}$ and $n_u^{(m)\prime}$ with values in the interval $[-1; 1]$ and a function defined $g_m(r)$ for each azimuthal wavenumber m:

$$g_m(r; r_1, r_2) = \frac{(r/r_1)^m}{1 + (r/r_1)^m} e^{-(r/r_2)^6}. \tag{8.15}$$

The fraction in formula (8.15) ensures that for $m \neq 0$, $\omega_B'^{(m)}$ and $u_B'^{(m)}$ tend to zero at the origin while the exponential part causes the noise to vanish in the vicinity of the outer boundary at $r = R_{ext}$ where the flow is supposed to be potential. The random fields thus take significant values within the interval $[r_1, r_2]$. In our simulations these two parameters are set to $r_1 = r_A/2$ and $r_2 = 2r_A$. In order to improve the convergence of the algorithm, a second step was found necessary: the fields (8.14) are further multiplied by the respective base flow components $\omega_B(\tau_b)$ and $u_B(\tau_b)$ in the physical space. This eventually leads to initial random fields spatially localized within the vortex structures as shown in figure 8.1-b.

8.3.2 Time stepper approach

The instability features of the flow system are given by the eigenpairs $(\lambda_A, \boldsymbol{v}_A)$ of the Jacobian matrix $\mathbf{A}$. In practice, after discretisation, the dimension of such matrix becomes too large to even consider the storage and the direct computation of its eigenvalues. Instead, a time stepper and matrix-free approach is considered. The exact solution of (8.13) with initial condition $\boldsymbol{q}_1' = \boldsymbol{q}'(t_1)$ can be written as:

$$\boldsymbol{q}'(t_1 + \Delta t) = e^{\Delta t\, \mathbf{A}}\, \boldsymbol{q}_1' = \mathbf{E}\, \boldsymbol{q}_1', \tag{8.16}$$

the operator $\mathbf{E} \equiv e^{\Delta t\, \mathbf{A}}$, represents the time or exponential propagator of the system (8.13) between times t_1 and $t_1 + \Delta t$. At first sight, introducing this operator does not simplify the original computational cost and storage problem. The resulting matrix is also of large dimension as well, and numerical matrix exponentiation is known to be a challenging task. Although $e^{\Delta t\, \mathbf{A}}$ is as computationally expensive to construct as the Jacobian $\mathbf{A}$, the action of the exponential propagator onto a vector $\boldsymbol{q}_1'$ can be easily obtained by simply time-marching the linearised Navier-Stokes equations with $\boldsymbol{q}_1'$ as initial condition. Also,

```
$\boldsymbol{v_1} = \boldsymbol{q_1'}/\|\boldsymbol{q_1'}\|$ with $\boldsymbol{q_1'}$ a starting vector
Time advance
$\boldsymbol{w} \leftarrow \mathbf{E}\boldsymbol{v_1}$
Gram-Schmidt orthogonalization
$h_{11} \leftarrow (\boldsymbol{v_1}, \boldsymbol{w})$
$\boldsymbol{w_2} \leftarrow \boldsymbol{w} - \boldsymbol{v_1} h_{11}$
Normalisation
$h_{21} \leftarrow \|\boldsymbol{w_2}\|$
$\boldsymbol{v_2} \leftarrow \boldsymbol{w_2}/h_{21}$
for k=2,....K do
    $\boldsymbol{w} \leftarrow \mathbf{E}\boldsymbol{v_k}$
    $h_{lk} \leftarrow (\boldsymbol{v_l}, \boldsymbol{w})$ for $l = 1, ...., k$
    if $k \leq K - 1$ then
        $\boldsymbol{w_{k+1}} \leftarrow \boldsymbol{w} - \sum_{l=1}^{k} \boldsymbol{v_l} h_{lk}$
        $h_{k+1,k} \leftarrow \|\boldsymbol{w_{k+1}}\|$
        $\boldsymbol{v_{k+1}} \leftarrow \boldsymbol{w_{k+1}}/h_{k+1,k}$
    end if
end for
```

Figure 8.3 – Arnoldi algorithm implemented within the linearised version of HELIX, with the first step $k = 1$ of the algorithm detailed.

the eigenpairs $(\lambda_A, \boldsymbol{v}_A)$ of the Jacobian matrix $\mathbf{A}$ are related to those $(\lambda_E, \boldsymbol{v}_E)$ of the exponential propagator $\mathbf{E}$ by:

$$\lambda_E = e^{\Delta t \lambda_A}, \quad \boldsymbol{v}_A = \boldsymbol{v}_E. \tag{8.17}$$

Since the action of the exponential operator onto a given vector is obtained by temporal simulation steps, this technique is much more efficient than the direct determination of the spectrum of the Jacobian matrix.

8.3.3 The Arnoldi algorithm

The eigenvalue algorithm onto which the above time-stepper approach is relying is the Arnoldi algorithm. The Arnoldi algorithm was introduced in the early 1950s by W.E. Arnoldi as a generalisation of the Lanczos method for Hermitian matrices. The utility of the Arnoldi method comes from its ability to generate accurate eigenvalue approximations from a partial, rather than full, upper Hessenberg factorisation of a matrix (Carden, 2012). Both methods approximate eigenvalues by orthogonally projecting a matrix onto a Krylov subspace. Given the exponential propagator $\mathbf{E}$ and an initial vector $\boldsymbol{q_1'}$, a Krylov subspace $\mathcal{K}_K$ of dimension K is spanned by the iterates of the power method,

$$\mathcal{K}_K(\mathbf{E}, \boldsymbol{q_1'}) = \text{span}\left\{\boldsymbol{q_1'}, \mathbf{E}\boldsymbol{q_1'}, \mathbf{E}^2\boldsymbol{q_1'}, ..., \mathbf{E}^{K-1}\boldsymbol{q_1'}\right\}. \tag{8.18}$$

The power method is an eigenvalue method that approximates only one single eigenvector associated with the eigenvalue of largest magnitude. To overcome this restriction, the Arnoldi algorithm combines the power iteration method with a Gram-Schmidt orthogonalisation process. By generating an orthonormal basis for the Krylov subspace, one can look for an accurate approximation of the $K \ll N$ leading eigenpairs $(\lambda_E, \boldsymbol{v}_e)$ of the operator $\mathbf{E}$ without explicitly constructing $\mathbf{E}$. The sought eigenpairs $(\lambda_A, \boldsymbol{v}_A)$ of $\mathbf{A}$ are then recovered with equation (8.17). The first steps of the Arnoldi algorithm are sketched in figure 8.2 and the complete algorithm are provided in figure 8.3. Each step k of the algorithm generates a new basis vector $\boldsymbol{v_k}$ such that $\|\boldsymbol{v_k}\| = 1$ and $\boldsymbol{v_k} \perp \mathcal{K}_j$ for $j < k$ and $\boldsymbol{v_k} \in \mathcal{K}_k(\mathbf{E}, \boldsymbol{q_0'})$. At the kth iteration of the algorithm, the orthonormal matrix $\mathbf{V_k}$ containing the k basis vectors $\boldsymbol{v_1}, \boldsymbol{v_2}, ..., \boldsymbol{v_k}$ on its columns, satisfies

$$\mathbf{E}\mathbf{V_k} = \mathbf{V_k}\mathbf{H_k} + h_{k+1,k}\boldsymbol{v_{k+1}}\boldsymbol{e}_k^*, \tag{8.19}$$

with $\mathbf{H_k}$, an upper Hessenberg matrix with elements $[\mathbf{H_k}]_{i,j} = h_{i,j}$ and where $\boldsymbol{e}_k$ is the k-th element of the canonical basis. Note that the residual term $h_{k+1,k}$ indicates how far $\mathbf{V_k}$ is from an invariant subspace of $\mathbf{E}$. Indeed, if $h_{k+1,k} = 0$, the subspace generated by the columns of $\mathbf{V_k}$ is an eigenspace of $\mathbf{E}$ and the eigenvalues of $\mathbf{H_k}$ are also eigenvalues of $\mathbf{E}$. Generally, $h_{k+1,k}$ is not zero. However if this quantity is small enough, (i) the eigenvalues λ_H of $\mathbf{H}$ are good approximations of the leading eigenvalues of $\mathbf{E}$ i.e.

$$\lambda_E \approx \lambda_H \tag{8.20}$$

(ii) the eigenvectors $\boldsymbol{v_H}$ of $\mathbf{H}$ left multiplied by $\mathbf{V_k}$ provide the Ritz vectors $\boldsymbol{v_E^R}$ close to the eigenvectors of $\mathbf{E}$:

$$\boldsymbol{v_E} \approx \boldsymbol{v_E^R} = \mathbf{V_k}\,\boldsymbol{v_H}. \tag{8.21}$$

The residual norm r_k associated to the kth Ritz pair $(\lambda_H, \boldsymbol{v_E^R})$ can be computed as

$$\begin{aligned}
\mathbf{E}\boldsymbol{v_E^R} - \lambda_H\boldsymbol{v_E^R} &= \mathbf{E}\mathbf{V_k}\,\boldsymbol{v_H} - \lambda_H\mathbf{V_k}\boldsymbol{v_h} && (8.22)\\
&= \mathbf{V_k}\mathbf{H_k}\boldsymbol{v_H} + h_{k+1,k}\boldsymbol{v_{k+1}}\boldsymbol{e}_k^*\boldsymbol{v_H} - \lambda_H\mathbf{V_k}\boldsymbol{v_H} && (8.23)\\
&= \lambda_H\mathbf{V_k}\boldsymbol{v_H} + h_{k+1,k}\boldsymbol{v_{k+1}}\boldsymbol{e}_k^*\boldsymbol{v_H} - \lambda_H\mathbf{V_k}\boldsymbol{v_H} && (8.24)\\
&= h_{k+1,k}\boldsymbol{v_{k+1}}\boldsymbol{e}_k^*\boldsymbol{v_H} && (8.25)
\end{aligned}$$

and hence

$$r_k = \left\|\mathbf{E}\boldsymbol{v_H^R} - \lambda_H\boldsymbol{v_E^R}\right\| = |h_{k+1,k}||\boldsymbol{e}_k^*\boldsymbol{v_H}|. \tag{8.26}$$

This quantity is useful to monitor the accuracy of the Ritz pairs as approximations of the eigenpairs of $\mathbf{E}$. Note that quantities r_k can only be computed at the end of the process because $\boldsymbol{v_H}$ is only obtained at the end and depends on K the total number of Ritz pairs determined.

8.3.4 Time-stepping and orthogonalisation

In practice the Arnoldi algorithm is exploited as follows (Edwards et al., 1994). The action of $\mathbf{E}$ is obtained by time marching the linearised code over a time interval Δt. This process is repeated K times: the orthonormal basis $\boldsymbol{v_1}, ..., \boldsymbol{v_K}$ of the Krylov subspace as well as the upper Hessenberg matrix $\mathbf{H_K}$ are progressively generated during the computation. As the upper Hessenberg matrix $\mathbf{H_K}$ is of a relatively small dimension ($K \times K$), the direct computation of its eigenpairs $(\lambda_H, \boldsymbol{v}_H)$ is done at low computational cost and memory requirement. The Arpack routine zgeemm is used for the diagonalisation.
Using formulas (8.17), (8.20) and (8.21) the eigenpairs $(\lambda_A, \boldsymbol{v}_A)$ are such that:

$$\begin{aligned}
e^{\lambda_A \Delta t} &\approx \lambda_H && (8.27)\\
\boldsymbol{v}_A &\approx \mathbf{V_K}\,\boldsymbol{v}_H, && (8.28)
\end{aligned}$$

where $\sigma = \Re\{\lambda_A\}$ is the growth rate of the instability mode and $\omega = \Im\{\lambda_A\}$, the associated temporal frequency. The time interval Δt and the number K of computed eigenmodes depend on the specific case under study. Modes are easily extracted if their growth rates are well separated. For two modes with growth rates $\sigma_1 > \sigma_2$, this means that $e^{\sigma_1 \Delta t} \gg e^{\sigma_2 \Delta t}$ so that $\Delta t \gg 1/(\sigma_1 - \sigma_2)$. As a consequence, selected values for Δt can be very large.

However choosing too large a Δt causes an additional issue: according to equation (8.27), the frequency ω is such that

$$\log \lambda_H = \sigma \Delta t + \mathrm{i}\omega \Delta t + 2\ \mathrm{i}p\pi, \qquad \text{with} \ \ p \in \mathbb{Z} \tag{8.29}$$

or

$$\omega = \frac{\Im \left\{\log \lambda_H\right\} + 2p'\pi}{\Delta t} \qquad \text{with} \ \ p' \in \mathbb{Z} \tag{8.30}$$

but the integer p' is not known. A solution to this problem is proposed on the next subsection.

8.3.5 Recovery of the temporal frequency ω of the modes when Δt is chosen too big.

As mentioned in this context by Loiseau et al. (2014), a mode oscillating at a given frequency ω, can be captured if the Nyquist criterion is satisfied: one needs at least four snapshots to appropriately represent one time period. Hence, a given sampling period Δt, gives only access to the modes oscillating at a frequency less than $2\pi/4\Delta t$. For a given ω, this imposes the following condition on Δt:

$$\Delta t \leq \frac{\pi}{2\omega}, \tag{8.31}$$

which implies that $p' = 0$ in equation (8.30). When Δt is chosen larger than $\pi/(2\omega)$ (for instance, in order to ensure a satisfactorily convergence for the companion growth rate), the information on the temporal frequency is a priori lost because the value of p' in equation (8.30) is unknown. We propose the following procedure to recover ω. We perform a short additional simulation where the real part of an eigenmode $\boldsymbol{v}_A$ is chosen as initial condition and time integrated over a short time interval Δt_ω to yield

$$\boldsymbol{v}'_A = \boldsymbol{v}_A e^{(\sigma + \mathrm{i}\omega)\Delta t_\omega}. \tag{8.32}$$

The frequency ω is then found by minimizing the correlation integral $I(\omega)$, defined by

$$I(\omega) \equiv \iint_S \Re \left\{ \boldsymbol{v}'_A e^{-\sigma \Delta t_\omega} - \boldsymbol{v}_A e^{\mathrm{i}\omega \Delta t_\omega} \right\}^2 \mathrm{d}S. \tag{8.33}$$

In practice, a value $\Delta t_\omega = 10\delta t$ is chosen. This procedure is applied for all the eigenmodes $j = 1, ..., K$ and frequencies ω_j are obtained with an accuracy of 10^{-10}.

8.4 Validation of the Arnoldi implementation in fixed frame

In the section, the validation of the Arnoldi algorithm is described. Unstable modes for two well documented cases are investigated with the Arnoldi method and the results are compared to those given by a dedicated stability code and also to the results of the literature.

8.4.1 Linear modes of the Batchelor or q-vortex.

The Batchelor vortex or q-vortex, is an analytical solution of the unsteady Navier-Stokes equations which is a suitable model for wake vortices and swirling jets. This widely studied, axisymmetric vortex model has the particularity that the axial velocity and vorticity

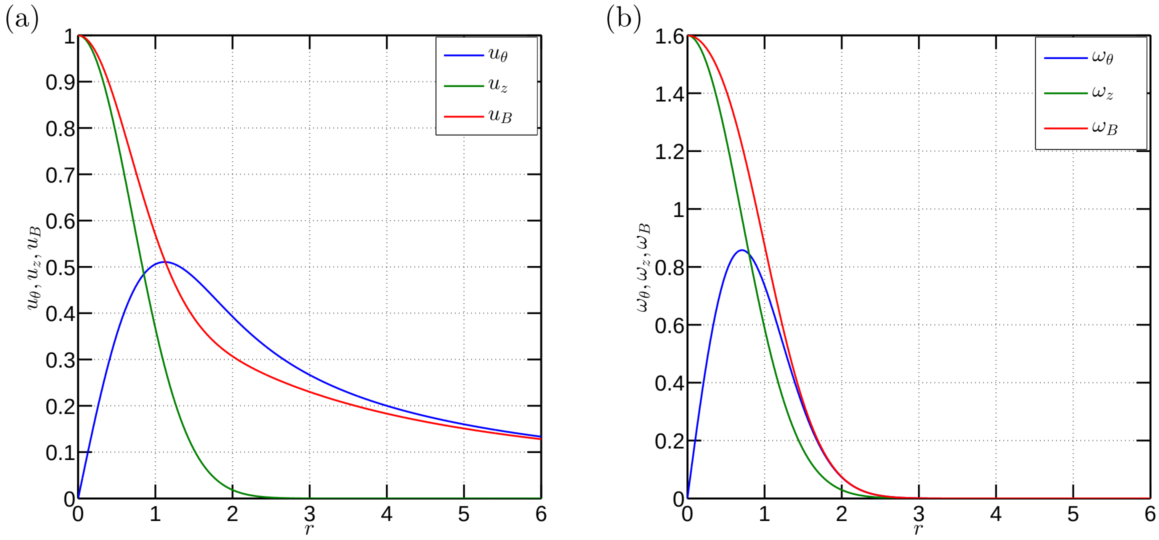

Figure 8.4 – Batchelor vortex for swirl parameter $q = 0.8$ in the helical framework with $L = 1.76$. (a) The azimuthal u_θ and axial u_z components are combined to yield the helical velocity component u_B (equation (8.37)). (b) The Azimuthal ω_θ and axial ω_z vorticity components are combined to yield the helical vorticity ω_B (equation by (8.38)).

profiles are both Gaussian. When expressed with dimensional quantities, (denoted by the + symbol) the axial and azimuthal components of velocity and vorticity are given by :

$$u_z^+ = U_z e^{-(r^+/a)^2}, \quad u_\theta^+ = \frac{\Gamma}{2\pi r^+}\left(1 - e^{-(r^+/a)^2}\right) \tag{8.34}$$
$$\omega_z^+ = 2qU_z e^{-(r^+/a)^2}, \; \omega_\theta^+ = 2U_z \frac{r^+}{a^2} e^{-(r^+/a)^2}$$

with the swirl parameter q defined as

$$q = \frac{\Gamma}{2\pi a U_z} \tag{8.35}$$

and where a and U_z are the characteristic length and velocity scale used to define the Reynolds number

$$Re = \frac{aU_z}{\nu}. \tag{8.36}$$

Introducing the dimensionless variables $r = r^+/a$ and $u = u^+/U_z$ the helical components of vorticity and vorticity read

$$u_B = \alpha\left(u_z + \frac{r}{L}u_\theta\right) = \alpha\left(\frac{q}{L} + e^{-r^2}\left(1 - \frac{q}{L}\right)\right) \tag{8.37}$$

$$\omega_B = \alpha\left(\omega_z + \frac{r}{L}\omega_\theta\right) = 2\alpha e^{-r^2}\left(q + \frac{r^2}{L}\right) \tag{8.38}$$

Velocity and vorticity profiles are plotted in figure (8.4) for swirl number $q = 0.8$. For any axisymmetric base flow, the perturbations can be expanded on modes with azimuthal wavenumber m, positive axial wavenumber k and complex frequency ω :

$$(u_r', u_\theta', u_z', p')(r, \theta, z, t) = (\hat{u}_r(r), \hat{u}_\theta(r), \hat{u}_z(r), \hat{p}(r)) \exp\left[\mathrm{i}(kz + m\theta - \omega t)\right], \tag{8.39}$$

where hat variables are complex eigenfunctions. The flow composed of the base flow plus one such instability mode displays helical symmetry. Indeed the expression $kz + m\theta =$

$m(\theta + kz/m)$ can be written as $m(\theta - z/L) = m\varphi$ with the reduced pitch $L = -m/k$. In that instance, components (8.39) become functions only on r, φ and t and since the complete phase writes $m\varphi - \omega t$, the mode rotates around the z-axis with angular velocity $\Omega = \omega/m$.

The Batchelor vortex is known to be unstable for swirl number $q \lesssim 1.5$ at $Re = 1000$, and is subject to a large family of unstable modes. For instance, at $q = 0.8$, azimuthal modes $-16 \leq m \leq -1$ are unstable and the flow is found stable with respect to perturbations with axial wavenumber $k > 10.4$. Moreover, for each fixed azimuthal wavenumber m and axial wavenumber k, there generally exists an infinite number of instability modes labelled by $j = 0, 1, 2, ...$ with increasingly complex radial structures and decreasing growth rates

$$\sigma_0 > \sigma_1 > \sigma_2 > \cdots . \tag{8.40}$$

Depending on the values m and k, some of these modes are amplified (or none of them). The Batchelor vortex is thus a good test case for the Arnoldi method discussed previously. The vortex, which is axisymmetric, is centred at the origin and thus complies with the helical symmetry for any value of L. The initial condition $\boldsymbol{q_0'} = (u_B', \omega_B')$ is set in spectral space using a random noise

$$\hat{u}_B'^{(m)}(r_i) = c\, n_u^{(m)}(r_i)\, r_i^m e^{-r_i^2} \tag{8.41}$$

where c is an amplitude and $n_u^{(m)}$ is a random function with values in $[-1, 1]$. A similar formula is used for the helical vorticity component $\hat{\omega}_B'^{(m)}(r)$. For a given value of L, all the modes with azimuthal wavenumber m and axial wavenumber k, satisfying the relation

$$L = -m/k \tag{8.42}$$

will be excited. In the following only the range of azimuthal modes $0 \leq m \leq 4$ are chosen to be excited in order to limit the number of unstable mode and hence the number K of Krylov vector to be computed. Note that equation (8.41) is slightly different from (8.15) and is actually an earlier version of the noise initialisation yielding similar results.

Results and comparisons for $q = 0.8$ and $Re = 1000$ and $L = 1.76$

We apply the Arnoldi method to the case $q = 0.8$ and $Re = 1000$ with the helical pitch $L = 1.76$. For this test, we chose parameters $K = 20$ and $\Delta t = 20$. The dominant modes are represented in figure 8.5. It is seen that they correspond to azimuthal structures $m = -4, -3$ and $m = -2$. For comparison purposes, the axial wavenumbers are deduced from (8.42) to be respectively $k = 2.266, k = 1.700$ and $k = 1.133$. It can also be seen on figure 8.5, that the radial structure of the modes corresponds to $j = 0$ on the top row and to $j = 1$ on the bottom row. The growth rates are given in table 8.1 (column $\sigma_{Arnoldi}$ and compared with the theoretical values obtained from Delbende and Rossi (2005) (column σ_{th}). The comparisons of the frequencies are also presented. For $K = 20$ and $\Delta t = 20$, we obtain a relative error of the order of 10^{-4}. Note however that for the mode in the last line of table 8.1, the accuracy is deteriorated as confirmed by figure 8.5-f. Still, the dipolar structure of the mode is distinguishable, suggesting that it is possible to improve the accuracy on this mode by increasing K and/or Δt.

In this case for $L = 1.76$ and the set of Arnoldi parameters $K = 20$, $\Delta t = 20$, among all the modes which satisfies the relation (8.42), the following modes with their (first) secondary modes have emerged:

$$m = -2 \rightarrow k = 1.133$$
$$m = -3 \rightarrow k = 1.7$$
$$m = -4 \rightarrow k = 2.266$$

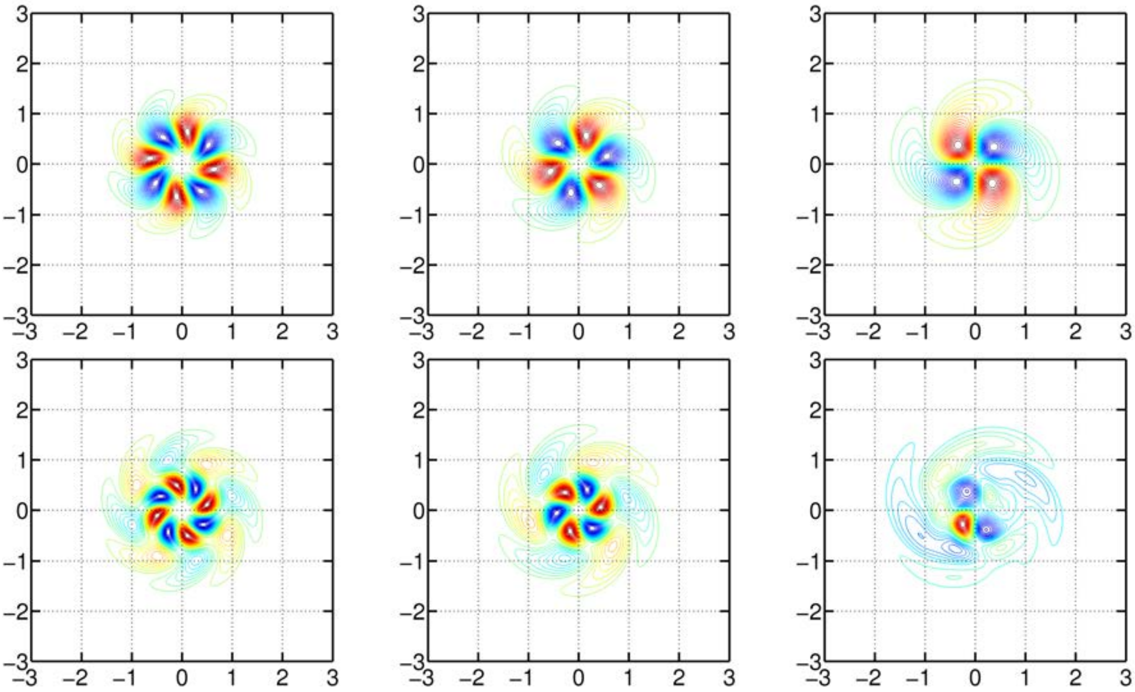

Figure 8.5 – Batchelor vortex: structure of the unstable helical modes obtained with the Arnoldi algorithm with parameters $K = 20$, $\Delta t = 20$. Left figures: mode $m = -4, k = 2.266$. Central figures: mode $m = -3, k = 1.7$. Right figures: mode $m = -2, k = 1.133$. First row : most unstable modes ($j = 1$ in (8.40)). Second row : Secondary modes with lower positive growth rates ($j = 2$ in (8.40)). Note that the last secondary mode $m = -2, k = 1.133$ didn't converge perfectly for this set of parameters. Still, the dipolar structure is distinguishable, suggesting that increasing the number K of the number of vectors spanning the Krylov subspace would improve this.

Mode label	σ_{th}	ω_{th}	$\sigma_{Arnoldi}$	$\omega_{Arnoldi}$
$m = -4, k = 2.266, j = 1$	0.33101	−1.04559	0.33100	−1.0393
$m = -3, k = 1.7, j = 1$	0.32332	−0.73151	0.32331	−0.72030
$m = -2, k = 1.133, j = 1$	0.28273	−0.41301	0.28278	−0.41380
$m = -4, k = 2.266, j = 2$	0.21110	−1.05328	0.21101	−1.05244
$m = -3, k = 1.7, j = 2$	0.19600	−0.75836	0.19600	−0.75954
$m = -2, k = 1.133, j = 2$	0.15731	−0.46873	0.15190	−0.45783

Table 8.1 – Batchelor vortex: comparisons for growth rate σ and temporal frequency ω obtained from the theory and through the Arnoldi method.

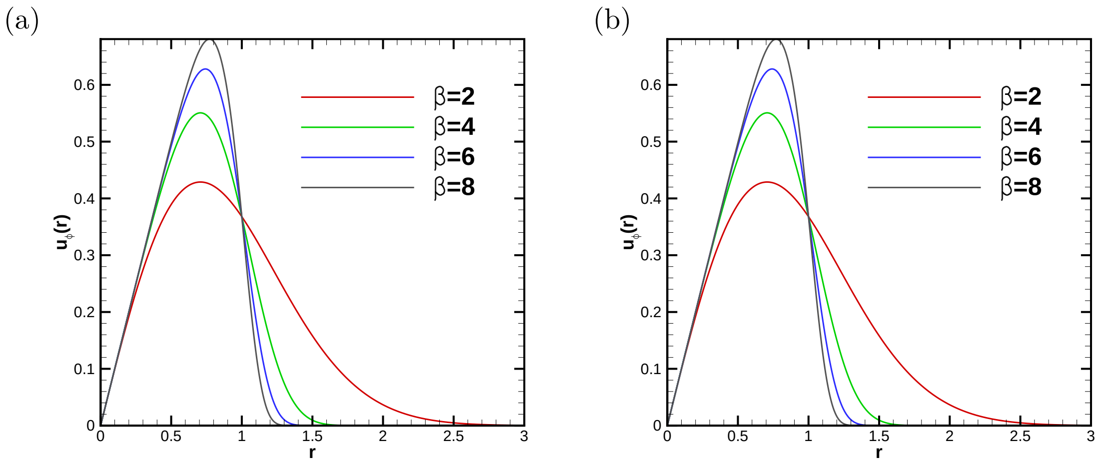

Figure 8.6 – Carton-McWilliams' vortex: profiles for various values of the steepness parameter β. (a) Azimuthal velocity $u_\theta(r)$. (b) Axial vorticity $\omega_z(r)$.

The computed growth rates are compared to the predicted values by the theory in the table (8.1). Globally the modes are recovered with a satisfactory precision. However, as the Batchelor vortex has a rich collection of unstable modes, all of them cannot be recovered without significantly increasing the number K of vectors spanning the Krylov subspace. This can be seen in the case the secondary mode $m = -2, k = 1.133$ in figure (8.5). This mode, which has the lowest growth rate among the other ones depicted, couldn't emerge sufficiently for this set of parameters. Still, the dipolar structure of the mode is distinguishable, suggesting that increasing K and/or Δt would greatly improve the results. This first benchmark suggests that the implementation of the algorithm is correct, but the separation of the modes is probably made easier in this case, because the vortex axis is centred at the origin of the domain, resulting in modes being distributed among different azimuthal Fourier components in the DNS code. A more stringent test would be to compute the same unstable helical modes when the basic Batchelor vortex is off-centred. Such a basic flow can only be represented within the framework of helical symmetry if L is infinite. The only instability modes available would then be the two-dimensional modes ($k = 0$). Unfortunately, the Batchelor vortex is known to be stable to such perturbations. Hence another vortex model, unstable to two-dimensional perturbation is selected in order to stress the algorithm further.

8.4.2 Linear modes of the Carton-McWilliams shielded vortex.

The Carton-McWilliams vortex model consists of a vortex core surrounded by an annulus of opposite vorticity so that the total circulation is zero. The azimuthal velocity distribu-

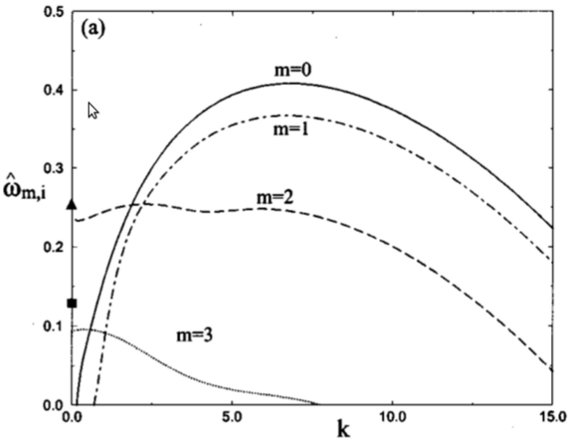

Figure 8.7 – Temporal growth rate as a function of the axial wavenumber k for $\beta = 4$ and various values of $m = 0, ..., 3$, at $Re = 667$. From (Gallaire and Chomaz, 2003)

tion thus goes to zero at infinite radial distance, the core vorticity is said to be shielded. There is no jet component for this model. Using dimensional quantities, the azimuthal velocity and the axial vorticity components are defined by

$$u_\theta^+ = U\frac{r^+}{R}e^{-\left(r^+/R\right)^\beta}, \quad \omega_z^+ = \frac{U}{R}\left[e^{-(r^+/R)^\beta}\left(2-\beta\frac{r^+}{R}\right)\right], \tag{8.43}$$

with U, a typical azimuthal velocity and R, a length linked to the core size. The Reynolds number is defined here as

$$Re = \frac{UR}{\nu}. \tag{8.44}$$

In dimensionless form, the base flow components are:

$$u_\theta(r) = re^{-r^\beta} \tag{8.45}$$

$$\omega_z(r) = e^{-r^\beta}\left(2-\beta r^\beta\right). \tag{8.46}$$

The azimuthal velocity and axial vorticity profiles are plotted for different values of the steepness parameter β in figure (8.6). The maximum of the azimuthal velocity u_θ^{max} and its radial location r_{max} both increase with β. On the axial vorticity profile, it is seen how the annulus of negative vorticity narrows and intensifies as β is increased. As explained in (Gallaire and Chomaz, 2003), the vortex is prone to instability with respect to two-dimensional $m \neq 0, k = 0$ unstable modes as well as axisymmetric ($m = 0, k \neq 0$) and helical ($m \neq 0, k \neq 0$) modes.

$$\frac{\mathrm{d}\omega_z}{\mathrm{d}r} = 0 \tag{8.47}$$

The growth rates of the modes for $\beta = 4$ and $Re = 667$ are plotted in figure (8.7) as functions of the axial wavenumber k. Two, unstable, two-dimensional modes are found for $m = 2$ and $m = 3$. We compare the growth rates of these modes in two cases: when the basic flow is centred at the origin of the numerical domain, and when it is off-centred.

Results and comparisons for $\beta = 4$, $Re = 667$, $L = \infty$

As we are looking for only two unstable modes, the number K of vector spanning the Krylov subspace is set to $K = 10$ and $\Delta t = 10$ for both the centred and the off-centred case. As shown in figure (8.8), we obtain the same results for both cases. However, the white noise should not be initialised in the same way. When centred, the process is similar

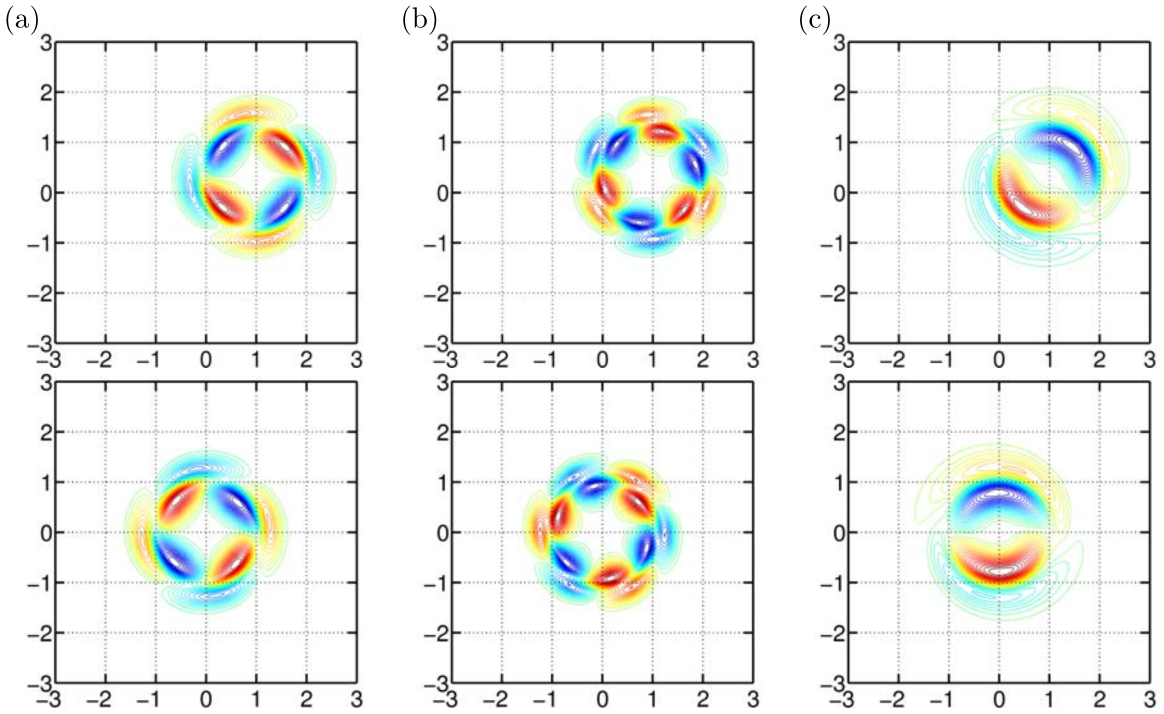

Figure 8.8 – Carton and & McWiliams vortex: structure of the modes, obtained with the Arnoldi algorithm, at $Re = 667$. First row: (a) Unstable mode $(m = 2, k = 0)$. (b) Unstable mode $(m = 3, k = 0)$. (c) Unstable mode mode $(m = 1, k = 0)$. Second row: modes obtained when the base flow is off-centred from the axis.

	Theoretical value	Centred	Off-centred
$\sigma_{m=1,k=0}$	0.0269	0.02685	0.0294
$\sigma_{m=2,k=0}$	0.2213	0.2306	0.2307
$\sigma_{m=3,k=0}$	0.0958	0.0965	0.0964

Table 8.2 – Carton & McWilliams vortex: Comparisons of the growth rates for the most unstable bi-dimensional $k = 0, m \neq 0$ modes at $Re = 667$. The associated eigenvectors are shown on figure 8.8.

to the investigation of the helical modes of the Batchelor vortex. The random perturbation (8.41) is only set on the two azimuthal modes investigated $m = 2$ and $m = 3$. Such a procedure cannot be used when the vortex is off-centred as the instability modes are defined with respect to the center-axis of the vortex and not the centre of the numerical domain. They thus require a broad spectrum of numerical Fourier modes. The initial condition for the perturbations is that described in section 8.3.1. The comparison of the growth rates for the two cases are summarised in table (8.2). The unstable modes are recovered with a good accuracy. A mode $m = 1$ is found with a small growth rate $\sigma = 0.027$, which is also predicted by the theory but not in reference (Gallaire and Chomaz, 2003).

8.5 Validation of the Arnoldi algorithm for rotating basic state

In this section, we address the issue arising from the finite precision of the method (see 5.1.2) used to compute the angular velocity $\Omega(\tau_b)$. This quantity is associated to the basic flow chosen at a particular instant τ_b (see 8.1 for more details) and is computed during the DNS. When the angular velocity is not accurately determined, the base flow is not exactly steady, which is the case in practice, due to the finite precision of the numerics.

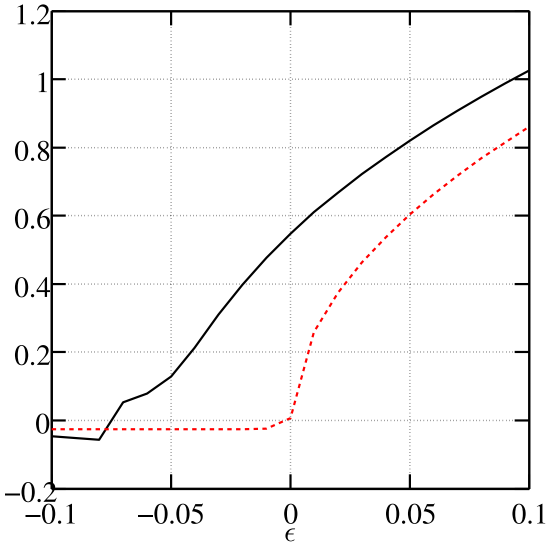

Figure 8.9 – Growth rates obtained with artificial angular velocities $\Omega(\tau_b)(1+\epsilon)$: dominant mode $\sigma_1(\epsilon)$ (black line) and "neutral" mode $\sigma_0(\epsilon)$ (red line).

One thus possibly gets errors on the determination of the growth rates.
In the following, we seek to quantify these errors. To do so, one artificially shifts the angular velocity to the value

$$\Omega^\star = \Omega(\tau_b)\,(1+\epsilon)\,. \tag{8.48}$$

where the parameter ϵ is varied within the range $[-0.1, 0.1]$. The whole linear stability analysis is then performed using the artificial angular velocity $\Omega^\star$ instead of $\Omega\,(\tau_b)$ in the set of equations (8.1)-(8.8). The growth rates are compared to the those obtained when $\epsilon = 0$.
We illustrate the above considerations in the case of two helical vortices with pitch $L = 0.4$ and core size $a = 0.06$. For this particular case, the angular velocity is found to be $\Omega(\tau_b) = -1.153753$ from the DNS. The instability analysis gives one unstable mode with positive growth rate $\sigma_1(\epsilon = 0) = 0.5468$ and a theoretically neutral mode which is found here to have a growth rate $\sigma_0(\epsilon = 0) = 0.0068$.
The linear stability analysis performed for various artificial angular velocities $\Omega^\star(\epsilon)$ with all the other parameters of the Arnoldi procedure kept constant ($\Delta t = 5, K = 20, \delta t = 1/4000$) yields the growth rates $\sigma_1(\epsilon)$ and $\sigma_0(\epsilon)$ plotted in figure 8.9. For $0 \le \epsilon \le 0.02$, the values $\sigma_0(\epsilon)$ has a very steep variation, which indicates a high sensitivity with respect to a wrong evaluation of Ω. In our simulations a typical value for ϵ is 10^{-3} leading to a precision of roughly 10^{-2} for σ_0, which explains the order of magnitude of the growth rate $\sigma_0(\epsilon = 0) = 0.0068$ instead of zero. The growth rate of the dominant mode σ_1 is also affected by variations of ϵ. For $\epsilon = 10^{-3}$, one obtains a precision of approximatively 10^{-4} for σ_1 which is a favourable case. However when σ_1 approaches σ_0, the precision deteriorates and the mode separation becomes difficult.

Chapter 9

Linear helical stability: results

Contents

The linear stability analysis previously described is applied to several regular arrays of N helical vortices: one helical vortex (section 9.1), two helical vortices (section 9.2), two helical vortices with a central hub vortex (section 9.3) and three vortices with a hub vortex (section 9.4), a situation relevant for wind turbine applications. In such arrays, the center line of one vortex is used as reference angle $\varphi = 0$ in plane Π_0. In the present section perturbations have the same helical symmetry as the regular array of N helical vortices. This assumption will be removed in chapter 11.

Let us indicate first how eigenmodes are normalized. The Arnoldi procedure gives a set of complex eigenvectors $\boldsymbol{v_A}$ with unit norm ($\|\boldsymbol{v_A}\|_2 = 1$). These vectors contain a mix of helical vorticity and velocity components since $\boldsymbol{v_A} = (\tilde{\omega}_B, \tilde{u}_B)^T$ and are obtained up to an arbitrary phase factor. In order to normalize the eigenvectors in a unique fashion, we enforce the vorticity component to be unity at a particular location (r_+, φ_+) chosen so that

$$|\tilde{\omega}_B(r_+, \varphi_+)| = \max|\tilde{\omega}_B|, \quad \text{with} \quad \varphi_+ \in [0; \pi/N]. \tag{9.1}$$

The hub vortex, when present, is not taken into account to define the appropriate normalization. The normalised eigenmodes become

$$\hat{\omega}_B = \frac{\tilde{\omega}_B}{\tilde{\omega}_B(r_+, \varphi_+)}, \qquad \hat{u}_B = \frac{\tilde{u}_B}{\tilde{\omega}_B(r_+, \varphi_+)}. \tag{9.2}$$

9.1 A single helical vortex

We present the spectrum and neutral mode found in the stability of a single helical vortex. For this vortex, the centre is located at $r \approx 1, \varphi = 0$. In figure 9.1-a, the stability spectrum is plotted for $L = 0.3$, $a = 0.09$ and $Re = 10000$. Only the 50 eigenvalues of largest growth

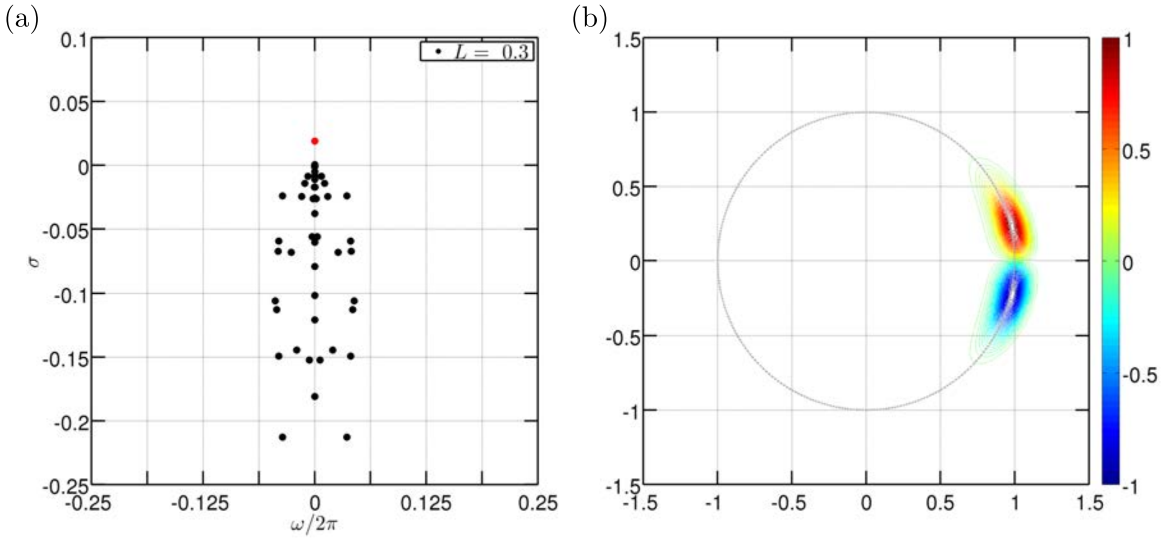

Figure 9.1 – (a) Spectrum in the $(\sigma, \omega/2\pi)$ plane for a single helical vortex with reduced pitch $L = 0.3$ and core size $a = 0.09$ at $Re = 10000$. The 50 dominant eigenvalues are displayed. (b) Mode structure of the mode represented with a red dot in graph (a): contours of the real part of $\hat{\omega}_B$ in Π_0. The associated imaginary part is zero.

rate are represented. One mode emerges with small positive growth rate. The associated structure is shown in figure 9.1-b where the real part of $\hat{\omega}_B$ is plotted. The imaginary part is zero. The mode is characterised by two lobes of opposite sign vorticity. When superimposed on the base flow, (which contains only positive vorticity), this induces a displacement of the whole structure in the azimuthal direction. Such a mode arises because of the invariance of the base flow with respect to rotation around the central axis: it is expected to be steady ($\omega = 0$) and neutral ($\sigma = 0$).

However, because of finite numerical precision (see discussion in section 8.5), this mode has very small but non zero growth rate (of order 10^{-2}). From a numerical point of view, this growth rate quantifies the accuracy of our results. In the framework of helical symmetry, such a linear mode does not play a role. However it might be related to an unstable phase mode for non helically symmetric instability perturbation at large wavelength (see chapter 11).

9.2 Two helical vortices

We analyse the stability of $N = 2$ helical vortices for different helical pitches, different core sizes and various Reynolds numbers. Figure 9.2-a displays the 50 most unstable eigenvalues, for the case $L = 0.3$, $a = 0.09$ and $Re = 10000$. It shows one dominant mode with growth rate $\sigma = 0.925$ and a marginally stable mode evaluated at $\sigma = 0.010$. Both modes are stationary ($\omega = 0$). Similarly to the single vortex case, the latter mode is the neutral mode, also present here; its structure is depicted in figure 9.3. Similar results are obtained when L, a and Re are varied. In figure 9.2-b, this is shown for several values of the pitch such that $0.3 \leq L \leq 0.7$.

The most unstable mode is represented for the particular case $L = 0.3$ in figure 9.4-a, where the contours of the real part of $\hat{\omega}_B$ are plotted. The associated imaginary part is zero. Its structure is localized within each basic vortex core where it takes again the form of two lobes with opposite sign vorticity. This is characteristic of displacement modes: on

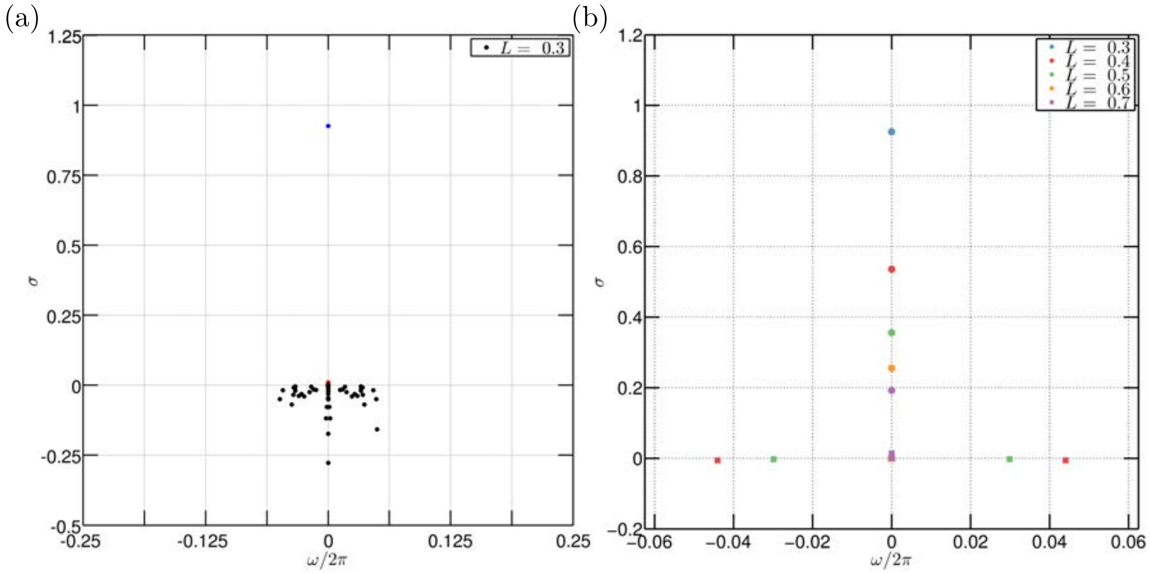

Figure 9.2 – (a) Spectrum in the $(\sigma, \omega/2\pi)$ plane for two helical vortices with $L = 0.3$ and $a = 0.09$ at $Re = 10000$. The first 50 eigenvalues are displayed. The dominant eigenmode is represented in red and the neutral one in blue. (b) Spectrum showing the first four dominant eigenvalues for various L at $Re = 10000$. The dominant mode is represented in filled circles.

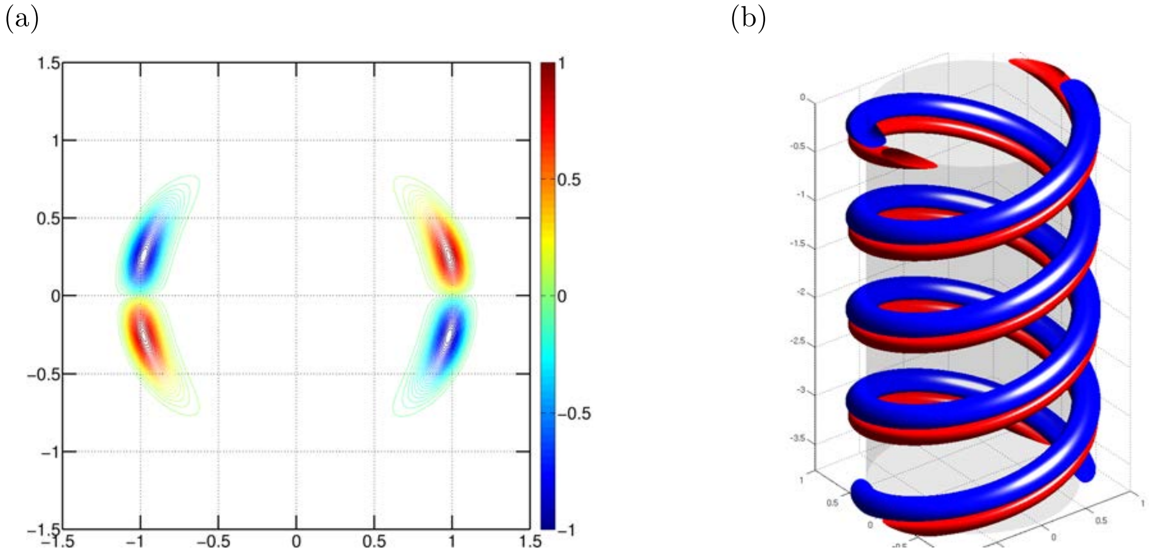

Figure 9.3 – Two helical vortices for $L = 0.3, a = 0.09$ at $Re = 10000$. Structure of the neutral mode represented with a filled red circle in figure 9.2-a. (a) Contours of the real part of $\hat{\omega}_B$ in Π_0. (b) Three-dimensional isosurface of vorticity corresponding to $\pm \max \Re\{\hat{\omega}_B\}/4$ (red for positive isovalue and blue for the negative one).

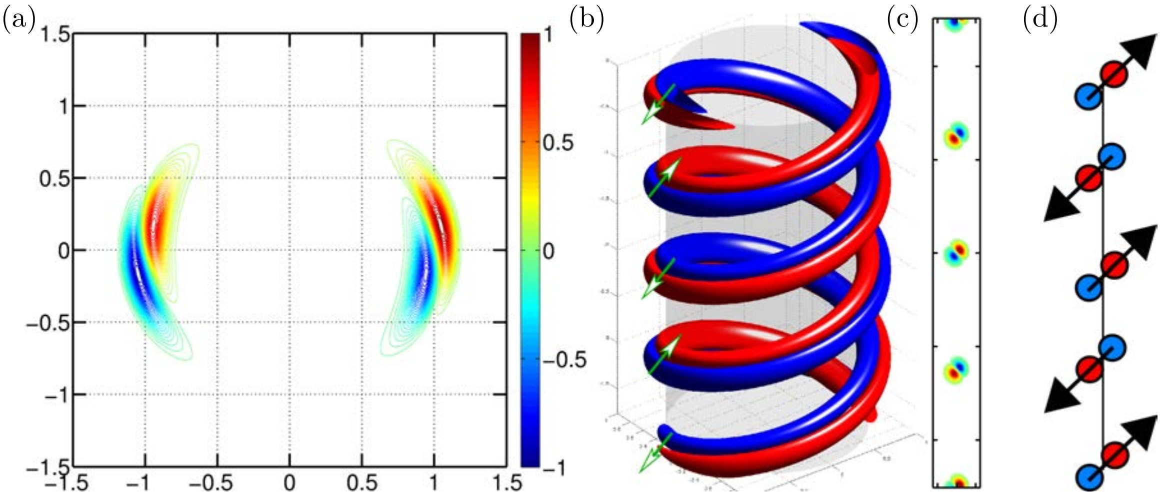

Figure 9.4 – The most unstable mode for the base flow corresponding to two helical vortices with $L = 0.3$ and $a = 0.09$ at $Re = 10000$. (a) Contours of $\Re\{\hat{\omega}_B\}$ in Π_0. The imaginary part is zero. (b) Three-dimensional isosurface of vorticity $\Re\{\hat{\omega}_B\}$ corresponding to $\pm\max\Re\{\hat{\omega}_B\}/4$. The arrows indicate the displacement induced by the mode: on the radial direction one vortex goes inwards while the other goes outwards. (c) Contours of $\Re\{\hat{\omega}_B\}$ in the meridian (r, z) plane. (d) Schematic representation: the structure is analogous to the pairing instability mode for an infinite row of point vortices.

the three-dimensional representation of the mode (see arrows on figure 9.4-b), it is seen that a radial inward displacement is induced for one vortex while the other vortex moves outwards. This motion has also an axial component: when viewed in a cut by a meridian (r, z) plane (see figure 9.4-c), this structure is very similar to a pairing instability mode arising in a row of identical two-dimensional vortices, as sketched in figure 9.4-d.

9.2.1 Influence of L on the dominant mode

In figure 9.5-a, we present the growth rate σ of the most unstable mode for core size $a = 0.09$ as a function of L. The growth rate decreases as L increases. For $L > 1.6$, σ is close to zero and its evaluation becomes difficult, because of the above numerical accuracy limitation. If the stability threshold is estimated as the value of L where the numerically estimated growth rate equals that obtained for the neutral mode, it corresponds to a

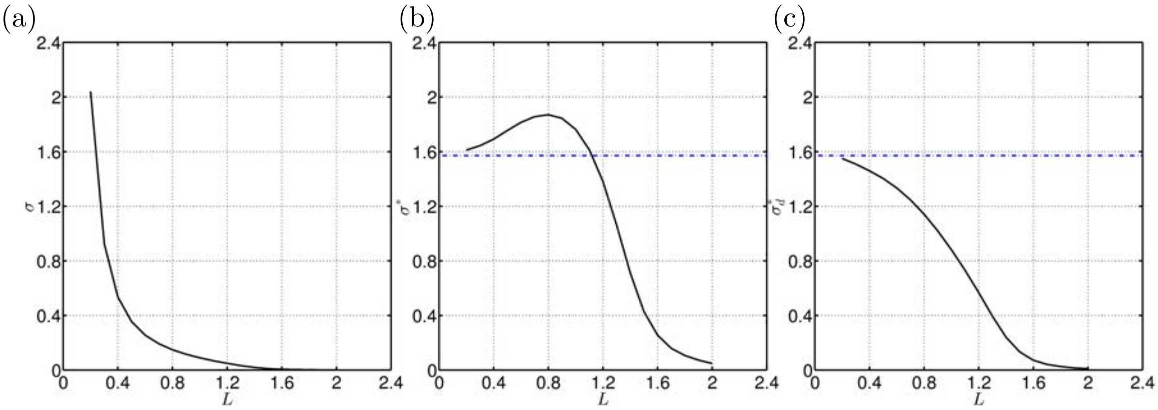

Figure 9.5 – Growth rate of the dominant instability mode for $N = 2$ helical vortices for $a = 0.09$ at $Re = 10000$ as a function of pitch L. (a) Growth rate σ. (b) Normalized growth rate σ^* as defined in (9.4). (c) Normalized growth rate σ_d^* as defined in equation (9.6). In figures (b) and (c) the horizontal dashed line is located at the value $\pi/2$.

value of $L_{threshold}$ close to 1.6. In the inviscid framework, Okulov and Sørensen (2007) predicted that two helical Rankine vortices are unstable for $L < 1.106$. For the present configuration, a higher threshold is found. This difference could be attributed to the nature of the underlying vorticity profile (it is nearly Gaussian) and to the finite Reynolds number effect, but this discrepancy remains unclear.

9.2.2 Point vortex analogy

For small L, when visualised in the meridian plane (see figure 9.4-c), the mode looks very similar to the unstable mode of an infinite row of point vortices separated by $h = \pi L$; the axial distance between two successive coils ($h = 2\pi L/N = \pi L$ for $N = 2$ vortices). Following Bolnot (2012), we can compare the above growth rates obtained for helical configurations to the values obtained for an array of point vortices.

The stability of an infinite array of two-dimensional point vortices with circulation Γ separated by a constant distance h has been analysed by von Kàrmàn and Rubach (1912) and Lamb (1932). The unperturbed vortices are situated at points $(mh, 0)$ with $m \in \mathbb{Z}$. After linearising the two-dimensional Biot-Savart motion equations, the system is shown to be unstable with respect to perturbations of wavelength $\lambda = 2\pi h/\phi$ with $\phi \in [0, 2\pi[$. More precisely, the motion of vortex m subject to such instability mode is $(mh + x_m(t), y_m(t))$ where $x_m(t) = A_0 e^{\sigma t + im\phi}$ and $y_m(t) = -A_0 e^{\sigma t + im\phi}$ and the corresponding growth rate is given by

$$\sigma(\phi) = \frac{\Gamma}{4\pi h^2}\phi(2\pi - \phi). \tag{9.3}$$

The maximum occurs for $\phi = \pi$ corresponding to an out-of-phase displacement of the neighbouring vortices (figure 9.4-d). The maximum growth rate is thus equal to $\sigma_{2D}(h) = \Gamma\pi/4h^2$. When normalised by $2h^2/\Gamma$ it gives the constant $\frac{\pi}{2}$. One may tentatively compare growth rates obtained for helical vortices to those obtained for point vortices separated by a distance $h = 2\pi L/N$:

$$\sigma^* \equiv \frac{\pi}{2}\frac{\sigma}{\sigma_{2D}(h)}, \tag{9.4}$$

or

$$\sigma^* = 2\frac{\sigma h^2}{\Gamma} = 8\frac{\sigma\pi^2 L^2}{\Gamma N^2}. \tag{9.5}$$

Figure 9.5-b depicts the normalised growth rate σ^* of the most unstable mode for core size $a = 0.09$ as a function of L. For small values of L, the growth rate tends towards $\pi/2$ indicating that the underlying mechanism is indeed similar to the pairing of point vortices. However for increasing L, σ^* is seen to exceed $\pi/2$. This overshoot might be due to a wrong choice of the separating length. The pairing mechanism occurs through the mutual induction of the vortices. In the case of an array of straight vortices, as well as vortex rings the separation distance h is obvious. For a helical vortex, however, the shortest length between two successive coils is not the helical pitch. Following Quaranta et al. (2015), we define the shortest length d between the successive coils by unwrapping the helices in a $(z, R\theta)$-plane as depicted in figure 9.6. Using the notations of this figure, one has $d = h\sin\alpha$ and $\sin\alpha = R/(L^2+R^2)^{1/2}$. Using d for instead of h leads to introduce σ_d^*

$$\sigma_d^* = \frac{\pi}{2}\frac{\sigma}{\sigma_{2D}(d)}, \tag{9.6}$$

or

$$\sigma_d^* = \sigma^*\frac{R^2}{L^2+R^2}. \tag{9.7}$$

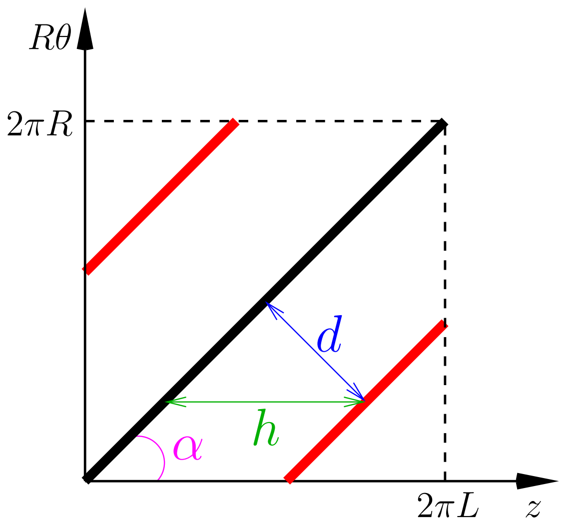

Figure 9.6 – Schematic representation of the shortest length d between two successive coils for $N = 2$ helical vortices.

The normalised growth rate σ_d^* is plotted in figure 9.5-c for $a = 0.09$. Similarly to σ^*, σ_d^* tends to $\pi/2$ for small values of L and is found to monotonically decrease when L increases. This corresponds to the fact that, as L increases to $+\infty$, the system tends to $N = 2$ straight thin core vortices, a situation known to be stable with respect to such perturbations (for $L = \infty$, the instability occurs only when $N \geq 7$).

9.2.3 Vortex ring array analogy

Growth rates may also be compared to those obtained in the case of an array of vortex rings. The temporal stability of an infinite array of vortex rings of circulation Γ and radius R has been studied by Levy and Forsdyke (1927) using a filamentary approach. They have obtained a formula for the maximum growth rate of the pairing instability for uniform vorticity rings. The dimensional growth rate σ reads

$$\sigma_{Ring} = \frac{\Gamma}{2\pi R^2}\sqrt{C\left(G + C/2 + H_0 - B\right)} \tag{9.8}$$

with

$$B = \sum_{p=1}^{\infty} \frac{\alpha_{2p-1}^3}{2}\left[\left(3 + \beta_{2p-1}^2\right) E\left(\alpha_{2p-1}^2\right) - K\left(\alpha_{2p-1}^2\right)\right], \tag{9.9}$$

$$C = \sum_{p=1}^{\infty} \alpha_{2p-1}^3\left[\left(1 - \beta_{2p-1}^2\right) E\left(\alpha_{2p-1}^2\right) - K\left(\alpha_{2p-1}^2\right)\right], \tag{9.10}$$

$$G = \sum_{p=1}^{\infty} \alpha_{2p}^3\left[2E\left(\alpha_{2p}^2\right) - K\left(\alpha_{2p}^2\right)\right], \tag{9.11}$$

$$\alpha_k = \left[1 + \left(\frac{kh}{2R}\right)^2\right]^{-1/2} \quad , \quad \beta_k = \frac{2R}{kh}. \tag{9.12}$$

The functions K and E are the complete elliptic integrals of the first and second kind, respectively (Abramowitz and Stegun, 1965). The last term H_0 reads

$$H_0 = \frac{1}{2}\left(\frac{7}{4} - \ln\frac{8R}{a_e}\right), \tag{9.13}$$

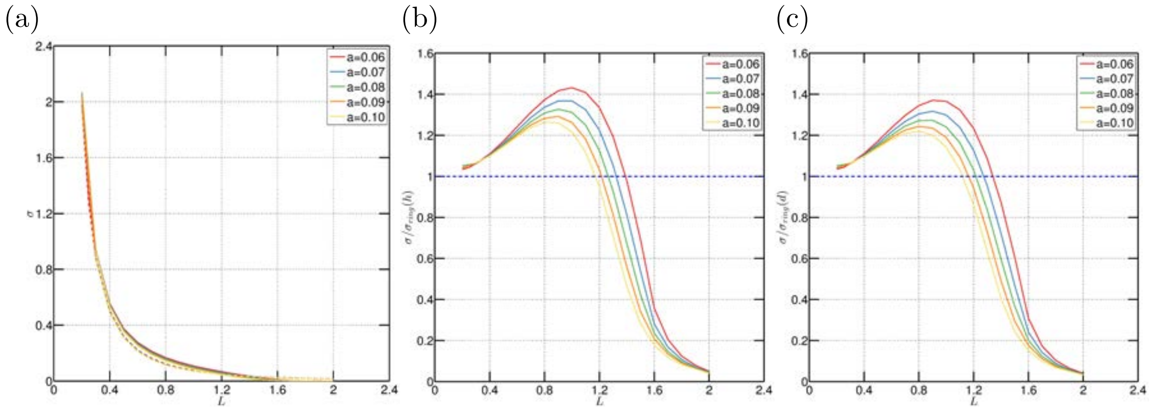

Figure 9.7 – Growth rate of the dominant instability mode for $N = 2$ helical vortices for $a = 0.06, 0.07, ..., 0.1$ at $Re = 10000$ as a function of pitch L (solid lines). (a) Growth rate σ (solid line) and σ_{Ring} (dashed lines). (b) Normalized growth rate $\sigma/(\sigma_{Ring}(h))$. (c) Normalized growth rate $\sigma/(\sigma_{Ring}(d))$. In all graphs, the dashed lines represent the growth rates computed with the extended formula (9.8) of Levy and Forsdyke (1927) by Bolnot et al. (2014) for vortex rings with Gaussian vorticity profiles.

and is associated to the self induced velocity of a single ring with uniform vorticity i.e. a Rankine profile of size a_e. Equation (9.13) can be used for arbitrary vorticity profiles if the equivalent core size a_e is used (Widnall et al., 1971). The above formula were extended by Bolnot et al. (2014) for vortex rings with arbitrary vorticity profiles. As shown in chapter 6 (figure 6.7), the vorticity profile within a developed helical vortex is found to be very close to a Gaussian with core size a. It is found (Bolnot et al., 2014) that for such profiles the equivalent core size is approximatively $a_e \approx 1.36a$. This value is used here for comparisons.

One may tentatively compare growth rates obtained for helical vortices to those obtained for vortex rings separated by a distance $h = 2\pi L/N$. The growth rate σ_{Ring} is plotted in figure 9.7-a with dashed lines. The normalised growth rates

$$\frac{\sigma}{\sigma_{Ring}(h)} \quad \text{and} \quad \frac{\sigma}{\sigma_{ring}(d)}, \tag{9.14}$$

for the vortex ring array are respectively plotted in figures 9.7b and c. For small pitch values $L < 0.4$, growth rates obtained for vortex rings compare well to the ones obtained for two helical vortices. A deviation is observed for $L > 0.4$. Selecting the distance d in the non-dimensionalisation of the growth rate leads to a slightly better agreement between helical and vortex ring configurations. For larger L, whatever the core size a investigated, growth rate monotonically decreases.

9.2.4 Influence of the core size a

The influence of the core size on the growth rate is found weak for the range of a investigated ($0.06 \leq a \leq 0.1$) (see figure 9.7). For fixed value of L, the growth rate increases when the core size is decreased. As shown in Brancher and Chomaz (1997), vortex concentration enhances the pairing instability mechanism even if this effect remains relatively weak. Note that the limit $L = 0$ cannot be reached because of the finite core size implying that $L \gtrsim 2Na/\pi$ (see discussion for the single vortex case in section 5.4). For $N = 2$, $a = 0.09$ this gives $L \gtrsim 0.11$.

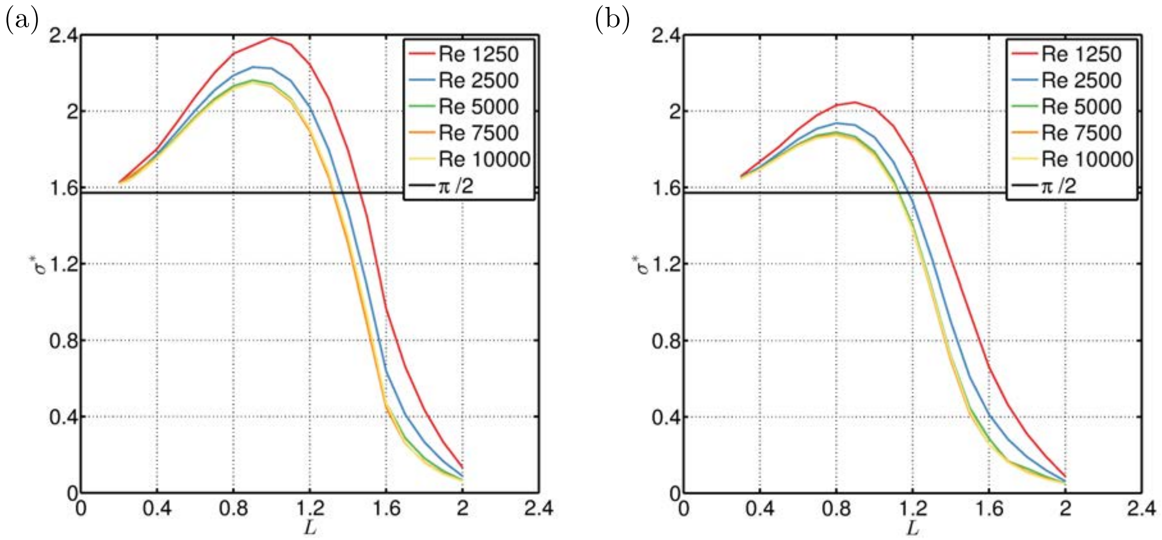

Figure 9.8 – Normalized growth rate σ^* of the displacement mode for $N = 2$ helical vortices. Influence of the Reynolds number with core size (a) $a = 0.06$; (b) $a = 0.09$.

9.2.5 Influence of Reynolds number

The influence of the Reynolds number is analysed. The normalised growth rate σ^* of the most unstable mode is plotted on figure 9.8 for various values of Re for core size $a = 0.06$ and $a = 0.09$. For both values of a, within the range of $Re \in [1250; 5000[$, the effect of lowering the Reynolds number is paradoxically to enhance the growth rate. This is a surprising behaviour as one would generally expects the instability to grow stronger with increasing Reynolds number.

9.3 Two helical vortices with a central hub vortex

We investigate the influence of a central hub on the stability of two helical vortices. The central hub is chosen with a circulation $-N\Gamma$, thus ensuring a global circulation of the base flow to be zero. This case is relevant for instance for propeller wakes (Felli et al., 2011). In our simulations, the hub core size is chosen equal to the helical core size a. The structure of the most unstable mode for $L = 0.3$, $a = 0.09$ and $Re = 10000$ is depicted in figure 9.9: it is seen that the mode structure is globally the same as without hub namely, a displacement mode which now also involves the central hub vortex. The effect of the mode is to displace the hub vortex towards the same half plane in Π_0 as shown by the green arrows in figure 9.9. This is reminiscent of what was observed by Felli et al. (2011) experimentally in a water channel.

The growth rate is plotted in figure 9.10 as a function of L. The presence of the central hub slightly enhances the instability for the range $L < 0.7$. For $L > 0.7$, the growth rate abruptly decreases and the mode stabilises near $L = 0.9$.

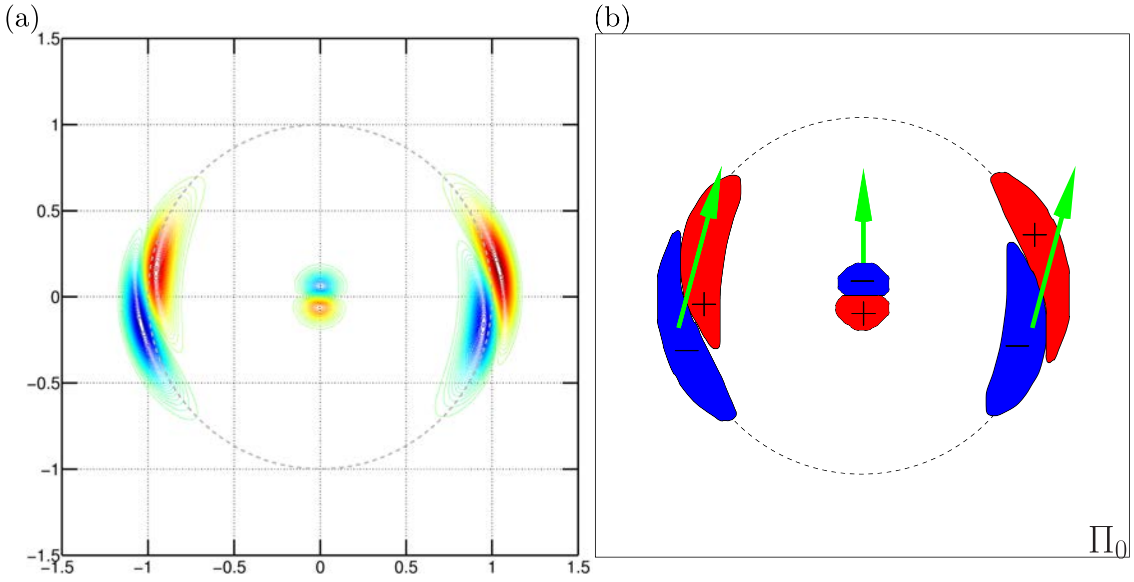

Figure 9.9 – The most unstable mode for the base flow corresponding to two helical vortices with $L = 0.3$, core size $a = 0.09$ and a central hub vortex of core size a. Reynolds number for perturbations is $Re = 10000$. (a) Contours of $\Re\{\hat{\omega}_B\}$ in Π_0. (b) Schematic representation: the displacement induced by the unstable mode when superimposed on the base flow are represented with the green arrows.

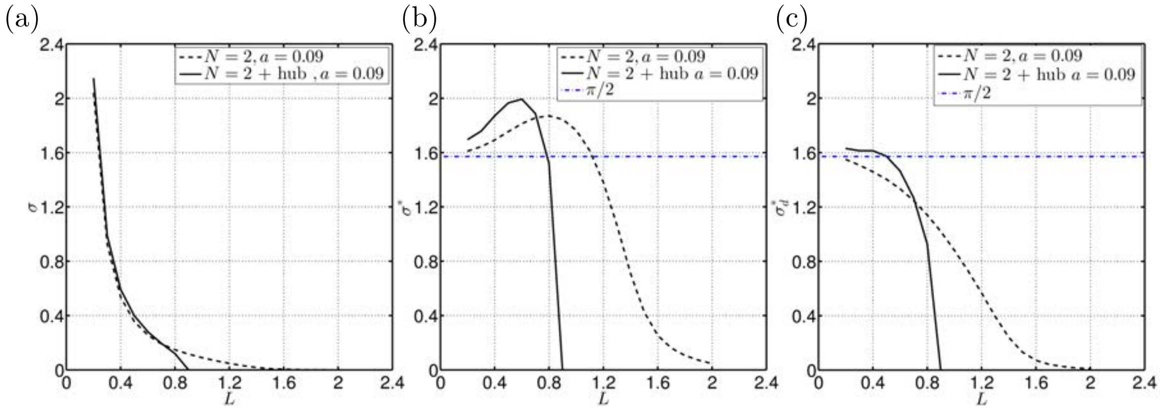

Figure 9.10 – Growth rate of the dominant instability mode for $N = 2$ helical vortices with the vortex hub (solid line) and without (dashed line) for $a_{hub} = a = 0.09$ at $Re = 10000$ as a function of pitch L. (a) Growth rate σ. (b) Normalized growth rate σ^*. (c) Normalized growth rate σ_d^*. In (b) and (c) the horizontal line represents $\pi/2$.

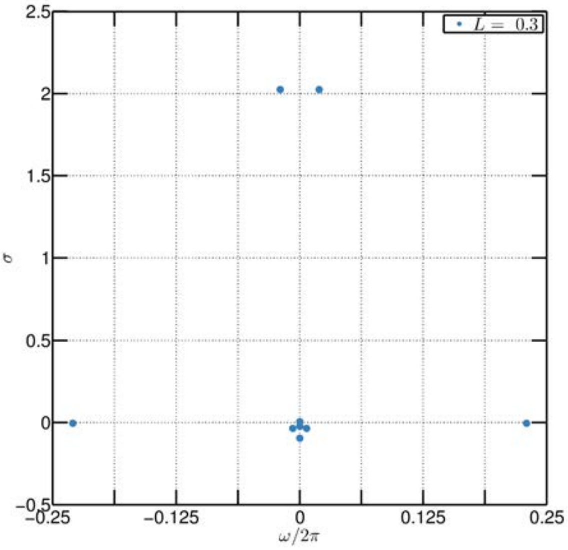

Figure 9.11 – Spectrum in the $(\sigma, \omega/2\pi)$ plane for $N = 3$ helical vortices with a central hub vortex at $L = 0.3$, $a = 0.09$ and $Re = 10000$. Only the first 9 dominant modes are shown.

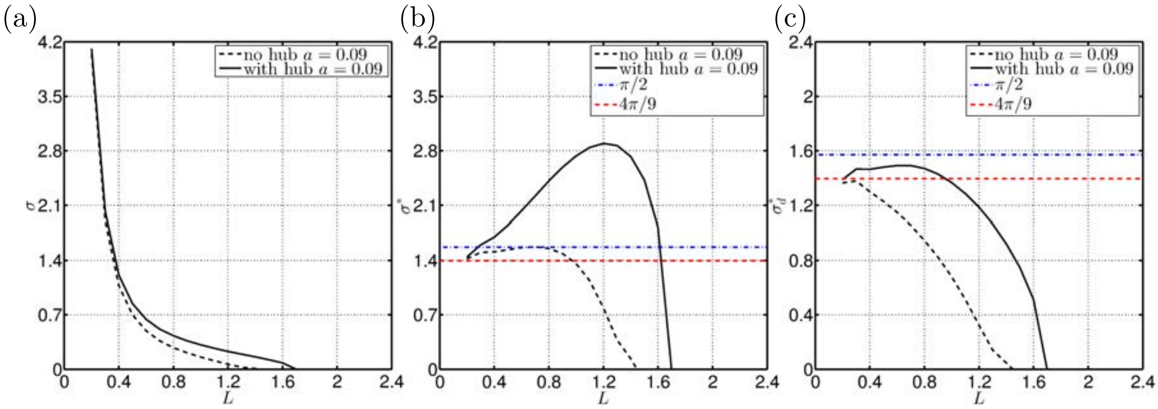

Figure 9.12 – Growth rate of the dominant instability mode for $N = 3$ helical vortices with the vortex hub (solid line) and without (dashed line) for $a_{hub} = a = 0.09$ at $Re = 10000$ as a function of pitch L. (a) Growth rate σ. (b) Normalized growth rate σ^*. (c) Normalized growth rate σ_d^*.

9.4 Three helical vortices with a central hub vortex

We now investigate the stability of $N = 3$ helical vortices of for core size $a = 0.09$ in the presence of a central hub vortex at $Re = 10000$. The core size of the hub vortex is chosen to be equal to those of the helical vortices ($a_{hub} = a$).

The spectrum obtained for $L = 0.3$ is presented in figure 9.11. Contrary to the cases for two helical vortices, there are two dominant unstable modes with the same growth rate $\sigma = 2.024$ and opposite nonzero frequencies $\omega = \pm 0.123$. The growth rates are plotted in figure 9.12. Note that the effect of adding a hub is different for $N = 2$ and $N = 3$ vortices : for $N = 3$ it tends to destabilize the system.

The real and imaginary part of the dominant eigenmode with positive ω are depicted in figure 9.13. The mode with negative ω has the same real part but opposite imaginary part. The real part is constituted of three lobes of vorticity of opposite sign and one of the vortex displacements has a larger magnitude. The imaginary part displays only two lobes of vorticity with equal magnitudes. The central hub vortex is also involved in the process.

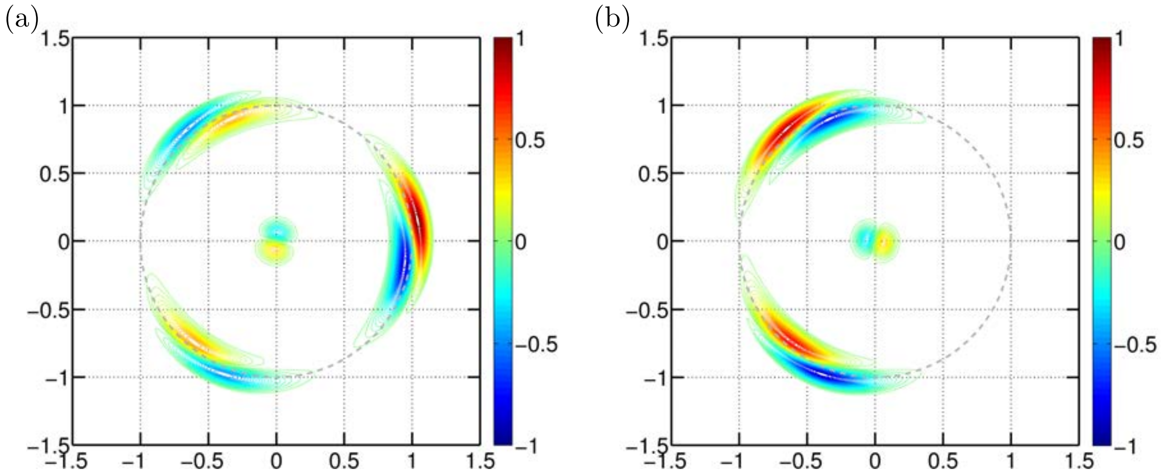

Figure 9.13 – Structure of the most unstable mode for $L = 0.30$, $a = 0.09$ with a central hub. (a) Real part of the eigenvector $\hat{\omega}_B$. (b) Imaginary part of $\hat{\omega}_B$.

Growth rate and mode structure can be interpreted in the framework of point vortex analogy. Let us first examine this analogy when N helical vortices are present. The helical symmetry imposes every Nth vorticity region in the meridian plane to be subject to the same displacement as it belongs to the same helical vortex. This means that only instability waves having spatial periodicity $\Lambda = Nh$ should be kept in the point vortex analogy: those are waves of wavelength $\lambda = \Lambda/p = Nh/p$ with $p = 1, ..., N-1$. In terms of ϕ, the waves pertinent for the array of N helical vortices are $\phi = 2\pi p/N$. For $N = 2$ vortices, this gives $\phi = \pi$, which is the dominant pairing mode with growth $\sigma^* = \pi/2 \approx 1.57$. However, for $N = 3$, two instability modes corresponding to $\phi = 2\pi/3$ and $\phi = 4\pi/3$ are pertinent. This is coherent with the two dominant modes shown in figure 9.11. In the point vortex analogy the two modes are found to be associated to a growth rate $\sigma^* = 4\pi/9 \approx 1.4$ smaller than for $N = 2$. This is again observed in figure 9.12-b and 9.12-c, for low values of L, where the normalised growth rates approach a value close to $4\pi/9 \approx 1.4$. The distribution of displacement amplitudes between real and imaginary parts as depicted in figure 9.13 can also be enlightened using the point vortex analogy. Indeed, the unstable mode induces a displacement of the form $e^{\mathrm{i}2\pi z/\lambda}$ on the vortex array. In figures 9.14-b and 9.14-c, the corresponding real and imaginary parts are plotted as functions of z/λ. It is seen that in the real part, the first vortex (at $z/\lambda = 0$) is subjected to a displacement which is larger in magnitude than the two other vortices (located at $z/\lambda = 1/3$ and $z/\lambda = 2/3$). In the imaginary part, the amplitude is zero for the first vortex and maximal for the two others. This is exactly the amplitude distributions which are observed for the $N = 3$ helical case in plane Π_0 (see figure 9.13).

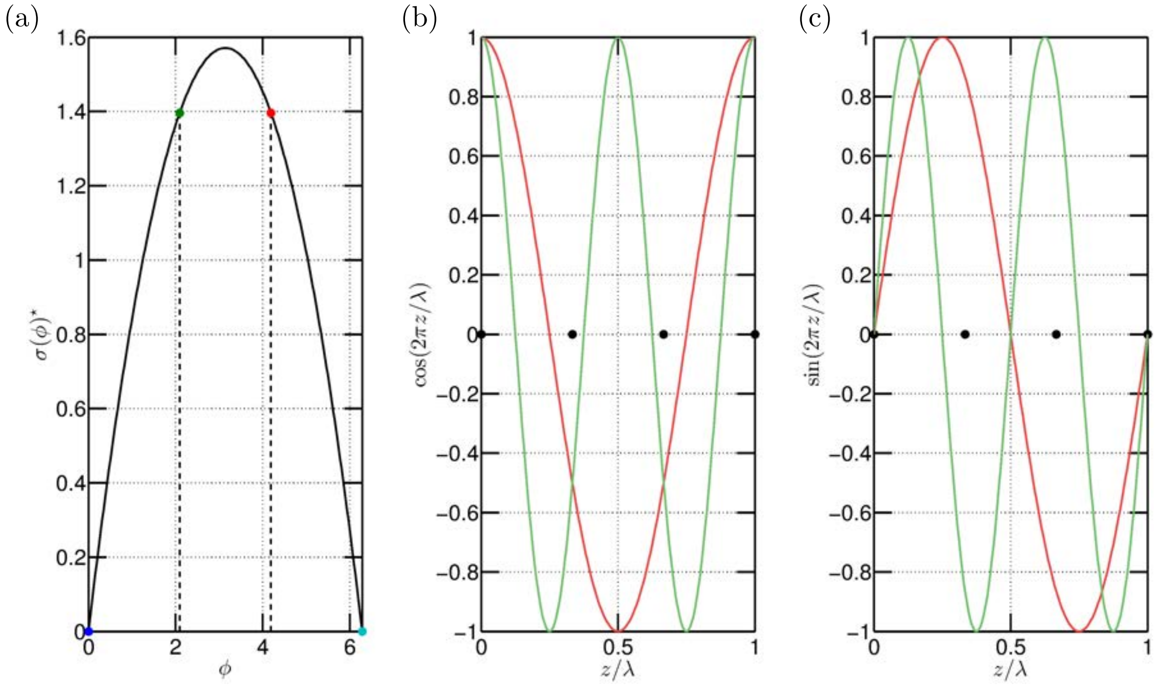

Figure 9.14 – Analogy with an array of point vortices for $N = 3$ separated by $h = 2\pi L/3$: (a) Dispersion relation, the full dots correspond to the modes pertinent for $N = 3$. (b) Real part of the induced displacement by the unstable mode $\phi = 2\pi/3$ (red curve) and $4\pi/3$ (green curve). (c) Imaginary part.

Chapter 10

Nonlinear evolution in the helical framework

Contents

Unstable pairing modes were obtained with the helical linear stability analysis in chapter 9. Here, we analyse the nonlinear evolution of this mode in the framework of helical symmetry using the HELIX code. The numerical computations are started with the most unstable mode $\hat{\boldsymbol{u}}$ multiplied by an amplitude A and superimposed on the helically symmetric base flow $\boldsymbol{u}^{\mathrm{BF}}$. Mathematically, this means that

$$\omega_B^{\mathrm{Total}} = \omega_B^{\mathrm{BF}} + A\Re\{\hat{\omega}_B\} \tag{10.1}$$

$$u_B^{\mathrm{Total}} = u_B^{\mathrm{BF}} + A\Re\{\hat{u}_B\}, \tag{10.2}$$

where $\Re\{\hat{u}_B\}$ and $\Re\{\hat{\omega}_B\}$ are obtained by the Arnoldi procedure and are both normalized such that $\max|\hat{\omega}_B| = 1$ on Π_0 (see introduction of chapter 8). In practice, amplitude A is set to $A = 0.01\,\|\boldsymbol{\omega}^{\mathbf{BF}}\|$ where $\|.\|$ is the Euclidean norm. This value guarantees that the initial evolution is linear and that the resulting nonlinear dynamics will be accessible in a reasonable computational time. On figure 10.1, base flow and pairing mode that are combined to yield the initial condition are plotted.

In the helical framework we found that vortices display complex dynamics such as merging, leapfrogging and overtaking. We briefly recall the first two mechanisms for two-dimensional straight vortices and vortex rings (section 10.1). The description and the characterisation of the overtaking mechanism can be found in section 10.2. The nonlinear dynamic of two helical vortices is described in section 10.3 up to their merging 10.4.

10.1 Leapfrogging and merging of vortices

The leapfrog mechanism of two identical vortex rings moving in the same direction is a well known phenomenon which has been observed and extensively studied. Helmholtz,

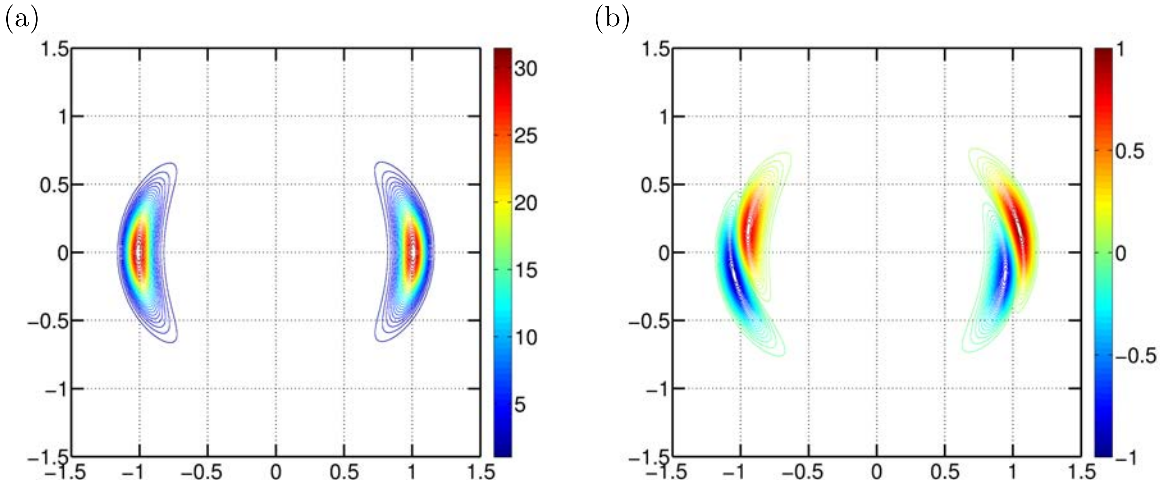

Figure 10.1 – (a) Base flow: Two helical vortices $L = 0.3$ with core size $a = 0.1$. Component ω_B^{Base} (b) Real part of the eingemode $\hat{\omega}_B$ of the helical pairing mode. These two fields will be combined and set as initial condition for the non linear computation.

on the basis of theorems he himself established, deduced that when two identical vortex rings travel in the same direction « ... the foremost widens and travels more slowly, the pursuer shrinks and travels faster, till finally, if their velocities are not too different, it overtakes the first and penetrates it. Then the same game goes on in the opposite order, so that the rings pass through each other alternately. » This description provides already an astonishingly accurate and detailed description of the leapfrogging process of two vortex rings. It is also known that the leapfrogging motion can be sustained indefinitely in an inviscid fluid when the cross-section of the vortex ring remains small with respect to the ring diameter and when the circular shape of the core is maintained (Riley and Stevens, 1993). When viscosity is present, only a given number of leapfrogs can be expected to occur due to the extension of the vortex core size. The numerical study of Riley and Stevens (1993) confirms this statement: increasing the Reynolds number from 500 to 4000 leads to an increase of the number of leapfrogs from 1 to 5.

The vortex merging is a generic mechanism for two-dimensional vortices. It occurs when two vortices are sufficiently close to each other. In the inviscid regime, a pair of co-rotating vortices separated by a distance b large with respect to their core size, rotates at angular velocity $\Gamma/\left(2\pi b^2\right)$ similarly to point vortices. When viscosity is present, the two vortices always end up merging due to the continuously increasing core size. Meunier et al. (2002) studied experimentally the merging of two co-rotating straight vortices and identified three evolution stages. A first viscous stage, where the square of the core size increases linearly in time, without merging, is followed by a second stage, where the two vortices merge on a convective (faster) time scale. The third stage is associated to the diffusion of the filaments of vorticity into a final axisymmetric vorticity distribution. They proposed a merging criterion based on the angular momentum of the vorticity. Fine et al. (1991) also proposed a similar criterion based on the first moment of vorticity. Both methods obtained similar results when compared to the experimental data of Meunier et al. (2002). The numerical counterpart was provided by Josserand and Rossi (2007) for a large range of Re number (from 1000 to 100000). They pinpointed the deficiencies of the previous criteria and proposed a new criterion based on the existence of a quasi-equilibrium.

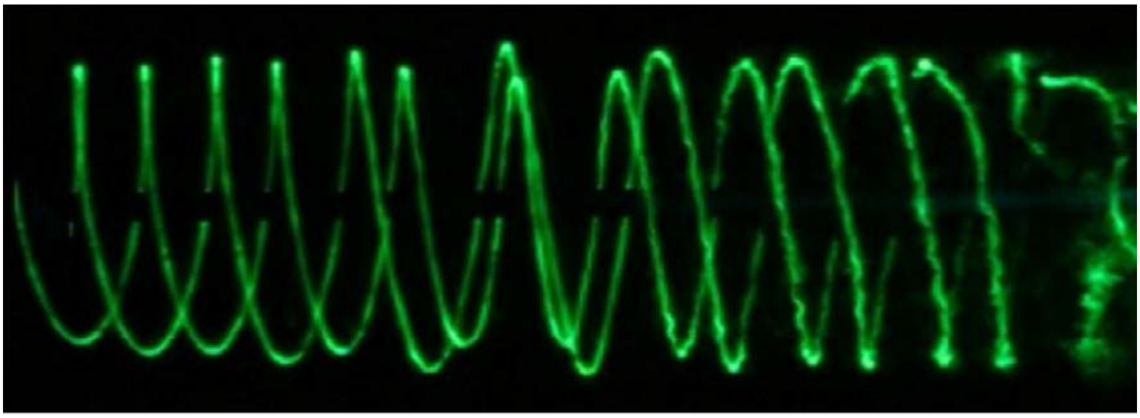

Figure 10.2 – Spatial evolution of $N = 2$ helical vortices generated by a two-bladed rotor in a water channel. The vortex system is perturbed with one blade being radially offset. Such perturbation can be understood in a context where the helical symmetry is preserved. (Bolnot, 2012).

10.2 General mechanism of two helical vortices

Helical vortices are topologically in-between vortex ring arrays and straight vortices. The first case corresponds to small L and the second to large L. Interestingly, they are subjected to the complex previously described dynamics: leapfrogging and merging. The leapfrogging for helical vortices can be described as follows: the radius of one of the two vortices decreases while the radius of the other one increases. Thereafter, the first one accelerates and passes through the other. The process repeats with the role exchanged. The leapfrog of helical vortices was first observed by Alfredsson and Dahlberg (1979) with smoke visualisation. Later, Sherry et al. (2013) and Bolnot (2012) employed particle image velocimetry (PIV) and dye visualisation, respectively, to observe the same phenomenon. In order to excite the helical pairing mode, Bolnot (2012) created a small asymmetry between the two blades of the rotor by radially shifting one of them. A typical visualisation is shown in figure 10.2 where one helical vortex shrinks and passes through the other one which is enlarged.

This leapfrog phenomenon is also observed numerically in the frame of the helical symmetry: snapshots of the evolution evolution at $Re = 10000$ of two helical vortices of pitch $L = 0.30$ with initial core size $a = 0.06$ are shown in figure 10.3.

For helical vortices, we observed also a different behaviour that we call the overtaking. It has been found for intermediate values of $L \geq 0.5$: one of the vortex accelerates and overtakes the other one as at the beginning of leapfrog but then the roles between the two vortices are not exchanged: it is the *same* helical vortex that overtakes again. The process may repeat itself several times before some leapfrogs occur and the vortices finally merge. Note that, by simply looking at figure 10.2, it is not possible to discriminate between a leapfrog or an overtaking event. A more reliable characterisation is provided in the next section.

The effect of the pitch L on the merging of helical vortices has been numerically investigated for two vortices by Delbende et al. (2015) and three vortices Delbende and Rossi (2013). Note however, that the Reynolds number of these studies prevented from observing any leapfrog or overtaking events.

Re	number of leapfrog events
1250	1
2500	2
3750	3
5000	4
6750	4
10000	5

Table 10.1 – Dependence of the number of leapfrogs with respect to the Reynolds number for two helical vortices of reduced pitch $L = 0.3$ with initial core size $a = 0.06$.

10.3 Results for two helical vortices

In order to characterize the nonlinear evolution of vortices, we track the radial position $r_A(t)$ of each vortex centreline. The tracking of the individual vortices is done by accurately locating the point of maximum vorticity in the vicinity of the previous location of the maximum.

This allows us to characterise this phenomena by separating the overtakings from the leapfrogs and investigate the effect of the parameters a, L and Re.

10.3.1 Influence of the reduced pitch L

We first investigate the influence of reduced pitch L on the dynamics of two helical vortices with initial core size $a = 0.06$ when perturbed with the helical pairing mode at Reynolds number $Re = 10000$. The time evolution of the vortex centres r_A for various values of L are plotted in figure 10.4. For $L = 0.3$ and $L = 0.4$, the resulting dynamics are similar: the vortices undergo several leapfrog events and then merge. From 10.4-a and 10.4-b, one can count 5 clear leapfrogs (light gray area) before the merging starts (dark gray area). Increasing L has been shown in chapter 9 to decrease the growth rate of the pairing mode which may explain that it also slows down the leapfrog dynamics.

For $0.5 \leq L \leq 0.8$, vortices are found to undergo several overtaking events (see middle and bottom rows of figure 10.4). Globally the number of overtaking events increases with L and they occur at reduced pace. Note that the peak amplitudes are not constant in time and sometime the inner vortex approaches the z axis (for $L = 0.7$ or $L = 0.8$, see figure 10.4 bottom row).

Once the overtaking events are over, the vortices start leapfrogging. From the same figures, it can be seen that the number of leapfrogs increases with L and that the events occur at reduced pace. Note also that between the last overtaking event and the first leapfrogging, the radial position of the vortices are often very close.

10.3.2 Influence of the Reynolds number Re

According to (Riley and Stevens, 1993), the Reynolds number is a key parameter for defining the number of leapfrogs before two rings merge. In order to verify whether or not this is also the case for helical vortices, we keep the initial core size a and reduced pitch L constant to 0.06 and 0.3 respectively, and perform simulations at different Reynolds numbers. It is seen on figure 10.5 that, as the Reynolds number increases, the number of leapfrogs also increases. The number of leapfrogs is reported in table 10.1.

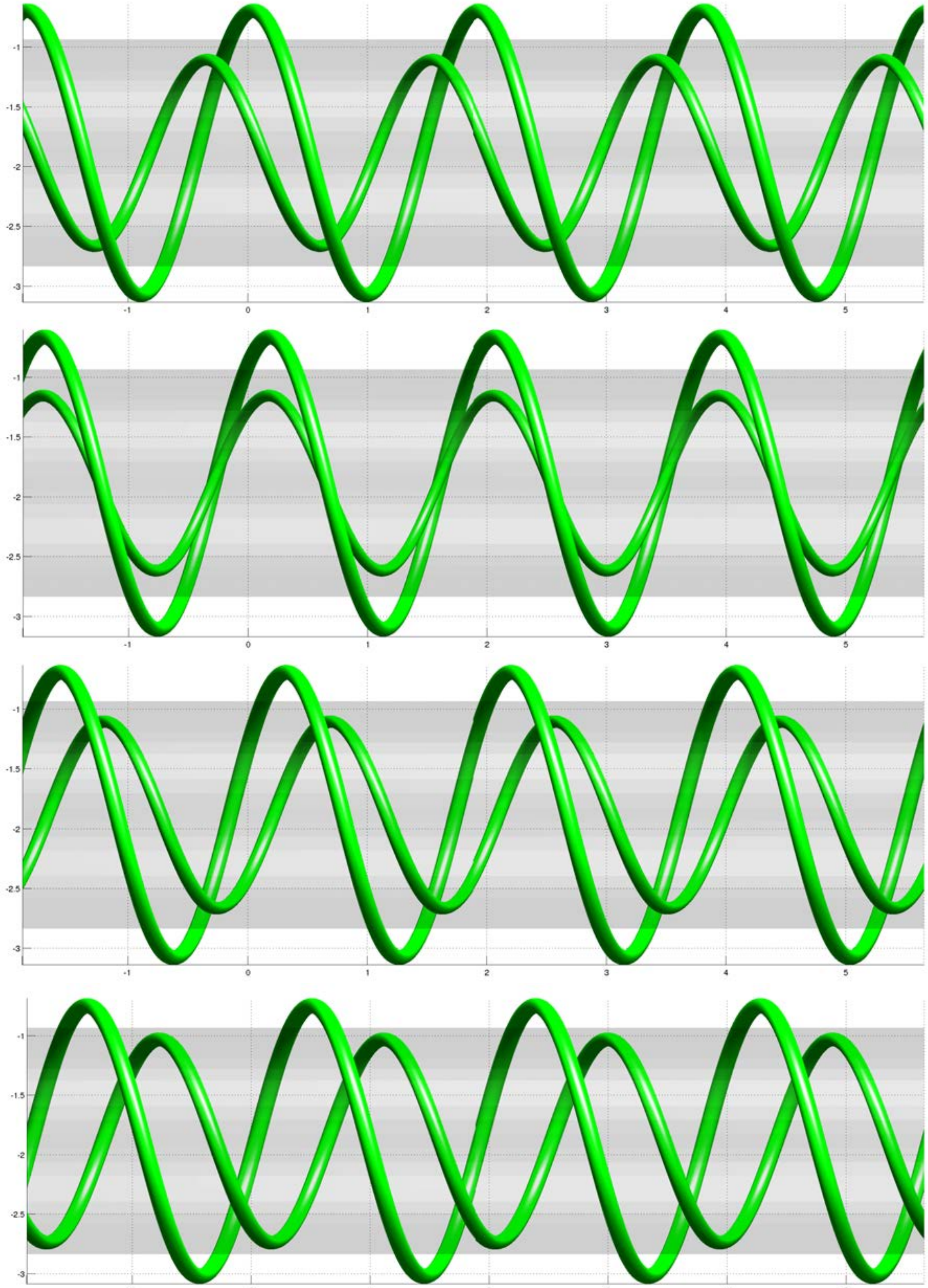

Figure 10.3 – $Re = 10^4$. Time evolution of $N = 2$ helical vortices of reduced pitch $L = 0.3$ with initial core size $a = 0.06$ perturbed with the helical pairing mode. The vortices undergo a leapfrogs process. Isovalue of the helical vorticity $\omega_B = \frac{1}{2}\omega_B^{max}$ at instants $\tau = 6.8, 7.3, 7.8, 8.3$. Time evolution goes from top to bottom. The grey region is the cylinder of radius $R = 1$ around which the unperturbed helical vortices would coil.

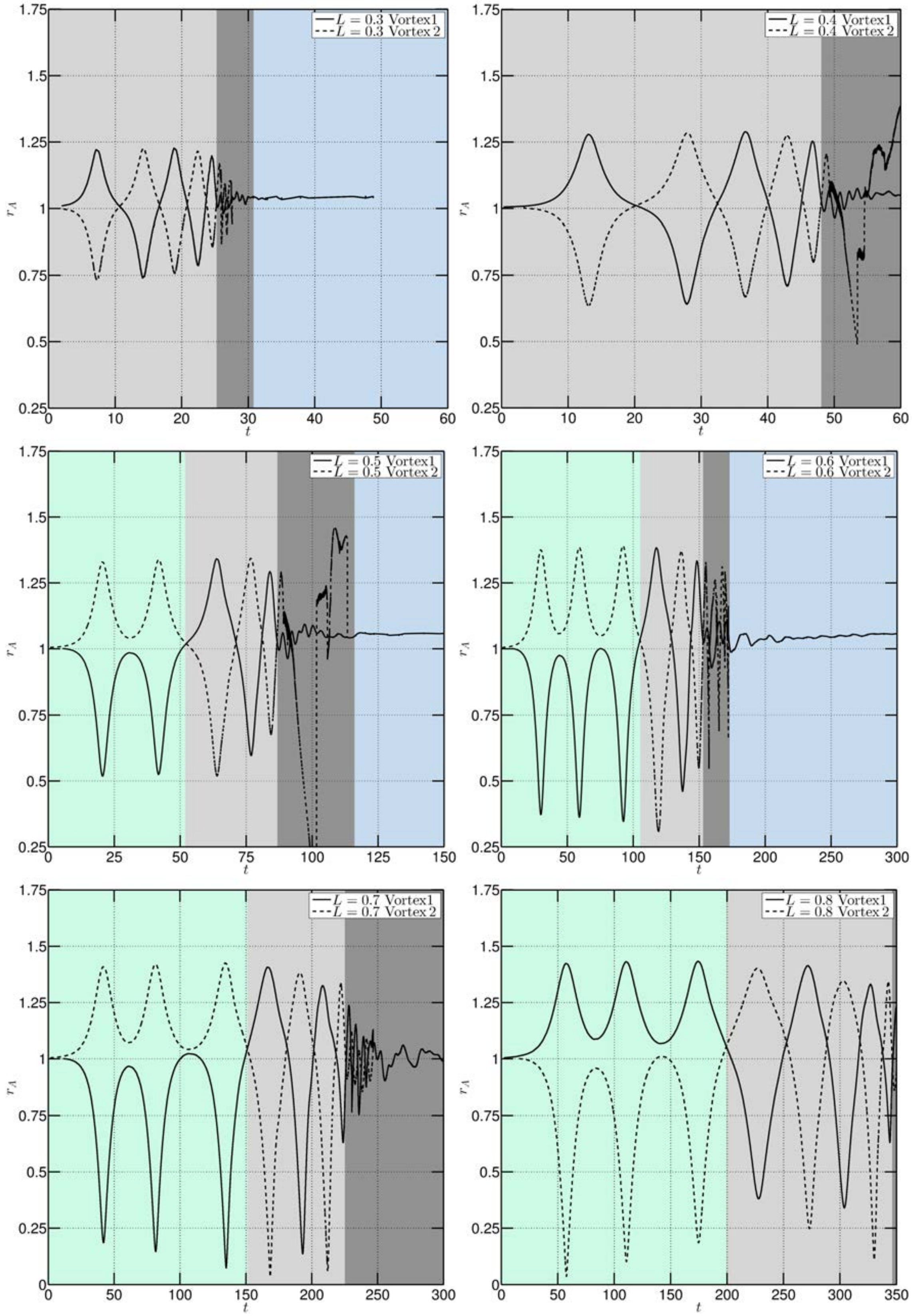

Figure 10.4 – Time evolution of the vortex centres r_A at $Re = 10000$ for $L = 0.3, .., L = 0.8$ with initial core size $a = 0.06$. The light grey area corresponds to the time interval where the leapfrogs occur, the light green region (when it exists) to the overtaking phase, the dark grey area to the merging instant (r_A is erroneously determined in this zone) and the blue region to the merged state.

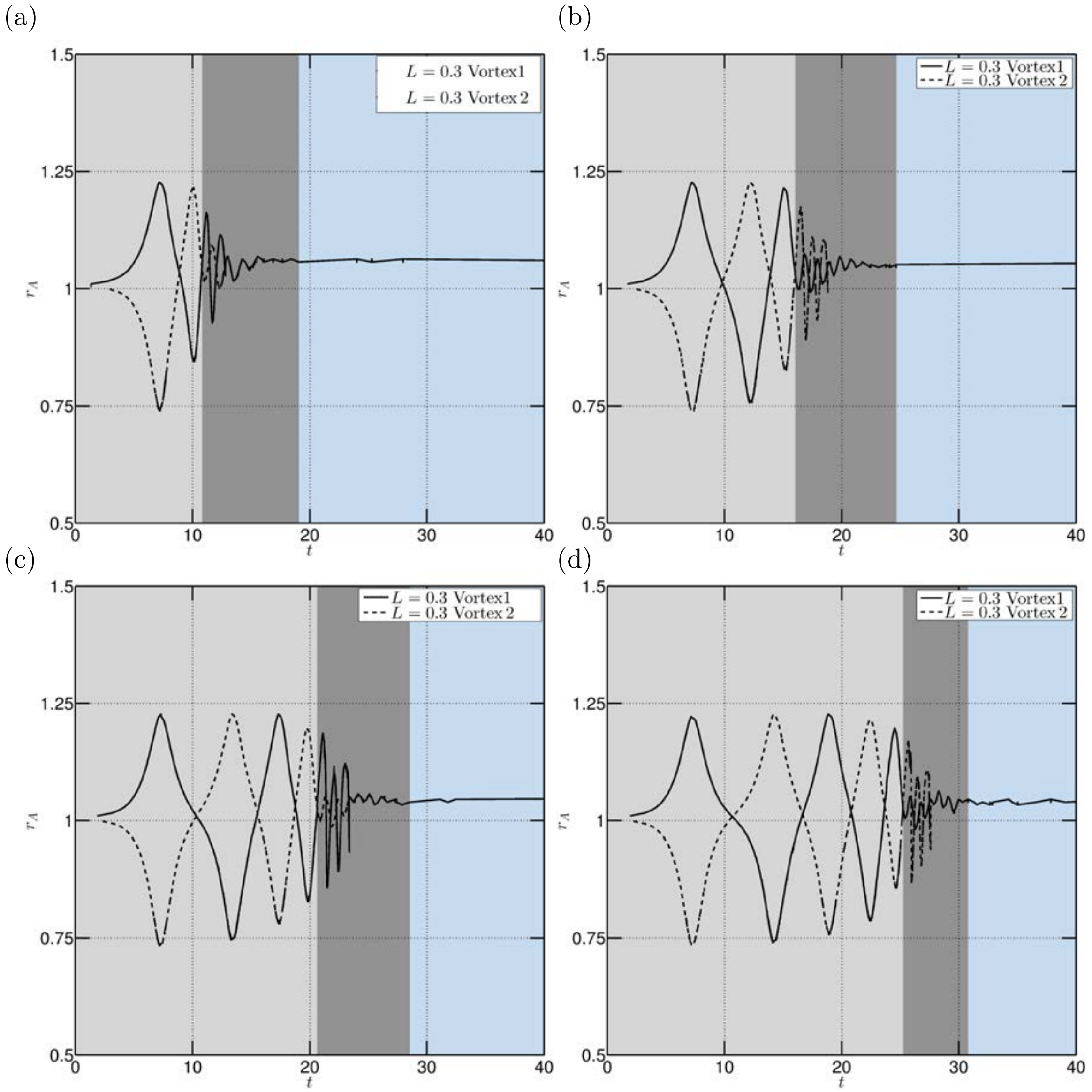

Figure 10.5 – Influence of the Reynolds number on the leapfrog mechanism of two helical vortices of pitch $L = 0.3$ with core size $a = 0.06$. (a) $Re = 2500$. (b) $Re = 5000$. (c) $Re = 7500$ and (d) $Re = 10000$. In all figures, the evolution of r_A is shown as a function of time. The grey region indicates the time interval when the leapfrogs occur, the dark grey represents the merging phase and the clear blue region indicates the merged state.

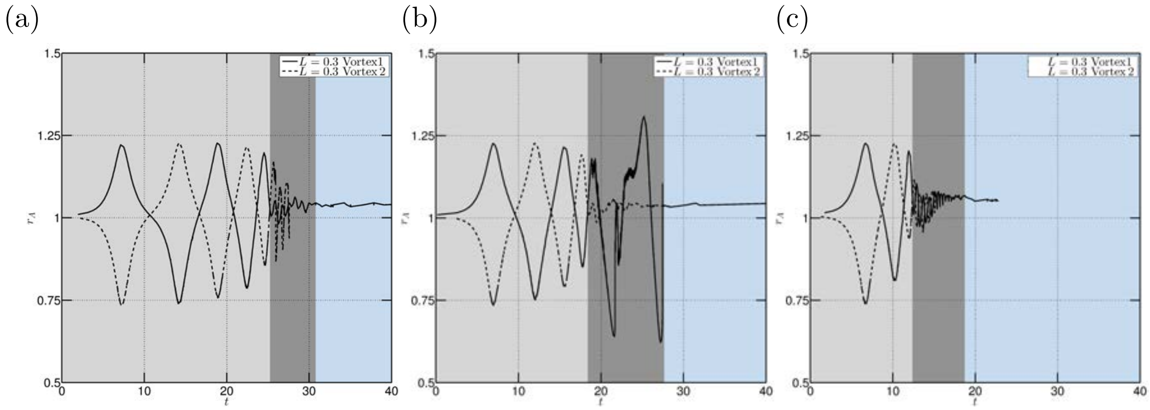

Figure 10.6 – Influence of the initial core size on the leapfrog mechanism of two helical vortices of pitch $L = 0.3$ at $Re = 10000$. Evolution of r_A as a function of time. The solid line represents the first vortex while the dashed one represents its companion. Simulations are initialised with core sizes (a) $a = 0.06$. (b) $a = 0.08$ and (c) $a = 0.10$. In all figures the grey region indicates the time interval when the leapfrogs occur, the dark grey represents the merging instant and the clear blue region shows the merged state.

10.3.3 Influence of the core size a

The influence of the initial core size is analysed by computing the nonlinear evolution of the pairing mode while keeping the Reynolds number Re and the reduced pitch L constant. The core size is varied from 0.06 to 0.1 while L and Re are set to 0.3 and 10000 respectively. In figure 10.6-a, the time evolution of the radial position of the vortex centres are plotted. As the initial core size increases the number of leapfrogs reduces. We observe $5, 4$ and 3 leapfrogs occurring for initial core size $a = 0.06, 0.08$ and $a = 0.10$ respectively. The amplitude of the initial leapfrog seems independent of the initial core size a.

10.3.4 Cut-off theory

We tried to reproduce the above phenomenology within the helical filament model introduced in section 4. The nonlinear evolution of two helical filaments is simulated. As initial condition, we use the positions of the vortex centres taken from the DNS when initially perturbed by the helical pairing mode.
In plane Π_0, the time evolution of the radial positions of the filaments is plotted in figure 10.7 for $0.3 \leq L \leq 0.6$ with core size $a = 0.06$. Strangely, only overtaking events are observed. A drift for the peaks of r_A is observed as in the DNS but it is larger here. The reason for such dynamics remains unclear for now and is left for future investigations.

10.4 Merging of two helical vortices

After the leapfrog events, the vortices merge. In figure 10.8, the time evolution of the merging is shown for $L = 0.3$. Actually, a leapfrog is initiated (see top row) but due to the large core size that the vortices have reached at that time, a full vortex merging occurs (see middle and bottom rows). When viewed in the meridian plane, (right column) this merging resembles a two-dimensional vortex merging.

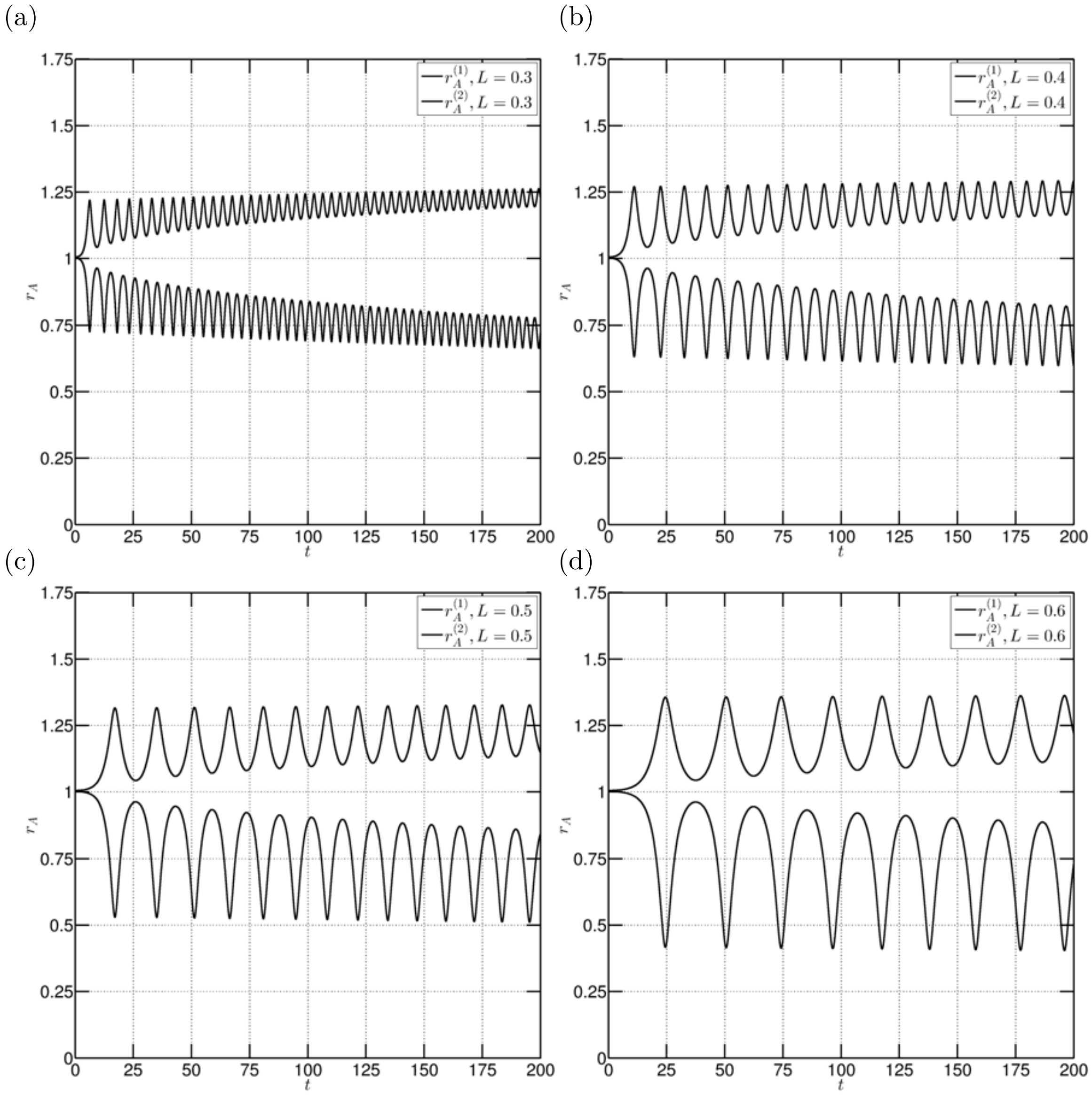

Figure 10.7 – Overtaking motion of $N = 2$ inviscid vortex filaments obtained with the cut-off theory: radial position as a function of time. The initial positions are obtained from the DNS. The core size is fixed at $a = 0.06$ in all figures. (a) $L = 0.3$, (b) $L = 0.4$, (c) $L = 0.5$, (d) $L = 0.6$.

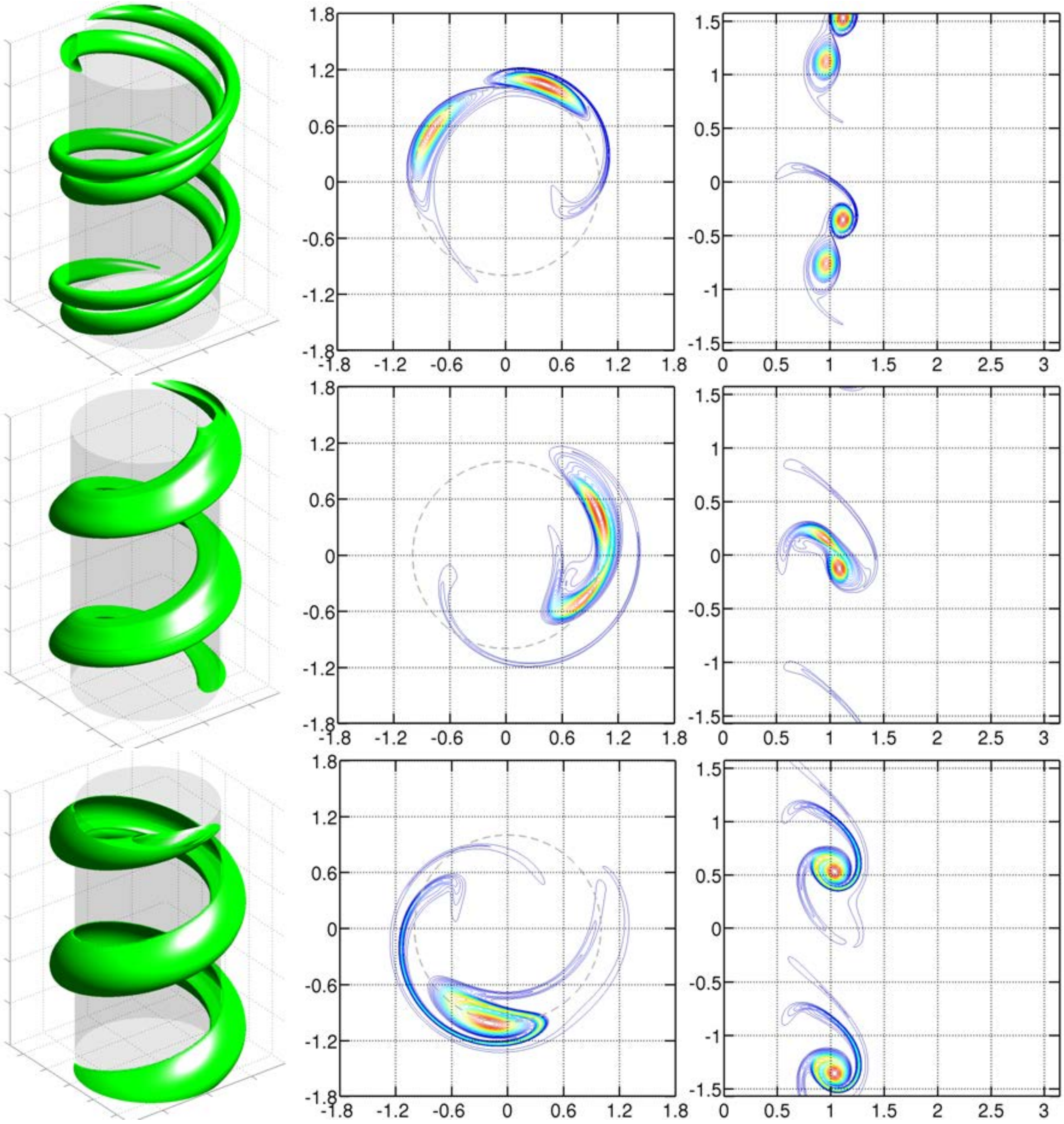

Figure 10.8 – $N = 2$ helical vortices of pitch $L = 0.3$ and core size $a = 0.06$ perturbed initially with the helical pairing mode at $Re = 10000$. Left column: isovalue of the vorticity component $\omega_B = \omega_B^{max}/4$. Central column: contours of the helical vorticity ω_B in plane Π_0. Right column: contours of the helical vorticity ω_B in the median $r - z$ plane. The chosen instants are $\tau = 24,\ 25,\ 26$ (top to bottom).

Chapter 11

Linear stability analysis with respect to general perturbations

Contents

In the previous chapters of the thesis, we considered only flows with a helical symmetry, even when the linear instability modes were concerned. In the present chapter, we investigate flow fields that break the helical symmetry. More precisely, we select helically symmetric base flows that are subject to small amplitude perturbations that do not have the helical symmetry: these perturbations depend on r and φ, but also explicitly on z, they hence display a more complicated structure.

Such analysis was first considered analytically during the 70's by Widnall (1972) for the case of one helical vortex in the inviscid framework. Widnall uses the filamentary approach with the cut off method to take the small core size into account. Within that context, infinitesimal displacement perturbations are introduced proportional to $e^{i\gamma s}$ where s is the arc length along the unperturbed filament and γ the associated wavenumber. The structure of the unstable modes is best understood when described by the non dimensional parameter

$$\gamma/k' = \gamma L(1 + R^2/L^2) \tag{11.1}$$

characterizing the ratio between the *axial* wavelength of the mode and the helical pitch $2\pi L$ (γ/k' is the number of perturbation wavelengths in a single turn of the unperturbed filament). Widnall classifies the unstable mode branches using the following terminology: a very short-wavelength mode, a long-wavelength mode (with axial wavelength larger than the helical pitch) and modes with intermediate wavelength interpreted as mutual-inductance modes between successive turns, for sufficiently low pitches. This work was later expanded to multiple helices by Gupta and Loewy (1974) with a different desingularisation technique.

Using DNS, we generalise the above results to viscous vortices with cores of finite extent. The stability problem is briefly formulated and, since perturbations cannot be described in a two-dimensional framework, a new code HELIKZ is introduced (section 11.1). We can extract the three-dimensional unstable modes for a single or several helical vortices

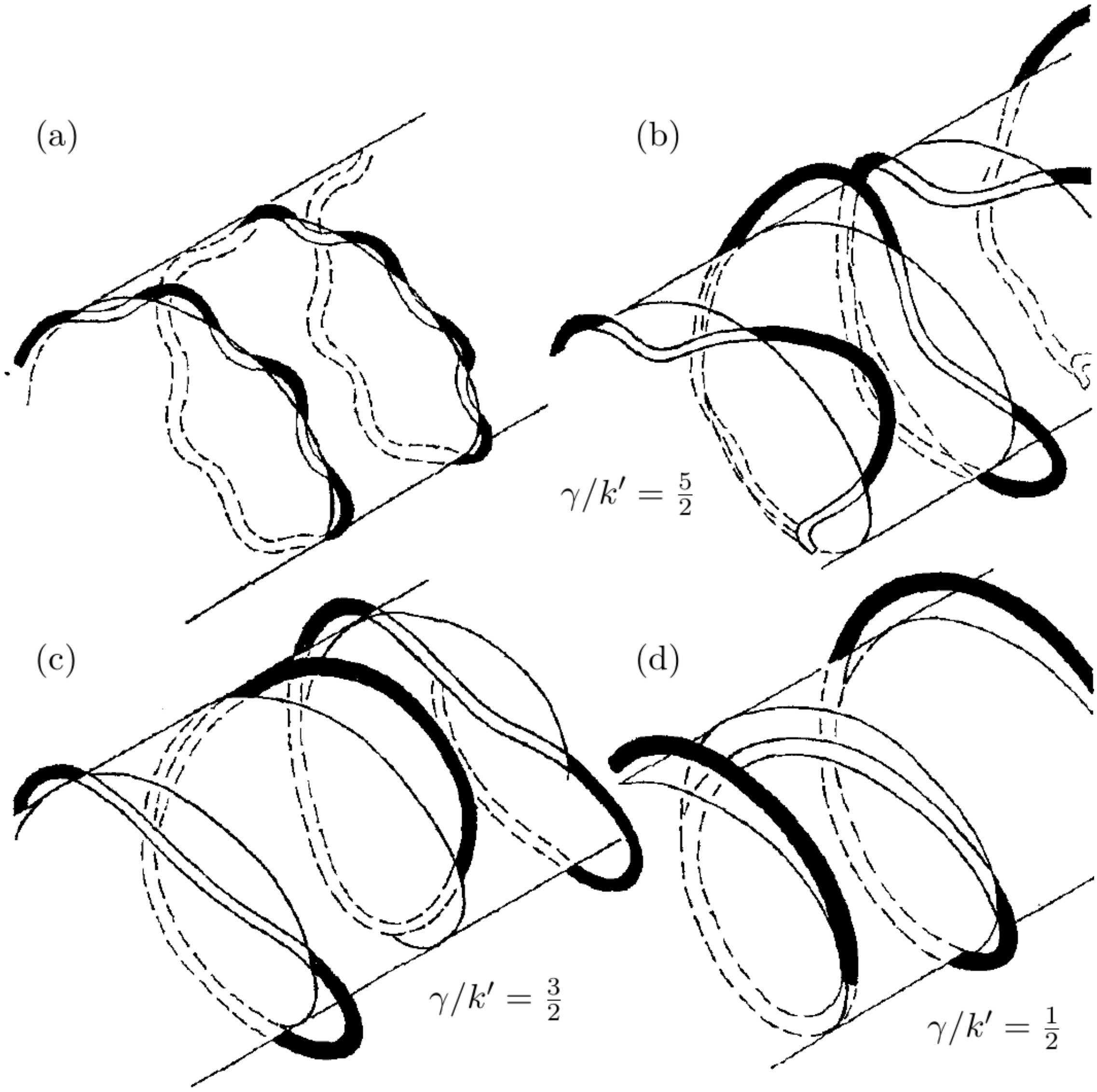

Figure 11.1 – General perturbation modes as sketched by Widnall (1972) for different values of the parameter γ/k'. Widnall makes a distinction between (a) short-wavelength modes, (b) and (c) intermediate wavelength or mutual induction modes and (d) long-wavelength modes. Taken from Bolnot (2012).

(section 11.2). Some of the modes we identify are displacement modes; short-wavelength modes that deform the vortex core can also be obtained using this technique.

11.1 Stability analysis

Here we briefly present the base flow, the linear equations governing the dynamics of perturbations and the dedicated numerical code HELIKZ.

11.1.1 Frozen helically symmetric base flow

The base flow possesses the helical symmetry of reduced pitch L along the z-axis. It is one of the quasi-equilibrium states obtained in chapter 6 by running the HELIX code in the inertial frame up to a certain time t_0. This state is now supposed frozen. Since in the inertial frame the vortex or vortex system rotates at angular velocity $\Omega_0 \equiv \Omega(t_0)$, we adopt the rotating non-inertial frame in which the flow is steady, with basic velocity $\boldsymbol{v}^{\mathrm{BF}}$ and vorticity $\boldsymbol{\omega}^{\mathrm{BF}}$. These latter fields are transferred to the new code HELIKZ and decomposed into cylindrical components which are the native components of HELIKZ (HELIX uses helical components).

In the frame rotating at angular velocity Ω_0, the basic flow components depend only on the two space variables r and $\varphi \equiv \theta - z/L$. For instance, the velocity field is expressed in the cylindrical coordinate system $(\boldsymbol{e_r}, \boldsymbol{e_\theta}, \boldsymbol{e_z})$ as

$$\boldsymbol{v}^{\mathrm{BF}} = v_r^{\mathrm{BF}}(r,\varphi,t_0)\boldsymbol{e}_r(\theta) + v_\theta^{\mathrm{BF}}(r,\varphi,t_0)\boldsymbol{e}_\theta(\theta) + v_z^{\mathrm{BF}}(r,\varphi,t_0)\boldsymbol{e}_z\,. \tag{11.2}$$

11.1.2 Equations for the perturbations

In the rotating frame, the velocity (resp. vorticity) reads $\boldsymbol{v}^{\mathrm{BF}} + \boldsymbol{v}$ (resp. $\boldsymbol{\omega}^{\mathrm{BF}} + \boldsymbol{\omega}$) and the infinitesimal perturbations of velocity $\boldsymbol{v}$ and vorticity $\boldsymbol{\omega}$ satisfy the linearized Navier-Stokes equations:

$$\partial_t \boldsymbol{v} + [\boldsymbol{\omega}^{\mathbf{BF}} + 2\Omega_0 \boldsymbol{e}_z] \times \boldsymbol{v} + \boldsymbol{\omega} \times \boldsymbol{v}^{\mathbf{BF}} = -\boldsymbol{\nabla}\left(\frac{P}{\rho}\right) + \frac{1}{Re}\Delta \boldsymbol{v}\,, \tag{11.3}$$

where P is the linearized dynamical pressure. Note that, in the above equation, the term $[\boldsymbol{\omega}^{\mathbf{BF}} + 2\Omega_0 \boldsymbol{e}_z]$ represents the absolute vorticity. At this point, since $\boldsymbol{v}^{\mathrm{BF}}$ only depends on (r, φ), a change of variables is applied from (r, θ, z) to $(\tilde{r}, \varphi, \tilde{z})$ where

$$\tilde{r} \equiv r, \qquad \tilde{z} \equiv z, \qquad \varphi \equiv \theta - \frac{z}{L}. \tag{11.4}$$

As shown below, this particular change of variable simplifies the system (11.3) governing the dynamics of generalised perturbations to a two-dimensional problem in variables $(\tilde{r}, \varphi)$. Through this change of variables, spatial derivatives become

$$\frac{\partial}{\partial r} = \frac{\partial}{\partial \tilde{r}}\,, \quad \frac{\partial}{\partial \theta} = \frac{\partial}{\partial \varphi}\,, \quad \frac{\partial^2}{\partial \theta^2} = \frac{\partial^2}{\partial \varphi^2}\,, \tag{11.5}$$

$$\frac{\partial}{\partial z} = \frac{\partial}{\partial \tilde{z}} - \frac{1}{L}\frac{\partial}{\partial \varphi}\,, \tag{11.6}$$

$$\frac{\partial^2}{\partial z^2} = \frac{\partial^2}{\partial \tilde{z}^2} - \frac{2}{L}\frac{\partial}{\partial \tilde{z}}\frac{\partial}{\partial \varphi} + \frac{1}{L^2}\frac{\partial^2}{\partial \varphi^2}\,. \tag{11.7}$$

The components of the linearised advective terms $\boldsymbol{ADV} = [\boldsymbol{\omega}^{\mathbf{BF}} + 2\Omega_0 \boldsymbol{e}_z] \times \boldsymbol{v} + \boldsymbol{\omega} \times \boldsymbol{v}^{\mathbf{BF}}$ can be written as

$$ADV_r = \omega_\theta^{\mathrm{BF}} v_z - (\omega_z^{\mathrm{BF}} + 2\Omega_0) v_\theta + \left(\omega_\theta v_z^{\mathrm{BF}} - \omega_z v_\theta^{\mathrm{BF}}\right)\,,$$

$$ADV_\theta = (\omega_z^{\mathrm{BF}} + 2\Omega_0)v_r - \omega_r^{\mathrm{BF}} v_z + \left(\omega_z v_r^{\mathrm{BF}} - \omega_r v_z^{\mathrm{BF}}\right) ,$$

$$ADV_z = \omega_r^{\mathrm{BF}} v_\theta - \omega_\theta^{\mathrm{BF}} v_r + \left(\omega_r v_\theta^{\mathrm{BF}} - \omega_\theta v_r^{\mathrm{BF}}\right) ,$$

where the vorticity is such that

$$\omega_r = \frac{1}{\tilde{r}}\frac{\partial v_z}{\partial \varphi} - \frac{\partial v_\theta}{\partial \tilde{z}} + \frac{1}{L}\frac{\partial v_\theta}{\partial \varphi} \tag{11.8}$$

$$\omega_\theta = \frac{\partial v_r}{\partial \tilde{z}} - \frac{1}{L}\frac{\partial v_r}{\partial \varphi} - \frac{\partial v_z}{\partial r} \tag{11.9}$$

$$\omega_z = \frac{1}{\tilde{r}}\frac{\partial}{\partial \tilde{r}}(\tilde{r}\, v_\theta) - \frac{1}{\tilde{r}}\frac{\partial v_r}{\partial \varphi} \tag{11.10}$$

Similarly, the viscous terms along the radial, azimuthal and axial direction can be written as

$$VT_r \equiv \frac{\partial}{\partial \tilde{r}}\left(\frac{1}{\tilde{r}}\frac{\partial(\tilde{r}v_r)}{\partial \tilde{r}}\right) + \frac{1}{\tilde{r}^2}\frac{\partial^2 v_r}{\partial \varphi^2} + \frac{\partial^2 v_r}{\partial \tilde{z}^2} - \frac{2}{L}\frac{\partial}{\partial \tilde{z}}\frac{\partial}{\partial \varphi}v_r + \frac{1}{L^2}\frac{\partial^2 v_r}{\partial \varphi^2} - \frac{1}{\tilde{r}^2}\frac{\partial}{\partial \varphi}(2v_\theta) ,$$

$$VT_\theta \equiv \frac{\partial}{\partial \tilde{r}}\left(\frac{1}{\tilde{r}}\frac{\partial(\tilde{r}v_\theta)}{\partial \tilde{r}}\right) + \frac{1}{\tilde{r}^2}\frac{\partial^2 v_\theta}{\partial \varphi^2} + \frac{\partial^2 v_\theta}{\partial \tilde{z}^2} - \frac{2}{L}\frac{\partial}{\partial \tilde{z}}\frac{\partial}{\partial \varphi}v_\theta + \frac{1}{L^2}\frac{\partial^2 v_\theta}{\partial \varphi^2} + \frac{1}{\tilde{r}^2}\frac{\partial}{\partial \varphi}(2v_r) ,$$

$$VT_z \equiv \frac{1}{\tilde{r}}\frac{\partial}{\partial \tilde{r}}\left(\tilde{r}\frac{\partial v_z}{\partial \tilde{r}}\right) + \frac{1}{\tilde{r}^2}\frac{\partial^2 v_z}{\partial \varphi^2} + \frac{\partial^2 v_z}{\partial \tilde{z}^2} - \frac{2}{L}\frac{\partial}{\partial \tilde{z}}\frac{\partial}{\partial \varphi}v_z + \frac{1}{L^2}\frac{\partial^2 v_z}{\partial \varphi^2} ,$$

and incompressibility reads

$$\boldsymbol{\nabla}\cdot\boldsymbol{v} = \frac{1}{\tilde{r}}\frac{\partial(\tilde{r}v_r)}{\partial \tilde{r}} + \frac{1}{\tilde{r}}\frac{\partial v_\theta}{\partial \varphi} + \frac{\partial v_z}{\partial \tilde{z}} - \frac{1}{L}\frac{\partial v_z}{\partial \varphi} = 0. \tag{11.11}$$

Since the base flow $\boldsymbol{v}^{\mathrm{BF}}$ do *not* depend on $\tilde{z}$, one may search for a **complex** solution for the linearised Navier-Stokes in the form of a normal mode in $\tilde{z}$:

$$\boldsymbol{v} = \exp(\mathrm{i}k_z\tilde{z})[\hat{v}_r(\tilde{r},\varphi,t)\boldsymbol{e}_r(\theta) + \hat{v}_\theta(\tilde{r},\varphi,t)\boldsymbol{e}_\theta(\theta) + \hat{v}_z(\tilde{r},\varphi,t)\boldsymbol{e}_z] , \tag{11.12}$$

where k_z is a wavenumber parameter along $\tilde{z}$. Note that for $k_z = 0$, helically symmetric perturbations are recovered.

Since all wavenumbers k_z behave independently, the linearized Navier-Stokes system is very much simplified: for each wavenumber k_z, it becomes a set of partial differential equations depending on time t, spatial variables $\tilde{r}$, φ and in which k_z appears as a prescribed parameter.

11.1.3 Numerical code HELIKZ

The above problem is similar to the one we had to solve with the linearised HELIX code for helically symmetric perturbations. However, the numerical resolution is more involved in the code HELIKZ as the flow is essentially three-dimensional: the three velocity components along with the pressure are unknowns and require the use of a projection method to ensure the divergence-free condition. As the solutions $\boldsymbol{v}$ are periodic along the direction φ, one uses a Fourier expansion in φ:

$$\hat{v}_r(\tilde{r},\varphi,t) = \sum_{m=-\infty}^{\infty} \exp(\mathrm{i}m\varphi)\hat{v}_r^{(m)}(\tilde{r},t) \tag{11.13}$$

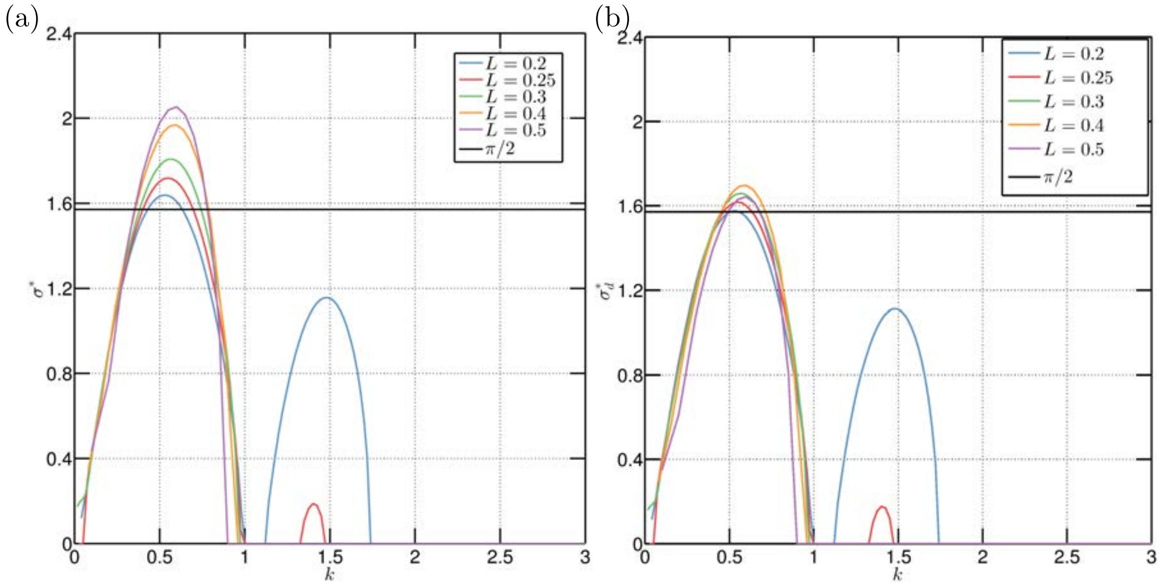

Figure 11.2 – Single helical vortex of core size $a = 0.06$ at $Re = 5000$. Normalized growth rates as a function of k for various values of the reduced pitch L: (a) σ^* and (b) σ_d^*.

$$\hat{v}_\theta(\tilde{r}, \varphi, t) = \sum_{m=-\infty}^{\infty} \exp(im\varphi)\hat{v}_\theta^{(m)}(\tilde{r}, t) \tag{11.14}$$

$$\hat{v}_z(\tilde{r}, \varphi, t) = \sum_{m=-\infty}^{\infty} \exp(im\varphi)\hat{v}_z^{(m)}(\tilde{r}, t) \tag{11.15}$$

However, note that quantities $\hat{v}_i(\tilde{r}, \varphi, t)$, and $\hat{v}_i^{(m)}(\tilde{r}, t)$ are *both* complex so that there is no relation between modes $\hat{v}_i^{(m)}$ and $\hat{v}_i^{(-m)}$, contrary to what we have in the HELIX code. For each k_z, the resulting dynamical equations are then solved in spectral space along φ and using finite differences along $\tilde{r}$. Boundary conditions are also dependent on k_z, this leads to technical developments which are not exposed in this thesis but will be included in future publications. The mode extraction is performed by coupling HELIKZ with an Arnoldi procedure described in chapter 8 and adapted to the HELIKZ primitive variables (velocity and pressure).

11.2 HELIKZ results

We present the results using a non dimensional wavenumber k defined as

$$k = k_z \frac{L}{N}. \tag{11.16}$$

The advantage of such definition is that k is identical to the original Widnall parameter γ/k' defined in (11.1).

11.2.1 Long wavelength and mutual induction instability

One helical vortex

In figure 11.2, the normalised growth rates σ^* and σ_d^* given respectively in (9.5) and (9.7) are plotted as a function of k for various values of L in the range $0.2 \leq L \leq 0.5$. At fixed L in the range investigated here, the growth rate curves take the form of one or several tongues with maxima occurring close to values $k = 1/2$ and $k = 3/2$ (but not exactly).

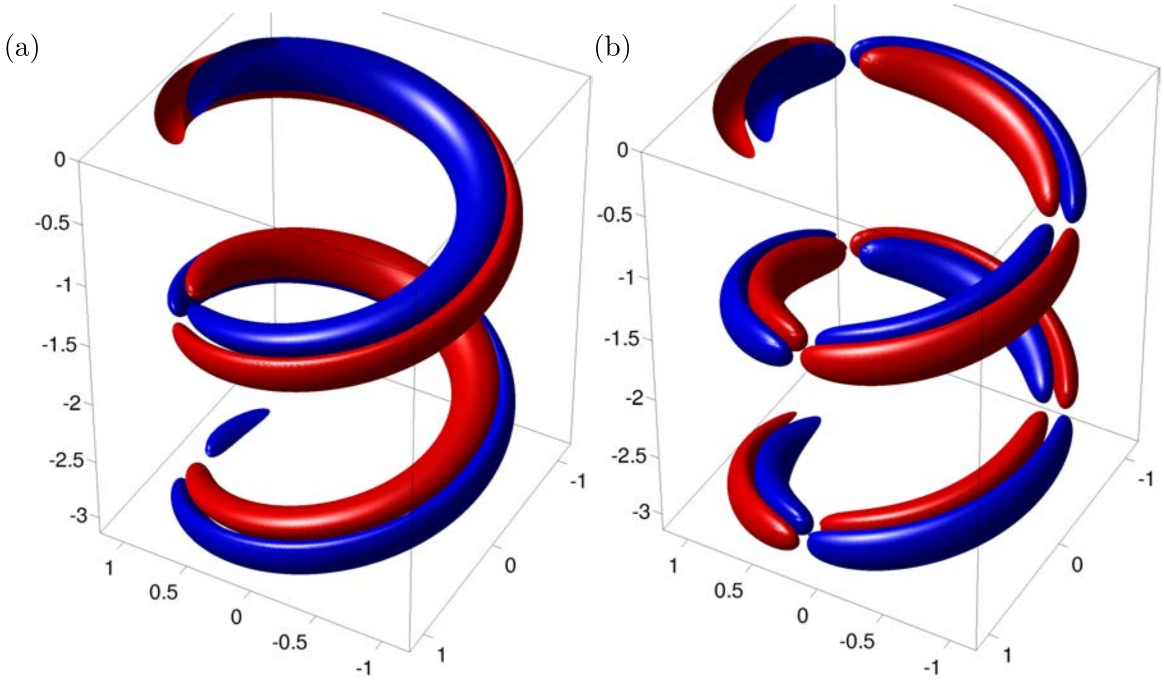

Figure 11.3 – Single helical vortex at $L = 0.25$: structure of the dominant instability modes (a) $k = 1/2$ and (b) $k = 3/2$.

The three-dimensional structure of the mode $k = 0.55$ close to the first maximum for $L = 0.25$ is presented in figure 11.3-a. This mode displays the typical vorticity structure of displacement modes but with signs changing every helix turn (the wavelength being of two helix turns). When superimposed on the basic flow, the mode induces the displacement or local groupings sketched in figure 11.4 (top). As described by Quaranta et al. (2015), the pattern repeats every two helix turns and there is only one azimuthal location where a local grouping between facing turns occurs.

The three-dimensional structure of the mode $k = 1.4$ close to the second maximum for $L = 0.25$ is presented in figure 11.3-b. The displacement mode structure here changes signs every third helix turn. When superimposed on the basic flow, the mode induces the displacement sketched in figure 11.4 (bottom): the pattern repeats every two turns and there are three azimuthal locations where local groupings occur.

Such modes have been experimentally investigated by Quaranta et al. (2015). They obtained normalised maximum growth rates for $k = 1/2$, $k = 3/2$ and $k = 5/2$. However, their pitch value is smaller ($L \approx 0.16$) than in the present study, and a low pitch enhances the instability of mutual inductance modes. This effect is observed here: no unstable mode is observed near $k = 5/2$ for our range $L \geq 0.2$ because the pitch is too large. Moreover, the maximum growth rate near $k = 3/2$ at $L = 0.20$ is $\sigma^* = 1.157$, while for $L = 0.25$ it is as low as $\sigma^* = 0.187$. This also agrees with Widnall (1972) who states that mutual inductance modes are no more unstable below $L = 0.3$.

The values of the maximum growth rates obtained for different values of L near $k = 1/2$ can be understood if we renormalise the growth rate using the local distance d between turns as was done in chapter 9.2.2. The growth rate σ_d^* is plotted in figure 11.2-b. The maximum growth rate is found very close to $\pi/2$ for all L investigated. This indicates that the mechanism driving the local groupings is similar to the pairing instability of an infinite array of point vortices.

In figure 11.5, the dominant eigenvalue for the case $L = 0.3$ is plotted in the $\sigma - \omega/2\pi$ plane for $0.03 \leq k \leq 0.9$ (first tongue in figure 11.2). For $k = 0$ the mode is known to be

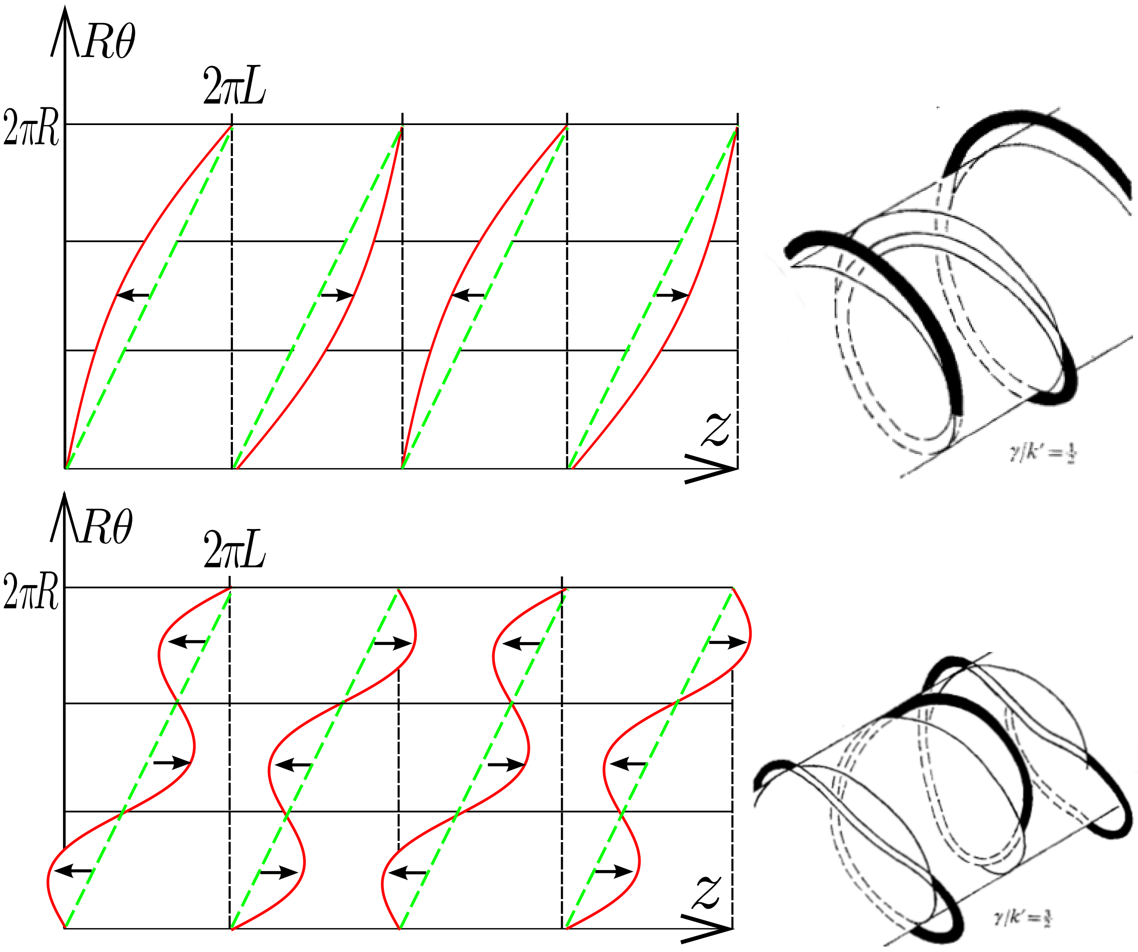

Figure 11.4 – Structure of the displacement modes. Left: sketch of the mode with the helix unwrapped in the $R\theta - z$ plane. Right: original figure of the mode from Widnall (1972). Top: mode $k = 1/2$. Bottom: $k = 3/2$.

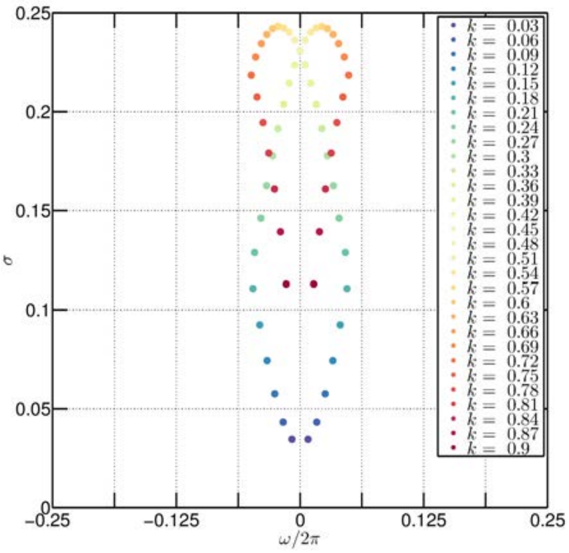

Figure 11.5 – Single helical vortex of reduced pitch $L = 0.3$ and core size $a = 0.09$ at $Re = 5000$. Dominant eigenvalue in the $\sigma - \omega/2\pi$ plane for various k.

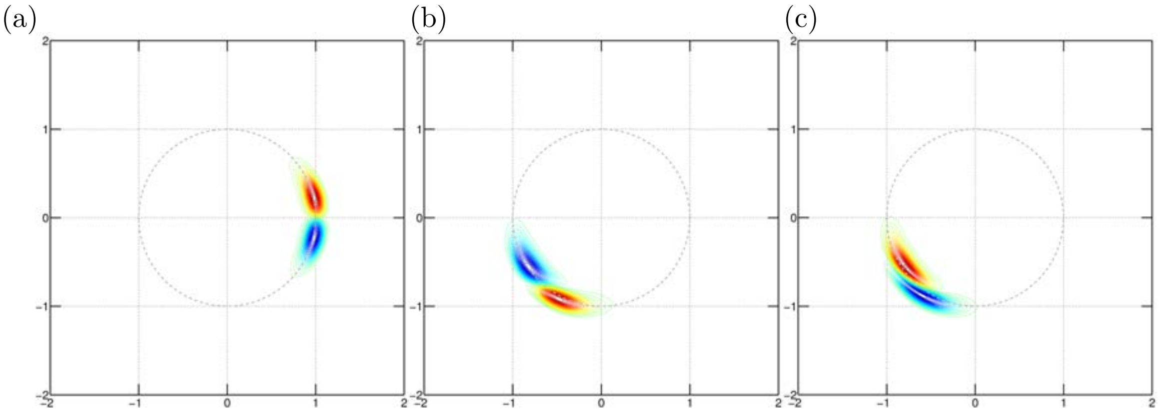

Figure 11.6 – Single helical vortex at $L = 0.3$ and core size $a = 0.09$. Real part of the dominant eigenmode for (a) $k = 0$ (helically symmetric perturbations), (b) $k = 0.09$ and (c) $k = 0.54$.

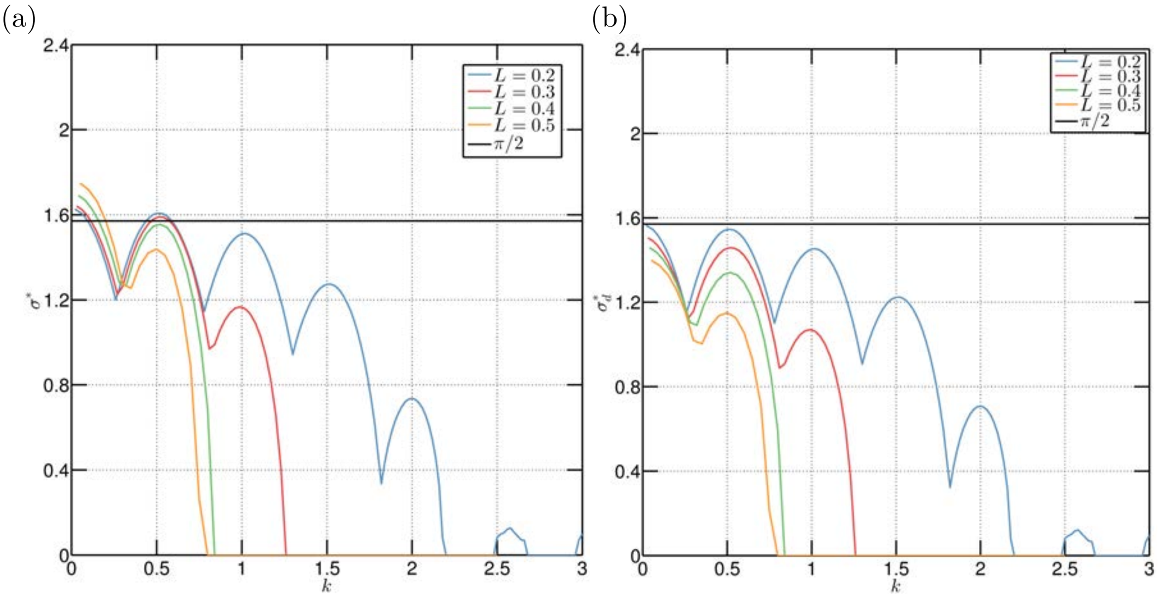

Figure 11.7 – $N = 2$ helical vortices of core size $a = 0.06$ at $Re = 5000$. Normalised growth rates as a function of k for various values of reduced pitch L: (a) σ^* and (b) σ^*_d.

neutral (see section 9.1) but as k is increased it is progressively destabilised, giving rise to an unstable long wavelength phase mode. The structure of such mode is plotted in figure 11.6-b for $k = 0.09$, and can be compared to the structure of the neutral mode at $k = 0$ (figure 11.6-a) and of the maximum growth rate mode at $k = 0.54$ (figure 11.6-c). It is seen on this figure how the eigenmode structure is progressively deformed from that of the neutral mode as k is increased from zero. Note that the phase mode has a non zero frequency which gives rise to a phase velocity ($\omega/k \approx 2$). The neutral mode is stationary and the modes near the maximum at $k = 1/2$ are found almost stationary.

Two helical vortices

We now investigate the stability properties of $N = 2$ helical vortices. The parameter $k = k_z L/N$ can be written as $k = \Lambda^{\mathrm{BF}}/\lambda$ where Λ^{BF} is the axial periodicity of the base flow ($\Lambda^{BF} = 2\pi L/N$) and λ the axial wavelength of the perturbation ($\lambda = 2\pi/k_z$). As a consequence, k represents the number of perturbation wavelengths over the spatial period of the basic flow. For $N = 2$, the periodicity of the base flow represents half a helix turn. The growth rates $\sigma^*(k)$ and $\sigma^*_d(k)$ are plotted in figure 11.7 for various pitch values in the

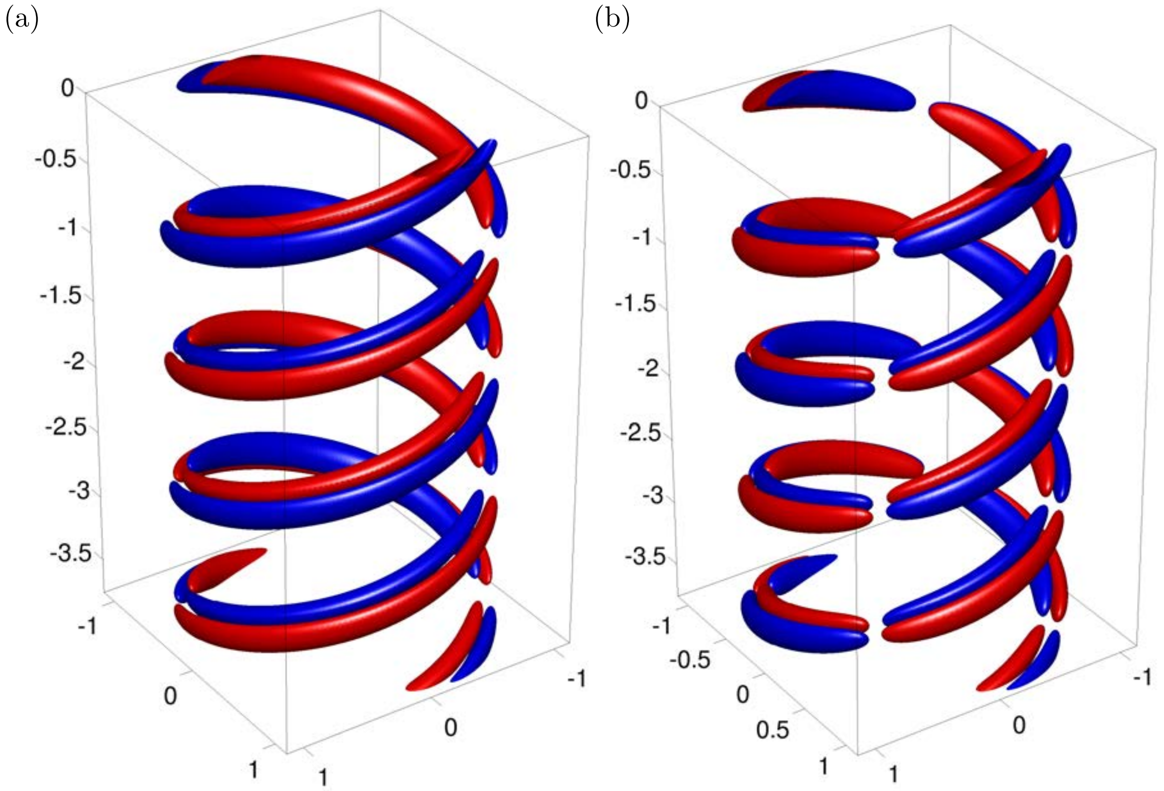

Figure 11.8 – $N = 2$ helical vortices at $L = 0.30$ and core size $a = 0.06$: structure of unstable modes (a) $k = 1/2$, (b) $k = 1$.

range $0.2 \leq L \leq 0.5$. As previously, local maxima are observed in the vicinity of $k = 1/2$, 3/2, ... and correspond to situations with 1/2, 3/2, ... perturbation wavelengths per half helix cycle. These modes have a similar structure as modes $k = 1/2, 3/2, ...$ for $N = 1$ vortex but the local groupings now involve different vortices (see figure 11.8-a). Additional instability tongues are observed which are centred on $k = 0$, 1, 2, ... and correspond to situations where there is an integer number of perturbation wavelengths within half a helix turn (see figure 11.8-b).

However for $N = 2$, the maximum amplification is obtained for helically symmetric perturbations ($k \to 0$) for which σ_d^* tends to a value slightly below $\pi/2$. This value decreases when L increases as already shown in figure 9.5. The dominant instability mode is thus the global helical pairing mode.

It is also observed that as L is increased, the range of k for which instability occurs reduces, since interactions between turns weaken.

11.2.2 Elliptical instability

In section 11.2.1, we have obtained instability modes which all were displacement modes. However, the HELIKZ code permits the investigation of modes which deform the internal structure of the vortex. An example of such mode is represented in figure 11.9. The structure is clearly not the structure of a displacement mode. Yet, a dipolar distribution of vorticity is present but it is localised inside each of the two vortex cores (in the figure the cores are materialised by dashed black circles). This is reminiscent of the radial structure associated to elliptical instability (see figure 18-c of reference (Leweke et al., 2016)). Indeed, the present configuration at large pitch $L = 2$ is relatively close to the case of two straight infinite vortices and the mode structure obtained here is the helical counterpart of the one revealed in Meunier (2001) (see his figure 5.13). This preliminary

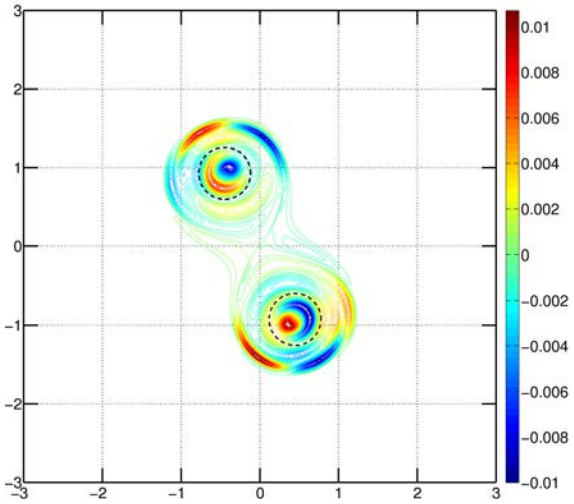

Figure 11.9 – $N = 2$ helical vortices of pitch $L = 2$, core size $a = 0.33$. structure of unstable mode for $k = 4.7$.

finding is a promising result and opens the way to further investigations, especially on elliptical instabilities in vortex systems with small pitch.

Chapter 12

Conclusion and perspectives

The work exposed in this manuscript is a contribution to the numerical study of helical vortices and their instabilities.

Using a dedicated DNS code we have simulated basic states for various helical vortex configurations and developed accurate tools for their characterisation. We have extended the inviscid two-dimensional relationship between stream function and vorticity which holds for steady flows to the helical viscous framework. We have deeply investigated the quasi-equilibrium state of a single helical vortex by analysing the slow viscous time evolution of properties such as helix radius, angular velocity, core size and ellipticity, and by highlighting a self-similar solution. In order to deepen the basic knowledge of helical vortices, it will be necessary to investigate the influence of a strong jet component within the vortex core. Indeed such feature was observed experimentally (Quaranta et al., 2015) and the temporal evolution of its amplitude in the quasi-equilibrium framework is still an open question.

In the thesis, we have shown the influence of pitch and core size on the streamline topology and the consequences for passive particle transport in a helical vortex. The case of inertial particles has been implemented but no extensive simulations could be done due to lack of time. It would be interesting to complement this study and extend the results of IJzermans et al. (2007) on the accumulation of inertial particles around a helical vortex filament. Other physical effects acting on the particles could also be introduced (e.g. pressure gradient).

We have successfully compared the internal structure of the helical vortex with the analytical predictions provided by the IRPHE partner using accurate multipolar decompositions of instantaneous flow fields. This collaboration work resulted in a publication (Blanco-Rodríguez et al., 2015).

We implemented an Arnoldi algorithm within a linearised version of the DNS code in order to determine the linear stability properties with respect to helically symmetric perturbations. For arrays of two or three helical vortices, we identified the displacement mode unstable at low pitch and investigated its dependency with respect to pitch, core size, Reynolds number and presence of a hub vortex. This mode was confirmed to be analogous to the pairing mode of an infinite array of point vortices or vortex rings.

We computed the nonlinear dynamics of helical vortices when perturbed by the latter instability mode initially set at a small amplitude, in the framework of helical symmetry. A complex dynamics was observed with a sequence of overtaking events, leapfrogging and eventually merging. The extension to more complex vortex systems (three vortices with or without hub, ...) and the analysis in terms of dynamical systems may be considered in the future.

Finally, we were able to compute linear instability modes that break the helical symmetry and generalise the displacement modes obtained by Widnall (1972). We investigated the dependency of the growth rate with respect to pitch and core size for one and two helical vortices. These results were successfully compared to the experimental work of Quaranta et al. (2015).

Using the same numerical tools, a different kind of mode could be extracted: a mode deforming the helical vortex cores arising through the elliptic instability mechanism. Theoretical and experimental works are currently carried on this subject at IRPHE. The preliminary numerical results presented in this manuscript open the way to a systematic investigation of their linear instability properties. A natural extension to this work would be to simulate the nonlinear evolution of the elliptical instabilities in helical vortices with a fully three-dimensional Navier-Stokes solver. Due to the huge difference of scales between the size of the helical vortex (pitch or radius) and the size of radial structures within the thin vortex core (a fraction of the core size), an optimised solver with adaptive mesh refinement (AMR) is *a priori* necessary.

Appendix A

Rate of strain tensor for helically symmetric flows.

The components of the rate of strain tensor are here given below for helically symmetric flows

$$
\begin{aligned}
\sigma_{rr}^{(m)} &= \frac{\partial u_r^{(m)}}{\partial r} \\
\sigma_{\varphi\varphi}^{(m)} &= \mathrm{i}m\left(\frac{1}{r\alpha} - \frac{2r^3\alpha^3}{L^4}\right)u_\varphi^{(m)} + \frac{\alpha^2 u_r^{(m)}}{r} \\
\sigma_{BB}^{(m)} &= \frac{\alpha^2 r}{L^2}\left(u_r^{(m)} - 2im\alpha u_B^{(m)}\right) \\
\sigma_{r\varphi}^{(m)} &= \frac{1}{2}\frac{\partial u_\varphi^{(m)}}{\partial r} + \frac{\mathrm{i}m}{2r\alpha}u_r^{(m)} - \frac{\alpha^2}{2r}u_\varphi^{(m)} \\
\sigma_{rB}^{(m)} &= \frac{1}{2}\frac{\partial u_B^{(m)}}{\partial r} - \frac{\alpha^2 r}{2L^2}u_B^{(m)} - \frac{\alpha^2}{L}u_\varphi^{(m)} \\
\sigma_{\varphi B}^{(m)} &= \frac{\mathrm{i}m}{2r\alpha}u_B^{(m)} + \frac{2\alpha}{L}\left(1-\alpha^2\right)\mathrm{i}mu_\varphi^{(m)}
\end{aligned}
$$

At the origin $r = 0$ they are obtained by using L'Hôpital's rule:

$$
\begin{aligned}
&\sigma_{\varphi\varphi}^{(0)}(r=0) = 0 \\
&\sigma_{\varphi\varphi}^{(1)}(r=0) = 0 \\
&\sigma_{\varphi\varphi}^{(m)}(r=0) = \frac{\mathrm{i}m}{2}\left.\frac{\partial u_\varphi^{(m)}}{\partial r}\right|_{r=0} \qquad m \geq 2 \\
&\sigma_{r\varphi}^{(0)}(r=0) = \left.\frac{\partial u_\varphi^{(0)}}{\partial r}\right|_{r=0} - \frac{1}{2}\omega_B^{(0)}(r=0) - \frac{1}{L}u_B^{(0)}(r=0) \\
&\sigma_{r\varphi}^{(m)}(r=0) = 0 \qquad for \quad m \neq 0 \\
&\sigma_{B\varphi}^{(0)}(r=0) = 0 \\
&\sigma_{B\varphi}^{(m)}(r=0) = \frac{\mathrm{i}m}{2}\left.\frac{\partial u_B^{(m)}}{\partial r}\right|_{r=0} \qquad for \quad m \neq 0
\end{aligned}
$$

Appendix B

Boundary conditions at the axis.

The conditions at the axis are defined by regularity conditions. They are based on the postulate that all quantities are infinitely differentiable, in particular at the origin. In this section, we extend the developments of (Lewis and Bellan, 1990) to the helical framework.

B.1 Symmetry of the Fourier coefficients

The transformation between cartesian coordinates (x, y) and cylindrical coordinates (r, φ) reads

$$x = r\cos(\varphi + z/L), \quad y = r\sin(\varphi + z/L), \tag{B.1}$$

Cartesian coordinates are not changed by replacing r by $-r$ and φ by $\varphi + \pi$. For a scalar function $f(r, \varphi)$, this is directly translated into

$$f(r, \varphi) = f(-r, \varphi + \pi). \tag{B.2}$$

When $f(r, \varphi)$ designates the component of a vector field, the above equation should be modified

$$f(r, \varphi) = \epsilon f(-r, \varphi + \pi), \qquad \text{with} \qquad \epsilon \pm 1. \tag{B.3}$$

Specifically, for an axial polar component, $\epsilon = +1$, for azimuthal and radial components $\epsilon = -1$. When $f(r, \varphi)$ is expanded in Fourier series, this implies

$$f(r, \varphi) = \sum_{m=-\infty}^{+\infty} f^{(m)}(r)\, e^{\mathrm{i}m\varphi} = \epsilon f(-r, \varphi + \pi) = \sum_{m=-\infty}^{+\infty} \epsilon f^{(m)}(-r)\, e^{\mathrm{i}m(\varphi+\pi)}. \tag{B.4}$$

Since $e^{\mathrm{i}m(\varphi+\pi)} = (-1)^m e^{\mathrm{i}m\varphi}$, this leads to a relation between Fourier coefficients:

$$f^{(m)}(r) = \epsilon(-1)^m f^{(m)}(-r) \tag{B.5}$$

which dictates the parity of coefficients $f^{(m)}(r)$: if $\epsilon = +1$, $f^{(m)}$ has the parity of m; if $\epsilon = -1$, $f^{(m)}$ has the opposite parity of m.

B.2 Regularity constraints on scalar fields

A scalar field $\Psi(r, \varphi)$ is expanded in Fourier series as:

$$\Psi(r, \varphi) = \sum_{m=-\infty}^{m=\infty} \Psi_m(r, \varphi) \;\; \text{with} \;\; \Psi_m = a^{(m)}(r) e^{\mathrm{i}m\varphi}. \tag{B.6}$$

The regularity of Ψ at the origin $(x, y) = (0, 0)$ implies a particular dependency for coefficients a_m with respect to r. Indeed,

$$e^{im\varphi} = \frac{(x \pm iy)^{|m|}}{r^{|m|}} e^{-\mathrm{i}mz/L}, \quad \text{with} \quad \pm \text{ being the sign of } m, \tag{B.7}$$

is not a regular function at the origin. The terms $\Psi_m(r, \varphi)$ can be expressed as:

$$\Psi_m(r, \varphi) = \frac{a^{(m)}(r)}{r^{|m|}} \, (x \pm iy)^{|m|} \, e^{-\mathrm{i}mz/L}. \tag{B.8}$$

For $a^{(m)}(r)/r^{|m|}$ to be non singular, it is required that

$$a^{(m)}(r) \sim r^{|m|} \text{ as } r \to 0. \tag{B.9}$$

Because of the symmetry condition (B.5), this imposes

$$a^{(m)}(r) = r^{|m|} F_m(r) \tag{B.10}$$

where $F_m(r)$ is a regular even function of r.

B.3 Regularity constraints on vector field components ($\epsilon \pm 1$)

Let $\boldsymbol{u}$ be a helical vector field (representing the velocity or the vorticity field) written in the standard cylindrical basis

$$\boldsymbol{u} = u_r\,(r, \varphi)\ \boldsymbol{e_r} + u_\theta\,(r, \varphi)\ \boldsymbol{e_\theta} + u_z\,(r, \varphi)\ \boldsymbol{e_z}. \tag{B.11}$$

The axial component u_z behaves as a scalar function described in the previous section. For the other components u_r and u_θ, the transformation from cylindrical to Cartesian coordinates is again exploited:

$$\boldsymbol{u} = u_r\,(\cos\theta\,\boldsymbol{e_x} + \sin\theta\,\boldsymbol{e_y}) + u_\theta\,(-\sin\theta\,\boldsymbol{e_x} + \cos\theta\,\boldsymbol{e_y}) + u_z\,\boldsymbol{e_z}.$$

The x-component u_x is given by

$$u_x = u_r\,\cos\theta - u_\theta\,\sin\theta. \tag{B.12}$$

Expanded in Fourier series along φ, the radial and azimuthal components of $\boldsymbol{u}$ yield

$$u_r = \sum_{m=-\infty}^{+\infty} u_r^{(m)} e^{\mathrm{i}m\varphi} \qquad u_\theta = \sum_{m=-\infty}^{+\infty} u_\theta^{(m)} e^{\mathrm{i}m\varphi}. \tag{B.13}$$

Hence,

$$u_x = \frac{1}{2} \sum_{m=-\infty}^{+\infty} \left[\left(u_r^{(m)} + \mathrm{i}\,u_\theta^{(m)} \right) e^{\mathrm{i}\theta(m+1)} e^{\mathrm{i}mz/L} + \left(u_r^{(m)} - \mathrm{i}\,u_\theta^{(m)} \right) e^{\mathrm{i}\theta(m-1)} e^{-\mathrm{i}mz/L} \right]$$

is decomposed as :

$$\begin{aligned} u_x = {} & \frac{1}{2} \sum_{m=1}^{+\infty} \left[\left(u_r^{(m)} + \mathrm{i}\,u_\theta^{(m)} \right) \frac{(x + \mathrm{i}\,y)^{|m|+1}}{r^{|m|+1}} + \left(u_r^{(m)} - \mathrm{i}\,u_\theta^{(m)} \right) \frac{(x + \mathrm{i}\,y)^{|m|-1}}{r^{|m|-1}} \right] e^{-\mathrm{i}mz/L} \\ & + \frac{1}{2} \left[\left(u_r^{(0)} + \mathrm{i}\,u_\theta^{(0)} \right) \frac{(x + \mathrm{i}\,y)}{r} + \left(u_r^{(0)} - \mathrm{i}\,u_\theta^{(0)} \right) \frac{(x - \mathrm{i}\,y)}{r} \right] \\ & + \frac{1}{2} \sum_{m=-\infty}^{m=-1} \left[\left(u_r^{(m)} + \mathrm{i}\,u_\theta^{(m)} \right) \frac{(x - \mathrm{i}\,y)^{|m|-1}}{r^{|m|-1}} + \left(u_r^{(m)} - \mathrm{i}\,u_\theta^{(m)} \right) \frac{(x - \mathrm{i}\,y)^{|m|+1}}{r^{|m|+1}} \right] e^{\mathrm{i}mz/L}. \end{aligned}$$

The above expression is written as an expansion in positive powers of $x \pm \mathrm{i}y$. Whether the full expression is regular or not depends on the coefficients of this expansion.
For case m=0, the regularity imposes

$$u_r^{(0)} \sim r \;\text{ and }\; u_\theta^{(0)} \sim r \text{ as } r \to 0. \tag{B.14}$$

For the case $m > 0$, the regularity imposes as $r \to 0$

$$u_+^{(m)} \equiv \left(u_r^{(m)} + \mathrm{i}\, u_\theta^{(m)}\right) \sim r^p, \quad \text{where } p \geq |m|+1 \tag{B.15}$$
$$u_-^{(m)} \equiv \left(u_r^{(m)} - i\, u_\theta^{(m)}\right) \sim r^q, \quad \text{where } q \geq |m|-1. \tag{B.16}$$

Some numerical codes (Lopez et al., 2002) use u_+ and u_- as variables which is not the case here. When looking at u_r and u_θ, one obtains the following behaviours

$$u_r^{(m)} = c_m r^{|m|-1} + r^{|m|+1} G_m(r), \tag{B.17}$$
$$u_\theta^{(m)} = \mathrm{i}\, c_m r^{|m|-1} + r^{|m|+1} H_m(r), \tag{B.18}$$

with c_m a constant, and $G_m(r), H_m(r)$ regular even functions of r (imposed by the symmetry of (B.5)).
For the case $m < 0$, a similar analysis shows that as $r \to 0$

$$u_+^{(m)} \left(u_r^{(m)} + \mathrm{i}\, u_\theta^{(m)}\right) \sim r^q, \quad \text{where } q \geq |m|-1 \tag{B.19}$$
$$u_-^{(m)} \left(u_r^{(m)} - \mathrm{i}\, u_\theta^{(m)}\right) \sim r^p, \quad \text{where } p \geq |m|+1, \tag{B.20}$$

Similarly, one obtains

$$u_r^{(m)} = c_m r^{|m|-1} + r^{|m|+1} G_m(r), \tag{B.21}$$
$$u_\theta^{(m)} = -\mathrm{i}\, c_m r^{|m|-1} + r^{|m|+1} H_m(r). \tag{B.22}$$

We have thus found that for $m \neq 0$:

$$u_r^{(m)} = c_m r^{|m|-1} + r^{|m|+1} G_m(r), \tag{B.23}$$
$$u_\theta^{(m)} = \pm\, \mathrm{i}\, m\, c_m r^{|m|-1} + r^{|m|+1} H_m(r), \qquad (m \gtrless 0) \tag{B.24}$$
$$u_z^{(m)} = r^{|m|} F_m(r). \tag{B.25}$$

The behaviour of the helical components is then deduced:

$$u_B^{(m)} = \alpha \left(u_z^{(m)} + \frac{r}{L} u_\theta^{(m)}\right) = r^{|m|} \mathcal{F}_m(r) \tag{B.26}$$
$$u_\varphi^{(m)} = \alpha \left(u_\theta^{(m)} - \frac{r}{L} u_z^{(m)}\right) = r^{|m|-1} \mathcal{H}_m(r), \tag{B.27}$$

where again $\mathcal{F}_m(r)$ and $\mathcal{H}_m(r)$ are regular even functions of r. Note that for the modes $|m| = 1$, the components $u_r^{(m)}$ and $u_\varphi^{(m)}$ take non zero values at the axis.
For $m = 0$, since the cylindrical components at $r = 0$ are of the form

$$u_r^{(0)} = r\, G_0(r), \qquad u_\theta^{(0)} = r\, H_0(r), \qquad u_z^{(0)} = F_0(r), \tag{B.28}$$

the additional helical components are such that

$$u_\varphi^{(0)} = r\, \mathcal{H}_0(r), \qquad u_B^{(0)} = \mathcal{F}_0(r). \tag{B.29}$$

Appendix C

HELIX code: Discretisation of first and second derivatives at second order accuracy on irregular meshes

In section 3.2.2, the radial mesh used to discretise the unknowns of the problem is divided into regularly and irregularly spaced grid points. The first and second derivatives are chosen to be discretised with first order accurate formulae for regions with irregularly spaced grid points. Here we provide the formulae to discretise these derivatives at second order accuracy.

The first and second order derivatives with respect to r are discretized with the finite differences method. Such method is based on the Taylor expansion. For a given stencil with irregular grid points such that

$$r_{i+1} - r_i \equiv h_i \neq cst, \tag{C.1}$$

one has at nodes r_{i+1} and r_{i-1}, the quantities $u\left(r_{i+1}\right) \equiv u_{i+1}$ and $u\left(r_{i-1}\right) \equiv u_{i-1}$ expanded as

$$u_{i+1} = u_i + h_i \left.\frac{\partial u}{\partial r}\right|_i + \frac{h_i^2}{2} \left.\frac{\partial^2 u}{\partial r^2}\right|_i + \frac{h_i^3}{6} \left.\frac{\partial^3 u}{\partial r^3}\right|_i + \mathcal{O}(h_i^4) \tag{C.2}$$

$$u_{i-1} = u_i - h_{i-1} \left.\frac{\partial u}{\partial r}\right|_i + \frac{h_{i-1}^2}{2} \left.\frac{\partial^2 u}{\partial r^2}\right|_i - \frac{h_{i-1}^3}{6} \left.\frac{\partial^3 u}{\partial r^3}\right|_i + \mathcal{O}(h_{i-1}^4). \tag{C.3}$$

An approximation of the first derivative at second order accuracy is possible when equations (C.2) and (C.3) are multiplied by h_{i-1}^2 and h_i^2, respectively and then subtracted.

$$\left.\frac{\partial u}{\partial r}\right|_i = \frac{h_{i-1}}{h_i\left(h_{i-1}+h_i\right)} u_{i+1} - \frac{\left(h_{i-1}-h_i\right)}{h_i h_{i-1}} u_i - \frac{h_i}{h_{i-1}\left(h_{i-1}+h_i\right)} u_{i-1} - \frac{h_i h_{i-1}}{6} \left.\frac{\partial^3 u}{\partial r^3}\right|_i + \mathcal{O}\left(h^3\right). \tag{C.4}$$

The leading term of the error is of second order. We further introduce the staggered points $r_{i+1/2}$ and $r_{i-1/2}$ such that

$$r_{i+1/2} = \frac{r_i + r_{i+1}}{2} \tag{C.5}$$

$$r_{i-1/2} = \frac{r_i + r_{i-1}}{2}, \tag{C.6}$$

and re express formula (C.4) of the first derivative at seconder order accuracy

$$\left.\frac{\partial u}{\partial r}\right|_i = \frac{2h_{i-1}}{h_i\left(h_{i-1}+h_i\right)} u_{i+1/2} - \frac{\left(h_{i-1}-h_i\right)}{h_i h_{i-1}} u_i - \frac{2h_i}{h_{i-1}\left(h_{i-1}+h_i\right)} u_{i-1/2} - \frac{1}{24}\left(h_i h_{i-1}\right) \left.\frac{\partial^3 u}{\partial r^3}\right|_i + \mathcal{O}\left(h^3\right). \tag{C.7}$$

After replacing u by $\dfrac{\partial u}{\partial r}$ in (C.7) and rearranging the terms, one obtains the second order accurate formula for the second derivative at nodes r_i

$$\begin{aligned}\left.\frac{\partial^2 u}{\partial r^2}\right|_i &= u_{i-1}\left\{\frac{h_i\left(h_{i-1}-h_i\right)}{h_i h_{i-1}}+\frac{2h_i}{h_{i-1}^2\left(h_{i-1}+h_i\right)}\right\}\\ &+\quad u_i\left\{\frac{-2h_{i-1}}{h_i^2\left(h_{i-1}+h_i\right)}+\frac{\left(h_{i-1}-h_i\right)^2}{h_i h_{i-1}}-\frac{2h_i}{h_{i-1}^2\left(h_{i-1}+h_i\right)}\right\}\\ &+u_{i+1}\left\{\frac{2h_{i-1}}{h_i^2\left(h_{i-1}+h_i\right)}-\frac{h_{i-1}\left(h_{i-1}-h_i\right)}{h_i h_{i-1}}\right\}+\mathcal{O}\left(h^2\right). \end{aligned} \tag{C.8}$$

Note that for regularly spaced grid points with $h_i = h_{i-1} = h$, the equation (C.8) becomes the general well-known formula of the second derivative at second order accuracy for regularly spaced grid points.

Appendix D

Velocity of a set of helical filaments for the cut-off theory

In section 4, the Lagrangian velocity $\boldsymbol{u_i}\left(\boldsymbol{r_i^0}\right)$ of a particular point $\boldsymbol{r_i^0}$ along a helical filament was computed. It was decomposed into two contributions: the induced motion of the filament $\mathscr{H}_i$ on itself and the velocity induced by the $N-1$ other filaments.

$$\boldsymbol{u_i}\left(\boldsymbol{r_i^0}\right) = \boldsymbol{u_j}\left(\boldsymbol{r_i^0}\right)^{\text{self}} + \sum_{j\neq i}^{N} \boldsymbol{u_j}\left(\boldsymbol{r_i^0}\right). \tag{D.1}$$

It is the purpose of this appendix to get both expressions. It is recalled that the ith helical vortex is given by its core size a and its location

$$\boldsymbol{r}_i(\theta,t) = \boldsymbol{i}\, r_i(t)\, \cos(\theta+\varphi_i(t)) + \boldsymbol{j}\, r_i(t)\, \sin(\theta+\varphi_i(t)) + \boldsymbol{k}\,\frac{\theta}{\gamma} = r_i(t)\,\boldsymbol{e}_r(\theta+\varphi_i(t)) + \boldsymbol{k}\,\frac{\theta}{\gamma} \tag{D.2}$$

$2\,\pi/\left|\gamma\right|$ stands for the wavelength along z, $r_i(t)$ the radius and $\varphi_i(t)$ the angular position of the helical filament at $z=0$.

D.1 Induced velocity by a helical vortex j on vortex $i \neq j$

First let us compute a simple case: the velocity induced by a vortex filament j at a position $\boldsymbol{r} = \boldsymbol{i}\, r_i$ which is a point exterior to the vortex filament location. The Biot and Savart law imposes that this velocity is given by the expression

$$\boldsymbol{u}_0^{(j)}(\boldsymbol{i}\, r_i) = \frac{\Gamma_j}{4\,\pi} \int_{-\infty}^{+\infty} \boldsymbol{t_j} \times \frac{(r_i \boldsymbol{i} - \boldsymbol{r_j}(\theta,t))}{\left\|(r_i\boldsymbol{i} - \boldsymbol{r_j}(\theta,t))\right\|^3}\, \mathrm{d}s_j. \tag{D.3}$$

To compute this Biot and Savart integral, the vector product in the integrand is expressed as

$$\boldsymbol{t}_j \times [r_i\boldsymbol{i} - \boldsymbol{r}_j(\theta,t)] = \frac{r_j}{\sqrt{1+\gamma^2 r_j^2}} \begin{pmatrix} \sin(\theta+\varphi_j) - \theta\, \cos(\theta+\varphi_j) \\ r_i/r_j - \cos(\theta+\varphi_j) - \theta\, \sin(\theta+\varphi_j) \\ \gamma\, r_j\, [1 - (r_i/r_j)\cos(\theta+\varphi_j)] \end{pmatrix}$$

or

$$\boldsymbol{t}_j \times [r_i\boldsymbol{i} - \boldsymbol{r}_j(\theta,t)] ds = \frac{r_j \mathrm{d}\theta}{\gamma} \begin{pmatrix} \sin(\theta+\varphi_j) - \theta\, \cos(\theta+\varphi_j) \\ r_i/r_j - \cos(\theta+\varphi_j) - \theta\, \sin(\theta+\varphi_j) \\ \gamma\, r_j\, [1 - (r_i/r_j)\cos(\theta+\varphi_j)] \end{pmatrix}$$

Similarly the denominator in the integrand becomes

$$|r_i \boldsymbol{i} - \boldsymbol{r}_j(\theta,t)|^{\,3} = \{r_i^2 + r_j^2 - 2r_j r_i \,\cos(\theta+\varphi_i) + \theta^2/\gamma^2\}^{3/2} = r_i^3[\{\theta^2/\left(\gamma^2 r_i^2\right) + 1 + (r_j/r_i)^2 - 2(r_j/r_i)\cos\left(\theta+\varphi_i\right)\}$$

The induced velocity can be written in the form

$$\boldsymbol{u}_0^{(j)}(\boldsymbol{i}\, r_i) = \frac{\Gamma_j}{4\,\pi r_i^2}\,[\boldsymbol{i}\, r_j A_j + \boldsymbol{j}\,(r_i B_j - r_j C_j) + \boldsymbol{k}\,(\gamma\, r_j^2\, B_j - \gamma\, r_i\, r_j\, D_j)].$$

where

$$A_j = \int_{-\infty}^{+\infty} \frac{\sin(\theta+\varphi_j) - \theta\,\cos(\theta+\varphi_j)}{\{\theta^2/\left(\gamma^2 r_i^2\right) + 1 + (r_j/r_i)^2 - 2(r_j/r_i)\cos\left(\theta+\varphi_i\right)\}^{3/2}}\,\frac{\mathrm{d}\theta}{|\gamma|\, r_i}.$$

$$B_j = \int_{-\infty}^{+\infty} \frac{1}{\{\theta^2/\left(\gamma^2 r_i^2\right) + 1 + (r_j/r_i)^2 - 2(r_j/r_i)\cos\left(\theta+\varphi_i\right)\}^{3/2}}\,\frac{\mathrm{d}\theta}{|\gamma|\, r_i}$$

$$C_j = \int_{-\infty}^{+\infty} \frac{\cos(\theta+\varphi_j) + \theta\,\sin(\theta+\varphi_j)}{\{\theta^2/\left(\gamma^2 r_i^2\right) + 1 + (r_j/r_i)^2 - 2(r_j/r_i)\cos\left(\theta+\varphi_i\right)\}^{3/2}}\,\frac{\mathrm{d}\theta}{|\gamma|\, r_i}$$

$$D_j = \int_{-\infty}^{+\infty} \frac{\cos(\theta+\varphi_j)}{\{\theta^2/\left(\gamma^2 r_i^2\right) + 1 + (r_j/r_i)^2 - 2(r_j/r_i)\cos\left(\theta+\varphi_i\right)\}^{3/2}}\,\frac{\mathrm{d}\theta}{|\gamma|\, r_i}$$

Let us now compute the induced velocity by a helical vortex j on a vortex $i \neq j$ at a point $\boldsymbol{r}_{\boldsymbol{i}}^0 \in \mathscr{H}_i$ which is not along $\boldsymbol{i}$ as above but at $\boldsymbol{x}_i = r_i(t)\,\boldsymbol{e}_r(\varphi_i(t))$. The above computation is easily generalized by a change of axes and provides

$$\boldsymbol{u}_0^{(j)}(\boldsymbol{x}_i) = \frac{\Gamma_j}{4\,\pi\,|\gamma|}\,[\boldsymbol{e}_r(\varphi_i(t))\, r_j E_{ij} + \boldsymbol{e}_\theta(\varphi_i(t))\,(r_i F_{ij} - r_j G_{ij}) + \boldsymbol{k}\,(\gamma\, r_j^2\, F_{ij} - \gamma\, r_i\, r_j\, H_{ij})].$$

$$E_{ij} = \int_{-\infty}^{+\infty} [\sin(\theta+\varphi_j-\varphi_i) - \theta\,\cos(\theta+\varphi_j-\varphi_i)]Y_{ij}\,\mathrm{d}\theta.$$

$$F_{ij} = \int_{-\infty}^{+\infty} Y_{ij}\,\mathrm{d}\theta.$$

$$G_{ij} = \int_{-\infty}^{+\infty} [\cos(\theta+\varphi_j-\varphi_i) + \theta\,\sin(\theta+\varphi_j-\varphi_i)]Y_{ij}\,\mathrm{d}\theta.$$

$$H_{ij} = \int_{-\infty}^{+\infty} [\cos(\theta+\varphi_j-\varphi_i)]Y_{ij}\,\mathrm{d}\theta.$$

$$Y_{ij} = \frac{1}{Z_{ij}^{3/2}} \tag{D.4}$$

$$Z_{ij} = \theta^2/\gamma^2 + r_i^2 + r_j^2 - 2r_j r_i \cos\left(\theta+\varphi_j-\varphi_i\right) \tag{D.5}$$

By using trigonometric relation in the above integrals, one recovers integrals 4.20 in section 3.

D.2 Self induced velocity of a helical vortex

Let us consider a vortex located at $\boldsymbol{i}\, r_0$ at $z=0$. The Biot et Savart law provides the self-induced velocity at this point. The integral however is singular and should be regularized using the cutoff theory which introduces a vortex core size a. More precisely the cut-off theory provides the velocity at this point $\boldsymbol{i}\, r_0$ under the form

$$\boldsymbol{u}_0 \equiv \boldsymbol{u}(\boldsymbol{x} = \boldsymbol{i}\, r_0) = \frac{\Gamma}{4\,\pi} \fint_{s=-\infty}^{s=+\infty} \frac{\boldsymbol{t} \times (\boldsymbol{i}\, r_0 - \boldsymbol{r}(s))}{|\boldsymbol{i}\, r_0 - \boldsymbol{r}(s)|^{\,3}}\,\mathrm{d}s \tag{D.6}$$

Where the cross on the integral means that the cut-off theory removes an arclength δ around the point at which velocity is evaluated (here this is $\boldsymbol{i}\, r_0$). In terms of θ, this indicates that one removes $|\theta| \leq \theta_0 = |\gamma|\ \delta / \sqrt{1+\gamma^2\, r_0^2}$ in the integral written in θ.
The cut-off provides a value for δ. If the vorticity field is compact,

$$\delta = a\delta_1, \qquad \ln(2\,\delta_1) = \frac{1}{2} + \frac{8\,\pi^2}{\Gamma^2} \int_0^a r_1 \left[w^2(r_1) - \frac{1}{2}\, v^2(r_1) \right] \mathrm{d}r_1. \tag{D.7}$$

δ_1 is a dimensionless factor with w the velocity profile along the vortex axis inside the vortex core and v its azimuthal counterpart. For a Gaussian vortex $\delta_1 = 0.8735$.

The various terms of the integral can be simplified

$$|\boldsymbol{i}\, r_0 - \boldsymbol{r}(s)|^{\,3} = \left\{ 2\, r_0^2\, [1-\cos(\theta)] + \theta^2/\gamma^2 \right\}^{3/2} = |\gamma|^{-1}\, \gamma^{-2} \left\{ 2\, \gamma^2\, r_0^2\, [1-\cos(\theta)] + \theta^2 \right\}^{3/2}$$

$$\boldsymbol{t} \times (\boldsymbol{i}\, r_0 - \boldsymbol{r}(s)) = \frac{\gamma\, r_0}{\sqrt{1+\gamma^2\, r_0^2}} \left[-\boldsymbol{i}\, \sin(\theta) + \boldsymbol{j}\, \cos(\theta) + \frac{\boldsymbol{k}}{\gamma\, r_0} \right] \times \left[\boldsymbol{i}\, r_0\, [1-\cos(\theta)] - \boldsymbol{j}\, r_0\, \sin(\theta) - \boldsymbol{k}\, \frac{\theta}{\gamma} \right]$$

The integrand can be written as

$$\begin{aligned} &\frac{\gamma^2\, r_0}{|2\, \gamma^2\, r_0^2\, [1-\cos(\theta)] + \theta^2|^{3/2}}\ \frac{|\gamma|\ \mathrm{d}s}{\sqrt{1+\gamma^2\, r_0^2}} \\ &\times \left\{ \boldsymbol{i}\, [\sin(\theta) - \theta\, \cos(\theta)] + \boldsymbol{j}\, [1-\cos(\theta) - \theta\, \sin(\theta)] + \boldsymbol{k}\, \gamma\, r_0\, [1-\cos(\theta)] \right\} \end{aligned} \tag{D.8}$$

The contribution in $\boldsymbol{i}\, [\sin(\theta) - \theta\, \cos(\theta)]$ vanishes since this is an odd function in θ. The final expression becomes

$$\boldsymbol{u}_0 = \frac{\Gamma}{4\,\pi}\, \gamma^2\, r_0 \not\int_{-\infty}^{+\infty} \frac{\boldsymbol{j}\, [1-\cos(\theta) - \theta\, \sin(\theta)] + \boldsymbol{k}\, \gamma\, r_0\, [1-\cos(\theta)]}{\{2\, \gamma^2\, r_0^2\, [1-\cos(\theta)] + \theta^2\}^{3/2}}\, \mathrm{d}\theta \tag{D.9}$$

By noting that

$$\frac{\partial}{\partial\theta} \frac{\theta}{\left\{2\gamma^2 r_0^2\, [1-\cos\theta] + \theta^2\right\}^{1/2}} = \gamma^2 r_0^2 \frac{2\, [1-\cos\theta] - \theta \sin\theta}{\left\{2\gamma^2 r_0^2\, [1-\cos\theta] + \theta^2\right\}^{3/2}},$$

$\mathbf{u_0}$ can be written as

$$\mathbf{u_0} = \frac{\Gamma}{2\,\pi}\, \gamma^2\, r_0\ \left\{ \left[K\left(\gamma r_0, \gamma\delta\right) - I\left(\gamma r_0, \gamma\delta\right) \right] \boldsymbol{j} +\ \gamma\, r_0\, I\left(\gamma r_0, \gamma\delta\right) \boldsymbol{k} \right\} \tag{D.10}$$

where

$$K\left(\gamma r_0, \gamma\delta\right) = \frac{1}{\gamma^2 r_0^2} \left\{ 1 - \frac{\theta_0}{[2\gamma^2 r_0^2\, [1-\cos\theta_0] + \theta_0^2]^{1/2}} \right\} \tag{D.11}$$

$$I\left(\gamma r_0, \gamma\delta\right) = \int_{\theta_0}^{\infty} \frac{[1-\cos(\theta)]\, \mathrm{d}\theta}{\{\theta^2 + 2\, \gamma^2\, \mathrm{r_0}^2\, [1-\cos(\theta)]\}^{3/2}} \tag{D.12}$$

with

$$\theta_0 = \frac{|\gamma|\ \delta}{\sqrt{1+\gamma^2\, r_0^2}} \tag{D.13}$$

To obtain the self-induced velocity $\boldsymbol{u_i}\left(\boldsymbol{r_i^0}\right)^{\mathrm{self}}$ by the filament $\mathscr{H}_i$ at a point $\boldsymbol{r_i^0} \in \mathscr{H}_i$, the above result can be translated by adequate change of variables leading to

$$\mathbf{u_0}^{(self)} = \frac{\Gamma_i r_i}{2\,\pi}\, \gamma^2\ \left\{ \left[K_i\left(\gamma r_i, \gamma\delta\right) - I_i\left(\gamma r_i, \gamma\delta\right) \right] \boldsymbol{e_\theta}(\varphi_i(t)) +\ \gamma\, r_i\, I_i\left(\gamma r_i, \gamma\delta\right) \boldsymbol{k} \right\} \tag{D.14}$$

avec

$$K_i\left(\gamma r_i, \gamma\delta\right) = \frac{1}{\gamma^2 r_i^2}\left\{1 - \frac{\theta_{0i}}{\left[2\gamma^2 r_i^2\left[1-\cos\theta_{0i}\right]+\theta_{0i}^2\right]^{1/2}}\right\} \tag{D.15}$$

$$I_i\left(\gamma r_i, \gamma\delta\right) = \int_{\theta_{0i}}^{\infty}\frac{\left[1-\cos\theta'\right]\mathrm{d}\theta'}{\left\{\theta'^2+2\,\gamma^2\,r_i^2\left[1-\cos(\theta')\right]\right\}^{3/2}} \tag{D.16}$$

avec

$$\theta_{0i} = \frac{|\gamma|\ \delta}{\sqrt{1+\gamma^2\,r_i^2}} \tag{D.17}$$

Appendix E

Vortex characterisation

E.1 Vortex characterisation: two-dimensional interpolations

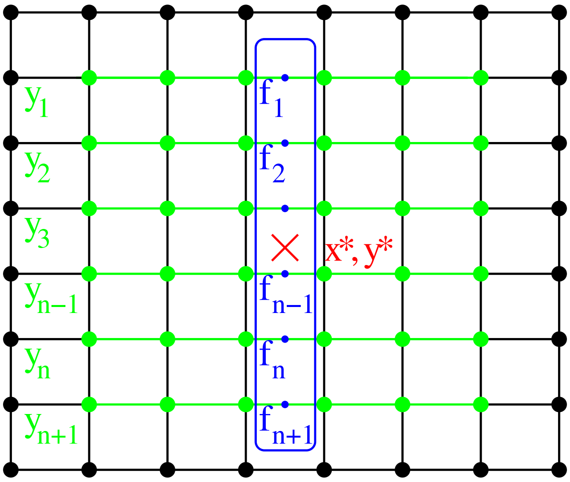

Figure E.1 – A two-dimensional interpolation is performed with successive uses of one-dimensional interpolations.

The visualisation and the analysis of numerical data in plane $\Pi_\perp$ require the use of high order and two-dimensional interpolation methods. To perform a two-dimensional interpolation, we successively use one dimensional interpolations. We illustrate the procedure on the Cartesian grid depicted in figure E.1. The point X with coordinate (x^*, y^*) is the location where the value of a given function f is sought (i.e. $f\,(x^*, y^*)$). Let use denote N, the accuracy order of the interpolation method. A first series of $N+1$ one dimensional interpolations are performed at x^* to yield $f_1(x^*, y_1)...f_{n+1}(x^*, y_{n+1})$. At each $y_1, ..., y_{N+1}$ level, the neighbouring nodes in the x direction are used (represented by the green filled nodes in E.1) . Finally, the function $f(x^*, y^*)$ is obtained with another one dimensional interpolation along the y direction involving the values $f_1(x^*, y_1)...f_{n+1}(x^*, y_{n+1})$. For one dimensional interpolation we use Chebyshev polynomials.

E.1.1 One dimensional interpolation: Chebyshev polynomials

Let us consider a function $f(x)$ evaluated at discrete nodes x_j, for $j = 0...n$ within the interval $[a, b]$ such that $a \leq x_j \leq b$. Let us define $P_n(y)$ a series of polynomials constituting a basis for an another interval $[A, B]$. In order to perform a one-dimensional interpolation we proceed with the following steps:

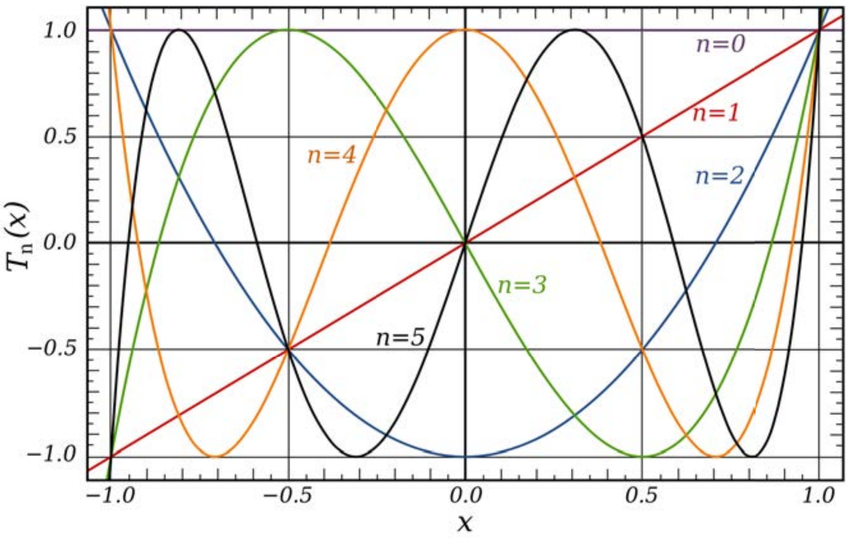

Figure E.2 – Chebyshev polynomials $T_n(y)$ for $n = 0 - 5$

1. We first map x_j within $[A, B]$ with:

$$y = [(B - A)\,x + A \cdot b - a \cdot B] \,/\, [b - a] \tag{E.1}$$

   for each $x_j \in [a, b]$ a corresponding $y_j \in [A, B]$ exists.

2. Let us denote $g(y_j) = f(x_j) = f_j$ and approximate $g(y_j)$ by:

$$g(y) \approx \sum_{i=0,n} a_i P_i(y) \tag{E.2}$$

3. The coefficients a_n are determined on the $n + 1$ collocation nodes.

$$a_0 P_0(y_j) + a_1 P_1(y_j) + a_2 P_2(y_j) + ... + a_n P_n(y_j) = f_j \qquad : j = 0, n \tag{E.3}$$

   This leads to a linear system of $n + 1$ equations for the $n + 1$ coefficients:

$$\begin{bmatrix} P_0(y_0) & \dots & P_n(y_0) \\ \vdots & & \vdots \\ P_0(y_n) & \dots & P_n(y_n) \end{bmatrix} \begin{bmatrix} a_0 \\ \vdots \\ a_n \end{bmatrix} = \begin{bmatrix} f_0 \\ \vdots \\ f_n \end{bmatrix} \tag{E.4}$$

We use as basis functions $P_n(y) = T_n(y)$, the Chebyshev polynomials defined on the interval $[-1, 1]$ (see figure E.2). The $T_n(y)$ can be expressed with the following recurrence relations:

$$\begin{aligned} &T_n(y) = 2yT_{n-1}(y) - T_{n-2}(y) \quad , k \geq 2 \\ &T_1(y) = y \\ &T_0(y) = 1 \end{aligned} \tag{E.5}$$

In practice the linear system is resolved with an LU decomposition method. Once the coefficients in (E.4) are obtained the function g can evaluated at any sought location y with (E.2).

E.2 Vortex characterisation: nonlinear least square method

In plane $\Pi_\perp$, he axisymmetric contribution of the helical vorticity is fitted by a Gaussian for comparison purpose. This section is devoted to the description of the method.
Consider a target function $y(x)$ evaluated on M discrete points $y_i = y(x_i)$ for $i = 1, ..., M$. We want to fit this function by an analytical function $f(x; \lambda_1, ..., \lambda_N)$ with N parameters $\boldsymbol{\lambda} = (\lambda_1, ..., \lambda_N)$. To find the best vector of parameters $\boldsymbol{\lambda}$, we minimize the sum of squared error

$$S = \sum_{i=1}^{M} \beta_i^2 \quad \text{where} \quad \beta_i = y_i - f\left(x_i; \lambda_1, ..., \lambda_N\right). \tag{E.6}$$

A necessary condition for S to be minimum is that its gradient to be zero :

$$\frac{\partial S}{\partial \lambda_j} = 2\sum_{i=1}^{M} \beta_i \frac{\partial \beta_i}{\partial \lambda_j} = 0 \quad \text{for} \quad j = 1, ..., N. \tag{E.7}$$

As the derivatives $\dfrac{\partial \beta_i}{\partial \lambda_j}$ do not have a closed form solution in a nonlinear system, one must use an iterative procedure to find the optimum vector of parameters $\boldsymbol{\lambda}$:

$$\boldsymbol{\lambda}^k = \boldsymbol{\lambda}^{k-1} + \boldsymbol{\Delta\lambda},$$

where at each step number k, the values are refined with an increment vector $\boldsymbol{\Delta\lambda}$ also called the shift vector. During each step k the fit function is approximated with a Taylor expansion to first order with respect to $\boldsymbol{\lambda}^k$:

$$f\left(x_i, \boldsymbol{\lambda}\right) \approx f\left(x_i, \boldsymbol{\lambda}^k\right) + \sum_{j=1}^{N} \frac{\partial f\left(x_i, \boldsymbol{\lambda^k}\right)}{\partial \lambda_j} \left(\lambda_j - \lambda_j^k\right) = f\left(x_i, \boldsymbol{\lambda}^k\right) + \sum_{j=1}^{N} A_{ij}\, \Delta\lambda_j \tag{E.8}$$

with $\boldsymbol{A}$ the Jacobian matrix of size $N \times M$ with elements :

$$A_{ij} = \begin{pmatrix} \dfrac{\partial f\left(x_1, \boldsymbol{\lambda}^k\right)}{\partial \lambda_1} & \cdots & \dfrac{\partial f\left(x_1, \boldsymbol{\lambda}^k\right)}{\partial \lambda_N} \\ \vdots & & \vdots \\ \dfrac{\partial f\left(x_M, \boldsymbol{\lambda}^k\right)}{\partial \lambda_1} & \cdots & \dfrac{\partial f\left(x_M, \boldsymbol{\lambda}^k\right)}{\partial \lambda_N} \end{pmatrix}.$$

The Jacobian, $\boldsymbol{A}$ has to be evaluated at each iteration as it depends on the parameters and the independent variable. With equation (E.8), the equation (E.6) for the error β_i becomes:

$$\beta_i = y_i - f\left(x_i, \boldsymbol{\lambda}^k\right) - \sum_{j=1}^{N} A_{ij}\, \Delta\lambda_j = \Delta\beta_i - \sum_{j=1}^{N} A_{ij}\, \Delta\lambda_j, \tag{E.9}$$

and

$$\frac{\partial \beta_i}{\partial \lambda_j} = -A_{ij}. \tag{E.10}$$

Injecting these two equations (E.9)-(E.10) into the gradient equation (E.7) yields:

$$-2\sum_{j=1}^{N} A_{ij} \left(\Delta\beta_i - \sum_{k=1}^{N} A_{ik}\, \Delta\lambda_k\right) = 0, \tag{E.11}$$

which becomes after rearrangement, N linear equations, called also the **normal** equations:

$$\sum_{i=1}^{M}\sum_{k=1}^{N} A_{ij}A_{ik}\Delta\lambda_k = \sum_{i=1}^{M} A_{ij}\Delta\beta_i \quad \text{for} \quad j = 1, ..., N. \tag{E.12}$$

This results in a linear system that has to be inverted in order to obtain $\boldsymbol{\Delta\lambda}$ at each step k:

$$\boldsymbol{A}^\intercal \boldsymbol{A}\, \boldsymbol{\Delta\lambda} = \boldsymbol{A}^\intercal \boldsymbol{\Delta\beta}$$

The principle is to prescribe an analytical function for $f(x; \lambda_1, ..., \lambda_N)$ with a set of guess values $\lambda_1^*, ..., \lambda_N^*$ for the parameters and iterate until convergence is achieved. i.e when :

$$\|\boldsymbol{\Delta\lambda}\|^2 < \xi.$$

with ξ the convergence criterion set to 1^{-11}.

```
Set a convergence (stop) criterion $\xi$
Set guess values for the parameters $\boldsymbol{\lambda}^0$
while $\|\boldsymbol{\Delta\lambda}\|^2 \geq \xi$ do
    $k = k + 1$
    $S^k = 0$
    for i=1,...,M do
        for j=1,...,N do
            $A(i, j) \leftarrow$ compute Jacobian
        end for
        $F0(i) \leftarrow$ compute $f(x_i; \boldsymbol{\lambda})$
    end for
    $\boldsymbol{\Delta\beta} \leftarrow \boldsymbol{y} - \boldsymbol{F0}$
    Inverse $\boldsymbol{A}^\intercal \boldsymbol{A}\, \boldsymbol{\Delta\lambda} = \boldsymbol{A}^\intercal \boldsymbol{\Delta\beta}$ with an LU iterative method or with any other direct/iterative method.
    $\boldsymbol{\lambda}^k \leftarrow \boldsymbol{\lambda}^{k-1} + \boldsymbol{\Delta\beta}$
    $S^k \leftarrow \sum_{i=1}^{M} \left(\Delta\beta_i - \sum_{p=1}^{N} A_{ip}\Delta\lambda_p\right)$
end while
```

The algorithm used to implement this method is represented figure 16.

Appendix F

Linear stability in the rotating frame

The basic flow is made steady by adopting the frame of reference rotating with the helical vortex at angular velocity Ω around the $z-$axis. This involves to subtract the corresponding uniform vorticity to the basic flow and to adapt the velocity field also. Then a Coriolis force intervenes, which reads as

$$\boldsymbol{f}_C = -2\boldsymbol{\Omega} \times \boldsymbol{u} = 2\Omega \boldsymbol{u} \times \boldsymbol{e}_z \, .$$

Using the helical basis, this develops into:

$$\boldsymbol{f}_C = 2\Omega \left(u_r \boldsymbol{e}_r + u_\varphi \boldsymbol{e}_\varphi + u_B \boldsymbol{e}_B \right) \times \alpha(r) \left(\boldsymbol{e}_B - \frac{r}{L} \boldsymbol{e}_\varphi \right) ,$$

$$\boldsymbol{f}_C = 2\Omega\alpha \left[\left(u_\varphi + \frac{r}{L} u_B \right) \boldsymbol{e}_r - u_r \boldsymbol{e}_\varphi - \frac{r}{L} u_r \boldsymbol{e}_B \right] .$$

The equation for $u_B^{(m)}$ involves the helical component of the Coriolis force:

$$\boxed{\boldsymbol{f}_C^{(m)} \cdot \boldsymbol{e}_B = -2\Omega\alpha \frac{r}{L} u_r^{(m)} \, .}$$

For the mode $m = 0$, the above term vanishes. The equation for $u_\varphi^{(0)}$ involves the component along φ

$$\boxed{\boldsymbol{f}_C^{(0)} \cdot \boldsymbol{e}_\varphi = -2\Omega\alpha u_r^{(0)} \, ,}$$

The equation for $\omega_B^{(m)}$ involves the rotational of the Coriolis force

$$\boldsymbol{\nabla} \times \boldsymbol{f}_C = 2\Omega \boldsymbol{\nabla} \times (\boldsymbol{u} \times \boldsymbol{e}_z) = 2\Omega (\boldsymbol{e}_z \cdot \boldsymbol{\nabla}) \boldsymbol{u} = 2\Omega \frac{\partial \boldsymbol{u}}{\partial z} \, .$$

Since the helical basis vectors do not depend on z, and since u_r, u_φ and u_B depend on (r, φ, t) hence on z through $\varphi \equiv \theta - z/L$, the above relation also reads:

$$\boldsymbol{\nabla} \times \boldsymbol{f}_C = -\frac{2\Omega}{L} \left(\frac{\partial u_r}{\partial \phi} \boldsymbol{e}_r + \frac{\partial u_\varphi}{\partial \phi} \boldsymbol{e}_\varphi + \frac{\partial u_B}{\partial \phi} \boldsymbol{e}_B \right) .$$

In particular, the equation for $\omega_B^{(m)}$ involves

$$\boxed{(\boldsymbol{\nabla} \times \boldsymbol{f}_C^{(m)}) \cdot \boldsymbol{e}_B = \frac{-2\mathrm{i}\Omega m}{L} u_B^{(m)} \, .}$$

Appendix G

Paper: Instabilities in helical vortex systems: linear analysis and nonlinear dynamics

Instabilities in helical vortex systems : linear analysis and nonlinear dynamics

Can Selçuk$^{(1,2)}$, **Ivan Delbende**$^{(1,2)}$, **Maurice Rossi**$^{(1,3)}$

$^{(1)}$ *UPMC, Université Pierre et Marie Curie-Paris 6, France*
$^{(2)}$ *LIMSI–CNRS, UPR3251, BP133, 91405 Orsay Cedex, France*
Email : Can.selcuk@limsi.fr, Ivan.Delbende@limsi.fr
$^{(3)}$ *IJLRA–UPMC, UMR7190, 75232 Paris Cedex 05, France*
Email : Maurice.Rossi@upmc.fr

1 Introduction

Helical vortices are important in engineering applications : the near wake behind helicopter rotors, ship propellers, turbine impellers or wind turbines are dominated by helical vortices. Helical vortices are also important fundamental flows : if a prototype flow for curvature effect on core dynamics structure is a vortex ring, a logical extension for the combined effect of both curvature and torsion is indeed a helical vortex. For the past decades, asymptotic analysis in the inviscid framework have been employed to find analytical solutions of the velocity field induced by idealised helical vortices. Namely the singular helical vortex filament [1] [2] and helical vortices with circular core structure and constant vorticity (ie : the Rankine vortex) [3] [4] [5]. In the present work, we compute the base flow by assuming that the wake is fully developed and that tip vortices can be viewed as infinite helical vortices with constant radius and pitch. This is correct sufficiently far from the rotating blades. Such flows can be thus considered helically symmetric : fields are invariant through combined axial translation of distance Δz and rotation of angle $\Delta\theta = \Delta z/L$ around the rotor z-axis, where $2\pi L$ denotes the helix pitch. In order to simulate the evolution of such flows, we use a DNS [6] code based on an original formulation in which the helical symmetry is enforced into the equations. In the present study we obtain basic states which consist of two diffusing helical vortices with or without a central hub vortex, for various values of helical pitch L and fixed core sizes. Investigating stability properties is a necessary step to understand and predict the dynamics of helical vortices. This is of importance since coherent structures in the wake are responsible for additional stresses and losses of performance in wind turbine farms. Instabilities can also trigger transition to the highly non-stationary Vortex Ring State which is responsible for some helicopter crashes. Widnall, in 1972 [7] first predicted the stability features of helical vortices. She performed the linear stability analysis of a helical vortex filament with respect to sinusoidal perturbations. She found that the system was subjected to three unstable modes : a short wavelength mode, a long wavelength mode and a mutual-inductance mode. In 2004, Okulov [8] [9] generalized this result to N helical vortices with circular cores and constant vorticity. He showed that such a system, in the particular case of two helical vortices [9], was unstable when the helical pitch was inferior to a threshold value $L < 1.106$. Later, in order to study the more realistic case of rotor wakes, Okulov *et al.* [9] investigated the effect of a central hub vortex. It was found that the stability of such flows strongly depends on the vorticity profile in the core and that the flow was unconditionally unstable [9]. The stability of such vortex systems have been also studied experimentally [10] [11] [12].

In the present work, we perform a linear temporal stability analysis of multiple diffusing vortices. In order to extract the dominant unstable modes, we use a linearised version of the helical DNS code coupled to an Arnoldi procedure. The influence of the presence of a hub vortex will also be presented. Finally nonlinear evolutions have been computed. Instability properties as well as nonlinear dynamics will be characterized for helical pitch values ranging from large ones (quasi-2D behaviour) to small ones more pertinent for helicopter and wind turbine applications.

2 Governing equations

The class of flows we consider can be, at least locally, modeled in the framework of helical symmetry. This geometrical property is enforced into the incompressible Navier-Stokes equations to reduce the full 3-D problem to a 2-D one. It is then possible to generalise the classical vorticity-streamfunction framework to helical flows [6]. The associated velocity field $\boldsymbol{u}$ and vorticity field $\boldsymbol{\omega}$ are computed in a helical coordinate system defined by the orthogonal Beltrami Basis $(\boldsymbol{e}_r, \boldsymbol{e}_\varphi, \boldsymbol{e}_B)$ depicted in figure 1 and expressed as

$$
\begin{aligned}
\boldsymbol{u} &= u_r(r,\varphi,t)\boldsymbol{e}_r(\theta) \\
&+ u_\varphi(r,\varphi,t)\boldsymbol{e}_\varphi(r,\theta) \\
&+ u_B(r,\varphi,t)\boldsymbol{e}_B(r,\theta) \\
\boldsymbol{\omega} &= \omega_r(r,\varphi,t)\boldsymbol{e}_r(\theta) \\
&+ \omega_\varphi(r,\varphi,t)\boldsymbol{e}_\varphi(r,\theta) \\
&+ \omega_B(r,\varphi,t)\boldsymbol{e}_B(r,\theta)
\end{aligned}
\tag{1}
$$

where $\varphi = \theta - z/L$. In this framework, as detailed in [6], the flow evolution is described with the only knowledge of the two components $\omega_B(r,\varphi,t)$ and $u_B(r,\varphi,t)$. The streamfunction $\psi(r,\varphi,t)$ is slaved to these quantities according to the relationship

$$
\mathbb{L}\psi = \frac{2\alpha^2}{L} u_B - \omega_B \tag{2}
$$

where $\mathbb{L}$ is a modified (but still linear) Laplacian operator. The other four components are then easily retrieved using :

$$
\begin{aligned}
u_r &= \frac{1}{r}\frac{\partial}{\partial\varphi}\psi, \quad u_\varphi = -\alpha\frac{\partial}{\partial r}\psi \\
\omega_r &= \frac{1}{r\alpha}\frac{\partial}{\partial\varphi}u_B, \quad \omega_\varphi = -\alpha\frac{\partial}{\partial r}\left(\frac{u_B}{\alpha}\right)
\end{aligned}
\tag{3}
$$

where the quantity $\alpha(r)$ is defined as

$$
\alpha(r) = \left(1 + \frac{r^2}{L^2}\right)^{-\frac{1}{2}}, \quad 0 \le \alpha(r) \le 1\,. \tag{4}
$$

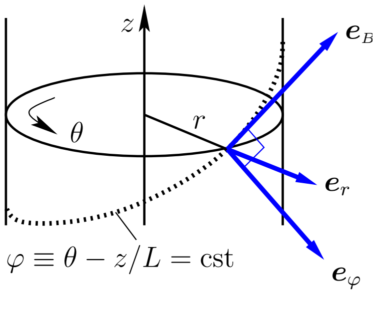

FIGURE 1 – *Local helical basis.*

The two dynamical equations for $\omega_B(r,\varphi,t)$ and $u_B(r,\varphi,t)$ are briefly reminded here for sake of clarity. The first equation reads as

$$
\partial_t u_B + NL_u = VT_u \tag{5}
$$

where the nonlinear and viscous terms are given by

$$
\begin{aligned}
NL_u &\equiv \boldsymbol{e}_B \cdot [\boldsymbol{\omega} \times \boldsymbol{u}]\,, \\
VT_u &\equiv \nu\left[\mathbb{L}(\frac{u_B}{\alpha}) - \frac{2\alpha^2}{L}\omega_B\right].
\end{aligned}
\tag{6}
$$

The dynamical equation for ω_B reads

$$
\partial_t \omega_B + NL_\omega = VT_\omega \tag{7}
$$

where the nonlinear term is given by

$$
NL_\omega \equiv \boldsymbol{e}_B \cdot \boldsymbol{\nabla} \times [\boldsymbol{\omega} \times \boldsymbol{u}]\,, \tag{8}
$$

and the viscous term by

$$
\begin{aligned}
VT_\omega &\equiv -\nu\, \boldsymbol{e}_B \cdot \boldsymbol{\nabla} \times [\boldsymbol{\nabla} \times \boldsymbol{\omega}] \\
&= \nu\left[\mathbb{L}(\frac{\omega_B}{\alpha}) - \left(\frac{2\alpha^2}{L}\right)^2 \omega_B \right. \\
&\qquad \left. + \frac{2\alpha^2}{L}\mathbb{L}(\frac{u_B}{\alpha})\right].
\end{aligned}
\tag{9}
$$

Numerical resolution

The dynamical equations (5) and (7) for $u_B(r,\varphi,t)$ and $\omega_B(r,\varphi,t)$ are solved numerically with the DNS code HELIX [6]. It is a pseudo-spectral code which uses Fourier series along the periodic direction φ and a centred second order discretisation (finite differences) in the radial direction r. We use N_r grid points along r and M modes along φ, the $2/3$ dealiasing rule implies the use of $N_\theta = 3M$ grid nodes points. The time advance is ensured by a second order backward scheme. Nonlinear terms are treated explicitly through a second order Adams-Bashforth extrapolation formula whereas the viscous terms are implicit. Variables are computed in dimensionless form based on a typical helix radius $R_\star$ as characteristic length and the vortex circulation Γ. The Reynolds number is defined as $Re = \Gamma/\nu$ where ν is the kinematic viscosity. For characterizing purposes, the following planes are defined as depicted in figure 2 :

Π_0 : horizontal plane of computation at $z = 0$
Π_v : meridian (r,z)-plane
$\Pi_\perp$: plane locally orthogonal to a vortex core.

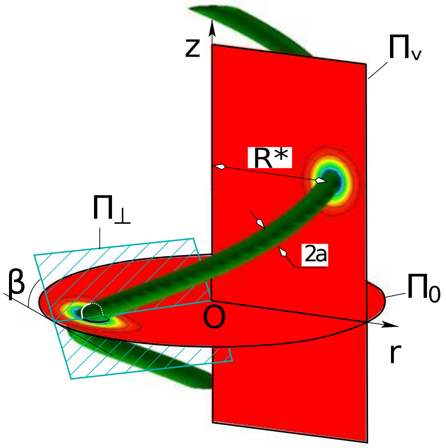

FIGURE 2 – *Planes* $\Pi_\perp$, Π_0, Π_v

3 Base Flow

Generic initial condition

In this section we are looking for a base flow which represents a quasi-equilibrium solution of N helical vortices of circulation Γ and pitch $2\pi L$ regularly set in the azimuthal direction (at the apexes of a regular polygon). In order to obtain such flow we simulate the dynamics of an initial condition at $t = 0$, which itself results from the time-evolution of N *singular* vortex filaments located at radial distance $R_\star$ from the axis at a past time $t_\star < 0$. This choice reduces the number of control parameters. This procedure is performed with the following steps :

1) Each vortex $k = 1, ..., N$ is centred at the positions $(R, \theta_k = 2\pi(k-1)/N)$ in the plane Π_0. A corresponding plane $\Pi_\perp^k$ is defined to be orthogonal to the vector $\boldsymbol{e_B}(R, \theta_k)$.

2) In each plane $\Pi_\perp^k$, we impose a **Gaussian** profile on ω_{Bk}^0 of half width a_0 and amplitude C. The core size a_0 is set to

$$a_0 = \sqrt{-4\nu t_\star} \qquad (t_\star < 0).$$

The underlying hypothesis is that each vortex filament diffuses as a point vortex. In practice we choose a_0 as parameter and deduce $t_\star$. This model is used because it is probably, in this plane, the closest profile to a quasi-equilibrium solution.

3) Using the invariance of scalar fields along the helices (according to the helical symmetry), the complete field ω_B^0 is obtained in the plane Π_0 by summing the contributions of each vortex.

4) The viscous coupling between u_B and ω_B (see equations (5)-(6)) is prone to create an axial velocity component along the vortex core. It can be shown that the following relation for u_B^0 holds for small values of $|t_\star|$:

$$u_B^0 = \alpha \left(\frac{2t^\star}{LRe} \alpha \omega_B^0 + K \right).$$

Here K is a constant that depends on the boundary conditions.

5) The amplitude C has to be determined in order to prescribe the circulation $N\Gamma$ to the whole vortex system. In the context of helical symmetry, the global circulation reads

$$N\Gamma = \iint \omega_z^0 \, r\mathrm{d}r\mathrm{d}\theta = \mathcal{K}_\omega + \mathcal{K}_u, \qquad (10)$$

$$\text{where} \quad \mathcal{K}_\omega \equiv \iint_S \alpha \omega_B^0 \, r\mathrm{d}r\mathrm{d}\theta$$

$$\text{and} \quad \mathcal{K}_u \equiv \iint_S r \frac{\alpha^2}{L} \frac{\partial}{\partial r} \left(\frac{u_B^0}{\alpha} \right) \, r\mathrm{d}r\mathrm{d}\theta.$$

Expression (10) is linear in C, so that C can be readily determined.

6) The conservation equation of the global angular momentum leads to :

$$R^2 = \frac{1}{\Gamma} \iint r^2 \omega_z^0 \, r\mathrm{d}r\mathrm{d}\theta = R_\star^2 - 4\nu t_\star$$

thus fixing R in a unique fashion.

With this generic procedure, we reduce the number of parameters to only two, the reduced pitch L, hereafter made non dimensional using $R_\star$, and the Reynolds number. Figure 3 illustrates the generic aspect of this procedure with three initialisations at $t = 0$ corresponding to three different values of times $t_\star = -3.125, -12.5, -28.15$. It is seen that the time evolution of the vortex core size a and of helix radius R only depend on $\tau = t - t_\star$.

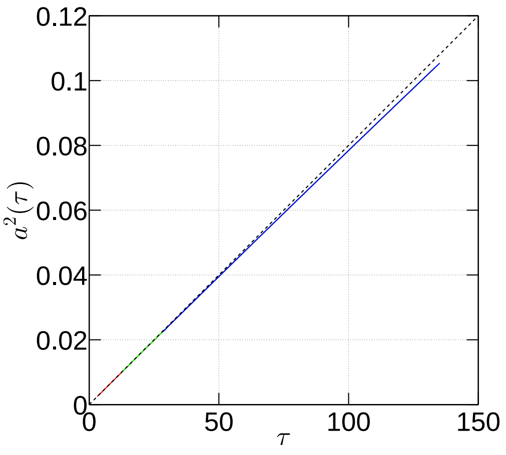

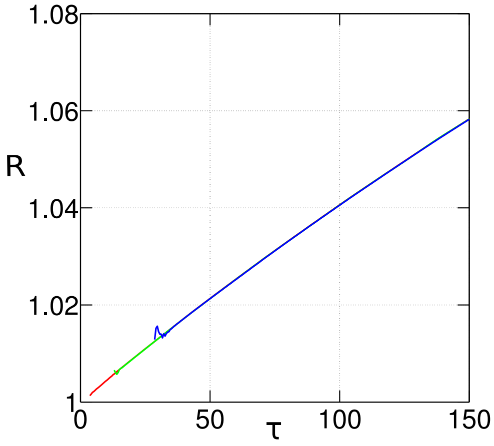

FIGURE 3 – *Generic initial condition for one helical vortex* $L = 1, Re = 5000$ *: three computations with different initialisations corresponding to times* $t_\star = -3.125$ *(red),* $t_\star = -12.5$ *(green) and* $t_\star = -28.15$ *(blue). (a) Squared core size* a^2 *vs* τ *; the dotted black line represents the 2-D diffusion law* $a^2 = 4\tau/Re$. (b) Radial position R of vorticity maximum versus τ.

Quasi-equilibrium solutions

The previously described procedure allows to compute solutions with controlled characteristics (L, Re) : we initialize at time $t = 0$, N helical vortices of core size a_0 resulting from an assumed evolution of N *singular* helical filaments and compute their dynamics.

During the first stage of their evolution, the vortices are going through a rapid relaxation process. The initial condition being not an exact (but close to) quasi-equilibrium solution, each vortex adapts its structure to the strain field it is subjected to. Indeed, the strain field felt by each vortex has two contributions : an external one generated by the presence of the other vortices, and a self-induced one generated by the helical vortex itself. This relaxation process can be seen for instance on figure 3b : the blue curve presents a small wiggle around $t = 30$.

The second stage of the temporal evolution is a slow diffusion process driven by viscosity. This state is also characterised by a global angular velocity $\Omega(\tau; L)$ at which the vortices rotate. This motion is due to the velocity field induced by remote vortices and also to a self-induced velocity. In this study, we are interested in the stability analysis of helical vortices with small core size a_b (with respect to $R_\star$) for various values of the reduced pitch L. In order to compute basic states, simulations are run using generic initial conditions and are stopped when the prescribed value of a_b is reached at time t_{end}. In the following a_b will be fixed at $a_b = 0.06$, the Reynolds number will be set to $Re = 10000$ and we consider $N = 2$ helical vortices. An example of such a computation is given for two vortices in figure 4 : it is observed that the final state corresponding to the quasi-equilibrium basic state is elliptically deformed due to strain.

In many application, a central hub vortex may also be present with a circulation $-N\Gamma$. The influence of such vortex will also be investigated. The parameters related to the computation of the basic states are summarised in the table 1. Once a basic state is computed for a given value of the reduced pitch L, it is frozen and ready for the temporal stability analysis.

L	$N_r \times N_\theta$	δt	t_{end}	$\Omega(t_{end}, L)$
0.2	1042×396	1/7000	5.07	-4.2
0.3	1042×396	1/5000	5.05	-1.96
0.4	1042×396	1/4000	5.05	-1.15
0.5	1042×396	1/4000	5.05	-0.76
0.6	1042×396	1/4000	5.02	-0.53
0.7	1042×396	1/4000	5.02	-0.39
0.8	1042×396	1/4000	5.02	-0.30

TABLE 1 – *Characteristics of the basic states*

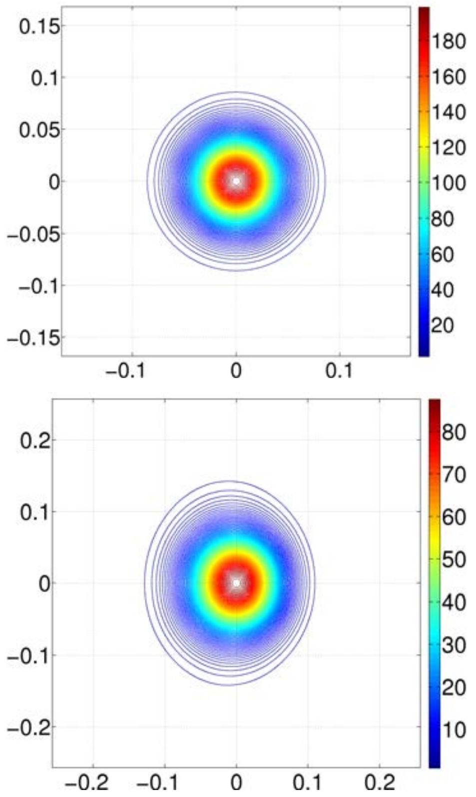

FIGURE 4 – $N = 2$ *helical vortices,* $L = 0.3$*. Helical vorticity* ω_B *in the plane* $\Pi_\perp$ *at instants (a)* $t = 0$ *and (b)* $t = t_{end} = 5.07$.

4 Temporal stability analysis : Arnoldi procedure

Let us consider now the stability of the quasi-equilibria computed in the previous section. We freeze the flow state obtained at time t_{end} and make it steady adopting the frame rotating with the vortices at angular speed $\Omega(t_{end} - t_\star; L)$. In this study, the stability analysis is restricted to a specific type of perturbations, namely to perturbations having the same helical symmetry as the base flow (of wavelength $2\pi L$). In that case one solves the linearised Navier-Stokes equations with helical symmetry in the frame rotating at $\Omega(t_{end} - t_\star; L)$ which implies to introduce the Coriolis force. More precisely, the dynamical equation for the velocity perturbation u'_B reads as

$$\partial_t u'_B + L_{u'} = VT_{u'} \tag{11}$$

where

$$L_{u'} \equiv \boldsymbol{e}_B \cdot \left[\boldsymbol{\omega'} \times \boldsymbol{u} + \boldsymbol{\omega} \times \boldsymbol{u'} - 2\Omega \boldsymbol{u'} \times \boldsymbol{e_z}\right] \tag{12}$$

$$VT_{u'} \equiv \nu \left[\mathbb{L}(\frac{u'_B}{\alpha}) - \frac{2\alpha^2}{L}\omega'_B\right]. \tag{13}$$

The dynamical equation for the vorticity perturbation ω'_B is

$$\partial_t \omega'_B + L_{\omega'} = VT_{\omega'} \tag{14}$$

where

$$\begin{aligned} L_{\omega'} \equiv\ & \boldsymbol{e}_B \cdot \boldsymbol{\nabla} \times \left[\boldsymbol{\omega'} \times \boldsymbol{u} + \boldsymbol{\omega} \times \boldsymbol{u'}\right] \\ & - 2\Omega \boldsymbol{\nabla} \times (\boldsymbol{u'} \times \boldsymbol{e_z}) \end{aligned} \tag{15}$$

$$\begin{aligned} VT_{\omega'} &\equiv -\nu\, \boldsymbol{e}_B \cdot \boldsymbol{\nabla} \times [\boldsymbol{\nabla} \times \boldsymbol{\omega'}] \\ &= \nu \left[\mathbb{L}(\frac{\omega'_B}{\alpha}) - \left(\frac{2\alpha^2}{L}\right)^2 \omega'_B \right. \\ &\quad \left. + \frac{2\alpha^2}{L}\mathbb{L}(\frac{u'_B}{\alpha})\right]. \end{aligned} \tag{16}$$

Introducing a perturbation vector $\boldsymbol{q'} = (u'_B,\ \omega'_B)^T$ of length $N = 2 \times N_r \times N_\theta$, the whole system can be written in a compact form :

$$\partial_t \boldsymbol{q'} = \mathbf{A}\, \boldsymbol{q'} \quad \text{with} \quad \boldsymbol{q'}(t_0) = \boldsymbol{q'_0} \tag{17}$$

where **A** is a linear operator and the initial condition $\boldsymbol{q'_0}$ is chosen adequately (see below). The exact solution of (17) is :

$$\boldsymbol{q'}(t_0 + \Delta t) = e^{\Delta t\, \mathbf{A}}\, \boldsymbol{q'_0} = \mathbf{B}\, \boldsymbol{q'_0} \tag{18}$$

We are looking for an accurate approximation of the $K \ll N$ leading eigenmodes $(\lambda_A, \boldsymbol{v}_A)$ of the operator **A** without actually constructing neither **A** nor **B**. Note that the action of **B** on $\boldsymbol{q'}$ is obtained by time marching the linearised code. Generally, one then constructs the set of K ("snapshots") vectors $\{\boldsymbol{q'_0},\ \mathbf{B}\boldsymbol{q'_0}, \ldots,\ \mathbf{B}^{K-1}\boldsymbol{q'_0}\}$ spanning the reduced Krylov subspace and thereafter one extracts informations on the unstable modes. Here, we proceed in a slightly different manner [13] : we progressively generate an orthonormal basis during the simulation from $t = t_0$ to $(K-1)\Delta t + t_0$. This orthonormal basis, the so-called *Krylov* vectors $\{\boldsymbol{v_1}, \ldots, \boldsymbol{v_K}\}$ is obtained as follows. Vector $\boldsymbol{v_1}$ is the normalized state at t_0 i.e. $\boldsymbol{v}_1 = \boldsymbol{q}'_0/||\boldsymbol{q}'_0||$. The kth *Krylov* vector $\boldsymbol{v_k}$ is obtained at time $t_{k-1} = (k-1)\Delta t + t_0$ of the simulation with the Arnoldi method :

$$\begin{aligned} \boldsymbol{w}_{k+1} = \mathbf{B}\boldsymbol{v}_k - \sum_{l=1}^{k} \boldsymbol{v}_l \mathbf{H}_{lk} \ \text{ with } \ \mathbf{H}_{lk} = (\boldsymbol{v}_l, \mathbf{B}\boldsymbol{v}_k) \\ \boldsymbol{v}_{k+1} = \boldsymbol{w}_{k+1}/||\boldsymbol{w}_{k+1}|| \end{aligned} \tag{19}$$

The above action is performed for $k = 1, ..., K-1$. At the end, we assemble the *Krylov* vectors in a $N \times K$ matrix **V**. It is the largest matrix we have to store and is needed to compute the eigenvectors of **A**. We also store the $K \times K$ upper Hessenberg matrix **H**, obtained during the orthogonalisation process. One can show that **H** is a low-dimensional approximation of $\mathbf{B} = e^{\Delta t \mathbf{A}}$ and that its eigenmodes $(\lambda_H, \boldsymbol{v}_H)$, also called the Ritz modes, are related to those $(\lambda_A, \boldsymbol{v}_A)$ of **A** by :

$$\lambda_A \sim \frac{\log(\lambda_H)}{\Delta t} \tag{20}$$

$$\boldsymbol{v}_A \sim \mathbf{V}\boldsymbol{v}_H \tag{21}$$

The matrix **H** being of small size, computational cost and memory storage of its eigenmodes are negligible. The time interval Δt and the number of computed eigenmodes K are chosen depending the cases. The Arnoldi method separates K modes by an orthogonalization process. Each mode k evolves during Δt and is being orthogonalized such that its contribution is removed from the (linearised) dynamic. Modes with high growth rates are easily separated from the others as they emerge even for low value of Δt. Modes with small growth rates needs longer time to emerge with sufficient accuracy. However choosing too big a Δt could be problematic : in that case, the snapshot information might be completely dominated by the most unstable mode. Here, for $L < 0.6$ (the most unstable cases) we chose $\Delta t = 5$ and $K = 50$ and for $L > 0.6$ $\Delta t = 20$, $K = 20$.

Initial condition $\boldsymbol{q'_0}$

The initial condition $\boldsymbol{q'_0}$ for the perturbation is chosen to be a random noise exciting all modes with equal amplitudes and having small amplitude outside the basic vorticity domain. In addition, q'_0 must have a zero circulation

$$\iint \omega'_z \, r\mathrm{d}r\mathrm{d}\theta = 0, \tag{22}$$

so that the circulation of the total flow remains unchanged with respect to the base flow. More precisely this can be written in the context of helical symmetry as

$$\iint \omega'_z \, r\mathrm{d}r\mathrm{d}\theta = \mathcal{K}'_\omega + \mathcal{K}'_u = 0 \tag{23}$$

$$\text{where} \quad \mathcal{K}'_\omega \equiv \iint_S \alpha \omega'_B \, r\mathrm{d}r\mathrm{d}\theta \tag{24}$$

$$\text{and} \quad \mathcal{K}'_u \equiv \iint_S r \frac{\alpha^2}{L} \frac{\partial}{\partial r} \left(\frac{u'_B}{\alpha} \right) r\mathrm{d}r\mathrm{d}\theta. \tag{25}$$

The initial perturbation field ω'_B and u'_B are obtained as follows :

$$\omega'_B(r,\theta) = C_1 \, \tilde{n}'_\omega(r,\theta) \, \omega_B(r,\theta) \tag{26}$$

$$u'_B(r,\theta) = C_2 \, \tilde{n}'_u(r,\theta) \, u_B(r,\theta) \tag{27}$$

where C_1 and C_2 are constants which are set to ensure $\mathcal{K}'_\omega + \mathcal{K}'_u = 0$ and $\tilde{n}'_\omega(r,\theta)$, $\tilde{n}'_u(r,\theta)$ are random noise components. We multiply the random noise by their corresponding base flow components to ensure that the initial perturbation field is localised within the basic vortex cores. The random noise components are computed in the Fourier space to get the quantities $\tilde{n}^{(m)'}_\omega(r)$, $\tilde{n}^{(m)'}_u(r)$. These quantities are further multiplied by a function in r^m to avoid singular behaviour near $r = 0$. We then compute the inverse Fourier transform to yield $\tilde{n}'_\omega(r,\theta)$ and $\tilde{n}'_u(r,\theta)$.

5 Results : Linear modes

Two Helical vortices

In this section we present the results of the linear stability analysis of two helical vortices with respect to helical perturbations of wavelength $2\pi L$. The most unstable mode is represented for the particular case $L = 0.3$ in figure 5 : its structure is localized within each basic vortex core where it takes the form of two lobs with opposite sign vorticity characteristic of a displacement mode. This structure can be better understood when looking at the 3-D representation of the mode as depicted in figure 5 : the mode induces a radial inward displacement for one vortex while the other vortex moves outwards. There exists also an axial displacement : indeed, if one looks at the vortices cut by a plane containing the $z - axis$ as depicted figure 5, the mode structure is very much similar to a pairing instability mode for a row of corotating vortices in two-dimensions.

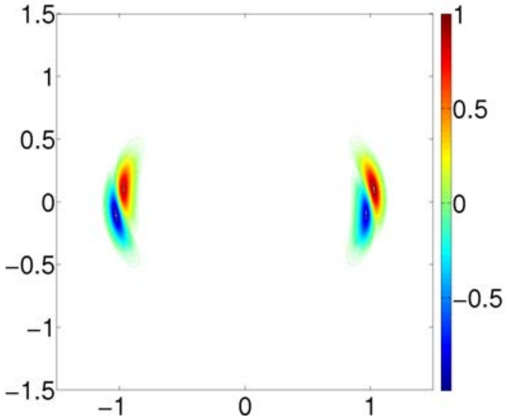

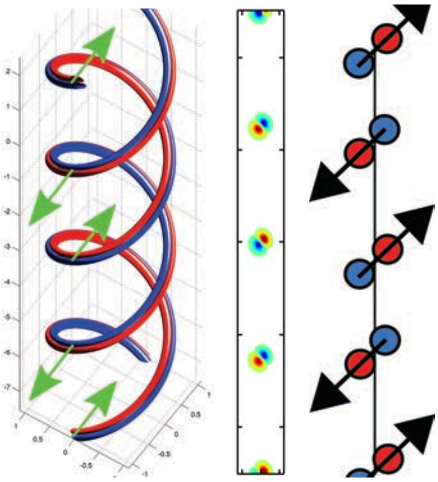

FIGURE 5 – *Structure of the most unstable mode. The base flow corresponds to two helical vortices with $L = 0.3$ and core size $a_b = 0.06$. (Top) Mode represented in the horizontal plane Π_0 by colored contours. (Bottom left) Mode in a 3-D representation. The arrows indicate the perturbation action on the base flow. The displacement induced by the mode has two components : one along the radial direction and one along the z direction. On the radial direction, one vortex goes inwards while the other goes outwards. (Bottom middle) Representation in the meridian (r,z) plane. (Bottom right) Schematic representation : the structure is analogous to the pairing instability mode for an infinite row of point vortices.*

The growth rate σ of the displacement mode is shown in figure 6 : as the pitch increases the growth rate decreases towards zero. This is coherent with Okulov *et al* results [9] that predicted that two helical Rankine vortices are unstable for $L < 1.1$ in the inviscid framework. For the present vortex configuration, we find that the threshold value is $L = 1.5$. This difference can be attributed to different values of core size and Reynolds number.

Another mode is always present : it is a stationary neutral mode shown in figure 7. It is also characterised by two lobs with opposite sign vorticity, which induces a displacement of the whole base flow in the azimuthal direction. This mode has no dynamical role and is due to the invariance of the base flow with respect to the azimuth.

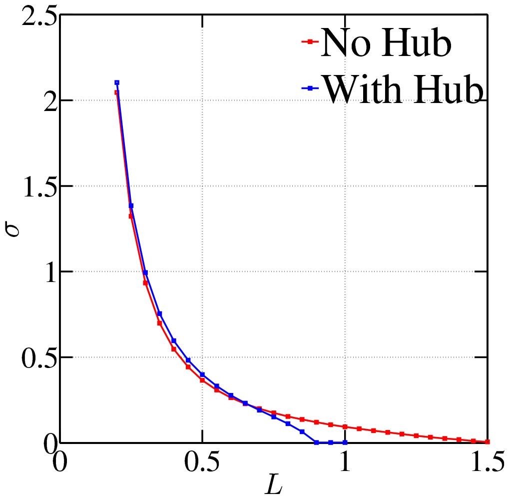

FIGURE 6 – *Growth rate σ of the displacement mode vs reduced pitch L. Red line : two helical vortices without a central hub. Blue line : two helical vortices with a central hub.*

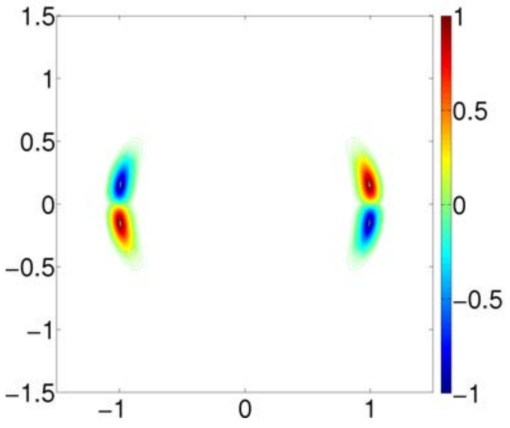

FIGURE 7 – *Neutral mode which exists due to the invariance of the base flow with respect to the azimuth. This mode only rotates the base flow in the clockwise direction.*

Two Helical vortices with a hub vortex

We investigate the influence of a central hub on the stability of two helical vortices. The core size of the hub is chosen as $2a_b$ that is twice the helical vortex core size and its circulation is $-N\Gamma$, ensuring a global circulation of the base flow be zero $\Gamma = 0$. The most unstable mode is also a displacement mode. Its structure is depicted in figure 9, the resulting mode resembles the previously obtained unstable mode for the case of two helical vortices with now a contribution arising from the hub vortex. The mode displaces the helical vortices the same manner as before, in addition the hub vortex moves off the axis. This reminds what was observed by Felli *et al.* [12] experimentally in a water channel. As seen in figure 6, the presence of the central hub does not significantly modify the growth rate for the range of parameters $L < 0.7$ while for $L > 0.7$ the growth rate abruptly decreases and the mode stabilises near $L = 0.9$.

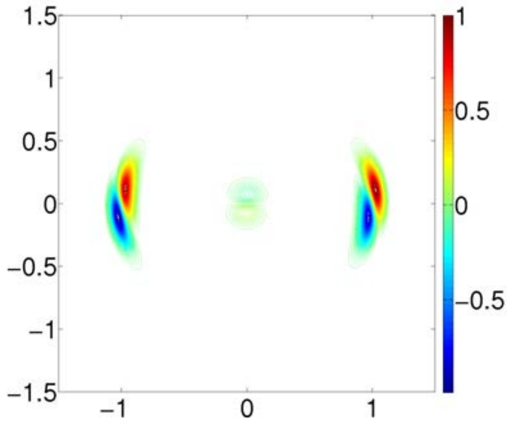

FIGURE 8 – *Most unstable mode for the case of two vortices with $L = 0.3$ and a central hub vortex of core size $2a_b$. The resulting instability mode can be described as a displacement mode for both helical vortices and the hub vortex as well.*

6 Results : Nonlinear evolution

Leapfrog mechanism

The nonlinear evolution of two helical vortices without hub is presented here when they are initially perturbed with an unstable displacement mode of small amplitude. It is observed that the two vortices undergo a leapfrogging process until they merge due to viscous diffusion. The number of leapfrog before the merging occurs seems to vary with L, the core size a_b and Re. The time evolution of the mechanism is showed figure 10 for the particular case of $L = 0.3$. This dynamic has been observed experimentally by Leweke *et al* [10] and Felli *et al* [12] in water channels and confirms that this instability also occurs in a non-helically symmetric framework.

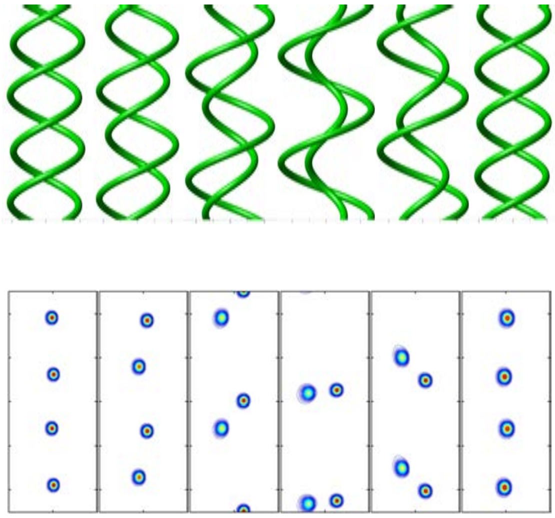

FIGURE 9 – *The vortices undergo a leapfrogging process. Time evolution goes from left to right. Top figures : Isovalue of the vorticity component $\omega_B = 10$ represented at different instants for two helical vortices of pitch $L = 0.3$ and core size $a_b = 0.06$. Bottom figures : vorticity component ω_B in the (r, z)-plane.*

Merging of two helical vortices

The vortices merge after a number of leapfrogs due to viscous diffusion. The time evolution of the merging is shown figure 11 in the meridian plane and with 3-D plot of iso-value of the helical vorticity. A first vortex attempts to leapfrog but its core size being too important, it touches the other vortex (see-figure 11a) thus prompting a vortex roll-up fallowed by a full vortex merging.

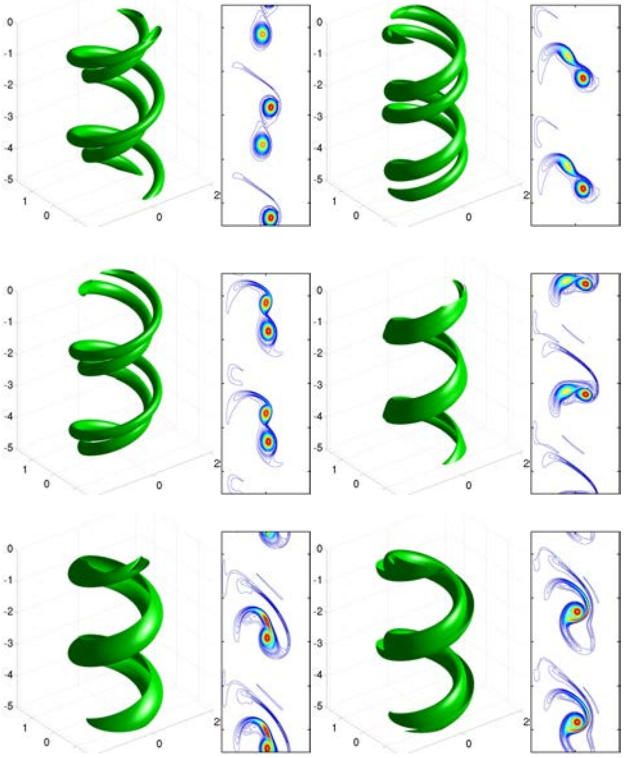

FIGURE 10 – *Isovalue of the vorticity component $\omega_B = 4$ of two helical vortices of pitch $L = 0.3$ and core size $a_b = 0.06$ represented at different instants. Time evolution goes from left to right and top to bottom.*

7 Conclusion

In this paper, we considered the linear stability analysis of 2 helical vortices of small core size a_b (with respect to the helix radius) with and without a central hub vortex. For the base flows, quasi-equilibrium solutions with controlled characteristics have been computed by using a generic initial condition procedure and by enforcing the helical symmetry into the Navier-Stokes equations. After freezing these quasi-equilibria basic states, we performed the linear stability analysis with respect to helical symmetric perturbations of wavelength $2\pi L$. Unstable modes were extracted with a linearised version of our DNS code

HELIX [6] coupled to an Arnoldi procedure [13]. The results are straightforward : within this framework, the dominant modes for all cases considered is a (helical) displacement mode. Growth rates have been computed for a large range of reduced pitch values. The results are found coherent with the analysis of Okulov *et al.* [9], but a higher threshold value has been found $L = 1.5$ instead of $L = 1.1$. The effect of a central hub vortex with core size $a_{hub} = 2a_b$ has been considered. Again the most unstable mode is a displacement mode slightly modified by the presence of the hub vortex. Its presence does not significantly modify the growth rate for the range of parameters $L < 0.7$ but the mode abruptly becomes neutral around $L = 0.9$. This mode shows that the hub moves off from the axis during the instability.

Nonlinear computations for two helical vortices perturbed with the unstable displacement mode have been performed. The vortices undergo a leapfrogging process before they merge due to viscous diffusion. These dynamics were observed experimentally by Leweke *et al* [10] and Felli *et al* [12] in water channels and confirm that this instability also occurs in a non-helically symmetric framework. A full 3-D computation would be of interest in order to characterize the spatial evolution of the vortices and the small scale structures generated within such dynamics (work in progress).

Acknowledgements

This work received support from the French *Agence Nationale de la Recherche* under the ANR HELIX project ANR-12-BS09-0023-01.
HPC resources from GENCI–IDRIS (grant 2014-2a1386) are also acknowledged.

References

[1] J. C. Hardin (1982) The velocity field induced by a helical vortex filament. *Phys. Fluids* **25**(11), 1949–1952.

[2] P. A. Kuibin, and V. L. Okulov (1998) Self-induced motion and asymptotic expansion of the velocity field in the vicinity of a helical vortex filament. *Phys. Fluids* **10**, 607–614.

[3] D. W. Moore, and P. G. Saffman (1972) The motion of a vortex filament with axial flow. *Philos. Trans. R. Soc. London, Ser. A* **272**, 403–429.

[4] J. Boersma and D.H. Wood On the self-induced motion of a helical vortex. (1998) *J. Fluid Mech.* **384**, 263–280.

[5] Y. Fukumoto, and V. L. Okulov (2005) The velocity field induced by a helical vortex tube. *Phys. Fluids* **17**, 107101.

[6] I. Delbende, M. Rossi and O. Daube DNS of flows with helical symmetry *Theo. Comp. Fluid Dyn.* **26**, 148–175.

[7] S. E. Widnall (1972) The stability of a helical vortex filament. *J. Fluid Mech.* **54**, 641–663.

[8] V. L. Okulov On the stability of multiple helical vortices *J. Fluid Mech.* **521**, 319–342.

[9] V. L. Okulov and J. N. Sørensen Stability of helical tip vortices in a rotor far wake *J. Fluid Mech.* **576**, 1–25.

[10] Th. Leweke, H. U. Quaranta, H. Bolnot, F. J. Blanco Rodriguez and S. Le Dizés Long and short wave instabilities in helical vortices (2014) *J. of Physics : Conference Series.* **524**

[11] H. Bolnot Instabilités de tourbillons hélicoïdaux : application au sillage des rotors *Ph.D. Thesis.*

[12] M. Felli, R. Camussi and F. Di Felice Mechanisms of evolution of the propeller wake in the transition and far fields *J. Fluid Mech.* **150**, 1–49

[13] W. S. Edwards, L. S. Tuckerman, R. A. Friesner and D. C. Sorensen (1994) Krylov Methods for the Incompressible Navier-Stokes Equations *J. Comp. Phys.* **110**, 82–102.

[14] D. Lucas, and D. G. Dritschel (2009) A family of helically symmetric vortex equilibria. *J. Fluid Mech.* **634**, 245–268.

[15] O. Daube (1992). Resolution of the 2D Navier–Stokes equations in velocity/vorticity form by means of an influence matrix technique. *J. Comp. Phys.* **103**, 402–414.

[16] C. Josserand, and M. Rossi (2007) The merging of two co-rotating vortices : a numerical study. *Eur. J. Mech. B/Fluid.* **26**, 779–794.

[17] N. Riley, and D. P. Stevens (1992) A note on leapfrogging vortex rings. *Fluid Dyn. Res.* **11**, 235–244.

Bibliography

M. Abramowitz and I. Stegun. *Handbook of Mathematical Functions*. Dover Publications, 1965.

P. H. Alfredsson and J. A. Dahlberg. A preliminary wind tunnel study of windmill wake dispersion in various flow conditions, part 7. 1979.

Mohamed Ali and Malek Abid. Self-similar behaviour of a rotor wake vortex core. *Journal of Fluid Mechanics*, 740, 2 2014. ISSN 1469-7645. doi: 10.1017/jfm.2013.636. URL `http://journals.cambridge.org/article_S0022112013006368`.

Morten Andersen and Morten Brøns. Topology of helical fluid flow. *European Journal of Applied Mathematics*, 25(03):375–396, 2014. ISSN 0956-7925. doi: 10.1017/S0956792514000084.

Francisco J. Blanco-Rodríguez, Stéphane Le Dizès, Can Selçuk, Ivan Delbende, and Maurice Rossi. Internal structure of vortex rings and helical vortices. *Journal of Fluid Mechanics*, 785:219–247, 12 2015. ISSN 1469-7645. doi: 10.1017/jfm.2015.631. URL `http://journals.cambridge.org/article_S002211201500631X`.

H. Bolnot, S. Le Dizès, and T. Leweke. Spatio-temporal development of the pairing instability in an infinite array of vortex rings. *Fluid Dyn. Res.*, 46(6):061405, 2014. ISSN 1873-7005. doi: 10.1088/0169-5983/46/6/061405. URL `http://stacks.iop.org/1873-7005/46/i=6/a=061405`.

Hadrien Bolnot. *Instabilités des tourbillons hélicoïdaux: application au sillage des rotors*. Thèse de doctorat, Aix-Marseille Université, France, 2012.

P. Brancher and J. M. Chomaz. Absolute and Convective Secondary Instabilities in Spatially Periodic Shear Flows. *Phys. Rev. Lett.*, 78(4):658–661, January 1997. doi: 10.1103/PhysRevLett.78.658. URL `http://link.aps.org/doi/10.1103/PhysRevLett.78.658`.

Russell Carden. *Ritz values and Arnoldi convergence for non-Hermitian matrices*. Thesis, Rice University, 2012. URL `https://scholarship.rice.edu/handle/1911/70215`.

I. Delbende and M. Rossi. Dynamics of the three helical vortex system and instability. 2013. URL `http://perso.limsi.fr/Individu/delbende/pub/icowes2013/DelbendeRossi2013.pdf`.

Ivan Delbende and Maurice Rossi. Nonlinear evolution of a swirling jet instability. *Physics of Fluids (1994-present)*, 17(4):044103, April 2005. ISSN 1070-6631, 1089-7666. doi: 10.1063/1.1868412. URL `http://scitation.aip.org/content/aip/journal/pof2/17/4/10.1063/1.1868412`.

Ivan Delbende and Maurice Rossi. The dynamics of a viscous vortex dipole. *Physics of Fluids (1994-present)*, 21(7):073605, 2009.

Ivan Delbende, Maurice Rossi, and Olivier Daube. Dns of flows with helical symmetry. *Theoretical and Computational Fluid Dynamics*, 26(1):141–160, 2012. ISSN 1432-2250. doi: 10.1007/s00162-011-0241-y. URL `http://dx.doi.org/10.1007/s00162-011-0241-y`.

Ivan Delbende, Benjamin Piton, and Maurice Rossi. Merging of two helical vortices. *European Journal of Mechanics - B/Fluids*, 49, Part B:363–372, January 2015. ISSN 0997-7546. doi: 10.1016/j.euromechflu.2014.04.005. URL `http://www.sciencedirect.com/science/article/pii/S0997754614000570`.

D. G. Dritschel. Generalized helical Beltrami flows in hydrodynamics and magnetohydrodynamics. *J. Fluid Mech.*, 222:525–541, 1991.

W. S. Edwards, L. S. Tuckerman, R. A. Friesner, and D. C. Sorensen. Krylov Methods for the Incompressible Navier-Stokes Equations. *Journal of Computational Physics*, 110(1):82–102, January 1994. ISSN 0021-9991. doi: 10.1006/jcph.1994.1007. URL `http://www.sciencedirect.com/science/article/pii/S0021999184710072`.

Maroi Felli, Roberto Camussi, and F. Di Felice. Mechanisms of evolution of the propeller wake in the transition and far fields. *Journal of Fluid Mechanics*, 682:5–53, 2011. URL `http://journals.cambridge.org/abstract_S0022112011001509`.

K. S. Fine, C. F. Driscoll, J. H. Malmberg, and T. B. Mitchell. Measurements of symmetric vortex merger. *Physical review letters*, 67(5):588, 1991. URL `http://journals.aps.org/prl/abstract/10.1103/PhysRevLett.67.588`.

Y. Fukumoto and V. L. Okulov. The velocity field induced by a helical vortex tube. *Phys. Fluids*, 17:107101, 2005.

François Gallaire and Jean-Marc Chomaz. Three-dimensional instability of isolated vortices. *Physics of Fluids*, 15(8):2113–2126, 2003. doi: 10.1063/1.1580481. URL `https://hal-polytechnique.archives-ouvertes.fr/hal-01024926`.

B.P. Gupta and R.G. Loewy. Theoretical Analysis of the Aerodynamic Stability of Multiple, Interdigitated Helical Vortices. *AIAA Journal*, 12(10):1381–1387, October 1974. ISSN 0001-1452. doi: 10.2514/3.49493. URL `http://dx.doi.org/10.2514/3.49493`.

J. C. Hardin. The velocity field induced by a helical vortex filament. *Phys. Fluids*, 25: 1949, 1982.

Charlotte Bay Hasager, Leif Rasmussen, Alfredo Peña, Leo E. Jensen, and Pierre-Elouan Réthoré. Wind Farm Wake: The Horns Rev Photo Case. *Energies*, 6(2):696–716, February 2013. doi: 10.3390/en6020696. URL `http://www.mdpi.com/1996-1073/6/2/696`.

Y. Hattori and Y. Fukumoto. Short-wavelength stability analysis of a helical vortex tube. *Physics of Fluids (1994-present)*, 21(1):014104, January 2009. ISSN 1070-6631, 1089-7666. doi: 10.1063/1.3054150. URL `http://scitation.aip.org/content/aip/journal/pof2/21/1/10.1063/1.3054150`.

Yuji Hattori and Yasuhide Fukumoto. Modal stability analysis of a helical vortex tube with axial flow. *Journal of Fluid Mechanics*, 738:222–249, January 2014. ISSN 1469-7645. doi: 10.1017/jfm.2013.591. URL `http://journals.cambridge.org/article_S0022112013005910`.

Rutger H. A. IJzermans, Rob Hagmeijer, and Pieter J. van Langen. Accumulation of heavy particles around a helical vortex filament. *Physics of Fluids (1994-present)*, 19(10): 107102, October 2007. ISSN 1070-6631, 1089-7666. doi: 10.1063/1.2771658. URL `http://scitation.aip.org/content/aip/journal/pof2/19/10/10.1063/1.2771658`.

Stefan Ivanell, Jens N. Sø rensen, and Dan Henningson. Numerical Computations of Wind Turbine Wakes. In Prof Dr Joachim Peinke, Prof Dr-Ing Peter Schaumann, and Dr Stephan Barth, editors, *Wind Energy*, pages 259–263. Springer Berlin Heidelberg, 2007. ISBN 978-3-540-33865-9 978-3-540-33866-6. URL `http://link.springer.com/chapter/10.1007/978-3-540-33866-6_48`. DOI: 10.1007/978-3-540-33866-6_48.

Stefan Ivanell, Jens N. Sø rensen, Robert Mikkelsen, and Dan Henningson. Analysis of numerically generated wake structures. *Wind Energ.*, 12(1):63–80, January 2009. ISSN 1099-1824. doi: 10.1002/we.285. URL `http://onlinelibrary.wiley.com/doi/10.1002/we.285/abstract`.

Javier Jiménez, H. K. Moffatt, and Carlos Vasco. The structure of the vortices in freely decaying two-dimensional turbulence. *Journal of Fluid Mechanics*, 313:209–222, 4 1996. ISSN 1469-7645. doi: 10.1017/S0022112096002182. URL `http://journals.cambridge.org/article_S0022112096002182`.

Ch Josserand and M. Rossi. The merging of two co-rotating vortices: a numerical study. *European Journal of Mechanics - B/Fluids*, 26(6):779–794, 2007. doi: 10.1016/j.euromechflu.2007.02.005. URL `http://dx.doi.org/10.1016/j.euromechflu.2007.02.005`.

Olga Kelbin, Alexei F. Cheviakov, and Martin Oberlack. New conservation laws of helically symmetric, plane and rotationally symmetric viscous and inviscid flows. *Journal of Fluid Mechanics*, 721:340–366, 4 2013. ISSN 1469-7645. doi: 10.1017/jfm.2013.72. URL `http://journals.cambridge.org/article_S0022112013000724`.

Shigeo Kida. Motion of an Elliptic Vortex in a Uniform Shear Flow. *J. Phys. Soc. Jpn.*, 50(10):3517–3520, October 1981. ISSN 0031-9015. doi: 10.1143/JPSJ.50.3517. URL `http://journals.jps.jp/doi/abs/10.1143/JPSJ.50.3517`.

P. A. Kuibin and V. L. Okulov. Self-induced motion and asymptotic expansion of the velocity field in the vicinity of a helical vortex filament. *Phys. Fluids*, 10:607, 1998.

Horace Lamb. *Hydrodynamics*. Cambridge university press, 1932.

Stéphane Le Dizès and Alberto Verga. Viscous interactions of two co-rotating vortices before merging. *Journal of Fluid Mechanics*, 467:389–410, 2002. URL `https://hal.archives-ouvertes.fr/hal-00084159`.

H. Levy and A. G. Forsdyke. The Stability of an Infinite System of Circular Vortices. *Proceedings of the Royal Society of London. Series A, Containing Papers of a Mathematical and Physical Character*, 114(768):594–604, 1927. ISSN 0950-1207. URL `http://www.jstor.org/stable/94831`.

Thomas Leweke, Stéphane Le Dizès, and Charles H. K. Williamson. Dynamics and Instabilities of Vortex Pairs. *Annual Review of Fluid Mechanics*, 48(1):507–541, 2016. doi: 10.1146/annurev-fluid-122414-034558. URL `http://dx.doi.org/10.1146/annurev-fluid-122414-034558`.

H. Ralph Lewis and Paul M. Bellan. Physical constraints on the coefficients of Fourier expansions in cylindrical coordinates. *J. Math. Phys*, 31(11):2592–2596, November 1990.

ISSN 0022-2488 (print), 1089-7658 (electronic), 1527-2427. doi: http://dx.doi.org/10.1063/1.529009. URL http://jmp.aip.org/resource/1/jmapaq/v31/i11/p2592_s1.

Jean-Christophe Loiseau, Jean-Christophe Robinet, Stefania Cherubini, and Emmanuel Leriche. Investigation of the roughness-induced transition: global stability analyses and direct numerical simulations. *Journal of Fluid Mechanics*, 760:175–211, 12 2014. ISSN 1469-7645. doi: 10.1017/jfm.2014.589. URL http://journals.cambridge.org/article_S0022112014005898.

J. M. Lopez, F. Marques, and Jie Shen. An Efficient Spectral-projection Method for the Navier–Stokes Equations in Cylindrical Geometries. *J. Comput. Phys.*, 176(2): 384–401, March 2002. ISSN 0021-9991. doi: 10.1006/jcph.2002.6993. URL http://dx.doi.org/10.1006/jcph.2002.6993.

Dan Lucas and David G. Dritschel. A family of helically symmetric vortex equilibria. *Journal of Fluid Mechanics*, 634:245–268, 9 2009. ISSN 1469-7645. doi: 10.1017/S0022112009007319. URL http://journals.cambridge.org/article_S0022112009007319.

Patrice Meunier. *Etude expérimentale de deux tourbillons corotatifs*. phdthesis, Université de Provence - Aix-Marseille I, December 2001. URL https://tel.archives-ouvertes.fr/tel-00011665/document.

Patrice Meunier, Uwe Ehrenstein, Thomas Leweke, and Maurice Rossi. A merging criterion for two-dimensional co-rotating vortices. *Physics of Fluids*, 14, n° 8:2757–2766, 2002. doi: 10.1063/1.1489683. URL https://hal.archives-ouvertes.fr/hal-00081683. 10 p.

Andras Nemes. *Helical vortices in rotor wakes*. thesis, Monash University. Faculty of Engineering. Department of Mechanical and Aerospace Engineering, 2015. URL http://arrow.monash.edu.au/vital/access/manager/Repository/monash:163689.

Karl Nilsson, Stefan Ivanell, Kurt S. Hansen, Robert Mikkelsen, Jens N. Sø rensen, Simon-Philippe Breton, and Dan Henningson. Large-eddy simulations of the Lillgrund wind farm. *Wind Energ.*, 18(3):449–467, March 2015. ISSN 1099-1824. doi: 10.1002/we.1707. URL http://onlinelibrary.wiley.com/doi/10.1002/we.1707/abstract.

V. L. Okulov. On the stability of multiple helical vortices. *J. Fluid Mech.*, 521:319–342, 2004.

V. L. Okulov and J. N. Sørensen. Stability of helical tip vortices in a rotor far wake. *J. Fluid Mech.*, 576:1–25, 2007.

Benjamin Piton. *Simulations de tourbillons à symétrie hélicoïdale*. PhD thesis, Université Pierre et Marie Curie-Paris 6, 2011.

Hugo Umberto Quaranta, Hadrien Bolnot, and Thomas Leweke. Long-wave instability of a helical vortex. *Journal of Fluid Mechanics*, 780:687–716, 2015. URL http://journals.cambridge.org/abstract_S0022112015004796.

Renzo L. Ricca. The effect of torsion on the motion of a helical vortex filament. *Journal of Fluid Mechanics*, 273:241–259, August 1994. ISSN 1469-7645. doi: 10.1017/S0022112094001928. URL http://journals.cambridge.org/article_S0022112094001928.

N Riley and D P Stevens. A note on leapfrogging vortex rings. *Fluid Dyn. Res.*, 11(5): 235, 1993. URL http://stacks.iop.org/1873-7005/11/i=5/a=A05.

P. G. Saffman. *Vortex Dynamics*. Cambridge University Press, 1992. ISBN 9780511624063. URL `http://dx.doi.org/10.1017/CBO9780511624063`. Cambridge Books Online.

Scott Schreck. The NREL full-scale wind tunnel experiment Introduction to the special issue. *Wind Energ.*, 5(2-3):77–84, April 2002. ISSN 1099-1824. doi: 10.1002/we.72. URL `http://onlinelibrary.wiley.com/doi/10.1002/we.72/abstract`.

Michael Sherry, András Nemes, David Lo Jacono, Hugh M. Blackburn, and John Sheridan. The interaction of helical tip and root vortices in a wind turbine wake. *Physics of Fluids*, 25(11):117102, 2013. ISSN 10706631. doi: 10.1063/1.4824734. URL `http://scitation.aip.org/content/aip/journal/pof2/25/11/10.1063/1.4824734`.

Denis Sipp, Laurent Jacquin, and Carlo Cosssu. Self-adaptation and viscous selection in concentrated two-dimensional vortex dipoles. *Physics of Fluids*, 12(2):245, 2000. ISSN 10706631. doi: 10.1063/1.870325. URL `http://scitation.aip.org/content/aip/journal/pof2/12/2/10.1063/1.870325`.

H. Snel, J. G. Schepers, and B. Montgomerie. The MEXICO project (Model Experiments in Controlled Conditions): The database and first results of data processing and interpretation. *J. Phys.: Conf. Ser.*, 75(1):012014, 2007. ISSN 1742-6596. doi: 10.1088/1742-6596/75/1/012014. URL `http://stacks.iop.org/1742-6596/75/i=1/a=012014`.

Jens N. Sørensen and Asger Myken. Unsteady actuator disc model for horizontal axis wind turbines. *Journal of Wind Engineering and Industrial Aerodynamics*, 39(1):139–149, January 1992. ISSN 0167-6105. doi: 10.1016/0167-6105(92)90540-Q. URL `http://www.sciencedirect.com/science/article/pii/016761059290540Q`.

L. J. Vermeer, J. N. Sø rensen, and A. Crespo. Wind turbine wake aerodynamics. *Progress in Aerospace Sciences*, 39(6–7):467–510, August 2003. ISSN 0376-0421. doi: 10.1016/S0376-0421(03)00078-2. URL `http://www.sciencedirect.com/science/article/pii/S0376042103000782`.

Theodor von Kàrmàn and H. Rubach. Über den mechanismus des flüssigkeits-und luftwiderstandes. *Phys. Z*, 13(2), 1912.

S. E. Widnall. The stability of a helical vortex filament. *J. Fluid Mech.*, 54:641–663, 1972. ISSN 1469-7645.

S. E. Widnall, D. Bliss, and A. Zalay. Theoretical and Experimental Study of the Stability of a Vortex Pair. In John H. Olsen, Arnold Goldburg, and Milton Rogers, editors, *Aircraft Wake Turbulence and Its Detection*, pages 305–338. Springer US, 1971. ISBN 978-1-4684-8348-2 978-1-4684-8346-8. URL `http://link.springer.com/chapter/10.1007/978-1-4684-8346-8_19`. DOI: 10.1007/978-1-4684-8346-8_19.

D. H. Wood and J. Boersma. On the motion of multiple helical vortices. *Journal of Fluid Mechanics*, 447:149–171, November 2001. ISSN 0022-1120, 1469-7645. doi: 10.1017/S002211200100578X. URL `http://www.journals.cambridge.org/abstract_S002211200100578X`.

J.Z. Wu, H. Ma, and M.D. Zhou. *Vorticity and Vortex Dynamics*. Lecture notes in mathematics. Springer Berlin Heidelberg, 2007. ISBN 9783540290285. URL `https://books.google.fr/books?id=P5yNCu44PiwC`.

Savaş Can Selçuk **May 9, 2016**

Sujet : Étude numérique des instabilités de tourbillons hélicoïdaux

Résumé : Le travail présenté dans ce mémoire est une contribution à l'étude numérique des systèmes tourbillonnaires hélicoïdaux qui sont émis dans le sillage des rotors (éoliennes, hélicoptères, ...) et de leurs instabilités. Ici, ces écoulements sont localement modélisés par un ensemble de tourbillons à symétrie hélicoïdale. À l'aide d'un code de simulation numérique directe dédié, des solutions de base quasi-stationnaires sont obtenues pour différents systèmes tourbillonnaires. Elles sont caractérisées avec précision : vitesse de rotation, taille et ellipticité du cœur, structure des champs de vitesse et de vorticité ... À l'aide d'un algorithme d'Arnoldi couplé à une version linéarisée du code, on détermine les modes dominants d'instabilité ayant la même symétrie que l'écoulement de base, en fonction des paramètres du système : nombre de vortex, pas hélicoïdal, taille de cœur, nombre de Reynolds et présence d'un vortex de moyeu. En dessous d'un certain pas hélicoïdal critique, l'instabilité est dominée par un mode de déplacement global analogue au mode d'appariement d'une allé infinie de points vortex ou d'anneaux tourbillonnaires. En régime non linéaire, ce mode est à l'origine d'une dynamique complexe du système : dépassements, saute-mouton et fusion. On utilise un autre code linéarisé pour déterminer les modes instables qui brisent la symétrie hélicoïdale de l'état de base, caractérisés par une longueur suivant l'axe. À faible nombre d'onde, ces modes induisent localement des rapprochements entre portions de spires voisines. À grand nombre d'onde, on observe un autre type de mode qui déforme les cœurs tourbillonnaires via l'instabilité elliptique.

Subject : Numerical study of helical vortices and their instabilities

Abstract : The work presented in this manuscript is a contribution to the numerical study of helical vortex systems and their instabilities, as encountered in the near wake of rotors (wind turbines, helicopters, ...). In this work, such flows are locally modelled within the framework of helical symmetry. Using a dedicated DNS code, helical quasi-stationary basic state solutions are obtained for several configurations, and accurate tools for their characterisation are developed: angular velocity, core size and ellipticity, structure of the velocity and vorticity fields... An Arnoldi algorithm is then coupled to a linearised version of the code. The dominant instability modes with the same symmetry as the base flow are extracted as a function of the system parameters: number of vortices, helical pitch, core size, Reynolds number, presence of a central hub vortex. Under a critical helical pitch, the instability is dominated by a global displacement mode analogous to the pairing mode of an infinite array of point vortices or vortex rings. In the nonlinear regime, this mode gives rise to complex dynamics: overtaking events, leapfrogging and merging. Another linearised code is then used to extract modes characterised by a wavelength along the helix, which break the helical symmetry of the base flow. At low wavenumbers, these modes induce local displacements of the vortices and bring together portions of neighbouring coils. At large wavenumbers, another type of mode is found, which deforms the vortex cores through the elliptical instability mechanism.